Three-dimensional Borehole Radar Imaging

by

Pradip Kumar Mukhopadhyay

M.Sc.Tech (Applied Geophysics)

A thesis submitted to the Department of Electrical Engineering,
University of Cape Town, in fulfilment of the requirements
for the degree of

Doctor of Philosophy

at the

University of Cape Town

November 2005

Declaration

I declare that this dissertation is my own, unaided work. It is being submitted for the degree of Doctor of Philosophy at the University of Cape Town. It has not been submitted before for any degree or examination in any other university.

Signature of Author . . . .

Department of Electrical Engineering
Cape Town, 22^{nd} November 2005

Abstract

Before embarking on any mining operation, it is advantageous to locate the subsurface orebody in three-dimensions with a high resolution (~1m) ahead of actual mining, because this will increase productivity and efficiency. Borehole radar is such an emerging mapping tool in the mining industry, that can be used to image the subsurface orebody with high resolution.

3-D subsurface imaging using two-dimensional aperture synthesis requires many boreholes and is thus not economically feasible in underground orebody imaging. Therefore, the main objective of this thesis is to develop 3-D imaging techniques, using a limited number of boreholes.

An interferometric synthetic aperture radar (InSAR) is a well established space-borne/air-borne technique for mapping the Earth's surface. A borehole InSAR simulation study was thus carried out, using a sidelooking antenna configuration to image the subsurface orebodies, such as potholes and cylindrical Kimberlite structures, in 3-D. A performance analysis of an interferometric experiment is presented.

In general, borehole radars are a wide-band system, often having bandwidths of 75% of the centre frequency. A 3-D image reconstruction technique was developed by means of correlation-type processing, using magnitude images of multiple boreholes coming from different view angles, which is more suitable for wide-band/ultra wide-band borehole radar signals. The technique was tested by using simulated multiple borehole radar magnitude images, as well as real acoustic images that had been captured in air and water media. The 3-D reconstructed grid spacing derivations are presented for a borehole trajectory fanning outward from the borehole centre. In this thesis, a 40kHz air-based sonar system was used in the laboratory environment to emulate inverse synthetic aperture radar (ISAR) data in the context of a real borehole experiment. A deconvolution processing approach was adopted to range-compress the 40kHz sonar data captured in air. A time domain focusing technique was used to focus the simulated borehole radar as well as the real acoustic data.

In the case of homogeneous, isotropic and non-dispersive media, a straight-line wave propagation is considered to process the data in range and azimuth. In a real borehole environment, however, an accurate electromagnetic (EM) wave propagation model is essential. For the purpose of modelling borehole EM propagation in a conductive medium, 3-D finite difference time domain (FDTD) code was written and implemented in a Cartesian coordinate system by using a uniaxial perfectly matched layer boundary wave absorber. The accuracy of the implemented code was first tested against published results. Thereafter, the code was used to simulate the EM responses from various geological settings, such as cross-well borehole EM wave propagation in a sedimentary layer, reflection from a geological reverse fault, and reflection from a pothole-type orebody structure. Different kinds of imaging modes have been used in the FDTD simulation experiment, such as common offsets, common source and transillumination mode. The radar traces, both transmitted as well as reflected, are affected by the size of the borehole and the electrical properties of borehole mud. It was found that the electrical properties of the borehole mud affect the radar traces more significantly than the size of the borehole. The effect of host rock conductivity on radar traces has also been investigated.

To ensure the accuracy and stability of the FDTD method, the discrete step size of the simulation needs to be set to less than $\frac{1}{10}$th of the minimum significant wavelength. Therefore, for realistic 3-D simulations, there is a requirement for large matrices to be allocated and processed, which easily exceed the limits of a standard desktop PC in terms of memory and speed. In order to overcome these limitations, a parallel version of the 3-D FDTD C code has been implemented using Parallel Virtual Machine (PVM) as *middleware* running on a *Beowulf-type* Linux cluster. A speed up of 2.7 was achieved, which corresponds to a 90% efficiency, where a speed of 3 for three slave processors is considered to be 100% efficient.

The signal processing techniques investigated in this thesis have been verified on simulated borehole radar data, as well as on real sonar data. These techniques can therefore also be applied to real borehole data, in order to construct 3-D images of subsurface orebodies.

… dedicated to

my brother, Sudip Mukhopadhyay,
my father

and in memory of my mother

Acknowledgements

I would most sincerely like to thank my supervisors, Professor Michael Inggs and Dr. Andrew J. Wilkinson, for all their guidance, support and numerous technical input in shaping up my thesis from its embryonic stage to its final stage. Over the years I have benefited greatly from their expertise throughout my research work.

I wish to thank Dr. Richard Lord for his help throughout the thesis period; I learned most of the signal processing techniques in electrical engineering from him. I would also like to thank all the fellow graduates in the Radar Remote Sensing Group for providing a cheerful and stimulating work environment.

I am thankful to Professor Iain Mason and Naomi Osman for supplying acoustic data from their test facility at Sydney University. I am also indebted to Professor David B Davidson for his help in FDTD work. I would like to acknowledge to the late Rolf Lengenfelder, whose SAR simulation software was used in the research work.

I would like to express my gratitude towards my family for their mental support throughout the research period. I would like to thank Sudeshna Mukhopadhyay, for helping me to carry out the acoustic experiment.

Greatful thanks to my friend, Dodul Bhattacharya, for inspiring and encouraging me to pursue higher studies. I would like to thank my aunt, Putul Benerjee and her husband for their support throughout my studies. I would also like to thank my bother-in-law, Manab Bhattacharya, for his constant encouragement for higher studies.

Finally, I would like to thank Regine Lord for her numerous useful comments at the time of editing.

Contents

5 Three-dimensional Borehole Radar Modelling Study using the Finite Difference Time Domain Method 115

6 Conclusions and Scope for Future Research 169

List of Tables

List of Symbols

B — Transmitted RF bandwidth [Hz]
B_x — Spatial bandwidth [cycles/m]
c — Speed of light [m/sec]
c_1 — Velocity of propagation in a medium [m/sec]
$V_{x,y,z}$ — $X, Y, Z-$velocity vector along the antenna trajectory
f_0 — Carrier frequency [Hz]
Δf — Frequency step [Hz]
D — Largest dimensional of antenna [m]
$\mathbf{E}$ — Electrical field [V/m]
$\mathbf{H}$ — Magnetic field [amp/m]
$X(f)$ — Spectrum of the function $x(t)$
$X^+(f)$ — Positive half of a real spectrum
$X^-(f)$ — Negative half of a real spectrum
G — Antenna gain
$h_{bb}(t)$ — Basebanded transducers and other linear system effect
$\delta(t)$ — Dirac delta function
$H_{MF}(f)$ — Matched filter response function
$H_{dec}(f)$ — Deconvolution filter response function
$H_s(f)$ — Baseband system response function
$S_n(f)$ — Power spectral density of noise
γ — Correlation coefficent between SLC images, also known as coherence
γ_{geom} — Geometrical coherence
γ_{SNR} — Coherence due to finite SNR of different SLC images
γ_{time} — Temporal coherence
σ_ψ — Phase standard deviation [cycles]
σ_z — Displacement standard deviation
$\triangle\varphi_{amb}$ — Phase ambiguity spacing [radian]
$\triangle r_{amb}$ — Range ambiguity spacing [m]

$\triangle\alpha$ — Difference in look angle [radian]
γ_{time} — Temporal coherence
γ_{time} — Temporal coherence
δt_{3-dB} — $3-dB$ time resolution [sec]
δR_{3-dB} — $3-dB$ range resolution [m]
δR — Slant range spacing [m]
δx_{3-dB} — $3-dB$ azimuth resolution [m]
ω_{factor} — Window constant
$V(f)$ — Basbanded spectrum
λ — Wavelength [m]
θ — Beamwidth of the antenna [degree]
n — Number of coherent pulses.
$v_{TX}(t)$ — Transmit waveform
$p(t)$ — Basebanded representation of the transmitting pulse
$v_{RX}(t)$ — Receive waveform
τ — Two-way time delay [sec]
ζ_0 — Reflection coefficent
$\zeta(f)$ — Target reflectivity spectrum
$h_{MF}(t)$ — Matched filter in time domain
$H_{MF}(f)$ — Matched filter in frequency domain
$H_c(f)$ — Ideal reconstruction filter in frequency domain
x_p, y_p, z_p — 3-D target position
x_0, y_0, z_0 — 3-D antenna position of the closest approach
R — Range to a scaterrer [m]
R_0 — Distance of the closest approach from antenna to target [m]
χ — Azimuth location [m]
L — Synthetic aperture length [m]
$rect()$ — Rectangular function
$Sa()$ — Sinc function
$v_{ptr}(f)$ — Point target response
$v_{system}(f)$ — System response function
ϕ — Baseband phase [radian]
f_{Di} — Instantaneous frequency [radian/m]
f_s — Samplying frequency [Hz]
B_D — Doppler bandwidth [Hz]
σ_1 — Radar cross-section [m^2]
δr — Range resolution [m]

t_{d1} — Time delay of antenna 1 [sec]

t_{d2} — Time delay of antenna 2 [sec]

ψ — Wrapped phase [radian]

φ — Absolute phase [radian]

b — Baseline [m]

$W()$ — Wrapping operator

ϵ_0 — Permittivity in free space

ϵ_r — Relative permittivity of a medium

μ_0 — Magnetic permeability in free space

μ_r — Relative permeability of a medium

σ — Conductivity of a medium [S/m]

$R(\theta)$ — Reflection error due to the PEC wall

m — Order of polyomial of PML

$\overline{\overline{s}}$ — Diagonal tensor of UPML

T – Time duraion of the Blackman-Harris window function [sec]

Nomenclature

ABCs— Absorbing Boundary Conditions.

A/D—Analog to Digital.

Azimuth—Angle in a horizontal plane, relative to a fixed reference, usually north or the longitudinal reference axis of the aircraft or satellite.

Beamwidth—The angular width of a slice through the main lobe of the radiation pattern of an antenna in the horizontal, vertical or other plane.

BGPR—Borehole Ground Penetrating Radar, a subset of ground penetrating radar.

BHR—Borehole Radar, a subset of ground penetrating radar.

BIC—Bushveld Igneous Complex of South Africa.

Chirp—A pulse modulation method used for pulse compression, also called linear frequency modulation. The frequency of each pulse is increased or decreased at a constant rate.

Coherence—A continuity or consistency in the phases of successive radar pulses.

DMT—Deutsche Montan Technologies (Germany).

DEM—Digital Elevation Model.

DTM—Digital Terrain Model.

Doppler frequency—A shift in the radio frequency of the return from a target or other object as a result of the object's radial motion relative to the radar.

EM—Electromagnetic.

FDTD—Finite Difference Time Domain.

FFT—First Fourier Transform.

FOPEN—Foliage Penetrating Radar.

GPR—Ground Penetrating Radar.

IDFT—Inverse Discrete Fourier Transform.

IFFT—Inverse Fourier Transform.

InSAR—Interferometric Synthetic Aperture Radar.

kHz— kilo Hertz $(= 10^3\text{Hz})$.

MCF—Minimum Cost Flow.

MHz—Megahertz $(= 10^6\text{Hz})$.

MPI—Message Passing Interface.

Narrowband—Describes radar systems that transmit and receive waveforms with instantaneous bandwidths less than 5 percent of the centre frequency (Taylor, 1995).

PEC—Perfectly Electric Conductor.

PGM—Platinum Group Metals deposits in the World.

PML—Perfectly Matched Layer.

Pothole—A semispherical hole in the bedrock of a stream bed, formed by abrasion of small pebbles and cobbles in a strong current.

PRF—Pulse repetition frequency.

PVM—Parallel Virtual Machine.

Radar—Radio Detection and Ranging.

Range—The radial distance from a radar to a target.

RF—Radio Frequency.

Roll-type structure—C-shaped deposit, most commonly in sandstones, formed by advancing mineralizing fluids.

RRSG—Radar Remote Sensing Group (UCT).

Synthetic Aperture Radar (SAR)—A signal-processing technique for improving the azimuth resolution beyond the beamwidth of the physical antenna actually used in the radar system. This is done by synthesizing the equivalent of a very long sidelooking array antenna.

Inverse Synthetic Aperture Radar (ISAR)—A signal-processing technique for improving the azimuth resolution beyond the beamwidth of the physical antenna actually used in the radar system. In this case, the scene moves across the fixed transducers two-way beamwidth. This is done by synthesizing the equivalent of a very long sidelooking array antenna.

SFCW—Stepped Frequency Continuous Wave.

SLC—Single Look Complex.

SNR—Signal to Noise Ratio.

TE—Transverse Electric.

TEM—Transient Electromagnetic.

Transducer—The radar antenna and the coaxial cables leading to the antenna.

UCT—University of Cape Town (South Africa).

UG2—Upper Group 2 of BIC.

UPML—Uniaxial Perfectly Matched Layer.

UWB—Ultra-Wideband. Describes radar systems that transmit and receive waveforms with instantaneous bandwidths greater than 25 percent of centre frequency (Taylor, 1995).

VHF—Very High Frequency. Nominal frequency range 30–300 MHz.

Wideband—Describes radar systems that transmit and receive waveforms with instantaneous bandwidths between 1 percent and 25 percent of the centre frequency (Taylor, 1995).

Chapter 1

Introduction

1.1 Background

Before embarking on any mining operations, it is both advantageous and essential to know the location of subsurface orebodies, as well as their types, structures and distributions. Similarly, it is important to be able to locate these subsurface orebodies with a high resolution (~1m) ahead of actual mining. This knowledge helps earth scientists and mining engineers to plan mining activities properly, which in turn will increase productivity and efficiency. Furthermore, as mining activities penetrate deeper and deeper into the earth (100m to more than 3500m), the underground rock accumulates a huge amount of stress, which causes faulting in the underlying rocks. Accurate three-dimensional mapping of subsurface orebodies, such as dykes, faults, potholes, fractures and rolls, will decrease the mining hazards encountered during mining, as well as reducing costs and limiting accidents and casualties. High-resolution imaging capabilities are also particularly useful for analysing reservoir subsidence in oil fields.

Among the available tools, the most widely used one at present is the surface seismic method to image subsurface acoustic structures. Three-dimensional seismology has been adapted from the oil industry and applied to the planning of ultra-deep mines (i.e. more than 3000m below the surface), but these tools unfortunately lack the resolution to reveal features that are smaller than 20m^3 in size. Such features can be particularly hazardous in mine workings (Pretorius et al., 1997). Due to lateral inhomogeneity, three-dimensional orebody geometry estimates derived from coring also produce insufficient detail. Other location methods include the geophysical methods of resistivity and magnetometry surveying, as well as low-frequency induction for detecting localised shallow metal objects or deeper metallic pipes and cables. In the case of nonmetallic targets, seismic methods form the alternative to subsurface radar (Daniels et al., 1988). A good comparison of seismic and ground penetrating radar methods in geological surveying can be found in (McCann et al., 1988).

An imaging system with three-dimensional capability has been implemented by using a stepped frequency radar that synthesizes a two-dimensional aperture (Lopez-Sanchez and Fortuny-Guasch, 2000). Two-dimensional aperture synthesis, however, requires many boreholes and is thus not economically feasible in three-dimensional underground ore-body imaging.

1.2 Review of Ground Penetrating Radar Application

The terms subsurface radar or Ground Penetrating Radar (GPR) refer to a wide range of electromagnetic techniques designed primarily to locate of objects or interfaces buried beneath the earth's surface (Daniels et al., 1988). The first use of electromagnetic signals to determine the presence of remote terrestrial metal objects is generally attributed to Hülsmeyer (1904), but the first description of their use to locate buried objects only appeared six years later in a German patent by Leimbach and Löwy (1910). New impetus was only given to the subject in the early 1970s, sixty years later, when lunar investigations and landings were in progress. The pulsed radar has been developed extensively and systems where radar antennas are moved along the ground surface have many applications: e.g. in the determination of ice thickness (Walford, 1985; Evans et al., 1988), in permafrost measurements (Annan and Davis, 1976), in civil engineering (Morey, 1974), in overburden characterization (Davis and Annan, 1989), in peat surveys (Ulriksen, 1982), in salt deposit measurements (Thierbach, 1974; Unterberger, 1978) and in coal-seam probing (Coon et al., 1981; Ralston, 2000). The range of applications has been expanding steadily, and now includes archaeology, road and rail bed quality assessment, location of voids, tunnels and landmines, as well as remote sensing by satellite. The recent advances of the use of GPR for the investigation of sediments can be found in Bristow and Jol (2003) and Bristow (2004).

The term Borehole Radar (BHR) or Borehole Ground Penetrating Radar (BGPR) refers to a special subset of GPR, where the transducers are placed into one or more boreholes to see the subsurface through the radar's eyes. BHR is a transient electromagnetic (EM) tool for detecting discontinuities in rock formation. Mainly pulsed radar systems have been used for borehole work for many years. In 1910, for example, Leimbach and Löwy buried electromagnetic dipole antennas in an array of vertical boreholes and compared the magnitude of the low frequency signals when successive dipole pairs were used to transmit and receive. They proved that a crude shadow image could be formed within the array of an ore body, which absorbed electromagnetic radiation.

Cross-hole and single-hole experiments were made in diabase by Rubin, Fowler and Marino (1978). A system for single-hole reflection measurements was developed by (Wright and Watts, 1982) and used in research related to radioactive waste (Bradley and Wright, 1987). In 1983, Nickel et al. described a borehole radar system with antenna centre frequencies of 20MHz and 40MHz, designed for both reflection and crosshole surveys, to determine the internal structure of salt domes. Reflections were obtained from targets that were at least 65m away. Thierbach (1994) presented results showing reflections from over 180m away in salt and between 120m and 300m away in potash seams. Halleux et al. (1992) carried out both surface GPR and borehole radar surveys at the Borth salt mine in Germany. At 120MHz, the bottom of the surface, as well as structures within the underlying anhydrite, were clearly visible. At 80MHz, a layer of clay at 30m depth and the base of the anhydrite around 50m depth were delineated. Halleux et al. (1992) then deployed 60MHz RAMAC borehole radar probes in horizontal boreholes running ahead of the mine drift. Reflections were visible from over 60m away, but with a single borehole and omni-directional antenna, the orebody interpretation suffered from rotational ambiguity problem. Continuous-wave systems have also been used for borehole work by a group at the Lawrence Livermore National Laboratory in the USA. Their work includes tomographic analysis and mapping of faults, tunnels, oil shale retorts, etc. (Dines and Lytle, 1979; Lytle et al., 1979; Daily, 1984; Ramirez and Daily, 1987).

High frequency EM surveying is increasingly used to detect highly conductive ore bodies in resistive hosts (Rao and Rao, 1983; Nickel and Cerny, 1989; Thomson et al., 1992; Fullagar and Livelybrooks, 1994; Pitts and Kramers, 1996). Trials in South African gold mines have established that wideband VHF borehole radars, working in the 10-100 MHz band, can be used to probe the rockmass over ranges from less than 5m to as much as 150m with submetre resolution (Trickett et al., 2000; Mason et al., 2001). Other applications of borehole radar in mining industry are massive sulphide deposits delineations (Bellefleur and Chouteau, 2001), delineation of nickel sulphide (Fullagar et al., 1996), limestone investigation (Fechner et al., 1998) and basalt-flow imaging using a directional borehole radar (Moulton et al., 2002). Its other applications are to detect and map structures such as fractures (Olsson et al., 1992; Miwa et al., 1999), tunnels (Cardarelli et al., 2003) and changes in lithology (Olhoeft, 1988*a*; Wanstedt et al., 2000).

BHR has been used extensively for cross-well tomographic applications for about a decade (Olhoeft, 1988*a*; Fullagar et al., 1996; Vasco et al., 1997; Clement and Knoll, 1998; Rucareanu et al., 2000; Zhou and Fullagar, 2000). Recent developments in this field include anisotropy in velocity tomography and many other algorithmic developments (Vasco et al., 1997; Lane et al., 1998; Liu, Lane and Quan, 1998*a*; Cai and McMechan, 1999; Valle et al., 1999; Jung and Kim, 1999; Zhou and Fullagar, 2000; Olhoeft, 2000;

Kim et al., 2004). The EM wave velocity (permittivity) and the attenuation (electrical conductivity) information of the media can be found from tomographic inversions of traveltimes and amplitudes, respectively (Olsson et al., 1992; Senechal et al., 2000; Tronicke et al., 2002; Tronicke and Holliger, 2004). The migration technique has been used to refocus the reflection signatures in the recorded data back to the true positions and, hopefully, the physical shape and orientation of the underlying objects (Leuschen and Plumb, 2000*a*; Moran et al., 2000; Olhoeft, 2000). Other important geophysical parameters, such as soil water content, fluid permeability, salinity, clay fraction and ore grade within the vicinity of the probed region can be obtained from the radar data (Topp et al., 1980; Annan, 1996; Gilson et al., 1996; Morey, 1998; Wright et al., 1998; Hammon-III et al., 2002; Galagedara et al., 2002; Giroux et al., 2004).

The maximum imaging range of a BHR is primarily determined by the conductivity of the formation in which the borehole lies, and the reflectivity of the targets. A detailed modelling study of EM wave propagation in a borehole environment is a milestone in understanding the propagation effect. The Finite Difference Time Domain (FDTD) method is capable of modelling layered regions and regions with complicated conductivity profiles. Numerical modelling of borehole data includes 3-D models (Ellefsen, 1999), 2-D and 2.5-D models (Wang and McMechan, 2002), and 3-D models (Sato and Thierbach, 1991; Holliger and Bergmann, 1999, 2002; Commer and Newman, 2004; Mukhopadhyay et al., 2004). A detailed modelling study of borehole radar in oil field applications can be found in (Chen and Oristaglio, 2002).

1.3 Borehole Radar Imaging

1.3.1 Borehole Synthetic Aperture Radar Interferometry

Interferometric Synthetic Aperture Radar (InSAR) is a well-established space-borne/airborne technique for creating high-resolution images of the Earth's surface (Bamler and Hartl, 1998). The terms *SAR interferometry, interferometric SAR* and *InSAR* are commonly used to describe radar interferometry involving images produced by using the synthetic aperture technique. In this technique, the information about the shape of the topography is primarily contained in the phase information of the received signals. The terrain height is reconstructed by using the phase information obtained from different view angles of a same scene. High ($\sim 1m$) azimuth resolution (in the direction of the flight track) is achieved by synthesizing a long antenna, which ranges in length from several metres to several kilometres (space-borne application).

A forward model borehole interferometric simulator using sidelooking antenna configuration is a useful tool to analyze the actual interferogram produced by two or more SAR images taken from boreholes with different view angles. This SAR image simulator is particularly useful for understanding the effect of the radar illumination angle, phase coherence (signal-to-noise ratio), phase discontinuities (layover), phase aliasing (surface slope), baseline separation and the effect of EM wave propagation through the host rock on SAR images. It also allows one to test and optimize different interferometric SAR processing algorithms (e.g., a multi-baseline interferometric, and a tomographic SAR) and to create a model of the forward problem, thereby providing insight into the more common inverse problem.

1.3.2 Three-dimensional Borehole Radar Imaging using Magnitude Images of Multiple Boreholes

Increased interest has developed in ultra-wideband/wide-band SAR because of its applications at VHF bands for foliage penetrating radar (FOPEN) and ground penetrating radar (Wilkinson et al., 2001; Berlin et al., 1986; Schaber et al., 1986; Elachi et al., 1984). The term wide-band describes radar systems that transmit and receive waveforms with fractional bandwidths between 1 percent and 25 percent of the centre frequency, and in the case of ultra-wide-band (UWB) refers to fractional bandwidths greater than 25 percent of the centre frequency (Taylor, 1995). Conventional narrow-band radar systems generally have fractional bandwidths that are less than 5 percent of the centre frequency. In a narrow-band InSAR experiment, the 3-D orebody geometry is related to the interferometric phase and the interferometric phase is a function of the centre frequency of the pulse. Alternatively, the 3-D location of the orebody geometry can be reconstructed by using a correlation-type processing between two signals coming from different view angle, which is more suitable for wide-band/ultra wide-band borehole radar experiment.

Mine boreholes are too thin to allow one to build an efficient directional radar antenna (Ebihara et al., 2000). With an axially omni-directional antenna, however, there will be ambiguity problems, due to the superposition of the signal from equal slant ranges. The borehole radar radiated carrier frequency has to be low (1 to 100MHz) to ensure low attenuation.

The formation of the focused image is usually implemented in two processes: range compression/focusing (across the direction to the flight path) and azimuth migration/focusing (along the direction of the flight path). The range compression can be achieved by using either matched filtering (for an optimal signal-to-noise ratio) or deconvolution processing with frequency domain windowing (for an optimal point target response). In the real borehole situation, the trajectories are neither parallel to each other nor straight. A time domain azimuth focusing processor calculates the expected signal trajectory in the data matrix for each scatterer, and then applies the appropriate phase correction along the signal trajectory before doing the integration in the time domain (Bamler and Hartl, 1998). A time domain azimuth focusing is computationally slow, but it is well suited to focus the data acquired along a curved trajectory.

A point in the 3-D reconstructed grid will be projected in different azimuth (along-track) and range (time-delay) locations in different borehole radar images, due to different view angles. A method has been investigated for 3-D reconstruction of the target orebody in three-dimensions by multiplying each analytical signal with the conjugate of the other and adding the two products together (Mason et al., 2001). But multiplying each analytical signal with the conjugate of the other may cause constructive and destructive interference due to their relative path lengths and moreover, this method is restricted for only two boreholes. Alternatively, the survey-target geometry in three-dimensions can be reconstructed by using two or more non-parallel borehole radar focused magnitude images.

1.3.3 Three-dimensional Finite Difference Time Domain Modelling of Borehole Radar in Mining Applications

Detailed characterizations of the internal structures of the subsurface orebodies are an important part of most engineering and environmental site evaluations. Borehole radar is an emerging tool in the mining industry to image the subsurface orebody with high resolution. This tool, however, suffers limitation due to attenuation of the EM wave in the host rock. To interpret the borehole received echo in complex geologic and antenna structures, a detailed modelling study is very useful.

Several schemes, based on field approximations such as ray theory modelling, have been proposed for interpreting such data. However, advances in computer software and hardware now permit rigorous modelling of such fields. Since the broad-band frequency content of the source waveform is important in maximizing resolution, there is an advantage in using a time domain source field. A time domain source also prevents overprinting of a modest target response by a large free-space source field. Although the time domain response can be synthesized from the frequency domain responses, there are computational economics in calculating the response directly in the time domain by using the FDTD approach (Johnson et al., 1998). The FDTD method is capable of modelling layered regions and regions with complex conductivity profiles. Furthermore, finite difference modelling of data can be used to estimate the correct time delay of the real received radar traces by varying the EM properties of the host media. This estimated time delay (or phase) can be used in the focusing stage of the real data for accurate location of target orebodies.

1.4 Thesis Objectives

This thesis investigates the following three aspects of borehole radar imaging:

1. Borehole synthetic aperture radar interferometry for high resolution 3-D subsurface imaging,
2. 3-D reconstruction of subsurface orebody geometry using multiple boreholes radar magnitude images, and
3. 3-D FDTD modelling of borehole radar EM wave propagation in mining applications.

Thus far, not much work has been done by the engineering community to create images of subsurface orebodies in three-dimensions with sub-metre resolution. The primary reason for this is that the success of borehole radar imaging depends on the penetration of EM waves through the host rock. A recent study in the South African gold mining environment has shown, though, that it is possible that features in highly resistive host rock (typical resistivities of the host quartzite are in excess of 1000 ohm metres) can be detected with high resolution by using borehole radar up to a distance of 95m (Trickett et al., 2000).

At the beginning of this research, it seemed possible to obtain real multiple borehole radar data for 3-D imaging of the subsurface orebodies in the South African gold and diamond mining industry by using the ARCOLab borehole radar imaging system (Claassen, 1995). Unfortunately, during the course of the research no multiple borehole radar data could be obtained. Therefore, the present research is confined to simulation studies, and the developed 3-D image reconstruction technique using multiple borehole magnitude images has been verified by means of the emulated real borehole acoustic data obtained in air and water. The Radar Remote Sensing Group (RRSG) at UCT is planning to build a step-frequency borehole radar, which will be deployed in South African mines for high resolution subsurface imaging. As the research progress, we will thus have access to multiple borehole radar data that will allow us to reconstruct subsurface orebodies in 3-D with sub-metre resolution.

The objectives of the thesis can be summarised as follows:

- To review and describe the current status of GPR applications.
- To discuss the types of borehole radar available at present. The available types of radar vary from short pulse systems, through to more sophisticated stepped frequency systems. The propagation of EM wave through earth medium and different data acquisition modes have also been discussed.

- To discuss the relevant antenna constraints in the borehole environment, antenna radiation patterns and the rotational ambiguity issue.

- To discuss the radar range resolution (across-track) and the target reflectivity spectrum issue. The high azimuth resolution (along- track) is achieved by synthesizing the equivalent of a long (~100m) side-looking array antenna.

- To implement a borehole radar interferometric SAR simulator in a parallel and non-parallel borehole environment. The interferometric phase was unwrapped by using a minimum cost flow (MCF) algorithm. Thereafter, a phase to height reconstruction technique was applied to convert the unwrapped phase into its corresponding height values for both a parallel and non-parallel borehole trajectories. This borehole interferometric height reconstruction technique was applied to two subsurface geological structures.

- To discuss the SAR and Inverse SAR (ISAR) image formation technique. We will discuss the range compression technique using matched filtering and also using deconvolution filtering. Practically, it is almost impossible to drill holes with precise geometries. Therefore, a suitable focusing method was implemented that will allow us to process the borehole radar data obtained from deviating boreholes. This focusing algorithm will be applied to simulated multiple borehole radar data as well as to real acoustic data acquired in both air and water.

- To develop and implement a 3-D image reconstruction method which will use 2-D focused magnitude images from a limited number of boreholes. In this regard, we will discuss the reconstruction grid spacing issue for a given borehole setup (fan outwards from the drilling station). This reconstructed algorithm will be applied to simulated borehole radar data as well as to real acoustic data acquired in both air and water.

- To implement a 3-D FDTD algorithm in a conductive medium by using a Uniaxial Perfectly Matched Layer (UPML) boundary absorber in the Cartesian coordinate system. The algorithm will be tested against published results. This modelling code will be used to study the borehole radar wave propagation in a sedimentary layer, the reflection from a geological reverse fault, and the reflection from a pothole-type geological orebody. We will also study the effect of layering on radar traces, guided wave propagation in layered media, the effects of borehole on reflected as well as transmitted radar traces, and also the effect of host rock conductivity on the radar traces. In order to overcome the limitations of large memory requirements and processing speed, the implementation of a parallel version of the 3-D FDTD C code using Parallel Virtual Machine (PVM) as middleware running on a Beowulf-type Linux cluster and the results achieved will be discussed.

1.5 Thesis Development

Chapter 2 reviews the types of borehole radar available at present and discusses the relevant antenna constraints. The radiation pattern of the antenna is also discussed. Radar bandwidth can be achieved instantaneously (transmitting a short pulse), or it can be achieved by transmitting a sequence of waveforms of varying bandwidth, thereby achieving the required range resolution. The concept of basebanding an analytical signal is also discussed. The insights of the target reflectivity spectrum, and range (along-track) and azimuth (cross-track) resolutions and sampling issue are also discussed.

Chapter 3 describes the insights of interferometric SAR simulator in a borehole environment, the types of simulators available and the usefulness of the forward model simulator. A incoherent image simulator was used to simulate two types of subsurface orebodies, one being a pothole-type and the other a half-sphere type orebody by using both parallel and non-parallel borehole trajectories. To study the potential of the InSAR imaging method in the borehole environment, we mainly considered the diffuse reflection between two homogeneous, non-dispersive dielectric interfaces. Different aspects of interferometric SAR, such as interferometric image formation, coherent estimation and the effect of coherence on reconstructed height values, slant range to ground range conversion etc. are discussed. The interferometric phase was unwrapped by using a minimum cost flow (MCF) algorithm. The relevant theory of a phase to height reconstruction algorithm in case of non-parallel borehole is discussed. Finally, a comparison has been done between simulated and expected height values in slant range. The chapter concludes with a summary of the results achieved and discusses the usefulness of this technique in the imaging of borehole subsurface orebodies.

Chapter 4 describes the SAR and ISAR image formation techniques. The range focusing has been achieved by using both a matched filter and a deconvolution filter. The principles of the time domain synthetic aperture radar focusing (migration) technique and related implementation aspects are discussed. The issue of focusing the borehole radar data from parallel and non-parallel boreholes is discussed. Each point in the object plane is projected into a two-dimensional focused image. A method has been developed and implemented to reconstruct a 3-D image from a 2-D focused magnitude image. In this regard, the issue of the reconstruction grid spacing for a given borehole setup (fan outwards from the drilling station) is discussed in detail. The method has been applied to simulated radar data as well as to real acoustic data. Lastly, the results achieved are discussed, and the chapter is summarised.

Chapter 5 discusses the importance of borehole radar wave propagation modelling in a conductive host by using the FDTD method. One of the greatest challenges with an FDTD implementation is to model an unbounded region accurately and efficiently. In order to maximize efficiency, the simulation grid should only enclose the area closest to the structure of interest. This is best achieved by implementing some form of Absorbing Boundary Condition (ABC), which reduces reflections of the waves leaving the grid. Perfectly Matched Layer (PML) boundary conditions facilitate modelling with an economically sized grid. A method known as the Uniaxial Perfectly Matched Layer (UPML) has been used to truncate the computational region. Here the PML is modelled as a uniaxial anisotropic medium. The accuracy of the implemented code is compared to the published results. The modelling of a dipole source in a conductive medium is discussed. Finally, the code is used to simulate the borehole radar EM wave propagation in some geological settings, such as the sedimentary layer, reflection from a geological reverse fault, and reflection from a pothole-type orebody structure. Thereafter, the effects of layering, guided wave formation, borehole mud permittivity and borehole size,and the effect of host rock conductivity on radar traces are discussed. In order to overcome the limitations of large memory requirements and processing speed in 3-D FDTD simulation, the implementation of a parallel version of the 3-D FDTD C code using Parallel Virtual Machine (PVM) as middleware running on a Beowulf-type Linux cluster and the results achieved are discussed.

Chapter 6 summarises the work and provides recommendations for future research.

1.6 Statement of Originality

The candidate's original contributions in this thesis can be summarised as follows:

- Chapter 2 (Borehole radar imaging): Although most of the topics discussed in this chapter are in no sense novel, this chapter provides a good overview of the fundamental aspects of borehole radar imaging and focuses specifically on the following aspects: types of borehole radar, antenna radiation patterns, borehole radar antenna constraints, target reflectivity spectrum, range compression, range and azimuth resolution and sampling issues. Some of the radar imaging concepts used in this thesis have been discussed and references are given where material is drawn from outside sources.

- Chapter 3 (Borehole Interferometric SAR): The implementation and coding of an interferometric SAR simulator in a borehole environment is the candidate's own original work. The measured interferometric phase is modulo 2π. In interferometry, the terrain height is related to the absolute phase. The wrapped phases are unwrapped by applying a minimum cost flow algorithm. The phase to height conversion method in the case of a deviating borehole geometry has been implemented. Some of the materials appearing in this chapter were previously published by the candidate in (Mukhopadhyay et al., 2001; Inggs et al., 2001). To the candidate's best knowledge, the application of interferometric SAR height reconstruction techniques in the context of the borehole environment is a novel approach.

- Chapter 4 (Three-dimensional image reconstruction using radar magnitude images from multiple boreholes): Although optimal for SNR, matched filtering results in an undesirable point target response if the passband of the transducers are not flat in magnitude and linear in phase. In this case, a deconvolution processing approach has been established and implemented for better result in range compression. The implementation of a deconvolution filter to range compress the real acoustic data acquired in air is a novel approach. The time domain azimuth focusing is more suitable for focusing radar data acquired from deviating borehole than the other frequency domain counterpart. The implementation and coding of time domain azimuth focusing algorithm of focusing simulated borehole radar as well as real acoustic data is the candidate's own work. A 3-D reconstruction algorithm has been developed by using a limited number of boreholes (two or more) 2-D focused magnitude image. The expression for 3-D grid spacing (boreholes fan outward from the borehole centre) has been derived. The issue of rotational ambiguity problem has been discussed in detail. The algorithm has been verified with simulated radar data as well as real acoustic data acquired in air and water. Some of the materials have been published in (Mukhopadhyay et al., 2005a; Wilkinson et al., 2004; Mukhopadhyay et al., 2002). To the candidate's best knowledge, this work is also novel.

- Chapter 5 (Three-dimensional finite difference time domain borehole radar modelling): The implementation and coding of a 3-D finite difference time domain algorithm by using a Uniaxial Perfectly Matched Layer boundary absorber for a borehole radar wave propagation study is the candidate's own work. The implementation issue has been discussed in detail, and the accuracy of implemented code has been verified against the published result. The study of borehole radar wave propagation in a sedimentary layer and reflection from a geological reverse fault in 3-D is the candidate's own original work. The formation of *guided wave* in a layered media, the effect of scattering from the sharp edge of the reverse fault on radar traces and also the effect of borehole mud and borehole size on radar traces has been discussed. Some of the results have been compared with previous published work. Some of the materials have been published in (Mukhopadhyay et al., 2005b; Mukhopadhyay et al., 2004b). The implementation of a parallel version of the 3-D FDTD C code to improve both the processing speed and large memory requirements by using Parallel Virtual Machine (PVM) as middleware running on a Beowulf-type Linux cluster is the candidate's own work (Mukhopadhyay et al., 2005c). To the candidate's best knowledge, the borehole radar simulation in a conductive host in detail is also novel work.

Chapter 2

Fundamentals of Borehole Radar Imaging

2.1 Introduction

In this chapter, we summarise the basic borehole radar imaging fundamentals with an emphasis on data acquisition modes, radar signal processing, resolution and borehole antenna constraints. Borehole radar technology is a subset of the general field of Ground Penetrating Radar (GPR). Daniels et al. (1988) has produced a good, practical background to the subject of GPR.

The radiation pattern of a borehole radar antenna is a function of frequencies, the geometry and size of the antenna, and the electromagnetic properties of the ground. The radar range resolution is a function of the radar's bandwidth. The radar bandwidth can be achieved instantaneously by transmitting a short pulse, or it can be achieved by transmitting a sequence of waveforms of varying bandwidth, thereby achieving the required resolution. This is best achieved by using the concept that the target has a time domain profile, which can be translated to the frequency domain, thereby known as the target reflectivity spectrum (Wilkinson et al., 1998).

Unfortunately, the media through which the EM wave propagates does not necessarily exhibit linear phase and constant amplitude responses as a function of frequency, i.e. they can exhibit dispersion. For an undistorted response, a linear system should have a linear phase response. In the process of propagating the EM wave in the host rock, generally, the high frequencies are more attenuated. This results in the reduction of the radar received signal bandwidth and, hence, the range resolution.

The narrow dimension of the borehole results in a very limited set of antenna geometries being viable, given the long wavelengths required to achieve low loss propagation.

2.2 Propagation of Radio Waves Through Earth Medium

2.2.1 Introduction

The electromagnetic properties of materials are related to their composition and water content, both of which exert the main control over the speed of radiowave propagation and the attenuation of electromagnetic waves in material. Maxwell's equations (Balanis, 1989) describe the propagation of electromagnetic energy as a coupled process between electrical and magnetic forces and fluxes. Maxwell's equations require parameters for the material properties describing the behavior of matter in response to force. For electromagnetic energy, the energy loss and storage parameters are the complex electrical and magnetic properties describing motions of electrical charge (transport, polarization and spin). The relations between these properties and their corresponding force fields and fluxes are called constitutive equations. At normal geophysical exploration field strengths and ground penetrating radar frequencies, these relations are linear (Olhoeft, 1998).

2.2.2 Electromagnetic Properties

The electromagnetic-wave propagation can be represented by a one-dimensional wave equation (propagation along the z axis) of the following form.

$$\frac{\delta^2 E}{\delta z^2} = \mu\epsilon \frac{\delta^2 E}{\delta t^2} \tag{2.1}$$

where the velocity of propagation

$$v = \frac{1}{\sqrt{\mu\epsilon}} \tag{2.2}$$

The constants

absolute electric permittivity of medium, $\epsilon = \epsilon_0 \epsilon_r$

the absolute magnetic permeability of medium, $\mu = \mu_0 \mu_r$

ϵ_r = relative permittivity, having a value in range 1 (air) to ≈ 80 (water) for most geological materials.

$\mu_r =$ relative magnetic permeability, being 1 for non-magnetic geological materials.

The intrinsic impedence of the medium

$$\eta = \sqrt{\frac{\mu}{\epsilon}} \tag{2.3}$$

A plane wave propagating in the positive z direction in a perfect dielectric medium can be described by the equation (solution of Equation 2.1)

$$E(z) = E_0 e^{-jkz} \tag{2.4}$$

where E_0 is an electric field constant, and the phase constant

$$k = \frac{\omega}{v} = \omega\sqrt{\mu\epsilon} \tag{2.5}$$

The radian frequency $\omega = 2\pi f$, where f is the electromagnetic frequency,

For a perticular frequency, k [per meter can be considered as a constant of the medium and it is known as the wave number.

From Equation 2.4 the propagation of an electromagnetic field E_0 originating at $z = 0,\ t = 0$ in a conducting dielectric can be described by $E(z,t)$ at a distance z and time t by

$$E(z,t) = E_0 \cdot e^{-\alpha z} \cdot e^{j(wt - \beta z)} \tag{2.6}$$

the first exponential function is the attenuation term and the second the propropagation constant.

Electromagnetic waves propagating through natural media experience losses which causes attenuation of the original electromagnetic wave. For most materials of interest in subsurface penetrating radar, the magnetic response is weak and need not be considered as a complex quantity; unlike the permittivity and conductivity. For lossy dielectric materials, absorption of electromagnetic radiation is caused by both conduction and dielectric effects (Daniels, 1996).

The complex dielectric permittivity and conductivity of materials are described by

$$\begin{aligned} \epsilon &= \epsilon^{'} - j\epsilon^{''} \\ \sigma &= \sigma^{'} - j\sigma^{''} \end{aligned} \tag{2.7}$$

where

$\epsilon^{'}$ and $\sigma^{'}$ are the real parts

$\epsilon^{''}$ and $\sigma^{''}$ are the imaginary parts

$$j = \sqrt{-1}$$

For many applications, the frequency dependence of electrical permittivity can be modelled using Debye-Pellat relaxation equation (Debye, 1929):

$$\epsilon(\omega) = \epsilon^{'} - j\epsilon^{''} = \epsilon_{\infty} + \frac{\epsilon_s - \epsilon_{\infty}}{1 + j\omega\tau} \tag{2.8}$$

where ϵ_{∞} is the high-frequency (infinite) permittivity, ϵ_s is the low-frequency (static) permittivity and τ is the relaxation time of water.

In general, single relaxations are rarely observed in natural systems (Olhoeft, 1998). Instead, there are distributions of relaxations corresponding to distributions of size scales that infulence movement of charge. The most common model in such systems are Cole and Cole (1941):

$$\epsilon(\omega) = \epsilon^{'} - j\epsilon^{''} = \epsilon_{\infty} + \frac{\epsilon_s - \epsilon_{\infty}}{1 + (j\omega\tau)^{\alpha}} \tag{2.9}$$

Here, the term α describes the breadth of the time comstant distribution, from a single relaxation, $\alpha = 1$, to an infinitely broad distribution, $\alpha = 0$, with a common process. The same parameter α has been used in the next section for other definition.

The nature of the parameter $\epsilon^{'}$ relates to the electric permittivity, which may also be expressed in terms of relative permittivity. The parameter $\epsilon^{''}$ relates to losses associated with both conductivity and frequency. For practical purposes at frequencies up to 1 GHz and conductivities below 0.1 S/m, the effect of $\epsilon^{''}$ term will be small and commonly disregarded (i.e. ϵ taken as the real components, $\epsilon^{'}$) in such circumstances.

The parameters attenuation factor (α) and the phase coefficient (β) can be related to σ and $j\omega\epsilon$ and expressed as

$$\alpha = \omega[\frac{\mu\epsilon^{'}}{2}\sqrt{1 + \tan^2\delta} - 1]^{1/2} \tag{2.10}$$

and

$$\beta = \omega[\frac{\mu\epsilon^{'}}{2}\sqrt{1 + \tan^2\delta} + 1]^{1/2} \tag{2.11}$$

The dimensionless factor, $\tan\delta$, commonly termed the material loss target

$$\tan\delta = \frac{\epsilon^{''}}{\epsilon^{'}} \tag{2.12}$$

The attenuation coefficient can be expressed in decibels per metre

$$\alpha^{'} = 8.66\alpha \tag{2.13}$$

From the above expression it is clear that the attenuation coefficient of material is , to a first order, linearly related (in dB/m) to frequency.

For a material which is dry and relatively lossless, it may be reasonable to consider that

$\tan\delta$ is constant over the frequency range of 1×10^{-7} to 1×10^{10} Hz. However, for materials which are wet and lossy such an approximation is invalid (Daniels, 1996), as

$$\tan\delta = \frac{\sigma^{'} + \omega\epsilon^{''}}{\omega\epsilon^{'} - \sigma^{'}} \tag{2.14}$$

In general, for lossy earth materials $\tan\delta$ is large at low frequencies, exhibits a minimum at around 1×10^{8} Hz and increases to a maximum at several GHz, remaining constant thereafter (Daniels, 1996). An approximation which enables an order-of magnitude indication is that when σ is small, then

$$\tan\delta \simeq \frac{\sigma^{'}}{\omega\epsilon^{'}} \tag{2.15}$$

The phase velocity, v, in the medium is

$$v = \frac{\omega}{\beta} \tag{2.16}$$

From equation 2.16, we can see that the propagation velocity is a function of frequency. As an electromagnetic pulse propagates through such a material, the pulse changes shape in a process called *dispersion.* The presence and influence of water in electrical properties, iron bearing minerals in magnetic properties, and geometric scattering are the causes of most dispersion observed in ground penetrating radar data (Olhoeft, 1998).

In the case of low-loss and non-magnetic media (i.e. $\tan\delta < 1$), equation 2.11 can be written as

$$\beta \;\approx\; \frac{1}{2}\omega\sqrt{\mu\varepsilon} \tag{2.17}$$

and from these the phase velocity can be written as

$$v \approx \frac{1}{\sqrt{\mu\varepsilon}} = \frac{c}{\sqrt{\varepsilon_r}} \tag{2.18}$$

where c is the speed of light in a vacuum.

The low-loss and non-magnetic assumption is valid for a wide range of ground materials encountered in GPR applications (Church et al., 1988).

The maximum penetration depth of a GPR system relates to the maximum depth at which a buried target can be detected. GPR performance in terms of maximum penetration depth is not only depends upon the medium properties (e.g. attenuation loss and dispersion), but is also related to other parameters, such as radar cross section, antennae directional gain, antennae coupling efficiency, and minimum detectable signal power. A detailed description of GPR performance is given in (Noon, 1996; Turner and Siggins, 1994).

2.3 Types of Radar

2.3.1 Pulsed Radar

An impulse radar transmits a narrow pulse (less than a few nano-seconds) associated with a spectrum of signals, with a large peak power at a constant pulse repetition frequency (PRF). This spectrum should be wide, in order to measure the target reflectivity profile at high resolution. The time delayed received waveform is then sampled. The radar electronics must be able to deal with the wide instantaneous bandwidth. In general, this also implies high A/D conversion rates. Improvements in the signal to noise ratio (SNR) are achieved by averaging the profiles, a process known as *stacking*, from the term used in seismology. If we add several random noises together, some of them will cancel each other because they are usually out of phase with each other. If they are statistically independent, the standard deviation of the sum of n random signals will be proportional to $\sqrt{n}$, whereas the sum of n coherent in-phase signals will be proportional to n so that the SNR will be improved by the factor of $\sqrt{n}$ (Sheriff and Geldart, 1982).

2.3.2 Stepped Frequency Radar

A stepped frequency system achieves the required resolution by radiating a succession of carriers stepped uniformly in frequency across a desired band. Signal to noise improvement is achieved by dwelling on each frequency and integrating them. A/D conversion rates are modest. Direct coupling of the transmit and receive signal leads to some dynamic range problems.

2.3.3 Pulsed Stepped Frequency Radar

A pulsed stepped frequency system transmits a spectrum of signals with a certain centre frequency and receives the return. The frequency is stepped up in the successive pulses to cover a range of frequencies to achieve high resolution. An advantage of the pulsed stepped frequency approach is the reduction of the instantaneous bandwidth and sampling rate requirements of the radar system, as well as the possibility of skipping frequencies that might be corrupted due to external interfering frequency sources (Wilkinson et al., 1998).

2.3.4 Stepped Frequency Continuous Wave Radar

The stepped frequency continuous wave (SFCW) waveform is implemented by transmitting a number of single frequency tones separated in frequency by $\triangle f$. At each frequency the amplitude and phase of the received signal is sampled and recorded. The received signal is transformed into the time domain using Inverse Discrete Fourier Transform (IDFT) to obtain a synthesised pulse (Langman and Inggs, 2001). In the case of the stepped frequency continuous wave radar system, direct coupling of the transmit and receive signal leads to dynamic range problems. The main advantage of the SFCW ground penetrating radar over the pulsed system is that the former has a higher average radiated power for transmission.

2.4 Antenna Radiation Pattern

In most GPR applications, it is assumed that the wave propagation is in the far field. The radiation pattern of an antenna is a function of the wavelength, the geometry and size of the antenna, and the electromagnetic properties of the ground. The GPR response in both near and far field has important applications. Some radar systems filter the data and remove the near field effects. However, under certain circumstances, the ground penetrating radar response in the near field can be very useful. The near field response has been used to detect incipient dessication cracks in clays), locate land mines, map density changes in soil compaction studies, and more. The far field is dominated by homogeneous waves and the near field is dominated by inhomogeneous (or evanescent) waves.

The space surrounding an antenna is usually subdivided into three reasons: (i) reactive near field, (ii) radiating near field (Fresnel) and (iii) far field (Fraunhofer) regions as shown in Figure 2.1. These regions are so designated to identify the electromagnetic field structure in each (Balanis, 1996). The boundaries separating these regions are not unique, although various criteria have been established and are commonly used to identify the regions.

2.4.1 Reactive Near Field Region

This region is the space immediately surrounding the antenna wherein the reactive field predominates. For most antennas, the extent of this region is $0 < R_1 < 0.62\sqrt{\frac{D^3}{\lambda}}$, where λ is the wavelength and D is the largest dimension of the antenna (Balanis, 1996). In this space the Poynting vector is predominantly reactive (non-radiating).

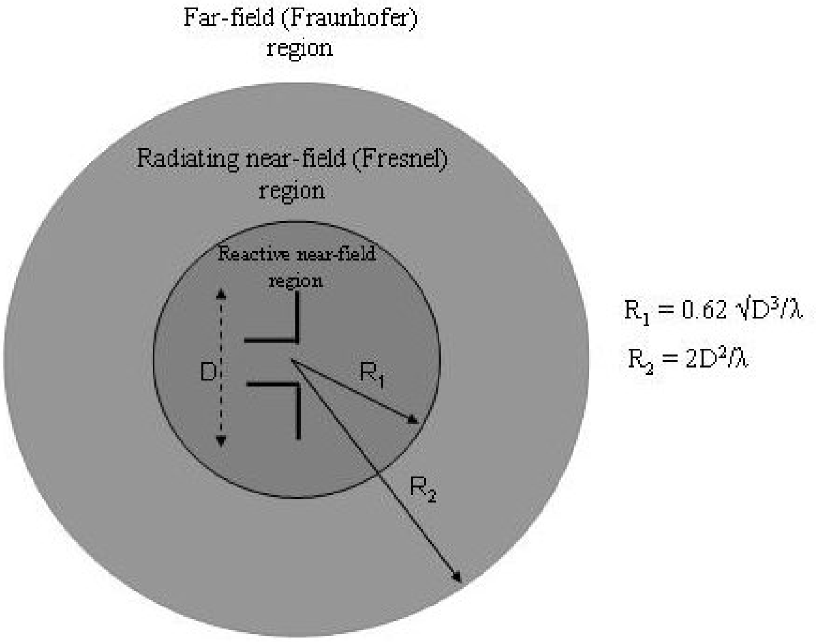

Figure 2.1: *Field regions of an antenna.*

2.4.2 Radiating Near Field Region

This region is defined as that region of the field of an antenna between the reactive near-field region and the far field region wherein radiating fields predominate and the angular field distribution is dependant on the distance from the antenna (Balanis, 1996). The extent of this region is defined as $0.62\sqrt{\frac{D^3}{\lambda}} \leq R_2 < \frac{2D^2}{\lambda}$. This region is often referred to as the Fresnel zone, a term borrowed from optics. If the antenna has a maximum overall dimension which is very small compared to the wavelength, this field region does not exist.

2.4.3 Radiating Far Field Region

This region is as that region of the field of an antenna where the angular field distribution is essentially independent of the distance from the antenna (Balanis, 1996). Beyond the radiating near-field region, the far field region is defined as $R_3 > \frac{2D^2}{\lambda}$ or $R_3 > 10\lambda$ (criterion for small antennas). The radiation pattern in this region is approximated by the Fourier transform of the aperture distribution with a phase error of less than 22.5^0. This region is often referred to as the Fraunhofer zone, a term also borrowed from optics. In the far field region the radiating field can be approximated as a plane wave.

2.5 Antenna Constraints for Borehole Radar

Any implementation of borehole radar (BHR) systems requires boreholes. In many South African mines cover drilling is used to detect dykes and water fissures. These boreholes are typically 48 mm in diameter; any feasible radar system must thus have probes of less than this diameter. The radiated carrier frequency has to be low (1 to 100MHz) to ensure low attenuation. This means that the antenna has to be long. Thus the antennas in boreholes are clearly constrained to be *long and thin*. Since most current systems are pulsed, the traditional approach is to use a damped structure (e.g. Wu-King) (Mason et al., 2001), i.e. the antenna is excited with the electric field in the direction of the borehole, with damping ensuring that ringing on the antenna does not obscure close-in targets. Another problem with BHR is the lack of azimuthal directionality found in most existing systems, resulting in angular ambiguity regarding reflector positions around the borehole. Two possible solutions to this problem are to drill multiple boreholes or to develop a directional borehole antenna. The antenna has to be rugged, since it will suffer a great deal of abrasion from the borehole walls during deployment. Finally, boreholes are often filled with acid water at high pressure, and the ambient temperature can be in excess of 70^0 C. All of these problems need to be considered when designing a suitable borehole radar antenna (Rutschlin and Cloete, 2000).

Commercial borehole radar systems include the following:

- The ARCOLab borehole radar imaging system has been developed at the Universities of Oxford and Sydney during the past decade (Claassen, 1995). The radar consists of two asymmetric dipoles, one transmitting and one receiving; each has one resistively loaded arm and one metallic arm. The antennas are placed in a PVC tube with a diameter of about 33 mm. The operating bandwidth is approximately 20 to 80 MHz at a centre frequency of 50 MHz. It transmits 900V pulses with a 6 ns rise time and a pulse repetition frequency (PRF) of 2 kHz. The data is transferred via a fibre optic connection.
- The most popular commercial system is the RAMAC short-pulse borehole radar developed by the Swedish company $Mal\grave{a}$ Geoscience. The system consists of 20 and 60 MHz dipole transmitting and receiving antennas, and a 60 MHz directional receiver, which consists of four symmetrically placed antennas. The four responses are then combined to produce a synthetic radargram looking in any direction. The range is about 60 to 70% of that obtained by the standard non-directional dipole ($Mal\grave{a}\, GeoScience$, 2004).
- The CSIR Miningtek have designed a borehole radar to address the local require-

ments of the South African mining industry (Vogt, 2001). This radar has a bandwidth of 90 MHz and a transmit pulse with voltage of 1000V. The borehole radar is 33mm in diameter and has two separate probes containing the transmitter and receiver. The pulse repetition frequency (PRF) of the transmitter is 1 kHz. The received signal is acquired in a single slot, with 8 bit resolution, and is stacked within the probe to improve resolution. The dynamic range is increased to 16 bit by stacking 256 traces. Four traces are delivered each second to the control unit outside the borehole. This system is capable of functioning in boreholes filled with air or water at temperatures up to 70^0C.

- Sato et al. (1995) have designed a system that can make measurements of co- and cross-polarised reflections. A half-wavelength dipole antenna was used to transmit a 10 ns pulse, the co- and cross-polarised reflection components of which were subsequently received by another half-wavelength dipole and a three quarter-wavelength slot antenna.

- Sato and Tanimoto (1992) have designed a directional receiver, which measured surface currents induced on a conductive cylinder by a reflected EM wave (Sato and Tanimoto, 1992). An omnidirectional discone antenna was used for transmission purposes. The incident angle of the incoming wave can be determined from the relative phase and amplitude of the current probes responses. The estimation of the reflector position using this antenna can be found in Ebihara et al. (1996).

- A borehole radar system with directional capability has been developed by a German Company, Deutsche Montan Technologies (DMT) (Siever, 2000). The transmitting antenna is an omnidirectional dipole, while the directional receiver consists of two orthogonal loops, which are used firstly as two magnetic field sensors and secondly as a single dipole. The combination and processing of the three received signals results in an unambiguous azimuth direction. Unfortunately, the diameter is about 80 mm and the length 20 m, and it is also very expensive, which makes it infeasible to be used in a borehole environment.

2.6 Radar Data Acquisition Modes

There are four main modes of radar data acquisition, namely: (i) common offset (reflection profiling); (ii) common source (wide-angle reflection and refraction (WARR)) (iii) common midpoint sounding (iv) Cross-hole radar tomography or transillumination. These different modes of radar data acquisition are explained in the following section.

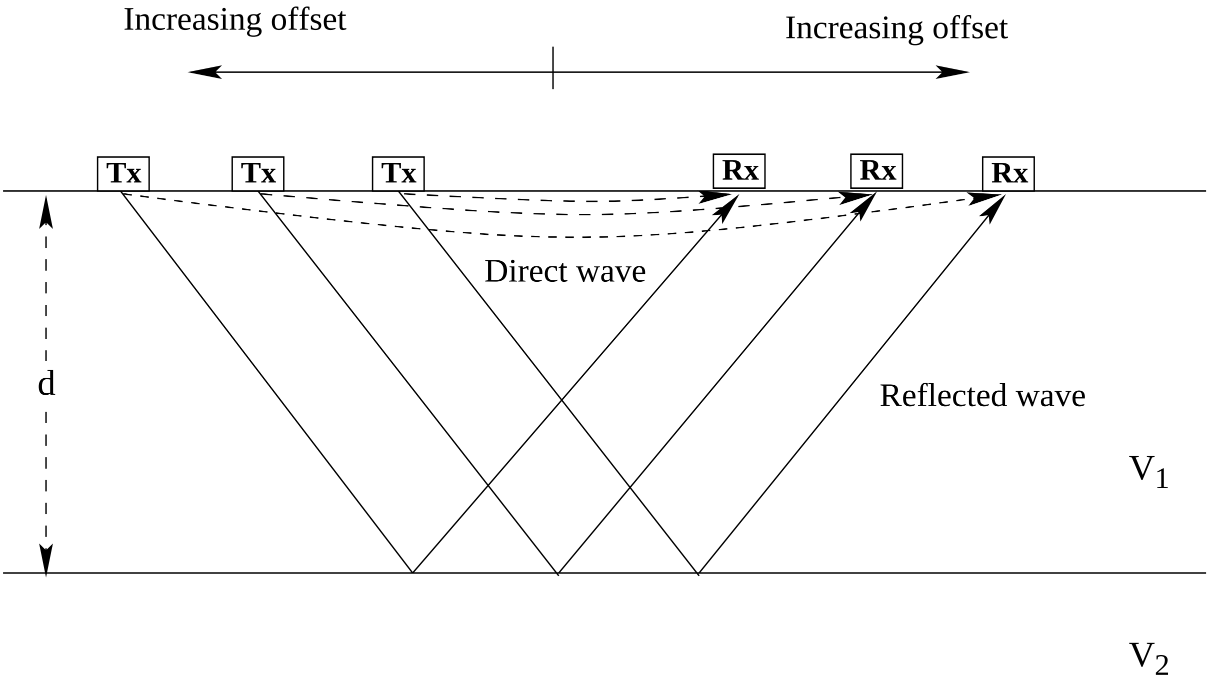

Figure 2.2: C*ommon offset bistatic mode data acquisition configuration in which the distance between transmitter and receiver antennae is fixed and the pair moves along a horizontal line.*

2.6.1 Common offset acquisition mode

A *profile* is a graph of a measured quantity against horizontal distance. In this mode of operation, the radar antennae (monostatic: the offset is zero and both antennae are at same point; bistatic: transmitter and receiver antennae are at a fixed distance) are moved over the surface simultaneously. The measured travel times to radar reflectors are displayed on the vertical axis, while the distance the antenna has travelled is displayed along the horizontal axis in a radargram display. Most GPR surveys, mainly borehole radar surveys use a common offset survey mode. This mode of data acquisition can be used to improve the azimuth or plan resolution, where a long aperture is synthesized along the azimuth line. This type of operation, in the radar field, is called synthetic aperture radar image formation. Figure 2.2 shows a common offset bistatic mode data acquisition configuration. A monostatic mode SAR and ISAR image formation mode will be discussed in detail in section 4.2. This mode of data acquisition is analogous to continuous seismic reflection profiling (Sheriff and Geldart, 1982).

2.6.2 Common Source Data Acquisition Mode

In a common source data acquisition system, sometimes called wide-angle reflection and refraction (WARR) sounding (Reynolds, 2000), the transmitter is kept at a fixed location

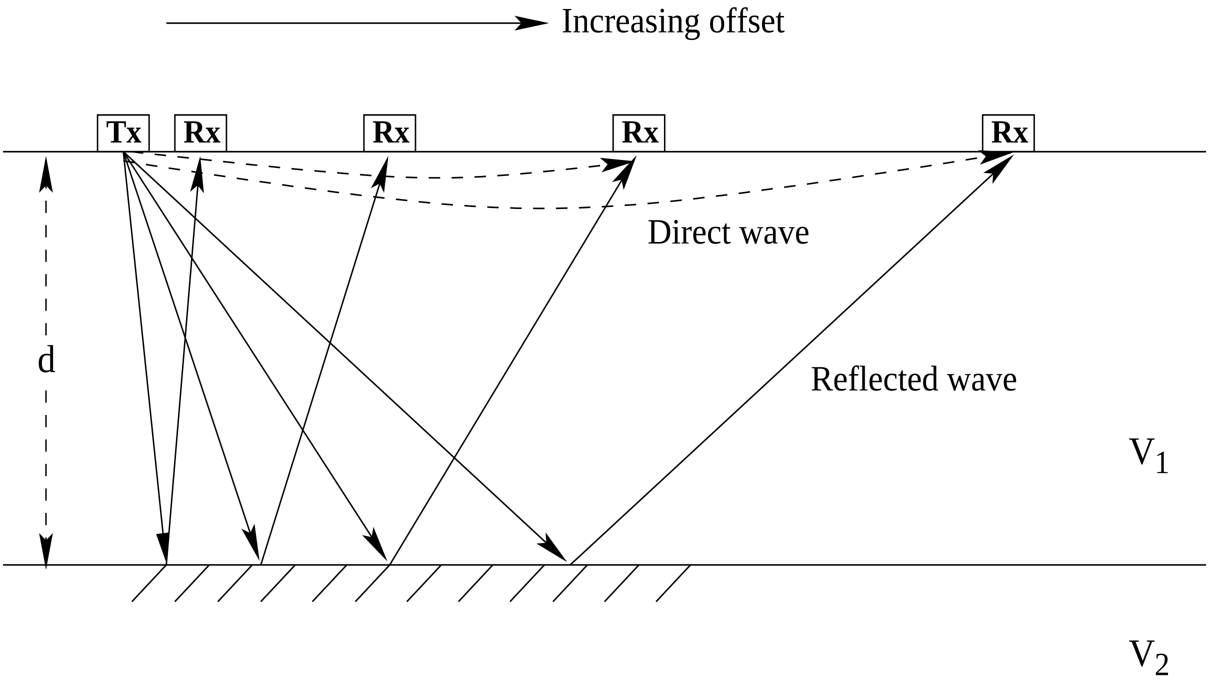

Figure 2.3: *Common source antenna configuration where the transmitter is kept at a fixed location and the receiver is towed away at increasing offsets.*

and the receiver is lowed away at increasing offsets. Figure 2.3 shows the antennae configuration of a common source data acquisition mode. This type of data acquisition mode is most suitable in an area where the material properties are uniform and the reflectors are planar in nature.

2.6.3 Common Midpoint Data Acquisition Mode

Figure 2.4 shows the antennae configuration of the common midpoint data acquisition mode. In this type of acquisition mode, the transmitter and receiver antennae are moved away at increasing offsets so that the midpoint between them stays at a fixed location. In this case, the point of reflection on each sub-surface reflector is used at each offset, and thus areal consistency at depth is not a requirement.

2.6.4 Cross-hole Radar Tomography or Transillumination

In the transmission mode of deployment, the transmitter and receiver antennae are on opposite sides of the medium being investigated. Two common cross-hole survey geometries are shown in Figures 2.5 and 2.6. The imaging configuration in Figure 2.5, where a receiver is moved in step with the transmitter antenna, is referred to as a scan. Assuming a constant velocity (as well as that the boreholes are parallel to each other), the direct

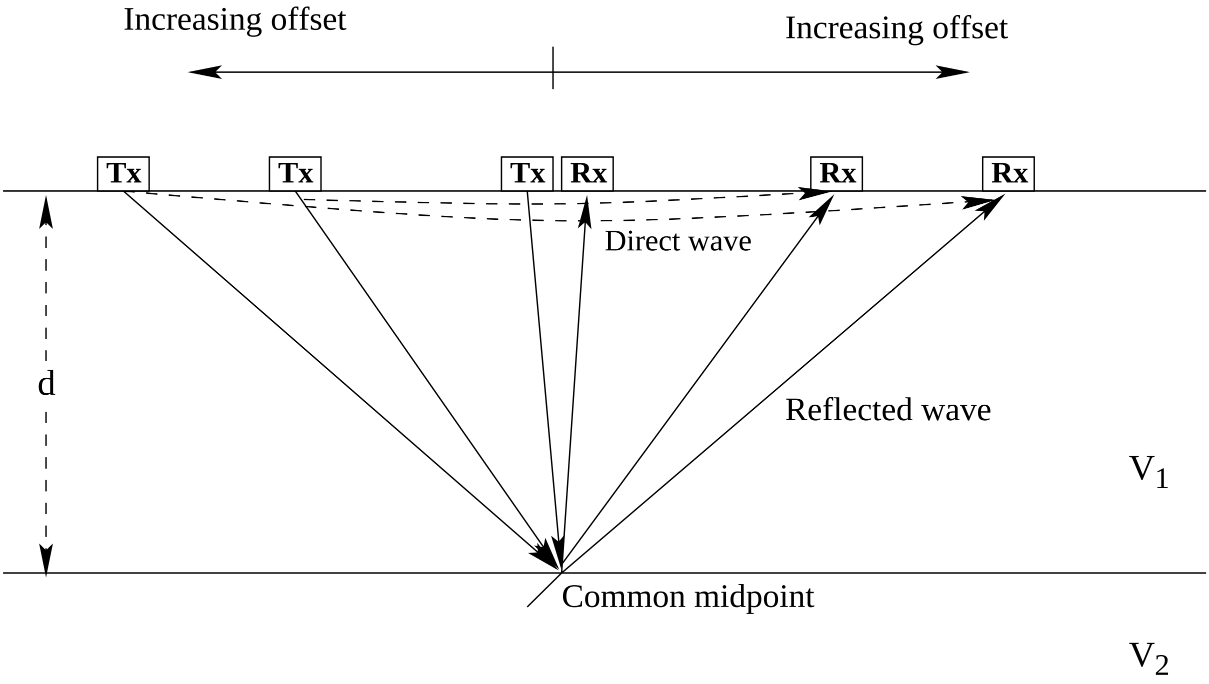

Figure 2.4: *Common midpoint (CMP) measurement configuration, both the transmitter and receiver antenna are moved away at increasing offsets.*

wave will produce a horizontal straight line across the time section. Deviations from such a straight line, as well as variations in the amplitude of the first break, may indicate the presence of an inhomogeneity, thus indicating the likely position of the targets. A plane reflector AB (Figure 2.5) intersecting the borehole plane at right angles will appear as a hyperbola in the time section, as its reflecting point stays fixed at the midpoint P between the boreholes.

The imaging configuration shown in Figure 2.6, in which the transmitter and receiver antennae move in opposite directions along parallel boreholes is called as ’Yo-Yo’ survey. The reflection point P on the plane AB moves from B towards A. As the distance between Tx-P-Rx remains constant, the reflection pattern of the plane AB will be a horizontal straight line on the time section (assuming constant propagation velocity). Thus endfire probes can profile surfaces perpendicular to the boreholes.

The third type of configuration, as shown in Figure 2.7, is often used in underground mines, for example, between mine galleries. As the relative positions of the radar antennae are known at all times, and hence the distances between them, the mean radiowave velocity can be derived from the time section. More details of this method can be found in Annan and Davis (1977).

The transillumination mode is common in non-destructive testing (NDT) investigations of man-made objects, such as testing concrete columns and masonry pillars.

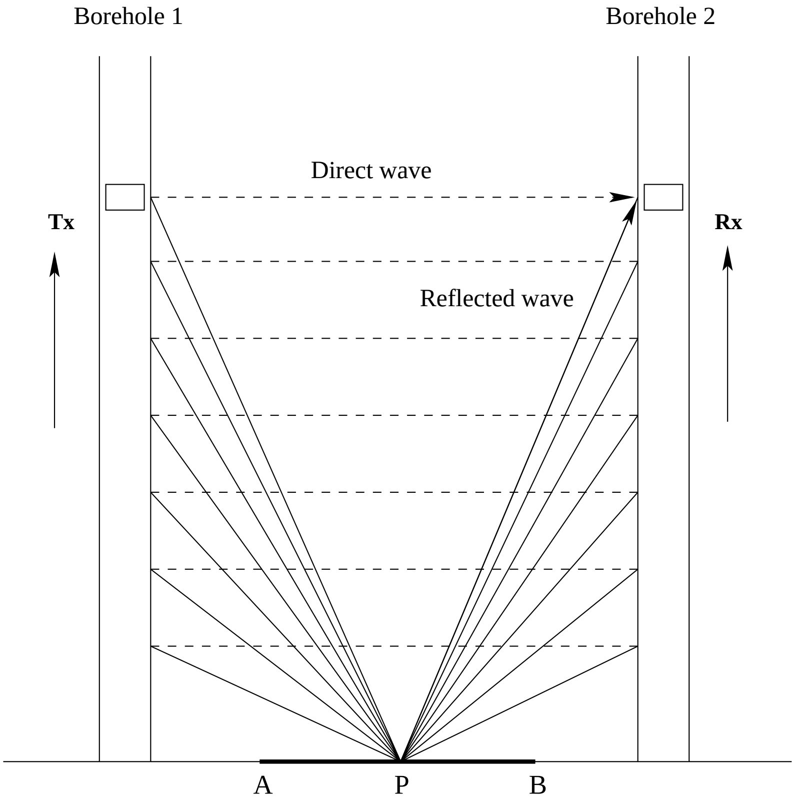

Figure 2.5: C*ross borehole scan in which transmitter and receiver move in step, keeping them equidistant.*

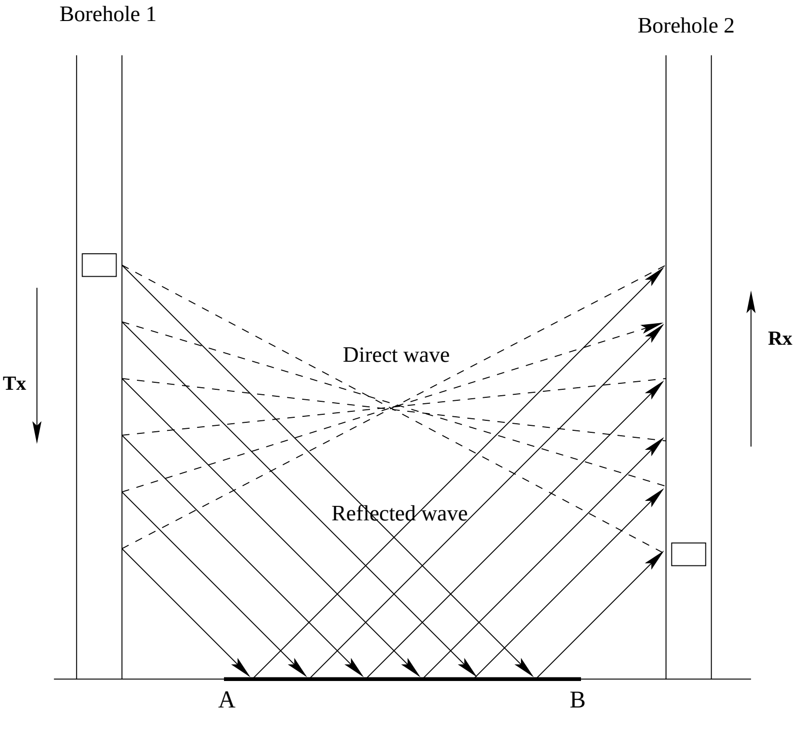

Figure 2.6: *A Yo-Yo in which the receiver moves in the opposite direction to the transmitter.*

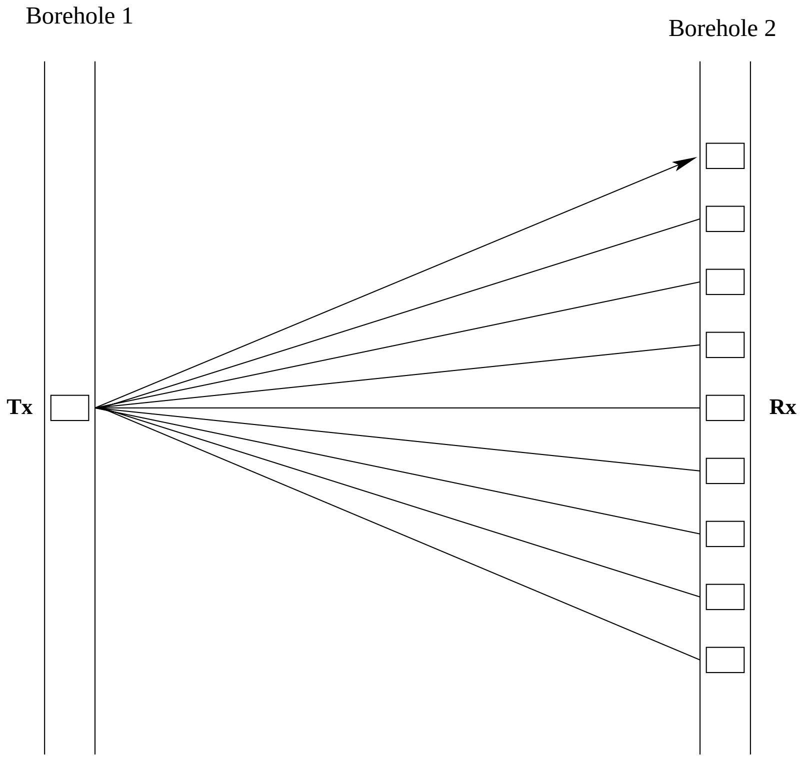

Figure 2.7: *Transmitter and receiver antenna are kept in different borehole. The different receiver locations are shown in the right borehole.*

2.7 Radar Signal Modelling and Resolution

The theory of the matched filter, the deconvolution filter, and the azimuth resolution that is presenting in this section, will be utilised in Chapter 4 for processing both the simulated radar data as well as the real acoustic data.

2.7.1 Baseband Analytic Signal

We note that the radar signal is generally clustered around a carrier frequency. This signal must be processed to baseband before proceeding (Wilkinson, 2001). For a real signal $x(t)$, the spectrum can be split into a negative and a positive half which together make up the full spectrum (Figure 2.8(a)):

$$X(f) = X^{+}(f) + X^{-}(f)$$

where $X^{+}(f)$ and $X^{-}(f)$ are the positive and negative half of the spectrum $X(f)$.

Now, for a real signal $x(t)$, we have

$$X(-f) = X^*(f) \tag{2.19}$$

Thus all the information in $X(f)$ is contained in the positive spectrum $X^+(f)$ and hence in the basebanded signal $V(f)$.

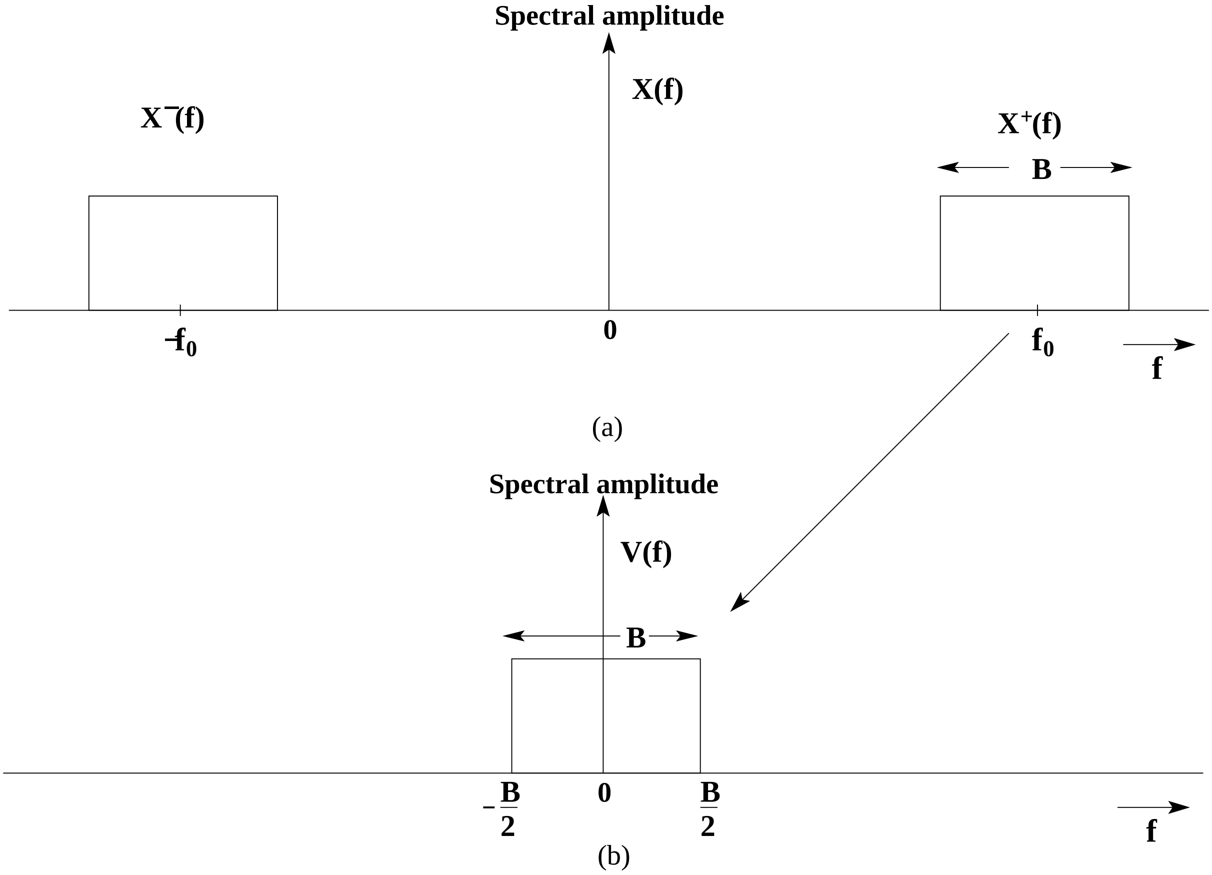

Figure 2.8: *(a) Fourier spectrum of real signal (b) Baseband analytic signal*

The basebanded signal $V(f)$ is a frequency-shifted version of the analytic representation of $X(f)$ (Figure 2.8(b)), i.e.

$$V(f) = 2X^+(f + f_0) \tag{2.20}$$

2.7.2 Radar Signal Modelling

Let the transmit signal be modelled by the analytic representation

$$v_{TX}(t) = p(t)e^{j2\pi f_0 t} \tag{2.21}$$

where f_0 is the carrier frequency, and $p(t)$ is a basebanded representation of the pulse.

The response from a point target can be modelled by

$$v_{RX}(t) = \zeta(t) \otimes v_{TX}(t - \tau) \tag{2.22}$$

where $\zeta(t)$ is the target response and $\tau = \frac{2R}{c}$ is the two-way time delay from the target to the antenna and the symbol $\otimes$ represents the convolution operation.

For a narrow-band radar, the target response can be related to the terms in the standard *radar equation* (Skolnik, 1988), by

$$\zeta \propto \sqrt{\frac{G^2 \sigma_1 \lambda^2}{(4\pi)^3 R^4}} \tag{2.23}$$

where G is the antenna gain, σ_1 is the radar cross-section of the target, λ is the wavelength and R is the range to the target.

Now, consider the case where there are N number of point targets at ranges R_i. In the case of a linear system the received signal is the sum of the signal returned from the point targets, i.e.

$$v_{RX}(t) = \sum_{i=1}^{N} \zeta_i v_{TX}(t - \tau_i) \tag{2.24}$$

We can extend the concept to a distributed target modelled by

$$v_{RX}(t) = \int_{-\propto}^{+\propto} \zeta(\tau) v_{TX}(t - \tau) d\tau = \zeta(t) \otimes v_{TX}(t) = \int_{-\propto}^{+\propto} \zeta(t - \tau) v_{TX}(\tau) d\tau \tag{2.25}$$

where $\zeta(t)$ is the impulse response of the target or scene.

In the frequency domain, we can write Equation 2.25 as

$$V_{RX}(f) = \zeta(f) \cdot V_{TX}(f) \tag{2.26}$$

Figure 2.9 explains the concept of the received signal spectrum, which is a convolution of the transmitted spectrum with the target reflectivity spectrum. Thus we can see that the radar observes a windowed portion of the scene's impulse response.

2.7.3 Pulse Compression and Radar Range Resolution

Pulse compression, also known as pulse coding, is a signal processing technique designed to maximise the sensitivity and resolution of radar systems. The sensitivity of a radar depends on the energy transmitted in the radar transmitted pulses. Pulse compression refers to a family of techniques used to increase the bandwidth of radar pulses. In the radar receiver, the echo pulses are compressed in the time domain, resulting in a range resolution which is finer than that associated with an uncompressed pulse (Wehner, 1987).

The basebanded form of the received signal (Equation 2.22) can be expressed as

$$\begin{aligned} v_{bb}(t) &= v_{RX}(t)e^{-j2\pi f_0 t} && (2.27)\\ &= [\int_\tau \zeta(t-\tau)\,p(\tau)\,e^{j2\pi f_0\tau}d\tau]\,e^{-j2\pi f_0 t} && (2.28)\\ &= [\zeta(t)\,e^{-j2\pi f_0 t}]\otimes p(t) && (2.29)\end{aligned}$$

Introducing the transducers and other linear system effects affecting the received response, we can write Equation 2.29 as

$$v_{bb}(t) = [\zeta(t)\,e^{-j2\pi f_0 t}]\otimes h_s(t) \tag{2.30}$$

where

$$h_s(t) = p(t)\otimes h_{bb}(t) \tag{2.31}$$

and $h_{bb}(t)$ contains the basebanded transducer and other linear system response.

In the frequency domain, Equation 2.30 can be written as

$$V_{bb}(f) \quad = \quad \zeta(f+f_0)\cdot H_s(f) \tag{2.32}$$

Now if we can design a linear filter such that $h_s(t)\otimes h_c(t) = \delta(t)$, then we can reconstruct the basebanded target response $[\zeta(t)e^{-j2\pi f_0 t}]$. In practice, $p(t)$ is a bandlimited signal of bandwidth B, and thus we can only reconstruct $\zeta(f)$ within this limited band.

Matched Filter

Matched filter theory deals with the optimal detection of a waveform in presence of additive noise (Stremler, 1990). Matched filter maximizes the peak SNR at its output. The design of such a filter will improve the chances of detecting a faint target in the presence of noise (additive noise).

In the presence of additive noise, the output receive signal (Equation 2.30) can be written as

$$v(t) = v_{bb}(t) + n_{bb}(t) \tag{2.33}$$

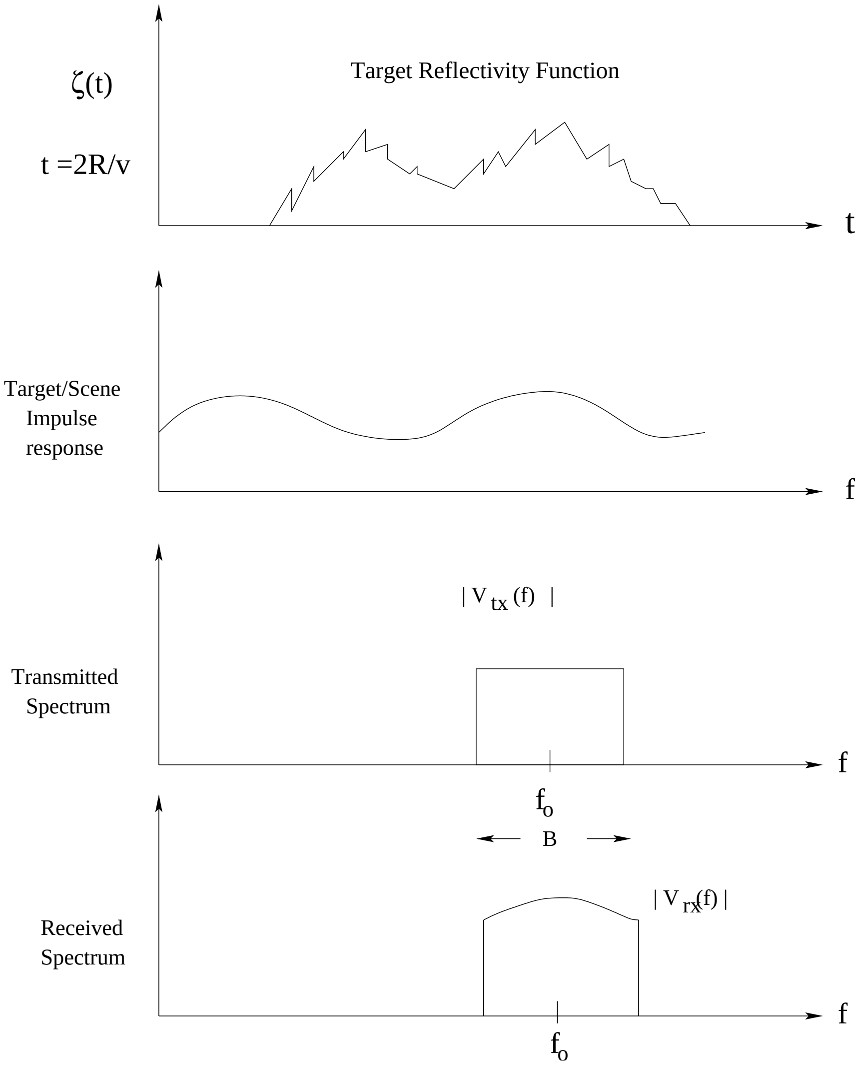

Figure 2.9: *Reflectivity spectrum of target/scene. The received spectrum is the convolution of the transmitted spectrum with the target/scene reflectivity spectrum* (Wilkinson et al., 1998).

where $v_{bb}(t)$ is the output baseband receive signal part and $n_{bb}(t)$ is the output baseband noise.

In case of the receiver passband is flat (i.e. $H_{bb}(f) \approx rect(\frac{f}{B})$), the desired matched filter is the time reverse complex conjugate of the transmitted pulse and is given by

$$\begin{aligned} h_{MF}(t) &= kv_1^*(-t) && (2.34) \\ H_{MF}(f) &= kV_1^*(f) \\ &= kP^*(f) && (2.35) \end{aligned}$$

where $v_1(t)$ is the baseband transmitted pulse and k is a constant. We are considering

$k = 1$ in our discussion.

The output signal after applying matched filter is given by

$$V_0(f) = V_{bb}(f) \cdot H_{MF}(f) \tag{2.36}$$

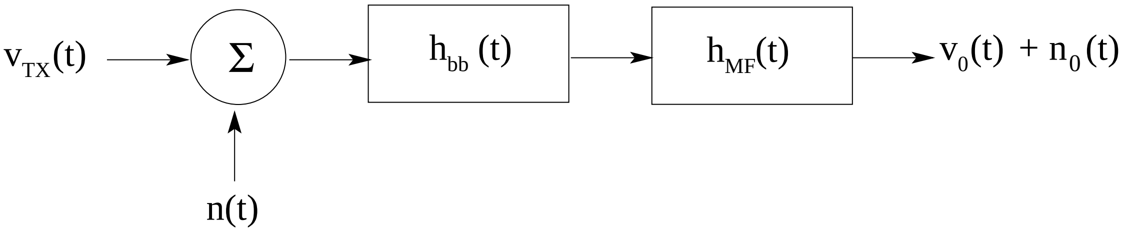

Figure 2.10: *Matched filter concept.*

By using Equation 2.32 in Equation 2.36, we obtain $V_0(f)$ as

$$\begin{aligned} V_0(f) &= \zeta(f+f_0) \cdot H_s(f) \cdot H_{MF}(f) \\ &= \zeta(f+f_0) \cdot P(f) \cdot H_{bb}(f) \cdot P^*(f) \\ &= \zeta(f+f_0) \cdot |P(f)|^2 \cdot H_{bb}(f) \end{aligned} \tag{2.37}$$

Considering $P(f)$ has a flat passband, as it is the case for chirp pulse, we can write Equation 2.37 as

$$V_0(f) = \zeta(f+f_0) \cdot rect(\frac{f}{B}) \tag{2.38}$$

Let the target reflectivity spectrum of a point target is given by

$$\zeta(t) = \zeta_0 \, \delta(t-\tau) \tag{2.39}$$

where ζ_0 is the point target backscatter amplitude.

By using Equation 2.39 in Equation 2.37, we can write the time domain signal $v_0(t)$ as

$$\begin{aligned} v_0(t) &= [\zeta(t)\, e^{-j2\pi f_0 t}] \otimes BSa(\pi Bt) \\ &= [\zeta_0 \, \delta(t-\tau)\, e^{-j2\pi f_0 \tau}] \otimes BSa(\pi Bt) \end{aligned} \tag{2.40}$$

where we have replaced the term $e^{-j2\pi f_0 t}$ with constant $e^{-j2\pi f_0 \tau}$ as the impulse is zero for all time expect at τ. Convolving with the Dirac impulse simply shifts the Sa function, and the desired output signal is given by (see Figure 2.10)

$$v_0(t) = \zeta_0 BSa(\pi B\,[t-\tau])e^{-j2\pi f_0 \tau} \tag{2.41}$$

Ideal Reconstruction or Deconvolution Filter

Although optimal for SNR, matched filtering results in an undesirable point target response if the passband of the transducers are not flat in magnitude and linear in phase. For optimal point target response, a deconvolution processing approach can be adopted, in which the baseband signal was passed through the filter $H_c(f) = [1/H_s(f)]\, rect(f/B)$. By using Equation 2.32, the output signal is given by

$$\begin{aligned} V_0(f) &= V_{bb}(f) \cdot H_c(f) \\ &= \zeta(f + f_0) \cdot rect(\frac{f}{B}) \end{aligned} \tag{2.42}$$

The time domain output is given by

$$v(t) = \zeta_0 B Sa[\pi B(t - \tau)] e^{-j2\pi f_0 \tau} \tag{2.43}$$

where the term $e^{-j2\pi f_0 t}$ is replaced with constant $e^{-j2\pi f_0 \tau}$ as the impulse is zero for all time except at τ.

It is noted that both filters have the same phase over the passband and equal to $-2\pi f_0 \tau = -\frac{4\pi R}{\lambda}$, but the magnitude differ by a factor approximately $\frac{1}{|P(f)|^2}$.

Range Resolution and Sample Spacing

For a *Sinc* function, the $3-dB$ width is given as

$$\delta t_{3-dB} \approx \frac{0.89}{B} \tag{2.44}$$

and hence the $3-dB$ range resolution is

$$\begin{aligned} \delta R_{3-dB} &= \frac{c_1 \delta t_{3-dB}}{2} \\ &\approx \frac{c_1}{2B}(0.89) \end{aligned} \tag{2.45}$$

where B is the pulse bandwidth and $c_1 = \frac{c}{\sqrt{\varepsilon_r}}$; c is the velocity of light in free space , ε_r is the relative permittivity of the medium.

According to Nyquist theorem the slant range sample rate f_s should be

$$f_s \geq 2 \cdot \frac{B}{2} = B \tag{2.46}$$

and the slant range spacing should be

$$\begin{aligned} \delta t &\leq \frac{1}{f_s} = \frac{1}{B} \\ \delta R &\leq \frac{c_1}{2} \cdot \delta t = \frac{c_1}{2B} \end{aligned} \tag{2.47}$$

The propagation of electromagnetic waves in subsurface rock formation is a complex phenomenon as discussed in section 2.2. At low frequencies and high losses, Maxwell's equations reduce to the diffusion equation and are thus called electromagnetic induction. At high frequencies, the energy storage in dielectric and magnetic polarisation creates wave propagation. In real materials, the electric and magnetic fields are out of phase, not completely polarised, propagated with a velocity lower than the speed of light in a vacuum, scattered by charges in electric and magnetic properties, and with all of the preceding varying as a function of frequency. In general, attenuation of electromagnetic waves increases with increasing frequency and water content(Lane et al., 1998).

Thus, all of the above complex phenomenon will affect the received signal, which is the convolution of the transmitting signal with the impulse response of the scene and thus, for a rectangular transmitting pulse, the received signal will no longer remain rectangular and hence the radar range resolution will be affected. A discussion of ultra-wideband waveform design for GPR applications is presented in Section 3.4 of Noon's PhD thesis (Noon, 1996).

2.7.4 Synthetic Aperture Radar Azimuth or Along-track Resolution and Sample Spacing

High ($\sim 1m$) azimuth resolution (in the direction of the flight track/borehole) is achieved by synthesizing a long antenna, which ranges in length from several metres to several kilometres (space-borne application). The azimuth or along-track resolution, δx, is achieved via the aperture synthesis technique (Curlander and McDonough, 1991), illustrated in Figure 2.11. An antenna with a beamwidth θ starts getting a point target $(x = 0)$ response from $x = -\frac{L}{2}$ to $x = \frac{L}{2}$, where L is the synthetic aperture length.

The range of target with the radar at some position x is

$$R(x) = [R_0^2 + x^2]^{1/2} \tag{2.48}$$

where R_0 is the distance of closest approach.

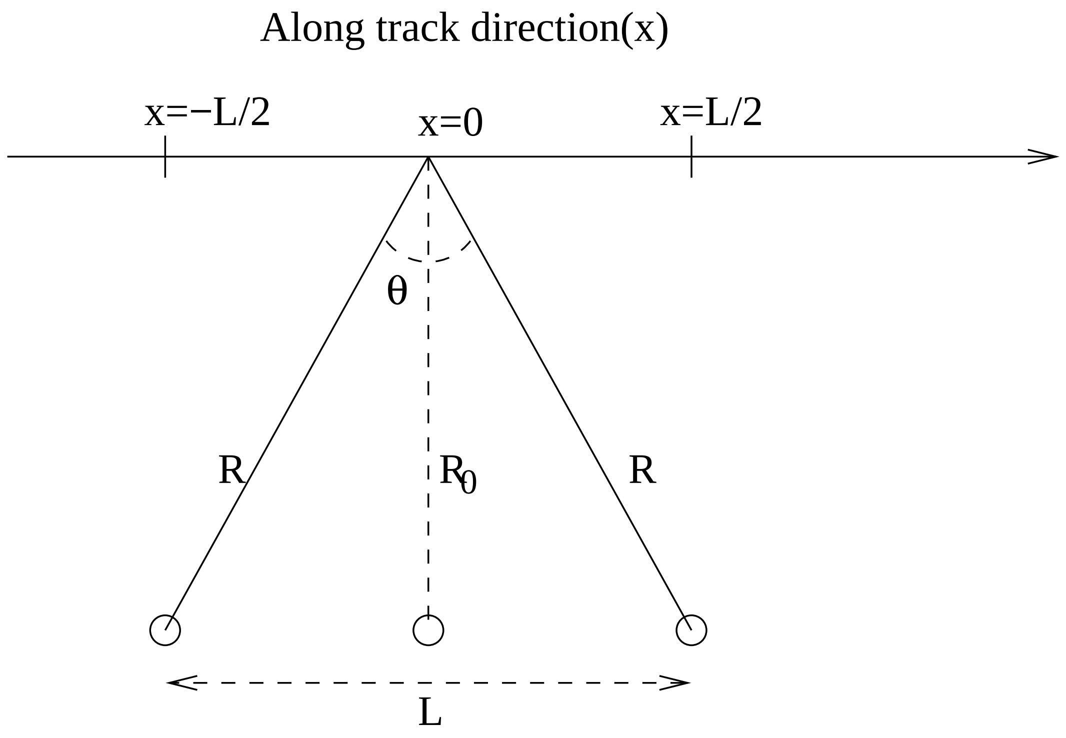

Figure 2.11: *Along-track direction antenna trajectory. The antenna has a two-way azimuth beamwidth of* θ*. The length L is the synthetic aperture length.*

The phase difference between transmitted and received waveforms due to two-way travel over the range R is

$$\phi = \frac{-4\pi R(x)}{\lambda} \tag{2.49}$$

where the time derivative of ϕ is the Doppler Frequency and λ is the wavelength at the centre frequency.

As the radar footprint passes over the target, the phase change over the two-way path from the radar to the target is

$$\triangle\phi = \frac{-4\pi \triangle R}{\lambda} \tag{2.50}$$

where

$$\triangle R = [R_0^2 + x^2]^{1/2} - R_0 \tag{2.51}$$

or

$$\triangle R \approx \frac{x^2}{2R_0}\ , \quad |x| << R \tag{2.52}$$

The along-track distance is $x = v_{st} \cdot s$, where v_{st} is the platform velocity and s is the along-track/slow time. The change of phase, $\triangle\phi$ is a quadratic function of the along-track time, s, and the change in Doppler frequency is linear with time (Curlander and McDonough, 1991). The complex Doppler waveform for the sensor at x due to a point target at $x = 0$

is given by

$$f(x) = exp[-j\phi(x)] \tag{2.53}$$

This signal has an instantaneous frequency

$$\begin{aligned} f_{Di}(x) &= \frac{1}{2\pi} \cdot \frac{d\phi}{dx} \\ &= \frac{1}{2\pi} \cdot \frac{d}{dx}[\frac{-4\pi R(x)}{\lambda}] \\ &= \frac{1}{2\pi} \cdot \frac{-4\pi}{\lambda} \cdot \frac{d}{dx}\left(\sqrt{R_0^2 + x^2}\right) \\ &= \frac{-2}{\lambda} \cdot \frac{x}{R(x)} \\ &= \frac{-2}{\lambda} \cdot \sin(\frac{\theta}{2}) \end{aligned} \tag{2.54}$$

Then a spatial bandwidth B_x (considering both sides) is

$$\begin{aligned} B_x &= 2 \cdot |f_{Di}(x)| \\ &= \frac{4\sin(\frac{\theta}{2})}{\lambda} \end{aligned} \tag{2.55}$$

corresponding to a Doppler bandwidth

$$B_D = \frac{4v_{st}\sin(\frac{\theta}{2})}{\lambda} \tag{2.56}$$

where v_{st} is the velocity along the along-track/azimuth direction.

The $3-dB$ azimuth resolution is given by

$$\begin{aligned} \delta x_{3-dB} &\approx \frac{0.89}{B_x} \\ &\approx \frac{0.89\lambda}{4\sin(\frac{\theta}{2})} \end{aligned}$$

According to Nyquist theorem, the azimuth sample rate should be

$$\begin{aligned} \text{Sample rate} &\geq 2 \cdot f_{max} \\ &\geq 2 \cdot \frac{B_x}{2} \\ &\geq B_x \end{aligned} \tag{2.57}$$

Therefore, the azimuth spacing should be

$$\begin{aligned}\text{Sample spacing} &\leq \frac{1}{\text{Sample rate}} \\ &\leq \frac{1}{B_x} = \frac{\lambda}{4\sin(\frac{\theta}{2})}\end{aligned} \tag{2.58}$$

2.8 Summary

As we have seen in this chapter, range resolution is a function of the signal bandwidth. The radar bandwidth can either be obtained instantaneously by transmitting a short pulse, or it can be obtained by transmitting a sequence of waveforms of varying bandwidth, thereby obtaining the required resolution. A description of the radio waves propagation through the earth medium has been presented. As the EM waves propagate through the earth medium, the pulse exibits dispersion. The higher frequency part of the travelling pulse attenuates more than the lower frequency component as it moves through the medium. In this present thesis, the frequency dependency of the medium has not been considered.

Different modes of radar data acquision have been discussed. The types of commercial radar currently available were discussed in this chapter. The antenna radiation pattern is a function of the largest dimension of the antenna and the pulse wavelength. The antenna radiation pattern and the antenna constraints for borehole radar were discussed in this chapter.

The radar receive signal is a convolution of the transmitted pulse with the target or scene reflectivity spectrum. The received signal needs to be range compressed to maximize the sensitivity and resolution of radar systems. In the presence of additive noise, the use of the matched filter gives an optimal SNR. Although optimal for SNR, matched filtering results in an undesirable point target response if the passband of the transducers are not flat in magnitude and linear in phase. In this case, a deconvolution filter would result in an optimal point target response. High ($\sim 1m$) azimuth resolution can be achieved by synthesizing a long antenna, which ranges in length from several metres to several kilometres (space-borne application). Lastly, the concept of SAR azimuth resolution and sampling was presented in this chapter.

Chapter 3

Borehole Radar Interferometry

3.1 Introduction

The term *radar interferometry* is broadly used to describe a range of measurement techniques involving the signal processing of coherent radar observations of a scene, taken either from different angles or at different times. The term *interferometry* refers to the *combination* or *interference* of the images, and particularly to the exploitation of the phase information contained in the radar images. The terms: *SAR interferometry*, *interferometric SAR* and *InSAR* are terms commonly used to describe radar interferometry involving images produced by using the synthetic aperture technique (Wilkinson, 1997). The information about the shape of the topography is primarily contained in the phase information of the received signals. For sidelooking real aperture radars, the smaller the azimuth beamwidth, the finer the azimuth resolution (in the direction of the flight track). To achieve a given azimuth resolution for such systems requires a much longer antenna at low frequencies than at high frequencies. Synthetic Aperture Radar (SAR) in contrast, makes it possible to use longer wavelengths and still achieve a good resolution with antenna structures of reasonable size. This is done by synthesizing the equivalent of a very long sidelooking array antenna. SAR has been shown to be very useful over a wide range of applications: ice monitoring (Drinkwater et al., 1990), detection of earth crustal movement (Massonnet et al., 1993), geology and mining (Lynne and Taylor, 1986), military surveillance, vegetation discrimination (Evans et al., 1988), hydrology (McCauley et al., 1986), urban mapping, fishing, oil pollution monitoring (Hovland et al., 1994) and oceanography (Wahl and Skoelv, 1994).

To study the potential of the SAR imaging method in the borehole environment, we carried out an InSAR simulation study in a borehole environment. The three-dimensional location of the reflecting orebody was then reconstructed from the interferometric phase.

The borehole radar experiments by Liu et al. (1998) has shown that orebodies reflect VHF radar signals both specularly and diffusely, much as the ground/air interfaces does. We have mainly considered the diffuse reflection at the interface between a homogeneous propagating medium and a reflecting orebody surface.

A simulator is a useful tool for analysing the actual interferogram. A SAR image simulator is particularly useful for understanding the effect of illumination angle and terrain relief on SAR images, testing and optimizing interferometric SAR processing algorithms, and modelling the forward problem, which lends insight to the more common inverse problem (Francheschetti et al., 1992).

The method described in this chapter adopts the start-stop approximation, which means that the radar-target range remains constant during the transmission of one burst of frequency. In a real borehole experiment, the transducers are pulled from bottom to top in the borehole and the pulses are recorded by the receivers. A two-antenna InSAR simulator for space-borne and airborne systems was first developed by Wray (2001) in the Radar Remote Sensing Group at UCT. Subsequently the simulator has been modified for multiple-antenna interferometry by Ashok (2001), using a straight flight trajectory. Van Leijen (2001) modified the simulator again for non-parallel fight trajectories. The candidate thereafter modified the simulator for borehole applications.

In this chapter, we will first present the basic InSAR principles, current state-of-the-art InSAR simulators, the InSAR simulator architecture developed in the Radar Remote Sensing Group (RRSG) at UCT, the 3-D borehole height reconstruction method using the interferometric phase, and the results achieved by using two types of orebody geometry.

3.2 Principles of Radar Interferometry

Consider a dual-pass InSAR system and a point target at point P as depicted in Figure 3.1. A pulse with a carrier frequency f_0 is transmitted from antenna 1 in the direction of the point target and the echo is received by antenna 1 with a round trip delay t_{d1}. On the second pass, antenna 2 transmits the pulse and receives the echo with a time delay t_{d2} given by

$$t_{d1} = \frac{2 \cdot r_1}{c_1} \tag{3.1}$$

$$t_{d2} = \frac{2 \cdot r_2}{c_1} \tag{3.2}$$

where c_1 is the speed of propagation in the medium.

The received signals $V_1(\tau, t)$ and $V_2(\tau, t)$ are demodulated to baseband and stored as

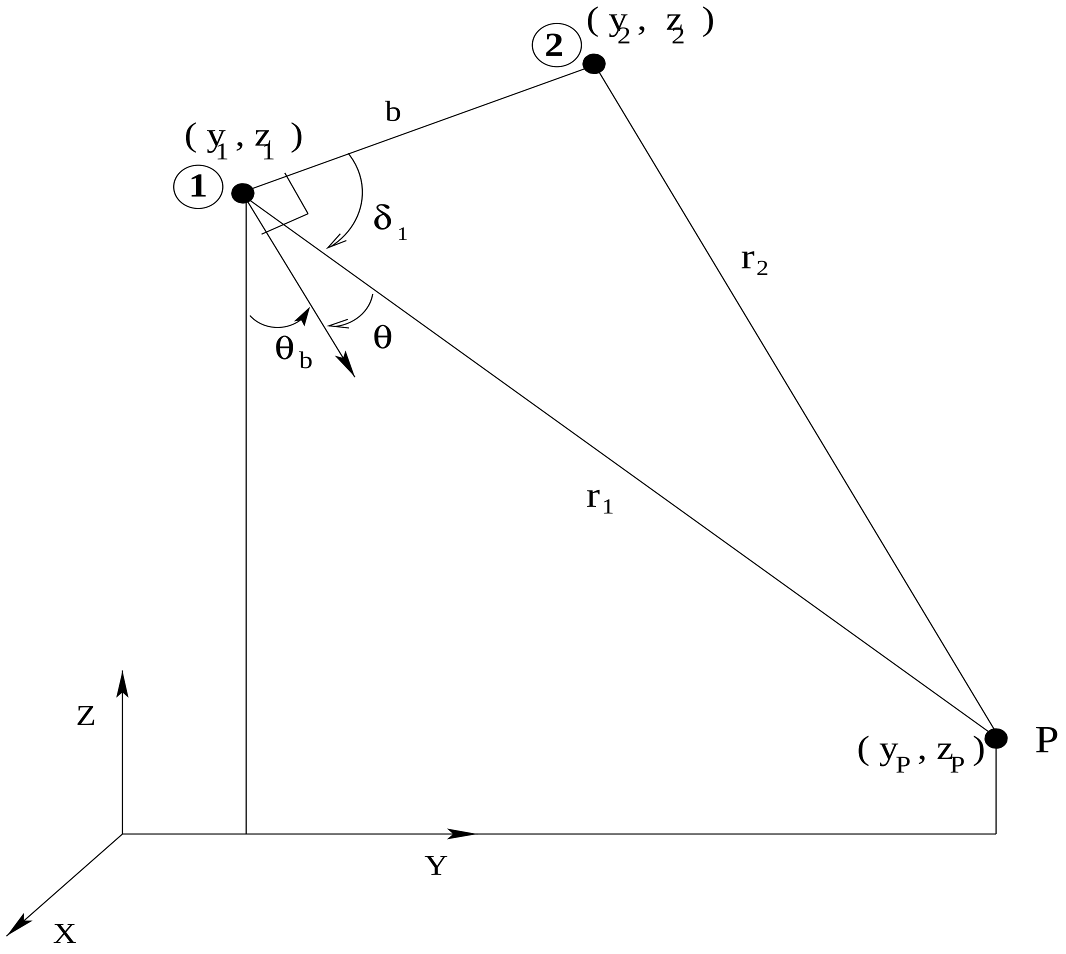

Figure 3.1: *Geometry of a dual-pass 2-D antenna InSAR system.*

complex sampled data. The point target response after pulse compression is represented as

$$\begin{aligned} V_1(\tau, t) &= |V_1(\tau, t)|\, e^{j\psi_1(\tau,t)} && (3.3)\\ V_2(\tau, t) &= |V_2(\tau, t)|\, e^{j\psi_2(\tau,t)} && (3.4)\end{aligned}$$

where τ is the azimuth sample time.

The phase of the received signals at antenna 1 and antenna 2 is related to the time delay t_{d1} and t_{d2} as

$$\begin{aligned} \psi_1(\tau, t) &= \arg\left\{e^{-j2\pi \cdot f_0 \cdot t_{d1}}\right\} = \arg\left\{e^{\frac{-j4\pi r_1}{\lambda}}\right\} && (3.5)\\ \psi_2(\tau, t) &= \arg\left\{e^{-j2\pi \cdot f_0 \cdot t_{d2}}\right\} = \arg\left\{e^{\frac{-j4\pi r_2}{\lambda}}\right\} && (3.6)\end{aligned}$$

The phase difference is of primary importance in interferometry. It is referred to as interferometric phase ψ_{12} and is defined as

$$\psi_{12} = arg\left\{V_1 \cdot V_2^*\right\} = arg\left\{e^{j(\psi_1 - \psi_2)}\right\} = arg\left\{e^{\frac{-j4\pi(r_1 - r_2)}{\lambda}}\right\} \tag{3.7}$$

The interferometric phase ψ_{12} is referred to as the $principal$ (or wrapped) phase, which lies in the range $[-\pi, \pi]$. Thus the measured phase difference ψ_{12} is a modulo of 2π measurement of the $absolute$ (or unwrapped) phase delay φ_{12},

$$\varphi_{12} = \frac{4\pi(r_2 - r_1)}{\lambda} \tag{3.8}$$

The principal phase and absolute phase are related by

$$\varphi_{12} = \psi_{12} + k \cdot 2\pi \tag{3.9}$$

$$\psi_{12} = W\left(\varphi_{12}\right) \tag{3.10}$$

where k is an integer constant and the function $W\left(\right)$ is the wrapping operator that converts the absolute phase to the interferometric phase. In interferometry, the terrain height is related to the $absolute$ phase, hence the measured modulo 2π interferometric phase has to be unwrapped in order to recover the terrain height (Goldstein et al., 1988).

The absolute phase is related to the angle between the baseline normal and r_1 by (Wilkinson, 1997)

$$\varphi_{12} = \frac{4\pi}{\lambda}\left(\left[b^2 + r_1^2 - 2r_1 b \sin\theta\right]^{1/2} - r_1\right) \tag{3.11}$$

The terrain height is directly related to the angle of arrival θ, which can be expressed in terms of the $absolute$ phase by rearranging Equation 3.11 as

$$\theta = \arcsin\left[\frac{-\lambda\varphi_{12}}{4\pi b} + \frac{b}{2r_1} - \frac{\lambda^2\varphi_{12}^2}{32\pi^2 b r_1}\right] \tag{3.12}$$

The position of the point target is then expressed by the angle of arrival and the antenna coordinates is given by (Figure 3.1)

$$y_p = y_1 + r_1 \sin\theta \tag{3.13}$$

$$z_p = z_1 - r_1 \cos\theta \tag{3.14}$$

where (y_1, z_1) are the coordinates of antenna 1, angle θ_b is the baseline elevation angle, r_1 is the measured range from antenna 1 to the target and θ is the direction of arrival of the received echo, which is calculated from the interferometric phase φ.

In the case of non-parallel boreholes or flight trajectories, the target location can be resolved by analyzing the 3-D vector relations. To apply these 3-D equations to the recon-

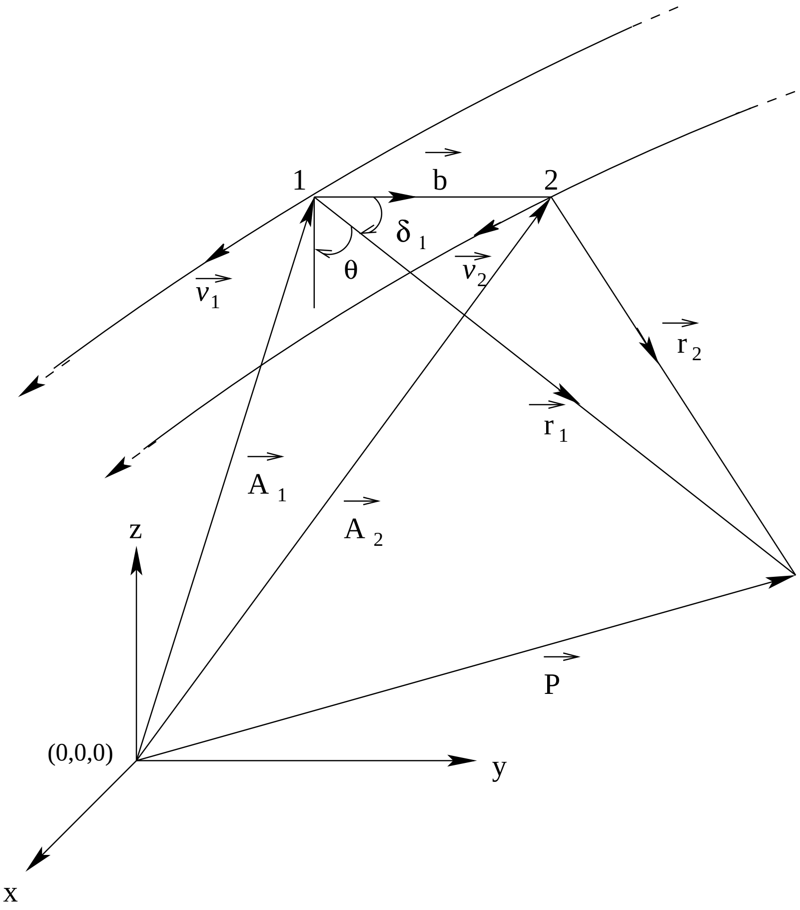

Figure 3.2: *Three-dimensional vector model of a dual-pass InSAR system.*

struction of an entire image, precise knowledge of the antenna locations for every point in the image is required.

The vector diagram shown in Figure 3.2 represents a general dual-pass interferometric imaging geometry in three-dimensions.

The positions of the two antennas in the boreholes, labelled as 1 and 2 respectively, are described by time-varying position vectors $\vec{A_1}$ and $\vec{A_2}$, and by the velocity vectors $\vec{v_1}$ and $\vec{v_2}$. The location of a point on the surface is defined by its position vector $\vec{P}$. The location of the point target can be reconstructed by solving the vector relations as (Wilkinson, 1997)

$$\vec{P}=\vec{A_1}+\vec{r_1} \tag{3.15}$$

where $\vec{r_1}$ is obtained by solving the following three simultaneous equations,

$$\vec{b}\cdot\vec{r_1} = \left|\vec{b}\right|\cdot\left|\vec{r_1}\right|\cos\delta_1 = r_1 b\sin\theta \tag{3.16}$$

$$\left|\vec{r_1}\right| = r_1 \tag{3.17}$$

$$\vec{v_1} \cdot \vec{r_1} \quad = \quad \frac{c_1 r_1 f_{D1}}{2 f_1} \tag{3.18}$$

where c_1 is the speed of propagation, b is the baseline, f_1 is the centre frequency and f_{D1} is the Doppler shift.

The solution of $\vec{r_1}$ is given in Appendix A.

3.3 Simulators in the Literature

As there are so many different types of imaging SAR systems, varying both in design and operation, many institutions have developed their own in-house SAR simulators. Several are described here, grouped by their functionality into three categories on the basis of the nomenclature as adopted by Leberl (Leberl, 1990).

3.3.1 Coherent System Simulators

The most accurate method of implementing a coherent SAR simulation involves two steps. In the first step, a phase history simulation is run, using the parameters of the actual SAR to be simulated. The product of the first step would be the raw SAR signal. In the next step, this raw SAR signal is passed through the appropriate SAR processor (doppler or phase history processor) to generate the complex slant range data set. SAR simulators in this class implement a complete end-to-end mathematically rigorous model of the radar imaging process. From an arrangement of targets, the raw SAR signal is computed, and processed through an internal SAR processor. This model focuses on an accurate representation of the scene's reflection properties, which can include terrain electromagnetic properties, frequency and polarization parameters and small- or large-scale statistics. Examples of this type of simulator are Franceschetti et al. SAR raw signal simulator (Francheschetti et al., 1992), and their later version for modelling the ocean surface (Francheschetti et al., 1999).

3.3.2 Incoherent Image Simulators

Incoherent Image Simulators are designed to produce realistic simulated images directly, replacing the combined raw signal generator and the SAR processor section with a SAR image model. Image statistics and terrain-to-sensor geometrical relations are computed without the need for a SAR processor. A trade-off exists between the simplicity (and hence the computational complexity) of the model and an accurate representation of a

SAR signal. This category includes Gelautz's image simulator (Gelautz et al., 1998), which is particularly relevant to layover areas, and Guindon's SARPLAN simulator (Guindon, 1993), which aids in the selection of the most suitable sensor and imaging geometry. The Kansas simulator by Holtzman et al. (Holtzman et al., 1978) also belongs into this category, focusing specifically on the development of an intricate backscatter model for more realistic power images.

3.3.3 SAR Image-based Simulators

In this category, the simulated image is formed by using information extracted from an actual SAR image, with the simulated image depicting a view from an alternate imaging configuration. Some successful implementations of this type include Domik's use of an ascending orbit image to generate a descending orbit image (Domik and Leberl, 1987) and Xu and Cumming's method (Xu and Cumming, 1997) of producing an interferometric pair from a single complex image.

3.4 Interferometric Simulators

The interferometric SAR simulator used in this thesis is of the class described in Section 3.3.2, i.e. it is based on the direct synthesis of a pair of single look complex (SLC) SAR images, from a given Digital Elevation Model (DEM). This type allows interferometric images to be formed with minimum complexity yet reasonable accuracy.

3.4.1 Simulator Architecture

The simulator uses several input parameters to specify the radar system parameters, radar scene geometry and scene model. It uses antenna position information (time and position state vectors), antenna transmission/receiving arrangement, radar system parameters, slant range and azimuth spacing and input scene height information. The simulator at the output produces a single look complex (SLC) for every antenna, as well as a coherence map for all image pairs, a simulated slant range height map from the input height map, layover and shadow maps, and angle of arrival. A block diagram of the simulator architecture is shown in Figure 3.3.

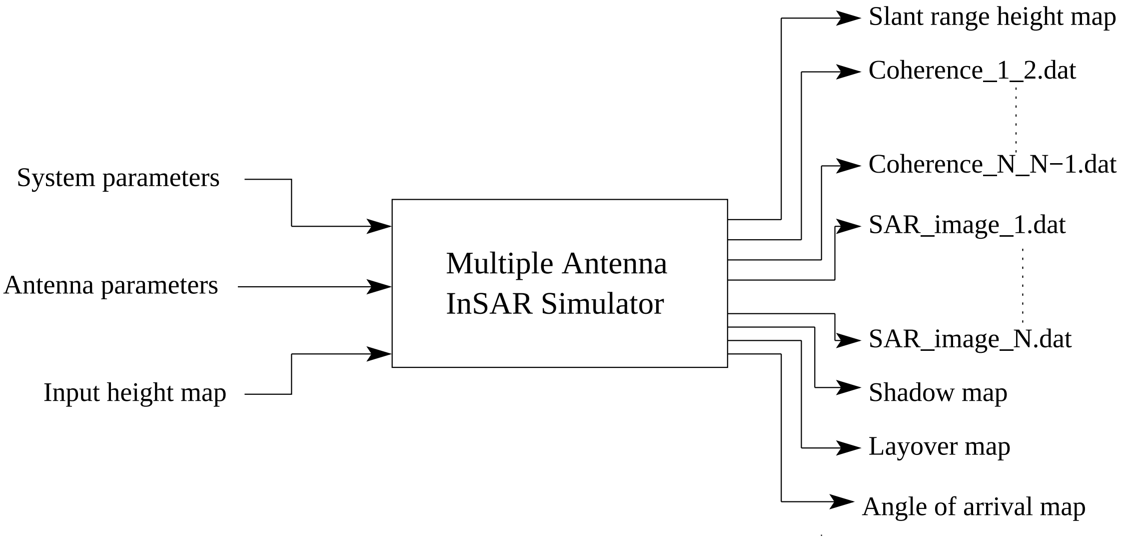

Figure 3.3: *Simulator architecture.*

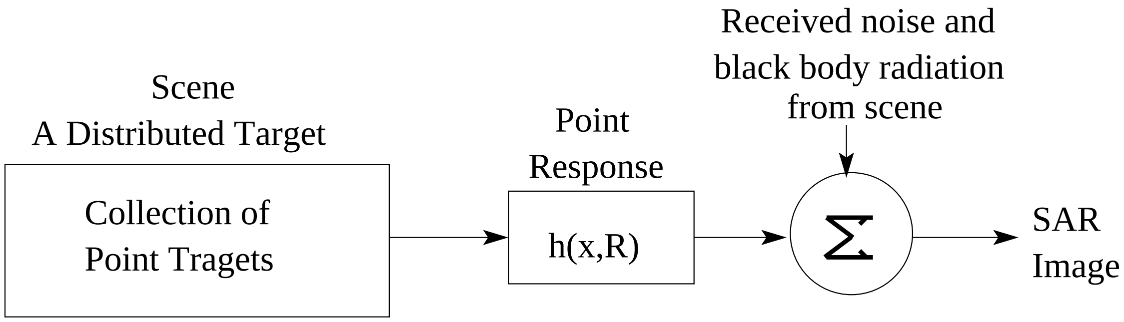

Figure 3.4: *SAR image formation model. Each resolution cell of the SAR image contains several point scatterers* (Ashok, 2001).

3.4.2 Simulation Geometry

The scene is represented by an input height map, which is a collection of height points given in ground range. The height values are split into three separate files, and within each file into the X, Y and Z coordinates respectively. The requirement is that points which lie next to each other on the scene surface, must also lie next to each other in the matrix. In the case of a non-parallel antenna trajectory, the flight path is modelled in a least-square sense, based on a best-fitting polynomial. The maximum order of the polynomial equals the length of the position vector of the platform minus one (van Leijen, 2001).

3.4.3 SAR Image Formation

A SAR image is composed of signal returns scattered from the illuminated surface. Each pixel in a focused SAR image represents the signal return from a patch on the ground (input DEM), referred to as a *resolution cell*. A resolution cell contains several point scatterers, and the received complex signal V is expressed as the weighted sum of all the returns

$$V(x, R) = \sum_i a_i \cdot e^{j\psi_i} \tag{3.19}$$

where a_i is the amplitude and $\psi_i = -\frac{4\pi r_i}{\lambda}$ is the phase of the complex signal return from the i^{th} point scatterer at range r_i. The variable x and R represent the azimuth and the slant range image coordinates respectively. The combined return from multiple scatterers in a resolution cell can be represented by an equivalent signal return as

$$V(x, R) = A(x, R) \cdot e^{j\psi(x,R)} \tag{3.20}$$

where the signal amplitude A fluctuates in accordance with the distribution of scatterers on the surface, characterised locally by its equivalent radar cross section σ^0 (Ulaby et al., 1982). The scene can be modelled as a distributed target. The SAR image formation process can therefore be represented by the returns from a scene, a distributed target, transformed by the radar system's point response with the addition of receiver noise and black body radiation from the scene (Ashok, 2001). The SAR image formation process is explained in Figure 3.4.

3.5 Reconstruction Algorithm

The terrain height reconstruction algorithm is shown in Figure 3.5. The borehole InSAR simulator produces a registered Single Look Complex (SLC) image for the given input height map (DEM) for each antenna setting. The complex interferogram is produced by multiplying one complex SAR image with the conjugate of the other. The terrain height is related to the absolute or unwrapped interferometric phase. The Minimum Cost Flow (MCF) phase unwrapping algorithm has been implemented by Van Dyk (2000) (van Dyk et al., 2000) in the Radar Remote Sensing Group at UCT. The wrapped phase is unwrapped by using the MCF algorithm. After removing the flat surface phase from the unwrapped phase, the residual phase values are converted into corresponding height values. Finally, the slant range reconstructed height values are projected into ground range values. The curved antenna trajectory was modelled by using five time state vectors and the three velocity vectors components (V_x, V_y, V_z) along the antenna trajectory.

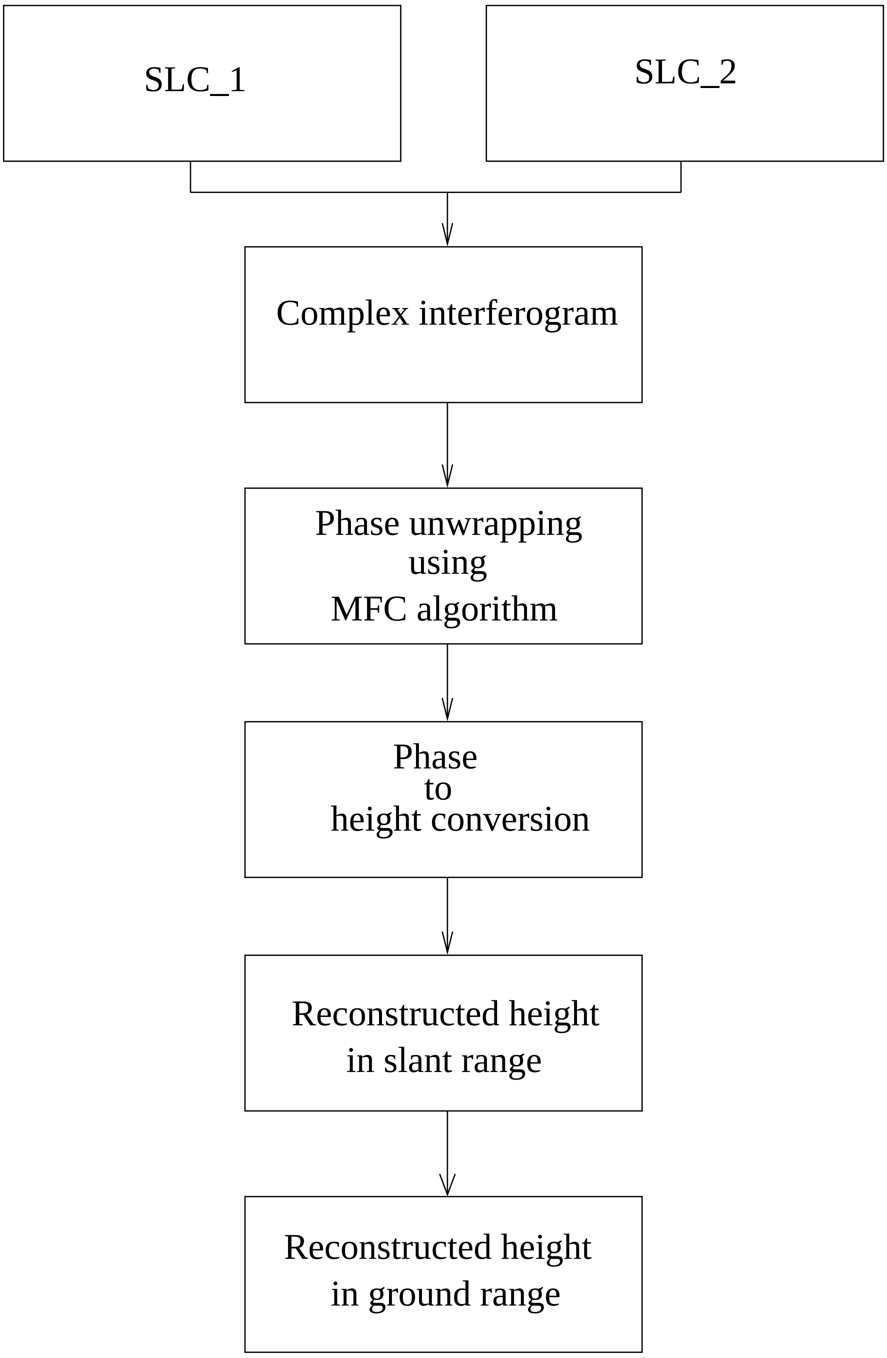

Figure 3.5: *Algorithm of the reconstruction height from the interferometric phase.*

3.6 Description of Borehole Interferometric Experiment

The borehole radar experiments in Australian mines have shown that orebodies reflect VHF radar signals both specularly and diffusely, much as the ground/air interfaces does (Liu, Osman, Manning, Hargreaves and Turner, 1998). To study the potential of the

InSAR imaging technique in the borehole environment, we have mainly considered the non-specular reflection at the interface between a homogeneous host rock medium and a reflecting orebody surface. The velocity of EM wave propagation in the host rock was considered to be 1.0×10^8 m/sec. Taking into consideration the attenuation of RF signals in the host rock and also the previous studies suggesting a usable range $100\,\mathrm{m}$ (Trickett et al., 2000), the master antenna was kept approximately 100 metres away from the nearest reflecting surface. Practically, however, boreholes do tend to drift considerably from the ideal straight line. For this purpose, the simulation has been carried out both for parallel and non-parallel borehole geometries. In the discussion below, we specifically considered a sidelooking antenna system.

3.6.1 Geometry 1 (pothole type orebody)

In the mining industry, particularly in the South African platinum mines, there is a need for high resolution imaging of pothole type structures. The Bushveld Igneous Complex (BIC) of South Africa is one of the richest deposits of platinum group metals (PGM) in the world (Geology of South Africa, 2003). Figure 3.6 shows the stratigraphic section of the critical zone of the BIC. Potholes in BIC are usually circular or almost circular in plan and ± 30m in diameter (Lomberg et al. 2000). The pothole-like structures can be imaged in 3-D with high resolution using multiple boreholes sidelooking antenna, as shown in Figure 3.6 (Borehole 1 and Borehole 2 are perpendicular to the plane of the paper). Bearing in mind the problems encountered in the mining industry, we have considered pothole-like target orebodies for our borehole InSAR experiment, as shown in Figure 3.7.

In this case, the boreholes were considered to be parallel to each other with a vertical baseline of 10m. The system and antenna parameters of the experiment are given in Table 3.1. The Y-axis corresponds to the range, whereas the X-axis corresponds to the azimuth direction, which is also the principal direction of the borehole. In both cases the master antenna was kept 100m away from the nearest reflecting surface. Lastly, the antenna in this setup was looking towards the orebody.

3.6.2 Geometry 2 (half-cylindrical orebody)

In the mining industry, kimberlite pipes are a good source of diamonds. Thus, it is extremely important to image the kimberlite pipe ahead of mining with high resolution. Kimberlite intrusions can be detected by GPR surveys because of the contrast in both dielectric permittivity and electric resistivity between kimberlites and surrounding rocks.

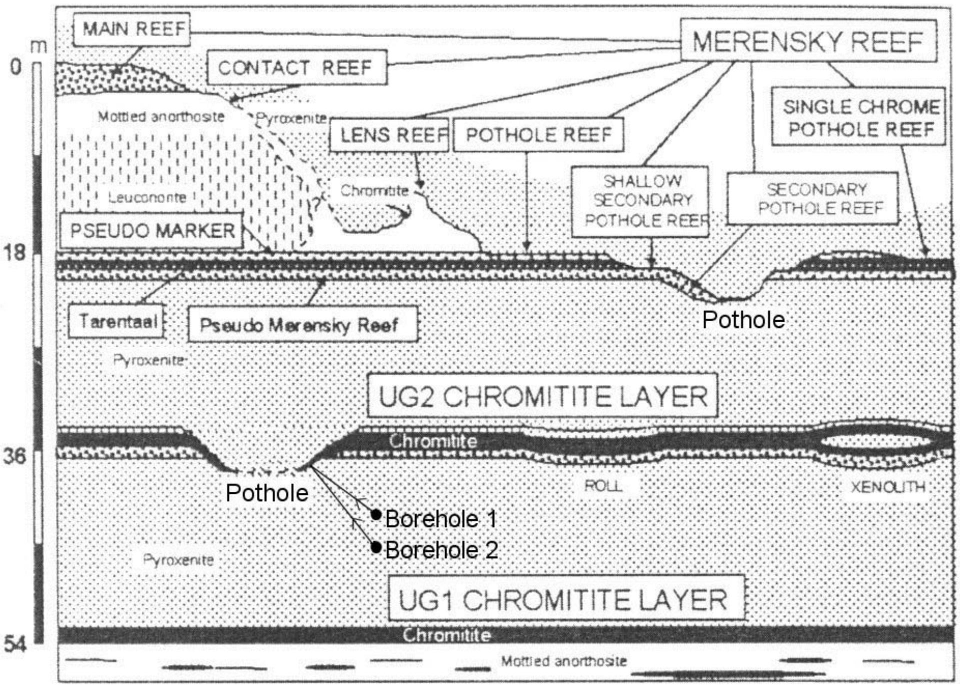

Figure 3.6: *Schematic dip section demonstrating local changes in dip, strike and thickness* (Lomberg et al. 2000).

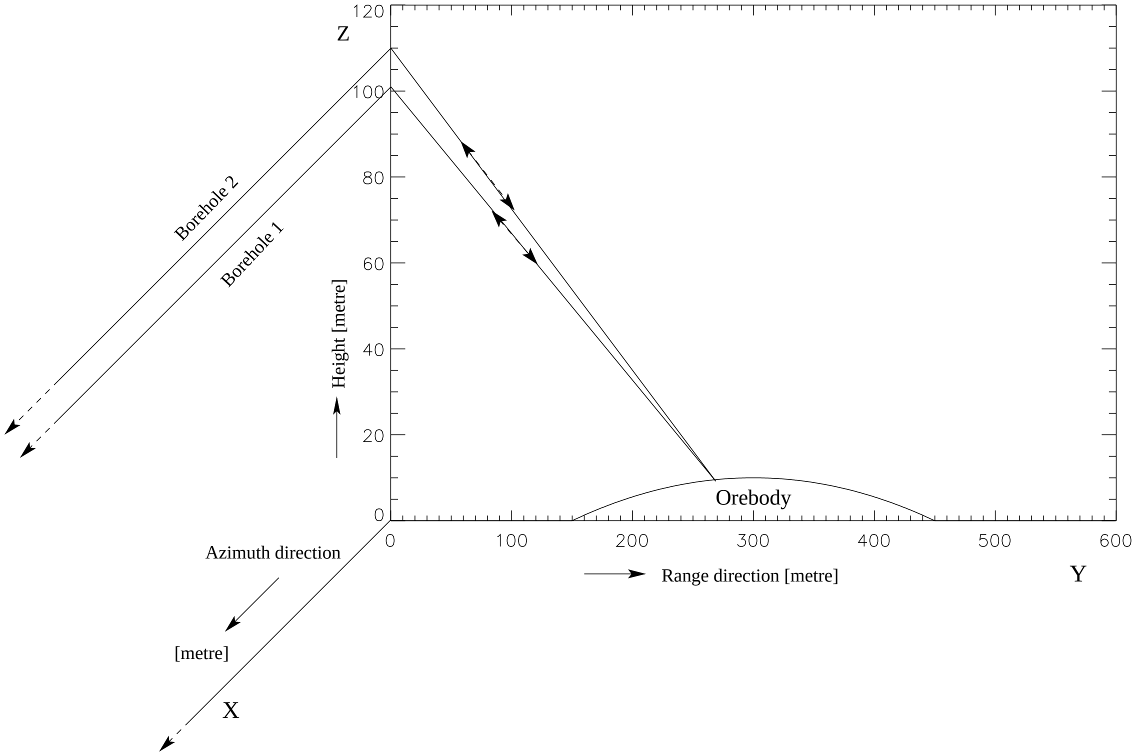

Figure 3.7: *3-D view of the input geometry (pothole type structure) of the borehole experiment. The boreholes were aligned along the X axis with a vertical baseline of 10m.*

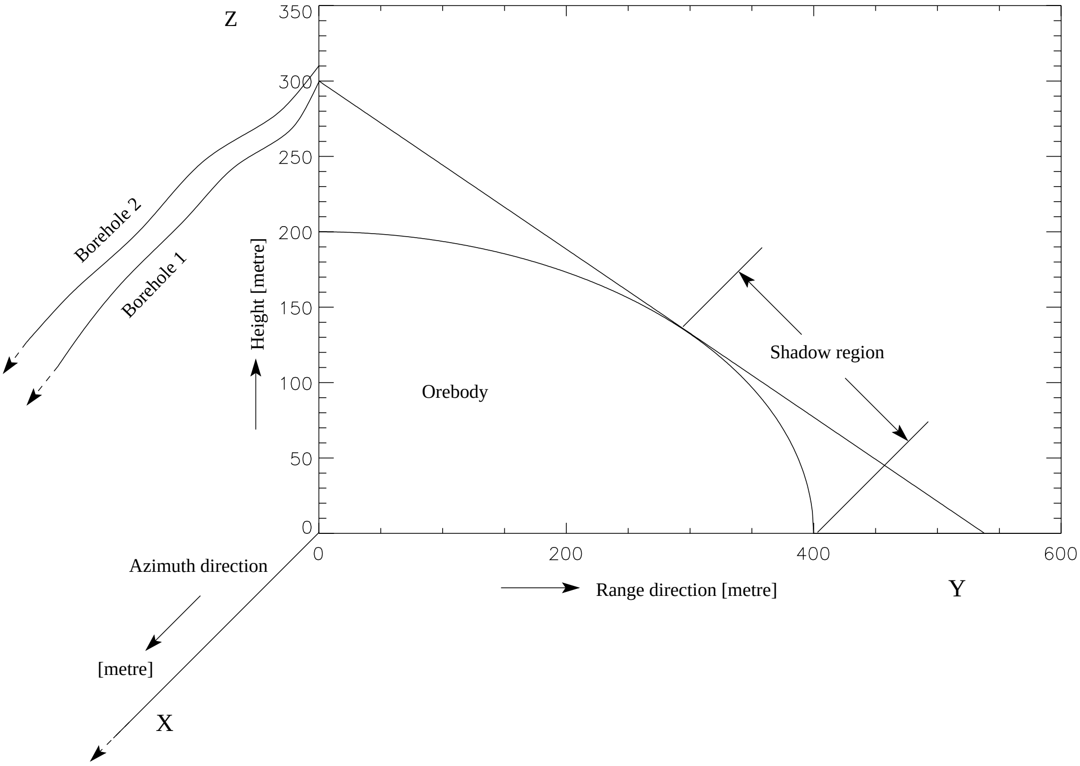

Figure 3.8: *3-D view of the input geometry (half-cylindrical structure) of the borehole experiment. The master antenna was kept parallel to the input DEM (X axis), and the slave antenna was made curved by keeping the vertical baseline constant at 10m.*

In general, kimberlites have a higher relative dielectric permittivity than host rocks and the contact between the two rock types is a radar reflector (Power et al., 2004). In general, these kimberlite pipes have a cylindrical shape. However, due to different geochemical, geophysical, such as tectonic activity, and other geological process they often deviate from the ideal cylindrical shape, and the orientation of the pipe is not always perpendicular with respect to the Earth's surface. In our simulation experiment, we have thus considered a half-cylindrical type structure, which was to be reconstructed by using the InSAR technique. As we were using a sidelooking antenna system, we could only image one side of the cylinder.

The geometry of the half-cylindrical orebody is shown in Figure 3.8. The system and antenna parameters of the borehole experiment are summarised in Table 3.2. To study the non-parallel borehole geometry, the master antenna was kept almost parallel to the input DEM (reflecting orebody geometry) whereas the slave antenna was made curved by keeping the vertical baseline constant at 10m. The trajectory of the antenna flight path was calculated with respect to the five time state vectors and three velocity state vectors. As in the previous experiment, the antenna in this setup, too, was looking towards the orebody.

Parameter	Value	Unit
Centre frequency	50	MHz
Bandwidth	80	MHz
Propagation speed	1×10^8	m/sec
Wavelength	2.0	m
SNR	120	dB
Slant range spacing	0.67	m
Azimuth spacing	1.0	m
Baseline (vertical)	10.0	m
Altitude (master antenna)	100.0	m

Table 3.1: *System and antenna parameters of the borehole experiment (pothole type structure).*

Parameter	Value	Unit
Centre frequency	50	MHz
Bandwidth	80	MHz
Propagation speed	1×10^8	m/sec
Wavelength	2.0	m
SNR	120	dB
Slant range spacing	0.67	m
Azimuth spacing	1.0	m
Time state vector (master and slave antenna)	0, 10, 20, 30, 40	sec
	0, 10, 20, 30, 40	
Master Antenna position state vector	X: 000 250 500 750 1000	m
	Y: 000 001 002 001 003	m
	Z : 100 100 100 100 100	m
Slave Antenna position state vector	X: 000 250 500 750 1000	m
	Y: 000 010 020 003 001	m
	Z : 110 110 110 110 110	m

Table 3.2: *System and antenna parameters of the borehole experiment (half-sphere type structure).*

3.7 Performance Analysis of an Interferometric Experiment

Phase Noise

The system and antenna parameters used in our subsurface simulation studies are listed in Tables 3.1 and 3.2. The interferometric phase noise is a function of receiver noise, registration errors, temporal decorrelation, baseline decorrelation etc. (Li and Goldstein, 1990; Just and Bamler, 1994). For the homogeneous jointly Gaussian statistical model, the phase noise is related to the magnitude of the correlation coefficient $|\gamma|$. The correlation coefficient γ between two singlelook complex SAR images, also known as coherence, can be expressed as (Bamler and Hartl, 1998)

$$|\gamma| = \gamma_{geom} \cdot \gamma_{SNR} \cdot \gamma_{time} \tag{3.21}$$

where γ_{geom} is the coherence factor due to the geometry of the antennas and the scene, γ_{SNR} is the factor accounting for the finite signal-to-noise ratio (SNR), and γ_{time} is the temporal coherence.

The factors γ_{SNR} is calculated according to

$$\gamma_{SNR} = \left[\frac{1}{\sqrt{1+(\mathrm{SNR}_1)^{-1}}}\right]\left[\frac{1}{\sqrt{1+(\mathrm{SNR}_2)^{-1}}}\right] = \left[\frac{1}{1+(\mathrm{SNR})^{-1}}\right] = \frac{1}{1+(10^{-12})^{-1}} \tag{3.22}$$

For flat surface inclined in range at angle α_1 to the incident ray (see Figure 3.9) the contribution to the coherence γ is given by (Equation 3.21)

$$\begin{aligned} |\gamma| &= |\gamma_{geom}| && (3.23)\\ &= \left|\frac{B-|\Delta f|}{B}\right| && (3.24)\\ &= \left|1 - f_0\frac{(1-\frac{sin\alpha_1}{sin\alpha_2})}{B}\right| && (3.25)\\ &\approx 1 - \left|\frac{Q \triangle \alpha \delta R_{3dB}}{\lambda tan\alpha_1}\right| && (3.26) \end{aligned}$$

where f_0 is the centre frequency, Δf is the spectral shift, B is the bandwidth, angle $\triangle\alpha$ is the difference in look angle i.e. $\triangle\alpha = \alpha_1 - \alpha_2$, and δR_{3dB} is the range resolution and $Q = 2$ for the dual pass system. In this calculation, we are considering zero registration error and time decorrelation equal to one, and we have excluded the receiver noise by setting the SNR value as 120 dB (Equation 3.22).

The coherence is a function of baseline and Figure 3.10 shows the relationship between coherence and baseline. For the case of a flat surface with an antenna height of $h_1 = 100$m and slant range value of $r_1 = 155$m (mid swath), the coherence value at a vertical baseline of 10m is about 0.964 which corresponds to a phase standard deviation of about $\sigma_\psi = 0.074$ cycles (see Figures 3.11 and 3.12). This phase standard deviation (0.074 cycles) corresponds to a displacement standard deviation of about $\sigma_z = 1.5\,$m (see Figure 3.13), where $\sigma_z = \left|\frac{\delta z}{\delta \varphi}\right| \sigma_\varphi$.

Ambiguity Analysis

The interferometric phase measurement is only known modulo of 2π, and the received signal might have come from one of several directions (see Figure 3.14). Over a continuous surface, the corresponding interferogram appears as a series of fringes. The interferometric fringe spacing refers to the spatial separation over which the interferometric phase changes by one cycle.

Consider the configuration depicted in Figure 3.15, showing a flat surface, inclined at an angle α_1 with respect to the incident ray.

The phase ambiguity spacing is one cycle i.e. $\triangle\varphi_{amb} = 2\pi$. Thus, the angular ambiguity spacing is given by (Wilkinson, 1997)

$$\begin{aligned} \triangle\theta_{amb} &= \left|\frac{\delta\theta}{\delta\varphi}\right| \triangle\varphi = \left|\frac{\delta\theta}{\delta\varphi}\right| 2\pi \\ &= \left|\frac{\lambda[b^2 + r_1^2 - 2r_1 b\sin\theta]^{1/2}}{2r_1 b\cos\theta}\right| \end{aligned} \tag{3.27}$$

In terms of angular ambiguity ($\triangle\theta_{amb}$), the interferometric fringe spacing is given by (Wilkinson, 1997)

$$\begin{aligned} \triangle r_{amb} &= \left|\frac{\delta r_1}{\delta\theta}\right| \triangle\theta_{amb} \\ &= \left|\frac{\lambda[b^2 + r_1^2 - 2r_1 b\sin\theta]^{1/2}\tan\alpha_1}{2r_1 b\cos\theta}\right| \end{aligned} \tag{3.28}$$

Figure 3.16 shows a plot of the range ambiguity vs the baseline ($h_1 = 100$m and $r_1 = 155$m). At a vertical baseline of 10m, the angular ambiguity is about 7.8^0, which cor-

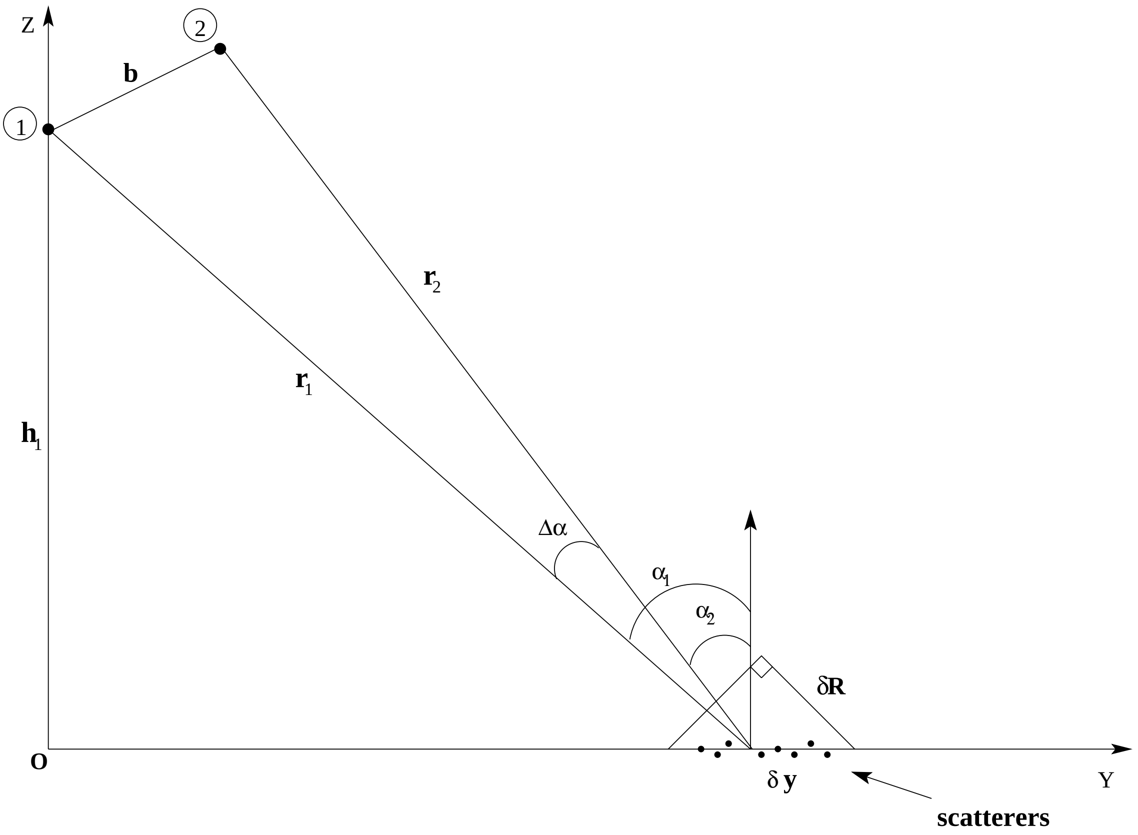

Figure 3.9: T*he effect of geometric phase decorrelation. The phase of the received signal changes with angle owing to fact that an echo is made up of contributions from several scatterers within the resolution cell.*

responds to the range ambiguity of 25.2m, and displacement ambiguity of 21.2m (see Figure 3.17). This ambiguity is removed by the phase unwrapping process.

3.8 Results and Discussion

Here we are presenting the results achieved in our borehole interferometric experiments. In both the experiments, we have excluded the receiver noise by setting the SNR value as 120 dB, which is modelled as an independent additive Gaussian process. The simulation starts at a slant range of 100.67m, corresponding to a ground range of 11.595m.

3.8.1 Geometry 1 (pothole type orebody)

We are presenting the results at an azimuth position $X = 10$m. The coherence is a measure of data quality. A lower coherence thus indicates higher data noise and hence a lower accuracy of estimation (Ashok and Wilkinson, 2001). The coherence value depends on

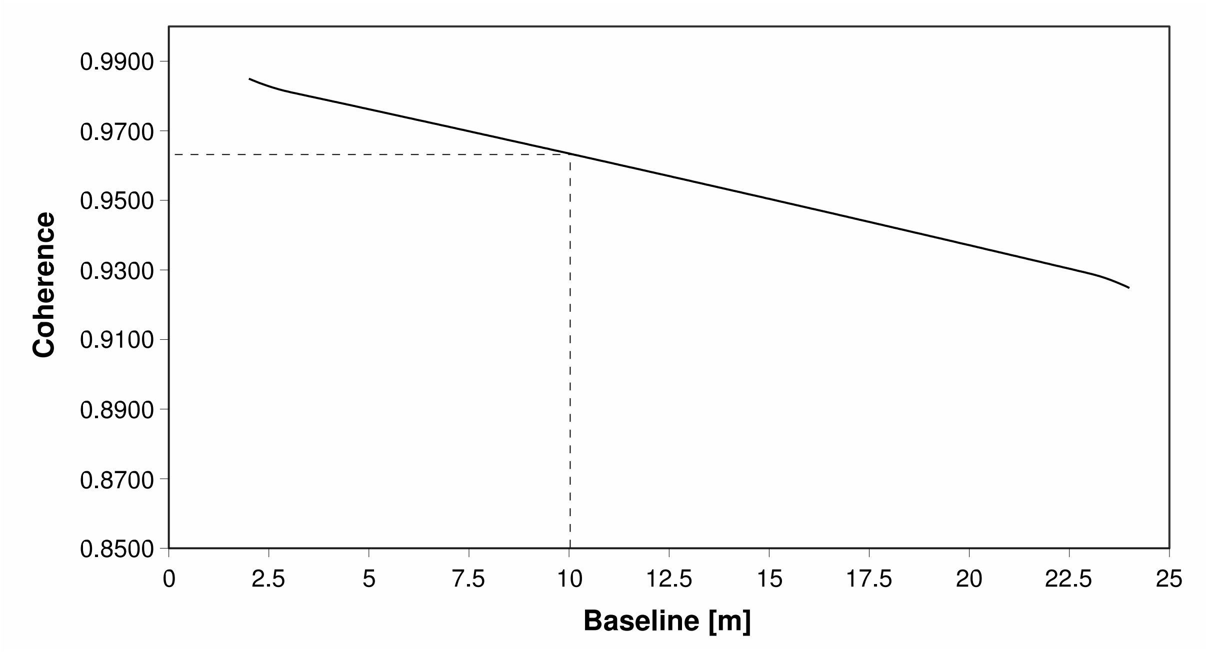

Figure 3.10: *Coherence Vs baseline.*

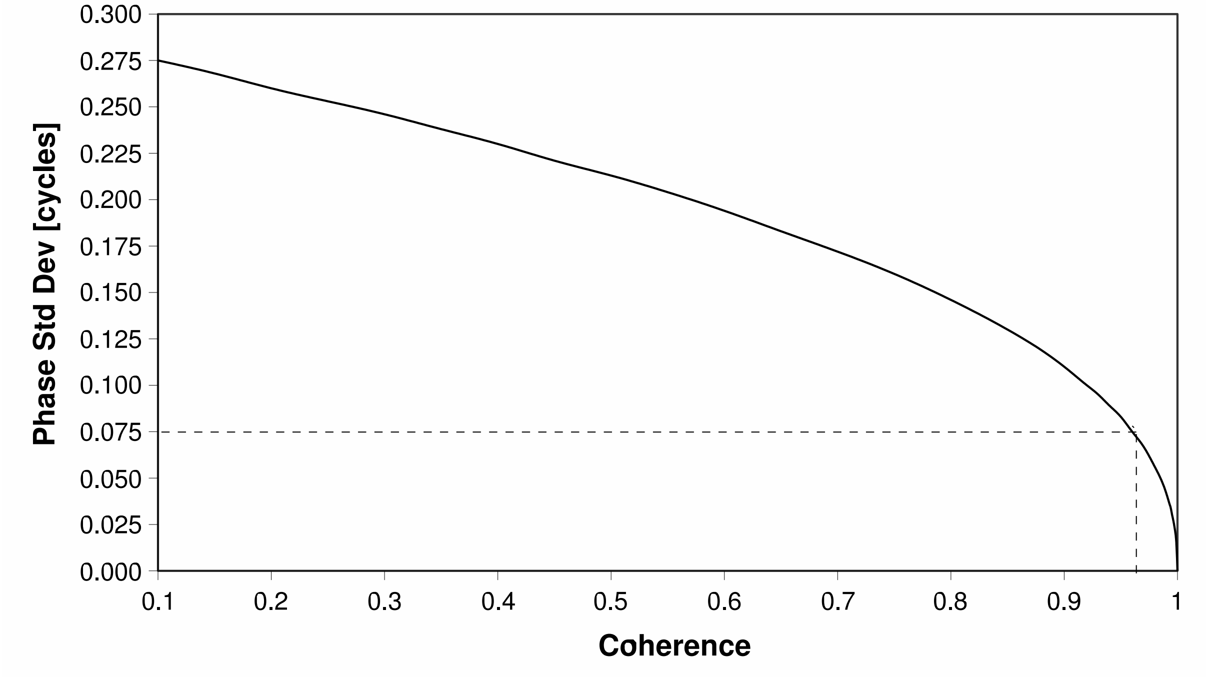

Figure 3.11: *Phase Standard Deviation Vs* Coherence.

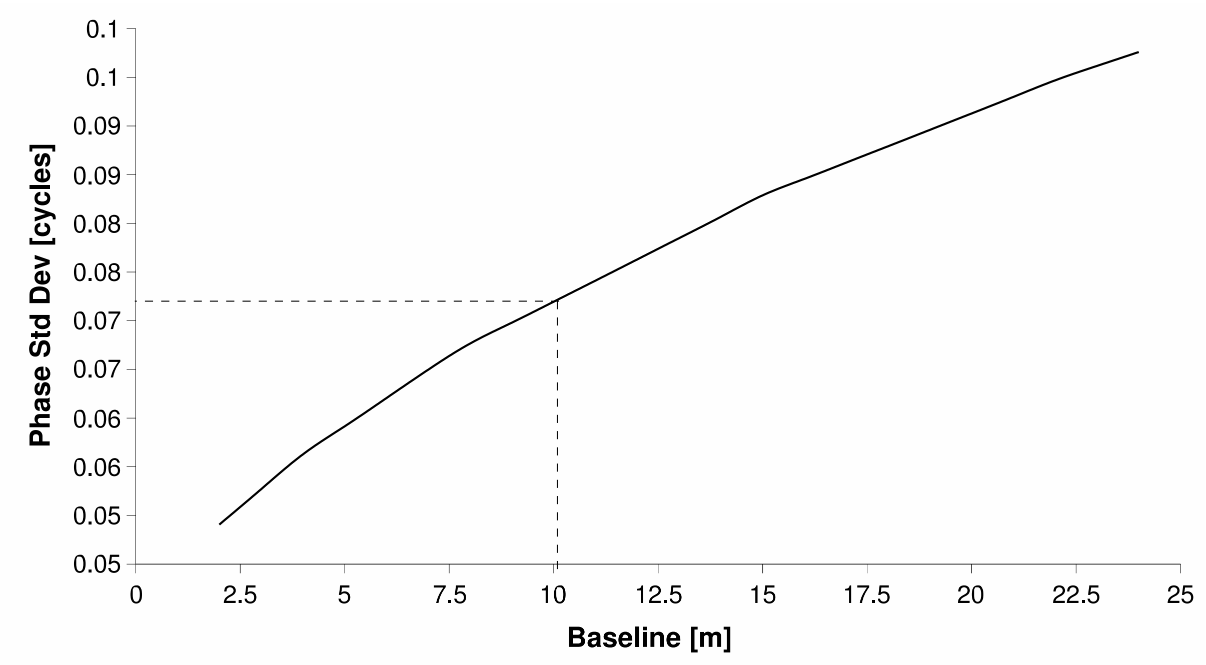

Figure 3.12: *Phase Standard Deviation Vs Baseline*.

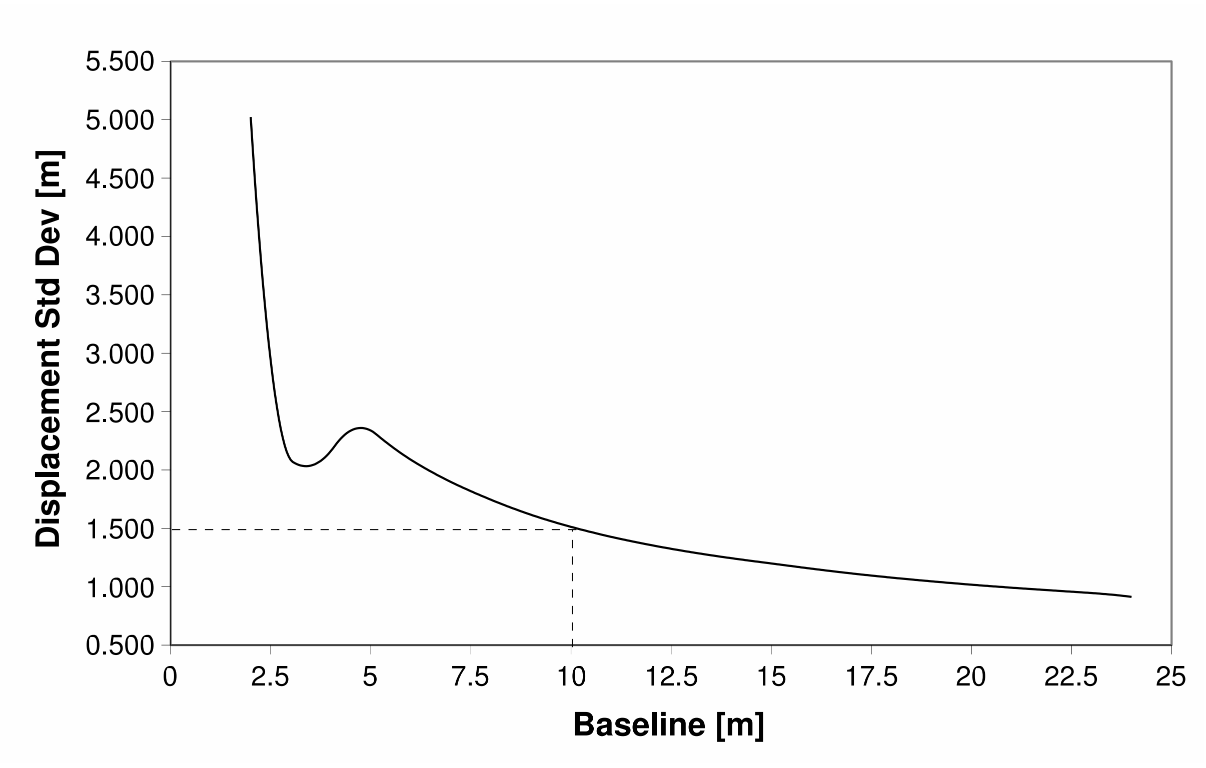

Figure 3.13: *Displacement Standard Deviation Vs Baseline.*

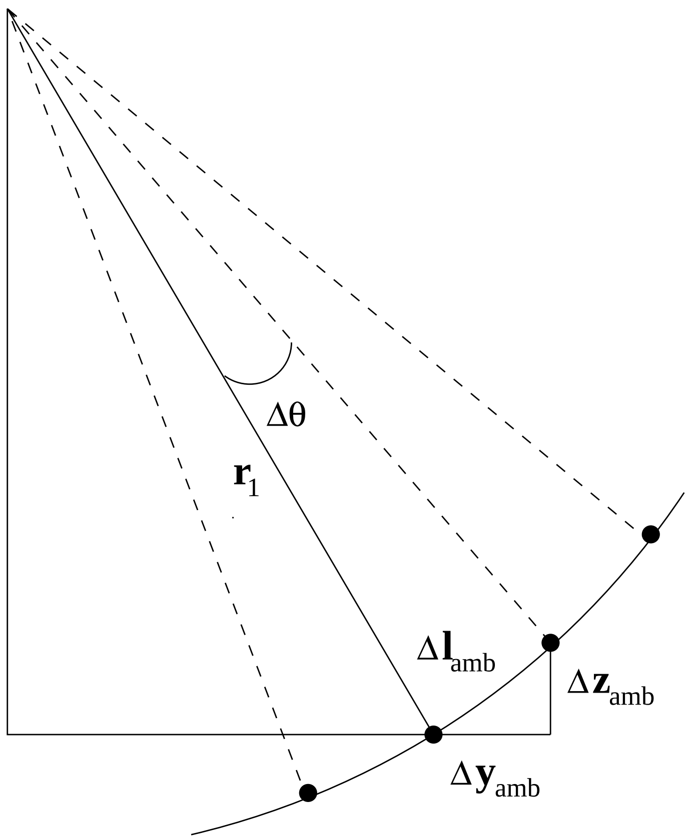

Figure 3.14: *Ambiguity spacing for flat surface geometry.*

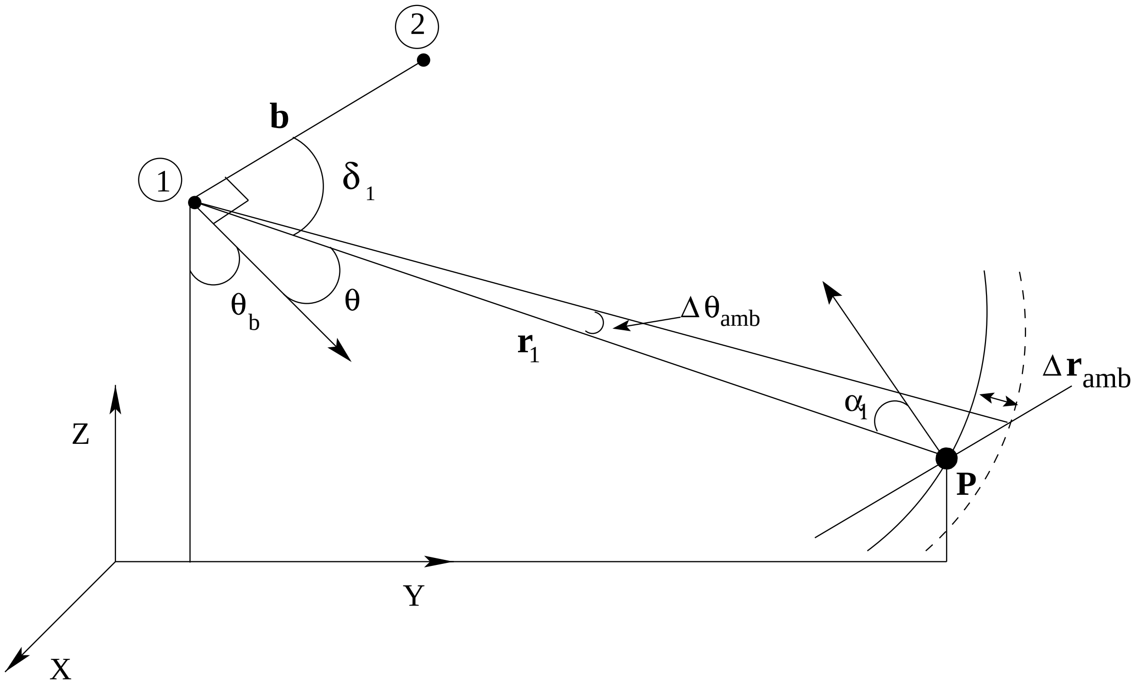

Figure 3.15: *Geometry for calculating interferometric fringe spacing.*

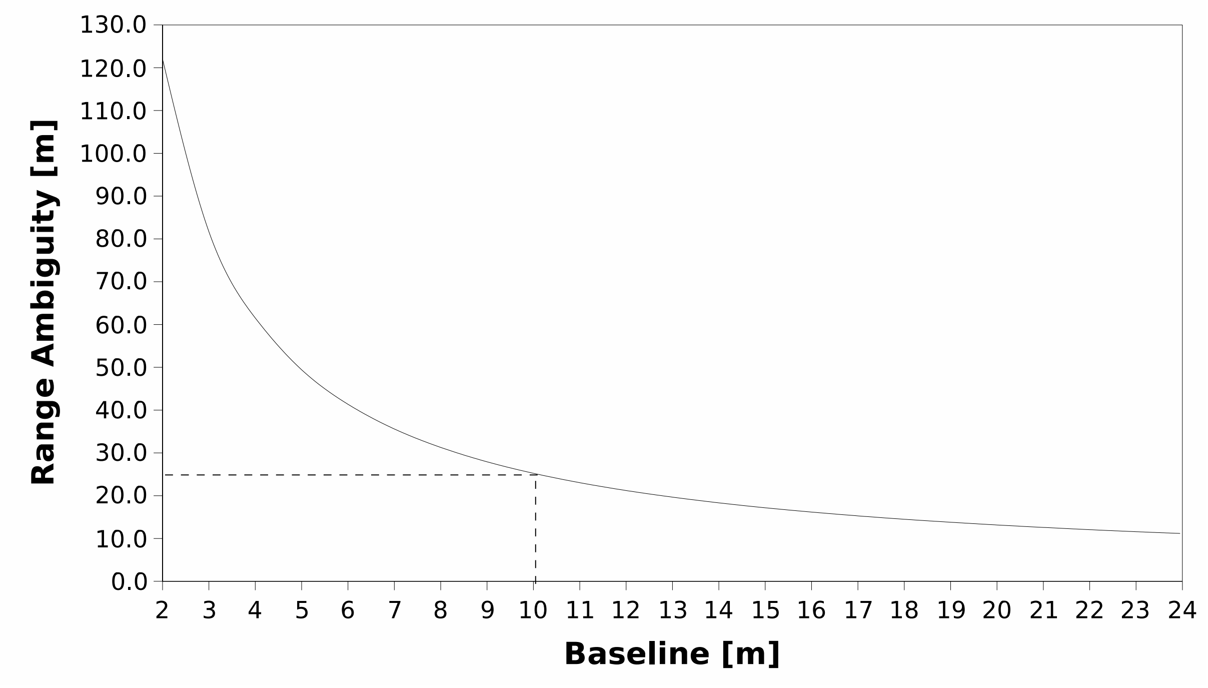

Figure 3.16: *Range Ambiguity Vs Baseline.*

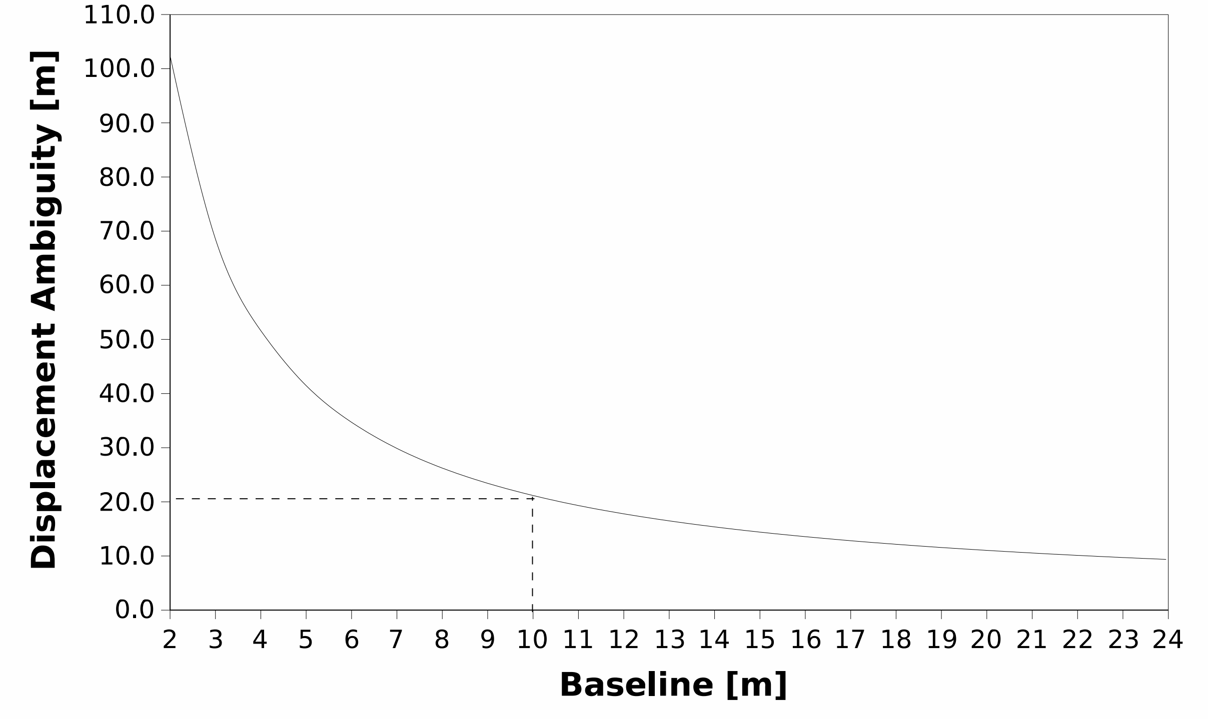

Figure 3.17: *Displacement Ambiguity Vs Baseline.*

the relative slope between the reflecting surface and the antennas position. The coherence value drops to zero, as the scene comes to the shadow region. In our given geometry (Figure 3.7), due to the gentle slope of the orebody, the coherence is expected to be high, as shown in Figure 3.18.

Figure 3.19 shows the wrapped phase values along the slant range (master antenna location at X = 10m) of both the reflecting and a flat surfaces. The interferometric phase is related to the two-way time difference between the antennas and the scene location. In Figure 3.19, we can see the difference in the interferometric phase between the flat surface and the reflecting orebody (Figure 3.7). As we move from the near slant range to the far range, the the rate of change of the two-way time difference between the antennas and the reflecting surface will decrease, which eventually increases the fringe spacing, as seen in Figure 3.19.

The $principal$ or wrapped phases are unwrapped by using a Minimum Cost Flow (MCF) algorithm. In interferometry, the terrain height is related to the absolute phase. Figure 3.20 shows the unwrapped phase along the slant range as well as the unwrapped phase due to a flat surface. As the unwrapping is a relative process, we added the appropriate $n\pi$ values to the unwrapped phase of the reflecting surface for comparison with a flat surface, where n is an integer. We can clearly see the difference in the unwrapped phase values, which indicates the presence of the reflecting surface. The unwrapped phase difference between the reflecting orebody surface and a flat surface is related to the height difference between these two. The angle of arrival has been calculated by means of Equation 3.12, whereas the reconstructed height values have been calculated by means of Equation 3.14. Figure 3.21 shows the plot of the reconstructed height ($Z-$coordinate) and the simulated height ($Z-$coordinate). The simulated height values are produced by the simulator, which is the intersection between the input DEM and the radar beam in the slant range. As we can see, the reconstructed height closely follows the simulated height values.

3.8.2 Geometry 2 (half-cylindrical orebody)

Here also, we are presenting the results at an azimuth position $X = 10$m. In our given geometry (Figure 3.8), the coherence value decreases as a result of the steep slope of the reflecting orebody, and after a slant range of 341m, the target orebody comes into shadow. Again, as expected, the coherence value drops to zero in the shadow region, which is shown in Figure 3.22. Low coherence means a poor correlation between two SAR images, which will negatively affect the interferometric phase, and eventually affect the reconstructed height values. A drop in coherence causes greater phase noise. Figure 3.23 shows the wrapped phase values in slant range at an azimuth position X = 10m.

In Figure 3.23 we can also see the difference in the interferometric phase values between the reflected orebody and a flat surface.

As we move from near slant range to far range the fringe spacing increases, as shown in Figure 3.23. The $principal$ or wrapped phases are unwrapped using by Minimum Cost Flow (MCF) algorithm. Figure 3.24 shows the unwrapped phase values in the slant range. We can clearly see the difference between the absolute phase values between the the reflecting orebody surface and a flat surface. The appropriate $n\pi$ values was added for comparison between these two. The unwrapped phase difference between the reflecting orebody and the flat surface is related to the height difference between these two. The angle of arrival has been calculated by using Equation 3.12, while the reconstructed height values have been calculated by using Equation 3.15. Figure 3.25 shows the plot of reconstructed height ($Z-$coordinate) with the simulated height ($Z-$coordinate) in slant range. The slant range reconstructed height values are projected to ground range as shown in Figure 3.26. The slant range projection is a one-to-one mapping, but ground range is not, which is clear from Figure 3.26. As we can see, there is a slight difference between the simulated and the reconstructed height values, as we move from near range to far range. This is due to slightly different equation used to calculate the phase of a scene in the simulated and reconstructed image.

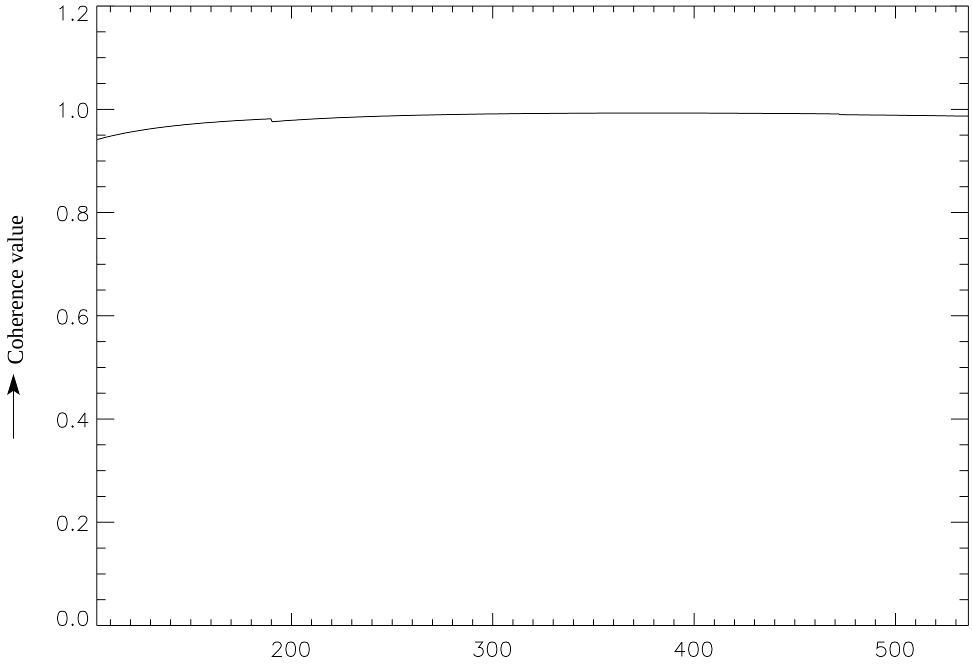

Figure 3.18: *Coherence value in slant range at an azimuth location X = 10m.*

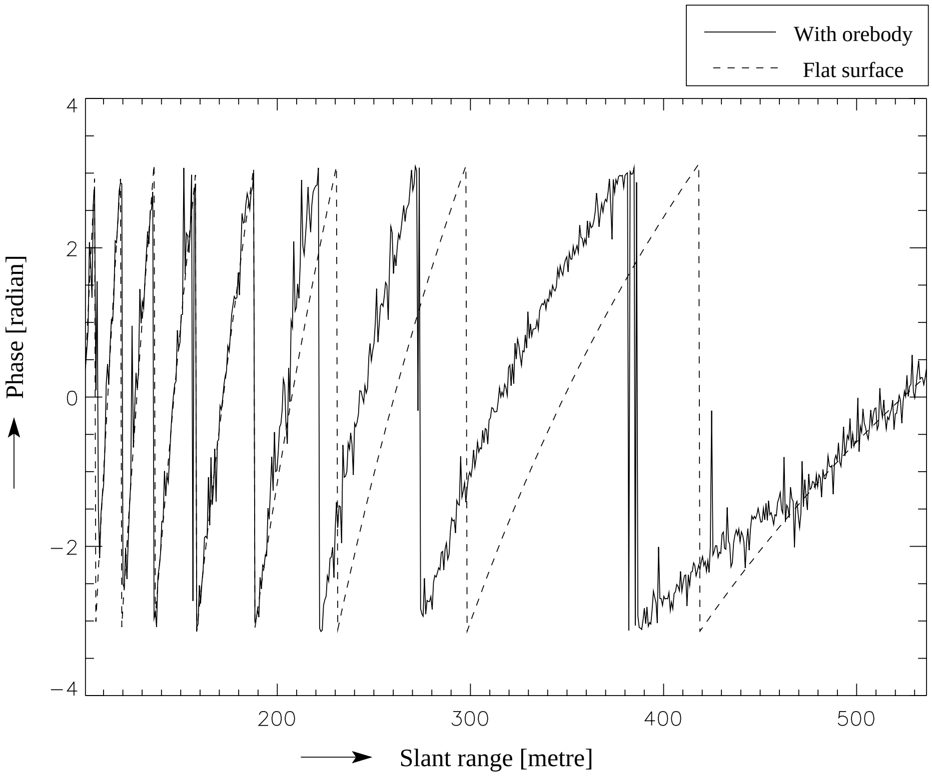

Figure 3.19: *Principal (or wrapped) phase values along the slant range at an azimuth location X = 10m. The solid line shows the phase values of the reflecting orebodies, whereas the dotted line shows the flat surface.*

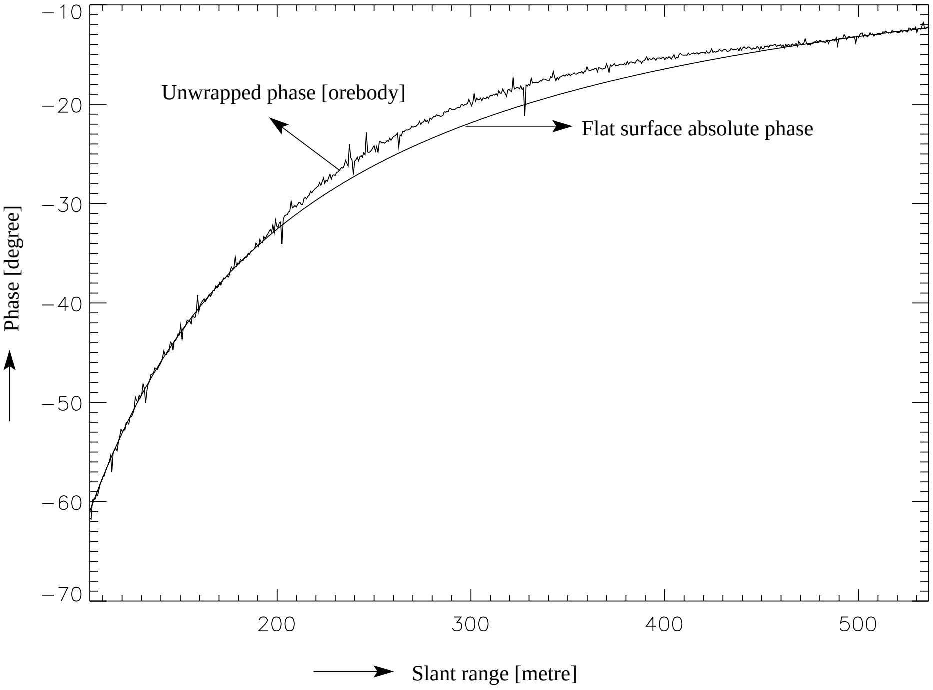

Figure 3.20: *Absolute (or unwrapped) phase values along the slant range at an azimuth position X = 10m.*

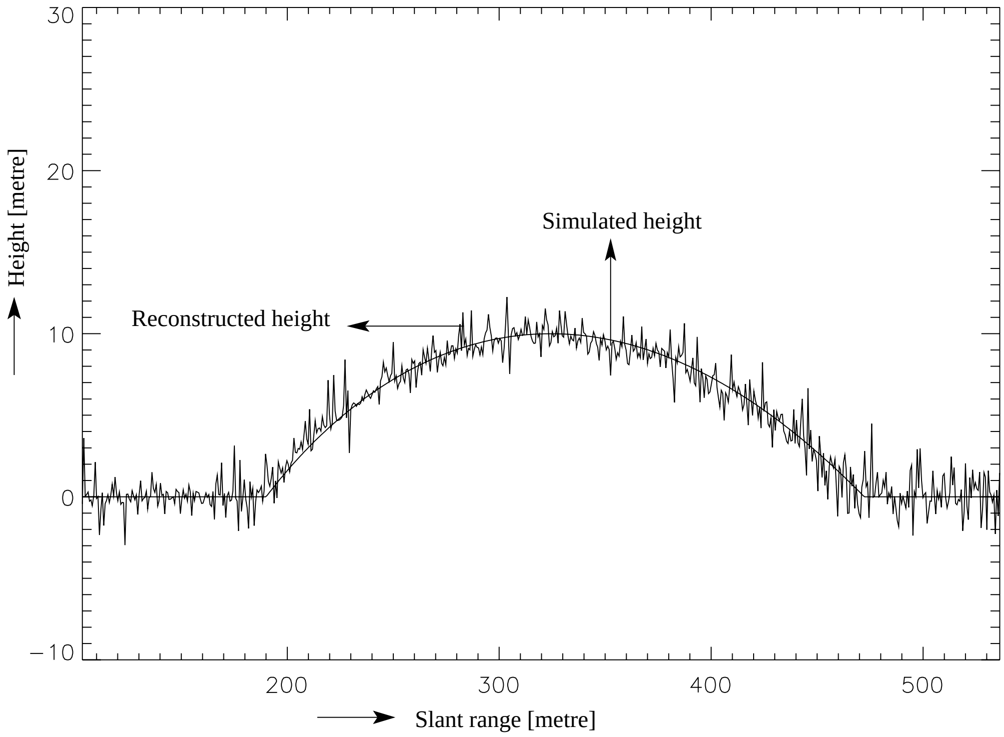

Figure 3.21: *Simulated and reconstructed height values of the input DEM in the slant range at an azimuth position X = 10m.*

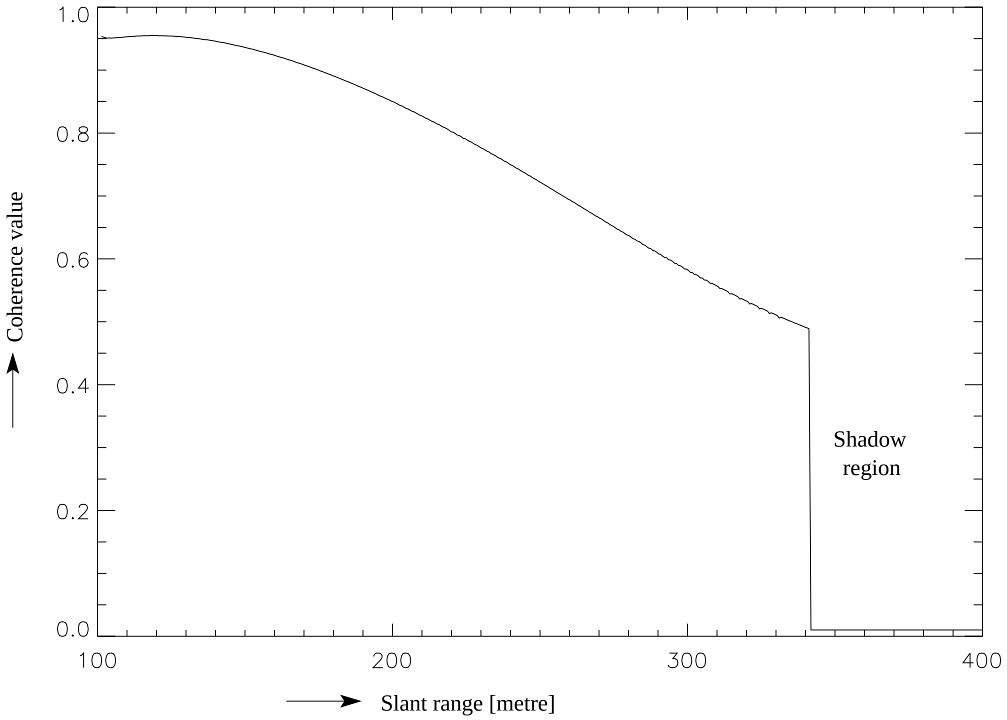

Figure 3.22: *Coherence values in slant range at an azimuth position of X = 10m.*

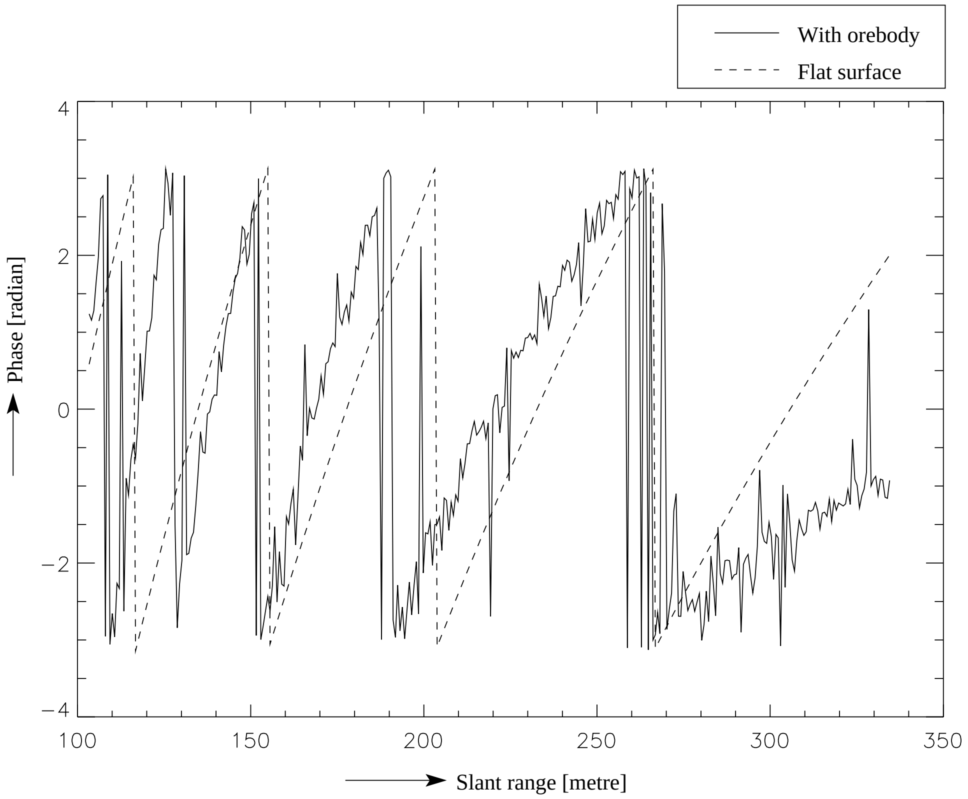

Figure 3.23: *Wrapped phase values in slant range at an azimuth position of X = 10m. The solid line shows the phase values of the reflecting orebodies, whereas the dotted line shows the flat surface.*

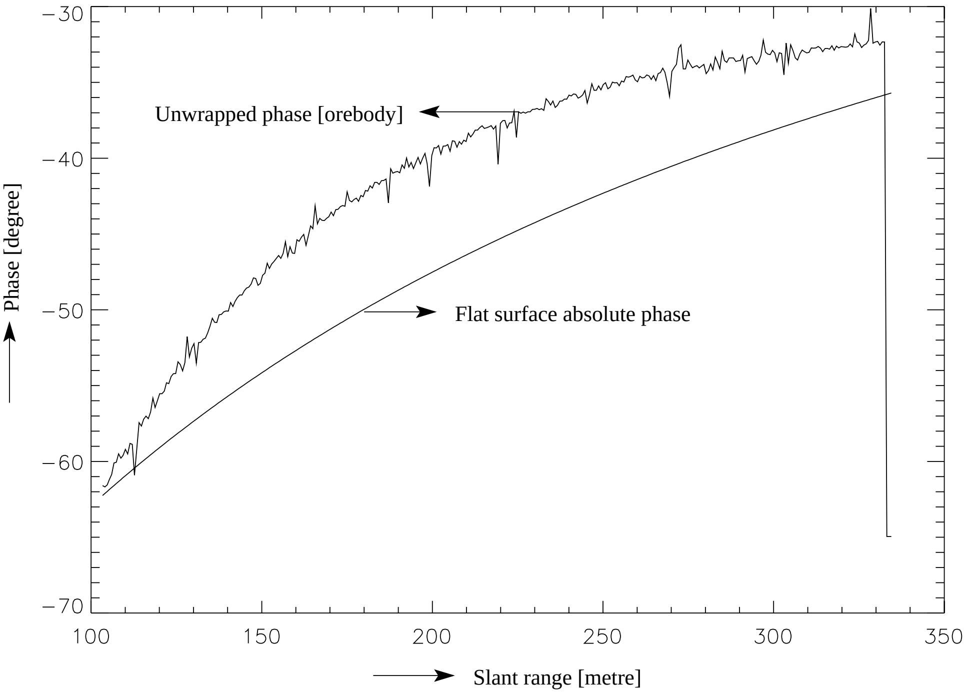

Figure 3.24: *Unwrapped phase values in slant range at an azimuth position X = 10m.*

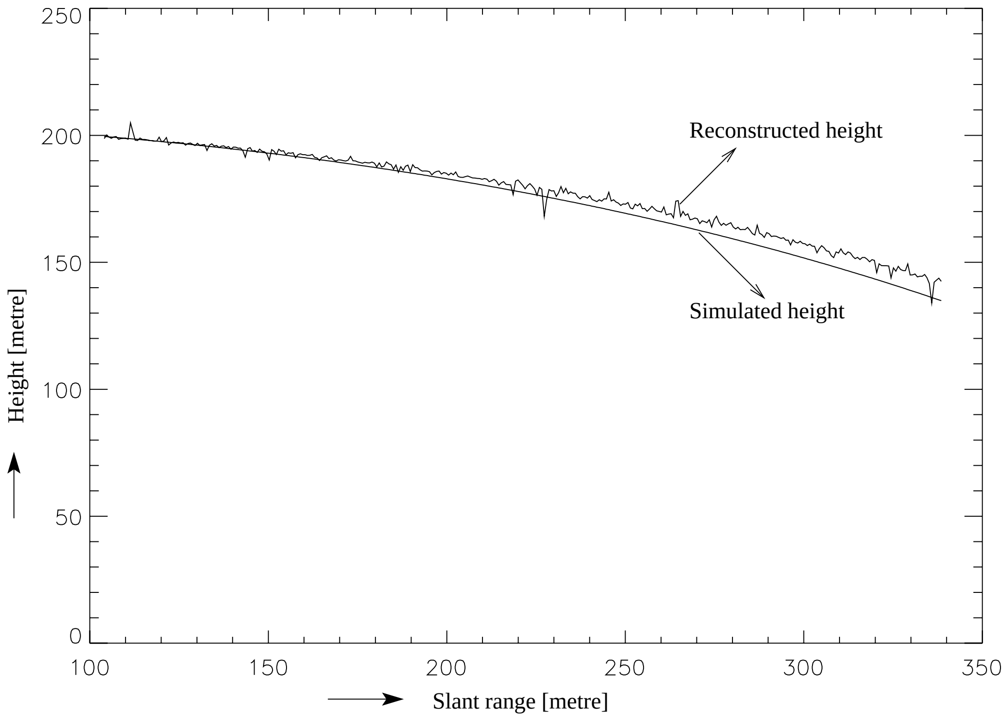

Figure 3.25: *Reconstructed and simulated height values in slant range at an azimuth position X = 10m.*

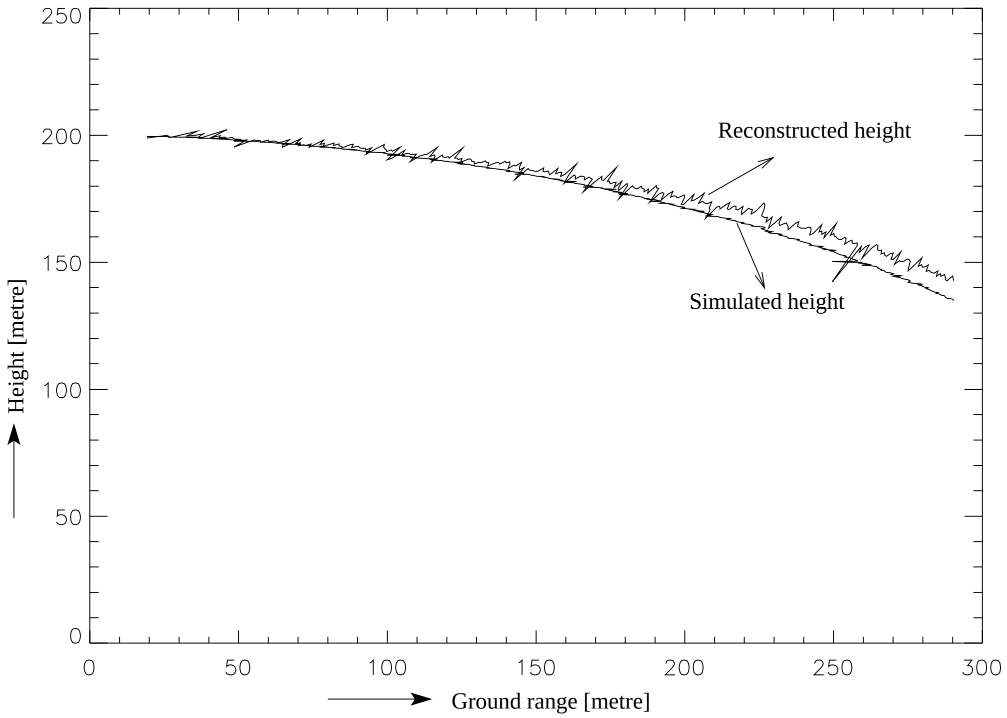

Figure 3.26: *Reconstructed and simulated height values in ground range at an azimuth position X = 10m.*

3.9 Summary

Interferometric height reconstruction techniques are mainly used in space-borne or airborne systems for topographic mapping. These methods require two or more flight paths to reconstruct the terrain height. Bearing in mind that the number of boreholes are restricted in practice, we have applied the interferometric height reconstruction technique to reconstruct the subsurface orebody by using two boreholes. Moreover, boreholes in the real mining environment drift considerably from the ideal straight line, and consequently, we have considered both parallel and non-parallel boreholes in our simulation experiment (Inggs et al., 2001; Mukhopadhyay et al., 2001).

The reconstructed subsurface height is related to the interferometric phase and the interferometric phase is affected by the receiver noise, registration errors, baseline decorrelation etc. If the medium through which the radar pulse travels is inhomogeneous, there will be weak returns from the inhomogenity boundary, as a result the noise lebel will increase. A design analysis is carried out by using the subsurface interferometric experiment's system and antenna parameters. These design analyses are very useful tool for any kind of interferometric experiment.

The present simulator uses two registered focused images to form the interferogram, but in an real subsurface experiment. focusing and registration of images to form the interferogram will be quite difficult. To make the simulation of subsurface 3-D height reconstruction experiment more realistic, we have to consider the propagation through inhomogeneous media. The success of the simulator depends mainly upon the EM wave propagation through the subsurface host rock. The subsurface interferometric technique will work for imaging an isolated target orebody in a homogeneous medium, i.e. the case with no layover. Clearly, the phase information will be corrupted by the process of EM propagation in a complex medium and also due to unavoidable subsurface layover problem, and a point will come when imaging is not possible.

The pioneer workers in the GPR field, such as Prof. Ian Mason (e.g. Simmat et al, GPR, 2002) and Prof. Gary Olhoeft (Olhoeft, G.R., Geophysics, 43, 2000), have demonstrated that coherent addition (migration) does work in real GPR data (although there must have been some dispersion). The fact that the migration works in real GPR data sets shows that the dispersion effect does not completely prevent coherent processing. Furthermore, the fact that SAR (coherent addition) processing is possible, shows that the interferometric processing technique will work. As the radar signals (in the case of two borehole radars) travel through the same medium (assuming that the lateral inhomogeneity is not too severe), the dispersion will be common to both signals, and ought not corrupt the interferometric phase. The spectral shift between the two signals gives rise to the interferometric phase, will still be present. Therefore, it is still feasible to perform interferometric experiments (i.e. to produce an interferogram) to map bedrock surfaces, even though there might be dispersion.

Chapter 4

Three-dimensional Image Reconstruction using Radar Magnitude Images from Multiple Boreholes

4.1 Introduction

Synthetic aperture ground penetrating radar imaging is an important emerging technology with the potential to produce high-resolution images for a variety of applications, including the non-destructive evaluation of civil structures, minefield clearing and unexploded ordnance detection and removal.

Using phase interferograms from sidelooking SAR configuration, a simulation study of 3-D imaging has been carried out by Mukhopadhyay et al. (2001). In general, bandwidths of 75% of the centre frequency are typical for borehole radar, while Interferometric SAR (InSAR) systems have bandwidths typically less than 5% of the centre frequency. In a narrow-band InSAR experiment, the 3-D orebody geometry is related to the interferometric phase and the interferometric phase is a function of the centre frequency of the pulse. Alternatively, the 3-D location of the orebody geometry can be reconstructed by using a correlation-type processing between two signals coming from different view angle, which is more suitable for wide-band/ultra wide-band borehole radar experiment.

Mine boreholes are too thin to allow one to build efficient directional antennas (Ebihara et al., 2000). Slimline borehole radar antennas are cylindrically omni-directional. Thus, reflection comes from the left and right side of the borehole at equal slant ranges. There will be ambiguity problems due to the superposition of the signals, which also restrict the application of the narrow-and interferometric height reconstruction techniques (Mukhopadhyay, Inggs, Lord and Wilkinson, 2002). The rotational ambiguity can be resolved by using multiple boreholes. In the real borehole situation, however, the trajectories are neither parallel to each other nor straight. A time domain SAR algorithm would thus be well suited to focus data acquired along a curved trajectory.

In this chapter, we will first present the image formation techniques of SAR and ISAR, the signal processing techniques used in this regard and the time domain SAR focusing technique. Thereafter, we will look at the 3-D reconstruction algorithm, using magnitude images from multiple boreholes. The reconstruction grid spacing issue will be discussed in detail. Lastly, we will discuss the 3-D reconstruction results achieved via numerical borehole radar simulation, and from acoustic real data captured in air and water medium.

4.2 Synthetic Aperture Radar and Inverse Synthetic Aperture Radar Image Formation Processes

In the field of radar, the technique known as *synthetic aperture radar* (SAR), involves the formation of an aperture by moving a sensor past a scene of interest along a track to achieve high azimuth resolution (Bamler and Schattler, 1993). The basic SAR image formation technique can be discussed using the idealised case of an object embedded in a homogeneous medium. As illustrated in Figure 4.1, moving an antenna along the X$-$axis operating in a mono-static mode, past the object position $P\left(x_p, y_p, z_p\right)$, allows collection of data for the formation of the synthetic aperture. Due to a scatterer at $P\left(x_p, y_p, z_p\right)$ location, the antenna starts receiving the target response from point A_1 up to point A_2, where θ is the two-way azimuth beamwidth of the antenna and A_1A_2 is the synthetic aperture length. The point scatterer range for the n^{th} position of the antenna is expressed as

$$r(x_n, y_n, z_n) \quad = \quad \sqrt{\left(x_n - x_p\right)^2 + \left(y_n - y_p\right)^2 \left(z_n - z_p\right)^2} \qquad (4.1)$$

where (x_n, y_n, z_n) is the n^{th} antenna position. The distance of closest approach can be expressed as

$$r_0 = \sqrt{\left(x_0 - x_p\right)^2 + \left(y_0 - y_p\right)^2 \left(z_0 - z_p\right)^2} \qquad (4.2)$$

where $O_1\left(x_0, y_0, z_0\right)$ is the antenna location at this closest approach distance.

The length $L = 2r_0 \tan\left(\frac{\theta}{2}\right)$ is called the synthetic aperture length. Alternatively, an aperture may also be synthesized by keeping the sensor stationary, and relying on the movement of the object of interest past the sensor as depicted in Figure 4.2. This approach is known as *inverse synthetic aperture imaging* (ISAR or ISAS) (Wehner, 1987). The point scatterer range for the n^{th} position of the target on the moving platform is expressed

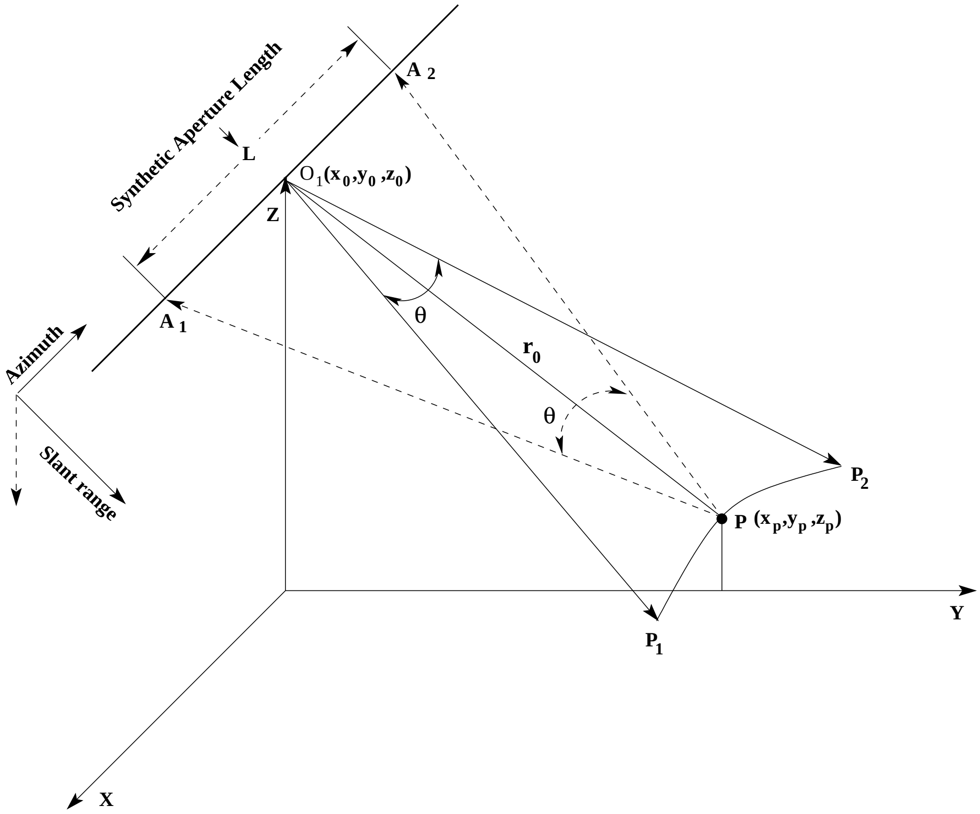

Figure 4.1: *Synthetic aperture imaging geometry in mono-static transducer mode. The transducers (transmitter and receiver) are moving across a fixed point scatterer.*

as

$$r(x_n, y_n, z_n) = \sqrt{(x_0 - x_n)^2 + (y_0 - y_n)^2\,(z_0 - z_n)^2} \tag{4.3}$$

where $O_1\,(x_0, y_0, z_0)$ is the fixed transducer's location and (x_n, y_n, z_n) is the n^{th} position of the target on the moving platform. The distance of closest approach can be expressed as

$$r_0 = \sqrt{(x_p - x_0)^2 + (y_p - y_0)^2\,(z_p - z_0)^2} \tag{4.4}$$

where $P\,(x_p, y_p, z_p)$ is the point scatterer's location on the moving platform at this closest approach distance.

The received echo at each azimuth location is the time delayed version of the transmit pulse as it travelled through the medium and was reflected back by the object in reflection mode. In the received radar image, the 3-D scatterer's location at (x_p, y_p, z_p) will be projected into 2-D, along the azimuth (along-track) and slant range direction (two-way time delay). The focus of this chapter is to develop a method to reconstruct the 3-D location of the target by using multiple borehole 2-D radar magnitude images.

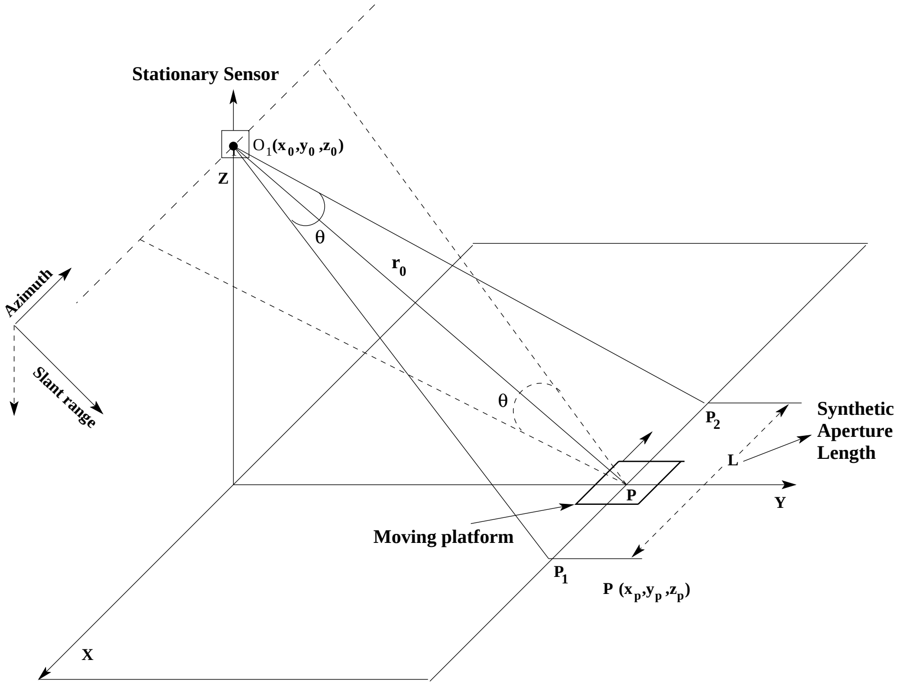

Figure 4.2: *Inverse synthetic aperture imaging geometry in mono-static transducer mode. The scene (platform) is moving across a fixed transducer (transmitter and receiver) location.*

4.3 Signal Processing Techniques

The focused image is formed by using correlation-type processing, carried out in two steps:

- range compression, using either matched filtering (for optimal SNR) or deconvolution processing with frequency domain windowing (for optimal point target response);
- azimuth focusing, using standard migration processing (also known as synthetic aperture focusing), which again may be tailored to give either optimal SNR or optimal point target response.

4.3.1 Range Compression

A commonly used transmitted pulse in radar applications is the linear *chirp* waveform, to satisfy the simultaneous requirements of high energy and wide bandwidth, similar to a vibroseis sweep signal used in reflection seismology. In the chirp waveform, the instantaneous frequency of a sine/cos wave is swept linearly over time, modelled by

$$v_{tx}(t) = rect\left(\frac{t}{T}\right)\cos\left(2\pi\left[f_0 t + 0.5Kt^2\right]\right)$$

where f_0 is the centre frequency, T is the pulse length and $K = \frac{B}{T}$ is the chirp rate in Hz/sec.

For optimal SNR, the received echo is processed by correlation filtering and implemented using fast FFT methods, i.e. the output is computed as

$$v_0(t) = IFFT\left[H_{MF}(f) \cdot v_{rx}(f)\right]$$

where $H_{MF}(f) = v_{ptr}^{conj}(f)$ is a matched filter, matched to the response $v_{ptr}(t)$ that would be recorded from a point target. If the passband linear system effects are small, then

$$v_{ptr}(t) \propto v_{tx}(t - t_d)$$

where t_d is the two-way time delay.

The results of the matched filtering theory under white noise conditions show that the SNR is proportional to the energy in the received signal, whereas the resolution is a function of the signal bandwidth (Bamler and Schattler, 1993).

For optimal point target response, the received echo is also processed by correlation filtering, implemented by using fast FFT methods, i.e. the output is computed as

$$v_0(t) = IFFT\left[H_{dec}(f) \cdot v_{rx}(f)\right]$$

where $H_{dec}(f) = \frac{1}{v_{system}(f)}$ is a deconvolution filter and $v_{system}(f)$ is the transfer function of the sensor.

Frequency domain windowing may also be applied to reduce the side-lobe levels in the response (Mitra, 1999). The corresponding range resolution, after processing, is given by

$$\delta r = \frac{c_1}{2B} \cdot w_{factor}$$

where c_1 is the velocity of propagation, B is the bandwidth of the signal and w_{factor} is the window constant.

The range compressed spectrum of the data is shifted down to baseband (i.e. positive spectral components are shifted to centre on zero Hz), and the resulting time domain waveform is a complex signal. For a point target, the baseband complex response (Bamler and Schattler, 1993) can be modelled by

$$v_{bb}\left(t\right) = A\,Sa\left(\pi B\left(t-t_d\right)\right)e^{-j2\pi f_0 t_d}$$

where $t_d = \frac{2r_0}{c_1}$ is the two-way delay to the scatterer.

In practice, the receiver passband magnitude is usually flat by design, and the magnitude spectrum of the transmitted pulse is approximately rectangular (Wilkinson, 2001). Cook and Bernfeld (1993) show that, even for linear frequency modulated (FM) signals with smaller time-bandwidth products (say>20), the range compressed signal will still have $\frac{\sin(\alpha)}{\alpha}$ form, provided that the appropriate matched filter is used for the signal.

It is important to note that over the main lobe of the processed baseband signal, the phase is constant and is equal to $-2\pi f_0 t_d$. As the range relationship with the azimuth position is hyperbolic, the phase of the received signal also unwraps according to a hyperbolic relationship with the azimuth position. The hyperbolic range variation leads to the concept of azimuth focusing, which will be discussed in the next section.

4.3.2 Time-domain Azimuth Focusing

Introduction

Wave field migration/focusing is routinely used in the seismic industry. A good overview of different migration techniques used in the seismic industry and some work in the GPR industry can be found in (Berkhout, 1981; Simmat et al., 2002; Olhoeft, 2000; Leuschen and Plumb, 2000*b*; Moran et al., 2000). In the case of frequency domain migration (spatial and temporal frequency), it is assumed that the data is acquired along a straight line, or at least that the data needs to be preprocessed to a straight line (usually referred to as motion compensation). Constant spatial sampling is a further requirement.

In this thesis, an azimuth compression was achieved by using standard migration processing, also known as time-domain synthetic aperture processing (Bamler and Schattler, 1993). A time-domain SAR processor is in principle straightforward and easy to implement. For small data volumes, this is probably the most efficient and correct technique. For successfully achieving the desired results, one has to take into account the imaging geometry (based on an approximate knowledge of the scene orientation with respect to the elevation angle) and also the platform trajectory in calculating the required matched filter, which depends on the range history of each target. This method is also the most flexible and useful imaging tool for processing the data acquired from a deviating borehole trajectory, with the prior knowledge of scene orientation and antenna trajectory. Since no approximations are made in this regard, this method is probably the most accurate and also the most flexible, as it is straightforward and able to take into account any kind of platform trajectory.

If the borehole is perfectly straight, there will be left-right ambiguities, since the phase histories of all targets at the same range from the antenna will be identical. However, for the general case where the borehole structure is curved, each target will, in general, have a unique range history (phase history), as shown in Figures 4.3 and 4.4. As a result, every target can be properly focussed, and the ambiguities can be resolved. A time-domain SAR processor is regarded as the most suitable processor, because it can easily process data obtained from such a geometry, even though no examples of such situations have been considered in the thesis. It is worth mentioning that, if the borehole trajectory is 3D in space then, as discussed above, the 3D location of the targets can be resolved exactly.

Some research had shown that the borehole curvature can be utilized to resolve the ambiguity around the elevation angle, where the borehole spirals with a pitch that is short compared to the aperture and with an amplitude that is comparable to the wavelength (Simmat et al., 2002).

In summary, the time-domain SAR algorithm is able to handle int the following situations:

- When the borehole geometry and target locations are both known, exact focusing can be achieved, even for severely curved trajectories.
- If the target location is approximately known (as in the case where some prior knowledge exists), good focusing is still possible, as precise knowledge of the target location is not essential (although degradation does occur as the difference between assumed and true location increases).
- If a genuine left and right ambuiguity exists, the ambiguity can be resolved (in the case of a curved borehole trajectory) by processing two or more images under assumed (approximate) target positions and choosing the image which focuses best.

In all three cases, the time-domain SAR algorithm is the most flexible and accurate technique. Other migration algorithms (e.g. frequency domain) generally degrade image quality in the case of curved trajectories (regardless of the knowledge of target location).

The biggest disadvantage is processing speed. Time-domain SAR processors are slow in comparison with their frequency domain counterparts. However, with computers becoming faster and faster, and with the relatively small sizes of the data matrix in the borehole experiment, this drawback may not be very significant in practice. In the field of GPR, the most important requirement is the precision in focusing, not the processing speed.

Time-domain Processor

A point in the focused image is constructed by coherently adding the data collected along the hyperbolic contour in the range compressed data matrix. In a complex baseband form, this requires phase correcting for each data point prior to addition. The baseband received signal in the far field can be expressed as

$$v_{bb}\left(\chi, r(\chi)\right) = \left|v_{bb}\left(\chi, r(\chi)\right)\right| e^{\frac{-j4\pi r(\chi)}{\lambda}}$$

where χ is the azimuth location and r is the slant range distance from the antenna to the target.

The azimuth compressed signal for a point scatterer located at (χ_0, r_0) is given by

$$v_{bb}\left(\chi_0, r_0\right) = \sum_{\chi=-\frac{L}{2}}^{\frac{L}{2}} v_{bb}\left(\chi, r(\chi)\right) e^{\frac{j4\pi\Delta r(\chi)}{\lambda}}$$

where L is the synthetic aperture length and

$$\Delta r(\chi) = r(\chi) - r_0$$

As explained in section 2.5.4, the azimuth resolution is a function of the azimuth spatial bandwidth and is given by

$$\delta\chi = \frac{1}{B_\chi} \cdot w_{factor}$$

where $B_\chi = \frac{4\sin\left(\frac{\theta}{2}\right)}{\lambda}$ is the bandwidth in cycles per metre, θ is the azimuth beamwidth in radians and w_{factor} is the window constant.

As with the range response, the side-lobe levels of the resulting azimuth compressed point target response may be tailored by appropriate weighting of the summed echoes.

Azimuth focusing has a drawback, mainly because of the range migration problem, which means that a point scatterer's signal does not remain in one integer range bin over the integration length. This problem can be overcome by proper interpolation of the data, which will however further reduce the speed of the focusing.

To apply the time-domain azimuth focusing technique to borehole data, we need to know the borehole positions. As illustrated in Figure 4.5, the deviation of the recorded borehole positions from the actual borehole positions should be less than $\frac{\lambda}{8}$, or the phase error should be less than 45^0, in order to achieve a good azimuth focused image.

The time domain focusing technique is well suited for processing the data from curved boreholes, as it calculates the focusing kernel at each azimuth location. The maximum

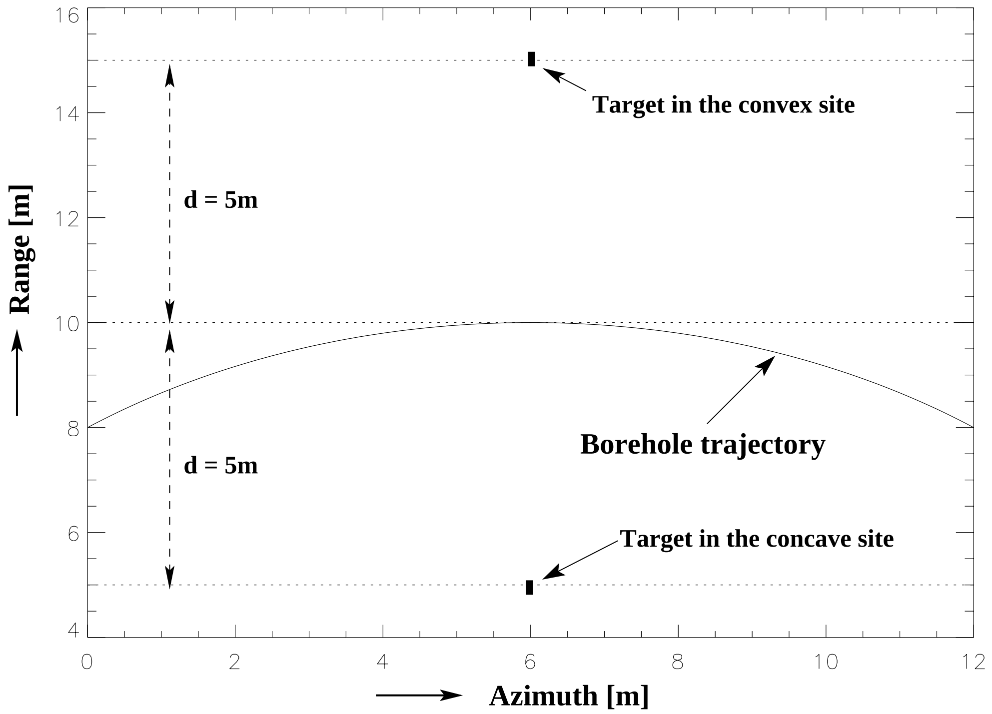

Figure 4.3: *For a curved borehole trajectory, the figure shows the position targets on the concave and convex sides with respect to the borehole trajectory.*

curvature of the borehole trajectory depends upon the dimension of the area to be imaged by the borehole radar survey. For example, a radar in a circular borehole trajectory always illuminates the point at the centre of the circle.

4.4 3-D Image Reconstruction Using Radar Magnitude Images from Multiple Boreholes

In the case of a InSAR system using a narrow-band sidelooking antenna, we use images of a scene from two or more different view angles to form the interferogram. In the ideal case, the interferometric phase of the two perfectly registered SAR images is related to the topographic height of the scene point as discussed in Chapter 3. In the mine borehole situation, due to the omni-directional property of the antenna and the inhomogeneous host rock medium, reflections will come from both sides of the borehole at equal slant ranges. There will be overlay problems and the superposition of the signals will degrade the interferometric phase quality.

But, the concept of the overlapping of signals of a point in the scene from different view

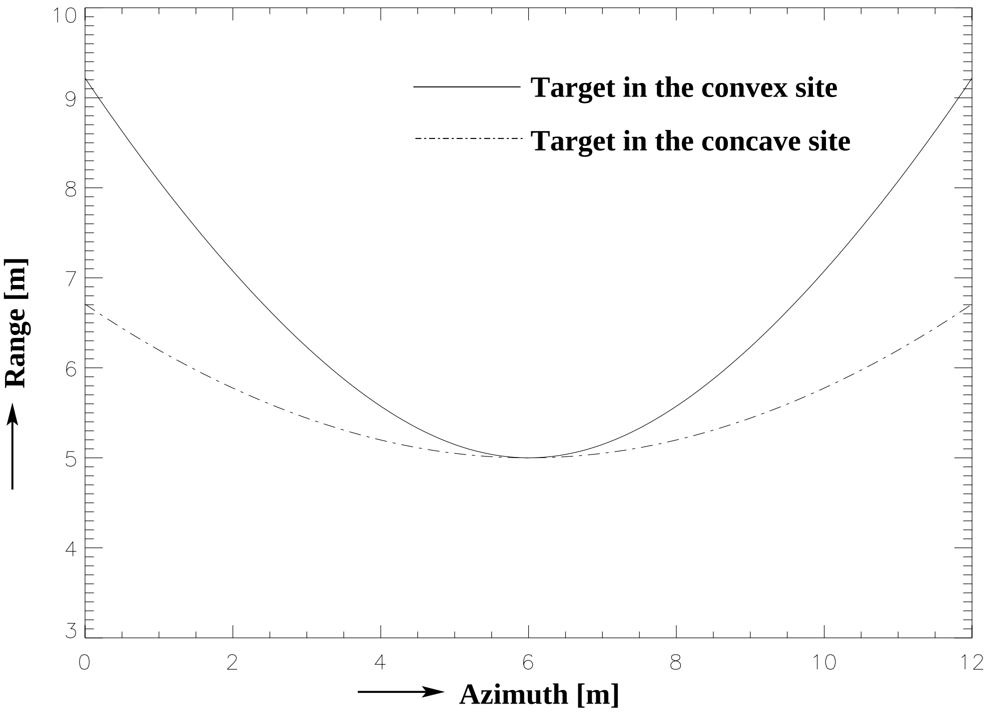

Figure 4.4: *The range history of two targets, located at the concave and convex side of the curved borehole trajectory.*

angles can be utilised to reconstruct the 3-D target position. In the case of only two boreholes, multiplying each analytical signal with the conjugate of the other and adding the two products together can cancel the phase of the resulting signal (Mason et al., 2001). But this method will not be applicable in a situation where there are more than two antennas, and it can also cause constructive and destructive interference between the two signals due to different path lengths. In the case of destructive interference, we will get zero or a very low value, although there is an overlap between the two signals. Alternatively, the 3-D target position can be reconstructed with only the magnitude images from different boreholes (Mukhopadhyay, Inggs, Lord and Wilkinson, 2002).

Each 3-D point scatterer is projected to different azimuth and slant-range positions in different borehole images due to different view angles. As shown in Figure 4.6, the reconstructed grid point P_1 will be projected on the borehole images at azimuth location OA and OB and range location AP_1 and BP_1.

Assuming that there is a point scatterer located at the (x, y, z) position in the reconstructed grid, due to a different view angle, the point scatterer's response will be projected at (χ_a, r_a) in borehole A, at (χ_b, r_b) in borehole B and at (χ_c, r_c) in borehole C focused images. For each point in the reconstructed grid, the azimuth and slant range position is

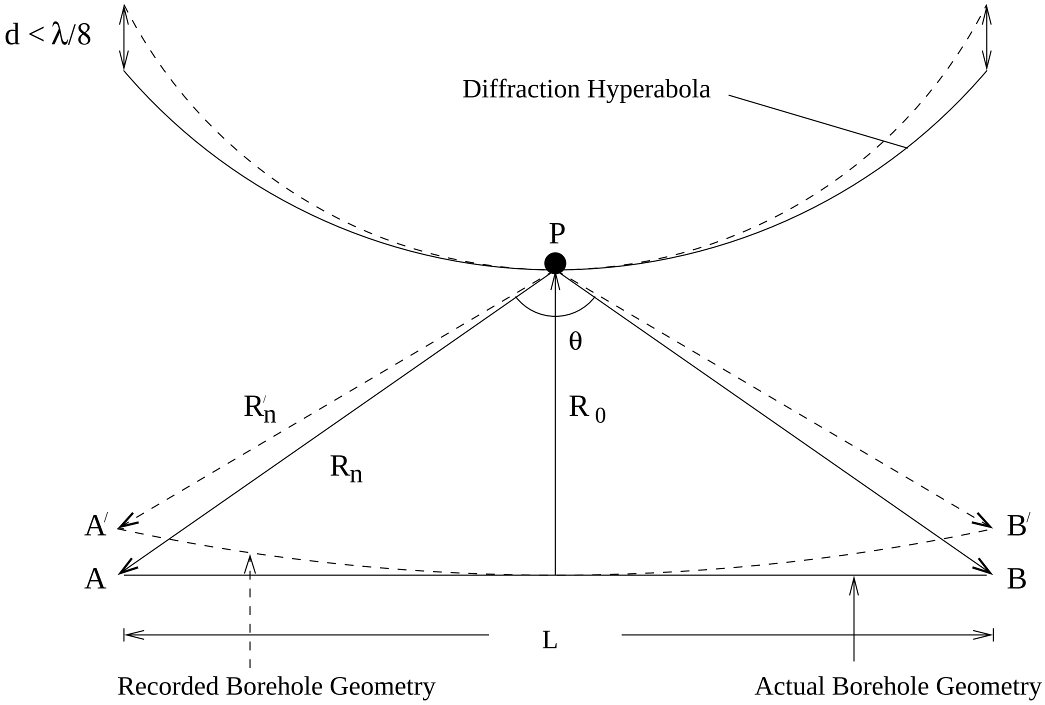

Figure 4.5: *The actual (AB) and the recorded* $(A'B')$ *borehole geometry in a mine borehole measurement. This error causes poor results in the azimuth compressed image.*

calculated in each image, and the corresponding magnitude values are multiplied to get resultant $G\left(x,y,z\right)$ as

$$G\left(x,y,z\right)=\left|A\left(\chi_a,r_a\right)\right|\cdot\left|B\left(\chi_b,r_b\right)\right|\cdot\left|C\left(\chi_c,r_c\right)\right| \tag{4.5}$$

where the analytical signals from different boreholes are

$$\begin{aligned} A\left(\chi_a,r_a\right) &= a_1e^{-\frac{4\pi r_a}{\lambda}} && (4.6)\\ B\left(\chi_b,r_b\right) &= b_1e^{-\frac{4\pi r_b}{\lambda}} && (4.7)\\ C\left(\chi_c,r_c\right) &= c_1e^{-\frac{4\pi r_c}{\lambda}} && (4.8)\end{aligned}$$

where a_1, b_1, c_1 are the amplitudes and r_a, r_b, r_c are the slant range distances to the scatterer.

In an ideal situation, we would get a high value of $G\left(x,y,z\right)$ in a grid position $\left(x,y,z\right)$ if there is a point scatterer present at $\left(x,y,z\right)$, and zero if there is no point scatterer. But in a real borehole situation, we will never get zero for G, because of the presence of noise in the received signal. So, in a real situation, the presence of a target is indicated when some threshold is exceeded.

The rotational ambiguity problem due to the omni-directional radiation pattern of the

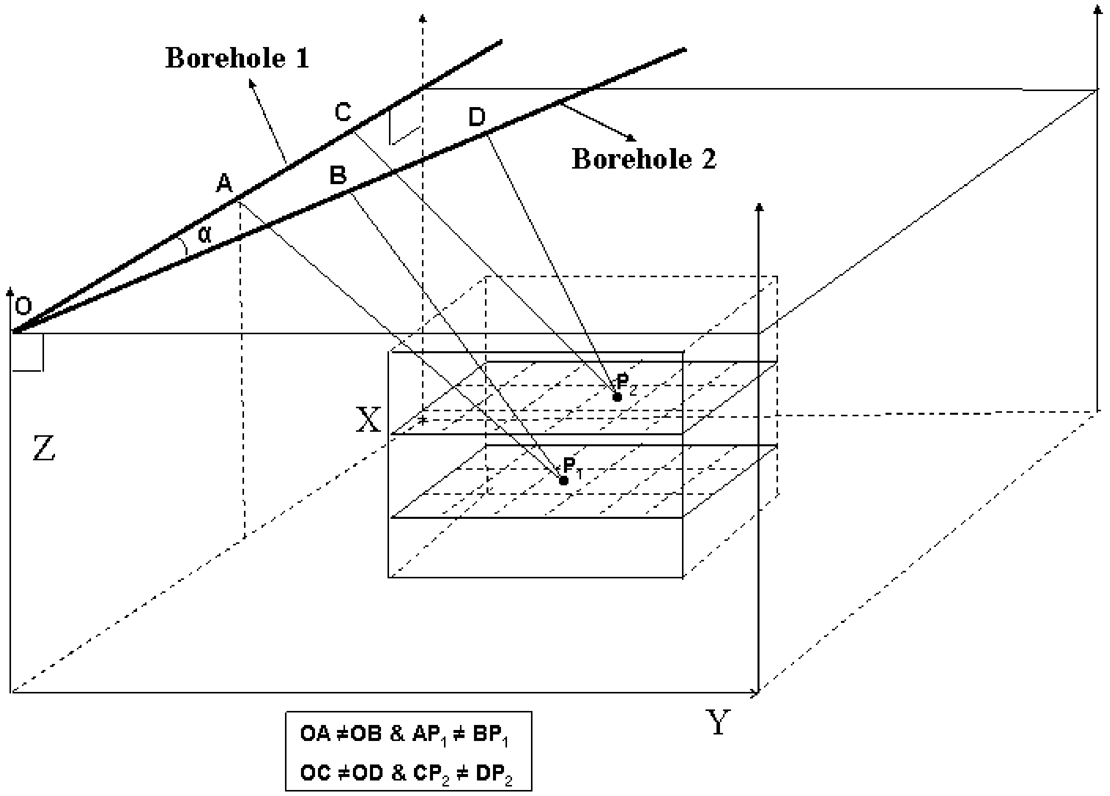

Figure 4.6: *A point scatterer in the 3-D reconstructed grid is projected at different azimuth and slant range position in different borehole data matrices due to different view angles (OA $\neq$ OB and AP$_1$ $\neq$ BP$_1$).*

borehole antenna can be resolved by using multiple boreholes (three or more). This point is discussed in detail later in this chapter.

4.5 Reconstruction Grid Spacing

In-mine boreholes are close to each other (few metres), but rarely parallel. They usually fan outwards from drilling stations in mine roadways. It is important to know the geometry of the boreholes to derive exact derivations for the reconstructed grid spacing, and it is also crucial to select the grid spacing correctly for proper 3-D image reconstruction. The grid spacing in the $X-$, $Y-$ and $Z-$ direction will be such that we should not miss the closely situated point scatterer within the resolution limit of the borehole radar. In our present derivation, we are deriving the expression of the reconstructed grid spacing by taking into consideration the case where the boreholes fan outwards from drilling stations as shown in Figure 4.7, in correspondence to both the simulated and the real acoustic

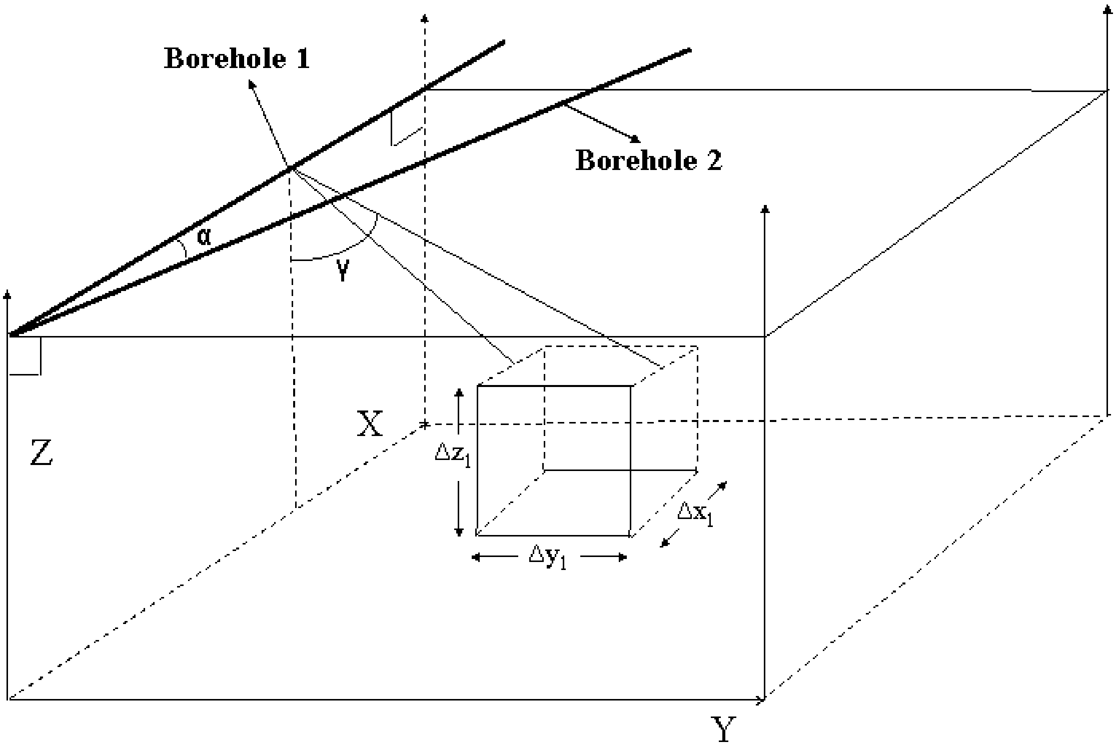

Figure 4.7: *3-D reconstructed grid spacing. The angle between two borehole trajectories in the horizontal plane is α and γ is the maximum look angle.*

experiment.

According to Figure 4.7, the grid spacing in the $X-$direction of borehole 1 should be less than the azimuth resolution of the borehole radar 1. As the borehole 1 is aligned in the X-direction, the $X-$direction grid spacing is given by

$$\Delta x_1 \leq \frac{1}{B_x} = \frac{\lambda}{4\sin\left(\frac{\theta}{2}\right)}$$

where λ is the wavelength and θ is the azimuth beamwidth.

The slant range spacing of the radar traces is constant, but the ground range spacing varies from near range to far range. The calculation of the grid spacing along the $Y-$direction is not straightforward, as it depends upon the radar slant range resolution and the maximum look angle. Figure 4.8 shows a slice of the 3-D reconstructed grid along the $Y-Z$ direction at a particular X position. The along-track direction ($X-$direction) is perpendicular to the plane of the paper.

As shown in Figure 4.8, the distance OC can be calculated as

$$OC \;=\; \sqrt{y_{max}^2 + z^2}$$

$$\sqrt{[r_0 + (n-1)\Delta r} \quad = \quad \sqrt{y_{max}^2 + z^2} \tag{4.9}$$

where y_{max} is the maximum distance in the $Y-$direction, r_0 is the initial vertical distance in the $Z-$direction, and $\Delta r = \frac{c_1}{2B}$ is the radar slant range resolution.

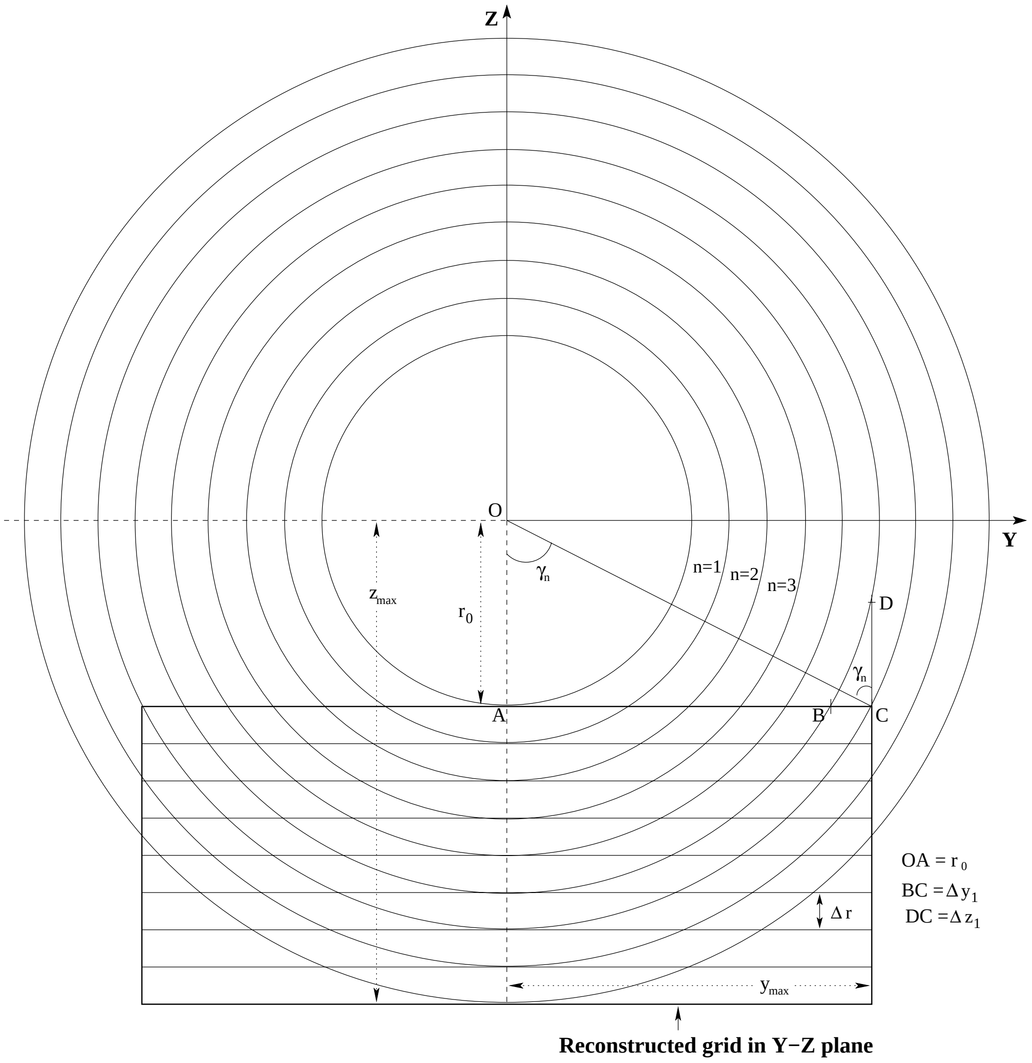

Figure 4.8: *The minimum reconstructed grid spacing calculation in the $Y-$direction. The distance y_{max} and z_{max} is the maximum reconstructed imaging dimension in the $Y-$ and $Z-$direction and γ_n is the maximum look angle.*

The value of n depends on the maximum distance to be imaged in the $Y-$direction and given as

$$n = 1 + \frac{r_0 \left[\frac{1}{\cos(\gamma_n)} - 1\right]}{\Delta r}$$

where γ_n is the maximum look angle (Figure 4.8).

The value of n must be taken to the nearest largest integer value.

Putting $z = r_0$ in equation 4.9, we get

$$y_n = \sqrt{(n-1)\,\Delta r\,[(n-1)\Delta r + 2r_0]} \tag{4.10}$$

Now the minimum distance between the successive points in the $Y-$direction, Δy, is given by

$$\Delta y = y_{n+1} - y_n = \sqrt{n\Delta r\,[n\Delta r + 2r_0]} - \sqrt{(n-1)\,\Delta r\,[(n-1)\,\Delta r + 2r_0]} \tag{4.11}$$

The grid spacing along the vertical direction ($Z-$direction) depends on the value of the look angle and on the radar range resolution, Δr; at a look angle of zero, the minimum value becomes the radar range resolution Δr.

As shown in Figure 4.7, considering the maximum look angle as γ_n , the grid spacing in the $X-$, $Y-$ and $Z-$ direction for borehole 1 is given as

$$\begin{aligned}
\Delta x_1 &\leq \frac{1}{B_x} = \frac{\lambda}{4\sin\left(\frac{\theta}{2}\right)} && (4.12)\\
\Delta y_1 &\leq \sqrt{n\Delta r\,[n\Delta r + 2r_0]} - \sqrt{(n-1)\,\Delta r\,[(n-1)\,\Delta r + 2r_0]} && (4.13)\\
\Delta z_1 &\leq \Delta r && (4.14)
\end{aligned}$$

Now, if we consider a second borehole, which is at an angle α with borehole 1 in the horizontal plane, the projected grid spacing in the $X-$ and $Y-$direction will be different to the calculated grid spacing of the borehole 1. The grid-cell $ABCD$ is projected as $AB^{/}C^{/}D^{/}$ due to the different view angle as shown in Figure 4.9.

Assuming the same kind of radar is used in the borehole 2 experiment, the 3-D grid spacing in the case of borehole 2 can be calculated as

$$\begin{aligned}
\Delta x_2 &\leq \Delta x_1 \cos(\alpha) + \Delta y_1 \sin(\alpha) && (4.15)\\
\Delta y_2 &\leq \Delta x_1 \sin(\alpha) + \Delta y_1 \cos(\alpha) && (4.16)\\
\Delta z_2 &\leq \Delta r && (4.17)
\end{aligned}$$

We must chose the resultant grid spacing in such a way that the value remains minimum between different borehole settings. Figure 4.10 shows the variation of the X and Y grid spacing values for borehole 2 with the horizontal angle between two boreholes, for given values of Δx_1 and Δy_1. As shown in Figure 4.10, the values of Δx_2 and Δy_2 are not linear with respect to the horizontal angle between the two boreholes. Therefore, we must choose a minimum value between Δx_1 and Δx_2 for our final reconstructed Δx grid spacing and a minimum value between $\Delta y_1$and Δy_2 for our final reconstructed Δy grid spacing.

Therefore, the resultant 3-D reconstructed grid spacing, satisfying the Nyquist criterion, will be

$$\Delta x \leq \min\left(\Delta x_1 \,\text{AND}\, \Delta x_2\right) \tag{4.18}$$

$$\Delta y \leq \min\left(\Delta y_1 \,\text{AND}\, \Delta y_2\right) \tag{4.19}$$

$$\Delta z \leq \Delta r \tag{4.20}$$

4.6 Rotational Ambiguity

In general, the radiation pattern of the borehole radar antenna is omni-directional and there will be a rotational ambiguity problem using a single borehole, as the points of equal slant range will appear as a single point. This effect will cause uncertainty about the actual location of the target orebody. This problem can be resolved by using three non-collinear boreholes, as shown in Figure 4.11. Given a spherical antenna radiation pattern, as shown in Figure 4.11, the response from points P_1 and P_2 will appear as a single point in the images from borehole A and borehole B. Now if we consider a third borehole C whose centre is non-collinear with A and B, then the response from points P_1 and P_2 will appear as a separate point in borehole C image, as the range CP_1 is greater than CP_2.

In our reconstructed image, in respect of points P_1 and P_2, we will get

$$G\left(x_{P_1}, y_{P_1}, z_{P_1}\right) = \left|A\left(\chi_a, r_{AP_1}\right)\right| \cdot \left|B\left(\chi_b, r_{BP_1}\right)\right| \cdot \left|C\left(\chi_c, r_{CP_1}\right)\right| \tag{4.21}$$

$$G\left(x_{P_2}, y_{P_2}, z_{P_2}\right) = \left|A\left(\chi_a, r_{AP_2}\right)\right| \cdot \left|B\left(\chi_b, r_{BP_2}\right)\right| \cdot \left|C\left(\chi_c, r_{CP_2}\right)\right| \tag{4.22}$$

As $r_{CP1} \neq r_{CP2}$, we will get high values of $G\left(x_{P_1}, y_{P_1}, z_{P_1}\right)$ and $G\left(x_{P_2}, y_{P_2}, z_{P_2}\right)$ if there are two distinct point scatterers present at P_1 and P_2. But we will get a high value of $G\left(x_{P_1}, y_{P_1}, z_{P_1}\right)$ and zero value of $G\left(x_{P_2}, y_{P_2}, z_{P_2}\right)$, as $\left|C\left(x_c, r_{CP_2}\right)\right|$ will be zero if there is only one scatterer present at P_1. So, by using more than two borehole antennas in the borehole experiment, we can resolve the ambiguity problem.

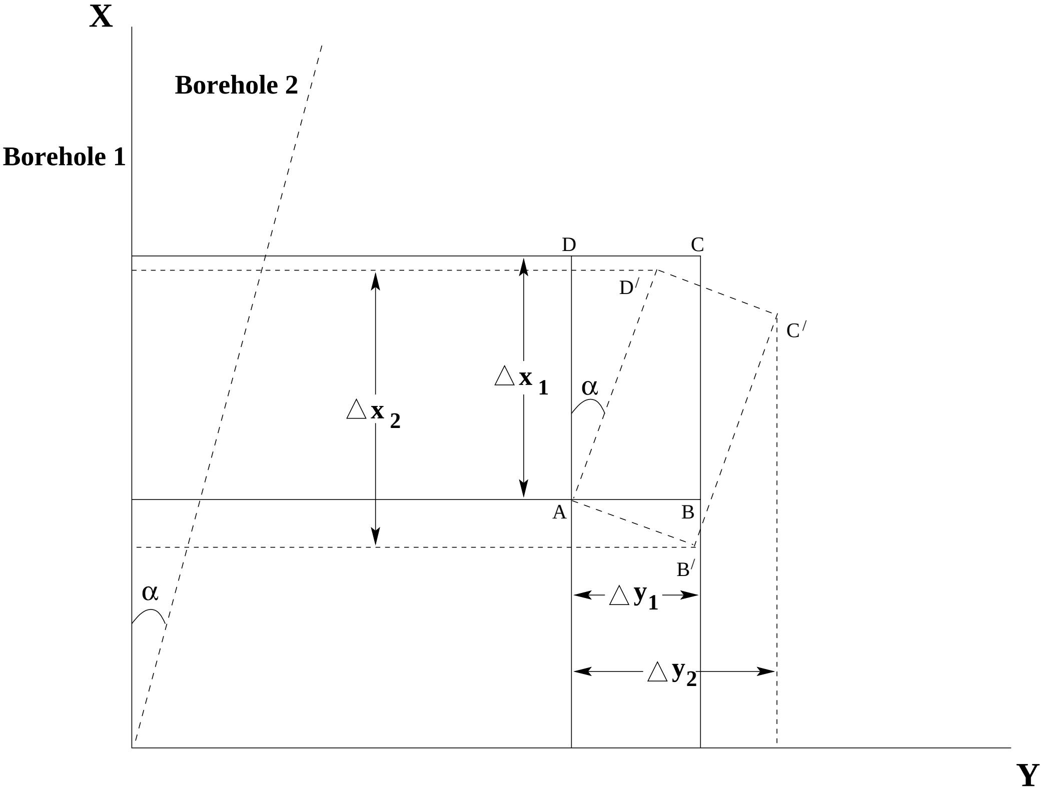

Figure 4.9: *The* $X - Y$ *projection of the borehole 1 and borehole 2 trajectories. The boreholes make an angle* α *to each other in the horizontal plane.*

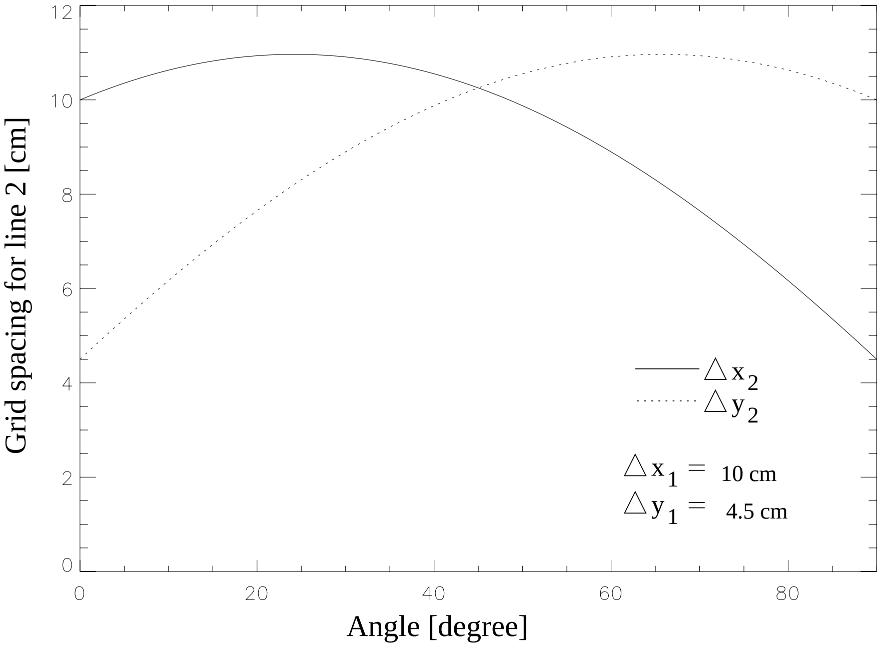

Figure 4.10: *A plot showing the angle dependency of the X and Y reconstructed grid spacing for borehole 2. For example, the grid spacing using borehole 1 is given as* $\Delta x_1 = 10$*cm and* $\Delta y_1 = 4.5$*cm.*

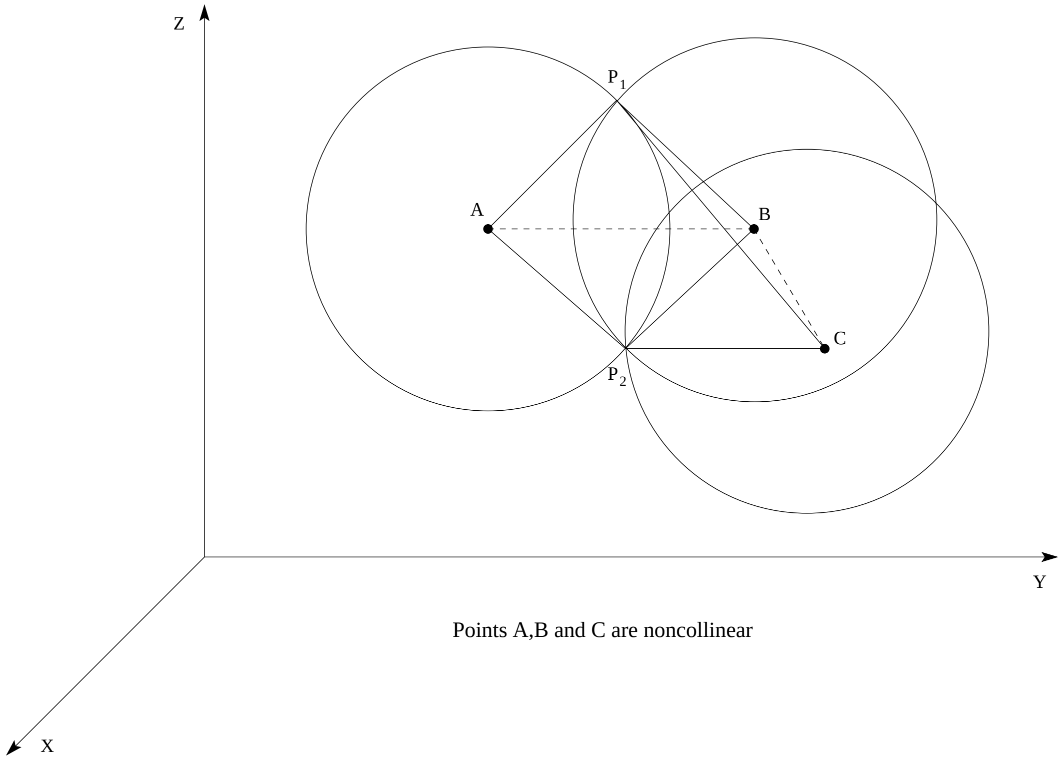

Figure 4.11: *Rotational ambiguity problem due to the radiation pattern of an omni-directional borehole radar antenna. Points* P_1*and* P_2 *will show as a single point in the images of boreholes A and B. But in the image of borehole C, points* P_1 *and* P_2 *will appear as separate points.*

4.7 Simulation Experiment

The numerical simulations shown here correspond to the dimensions of experimental results obtained using a 40 kHz acoustic radar emulator in air, discussed later in section 4.8.1. Figure 4.12 shows a sketch of the simulation model geometry. The transmitter and the receiver antennas are located at a fixed location at $(\mathrm{x}_a, \mathrm{y}_a, \mathrm{z}_a) = (150, 0, 126)$ cm. We are considering these to be in the mono-static, side-looking imaging mode. The antenna is directed at a 30° elevation angle towards the target. The azimuth and the elevation beamwidth of the radar are both 40°. The transmitted pulse was chosen to be a linear frequency modulated $chirp$ pulse. A pulse length of 8ms was used corresponding to a physical extent in air of 2.7 m and a pulse bandwidth was chosen of 4 kHz with a centre frequency of 40 kHz. The time-bandwidth product is 32. The medium was considered to be homogeneous, isotropic and non-dispersive, and the velocity of propagation was considered as 340 m/sec, the velocity of sound in air. These simulation parameters were chosen to correspond to an air-based 40 kHz acoustic experimental setup.

4.7.1 Experimental Setup

The three isotropic point scatterers are placed on a moving platform (Figure 4.12). The platform was moved along two lines, one along the X-axis and the other making an angle of 15^0 with the X-axis. Synthetic apertures were built up by collecting traces at 5 mm intervals along each line by moving the sensors platform across the antenna beam, satisfying the azimuth Nyquist criterion. The locations of the three point scatterers with respect to the moving platform are at $(x_1, y_1, z_1) = (-35, 30, 21)$ cm, $(x_2, y_2, z_2) = (0, 80, 0)$ cm and $(x_3, y_3, z_3) = (35, 70, 41)$ cm respectively.

4.7.2 Simulation Results

In this simulation experiment the transducer's passband magnitude spectrum was considered to be flat. The received echos from the scene were range compressed by applying a matched filter. The matched filter kernel is the time-reversed complex conjugate of the transmitted pulse. A Hamming window was applied to the matched filter kernel for sidelobe reduction. Figure 4.13 shows a dB plot of the range compressed down-range profile of a single scatterer. The 3-dB range resolution obtained by applying a Hamming Window was measured to be 5.58 cm. A value of 1.3 was measured, i.e. compared to $\frac{1}{B_t}$ as a window constant. The range compressed profiles were assembled into a data matrix, which is shown in Figures 4.14 and 4.15. The point target resulted in characteristic hyperbolic shaped signatures.

The range compressed data matrix were then compressed in azimuth by using a time-domain focusing algorithm, and the resulting azimuth compressed image is shown in Figures 4.16 and 4.17. In the two focused images, we can see that the points are projected in different azimuth and slant range positions. A dB plot across a single azimuth compressed point target is shown in Figure 4.18. The 3-dB azimuth resolution was measured to be 0.56 cm using a $40°$ two-way azimuth beamwidth.

Now, the 3-D image has been reconstructed by using the afore mentioned algorithm in which we used 2-D magnitude images from two platform trajectories. The 3-D reconstructed image is shown in Figure 4.19. The three input scatterers are seen in their respective positions. The X-Z and X-Y projections of the reconstructed image are shown in Figures 4.20 and 4.21 respectively. The reconstructed grid spacing is taken as $\Delta x = 3.2$mm, $\Delta y =$11mm and $\Delta z = 10.8$mm.

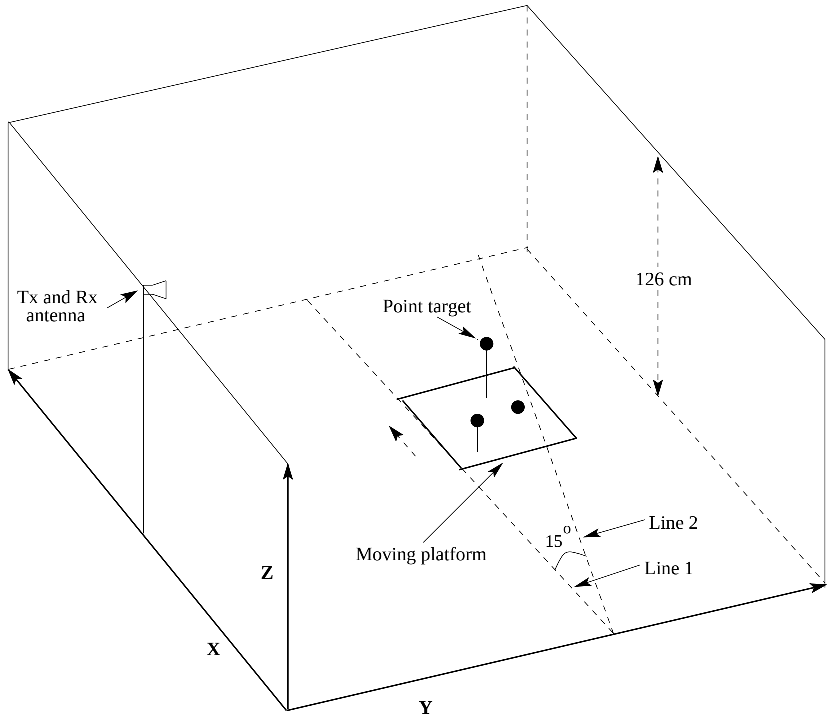

Figure 4.12: I*nverse synthetic aperture radar simulation setup geometry in air. The platform moves along two lines, making an angle 15*^{0}*to each other in the horizontal plane. Three point scatterers on the platform are located at* $(x, y, z) = (-35, 30, 21)$, $(0, 80, 0)$, $(35, 70, 41)$ *cm respectively. The Y distance between the transducers and the platform is 100cm.*

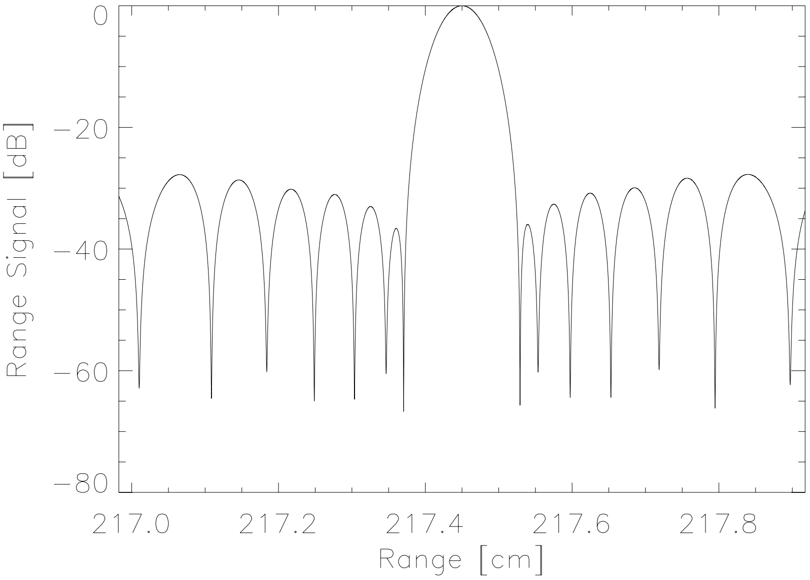

Figure 4.13: *A dB plot across the range compressed down-range profile of a single point scatterer. A Hamming window is used to reduce the side-lobe level. The first side-lobe is approximately at 41 dB.*

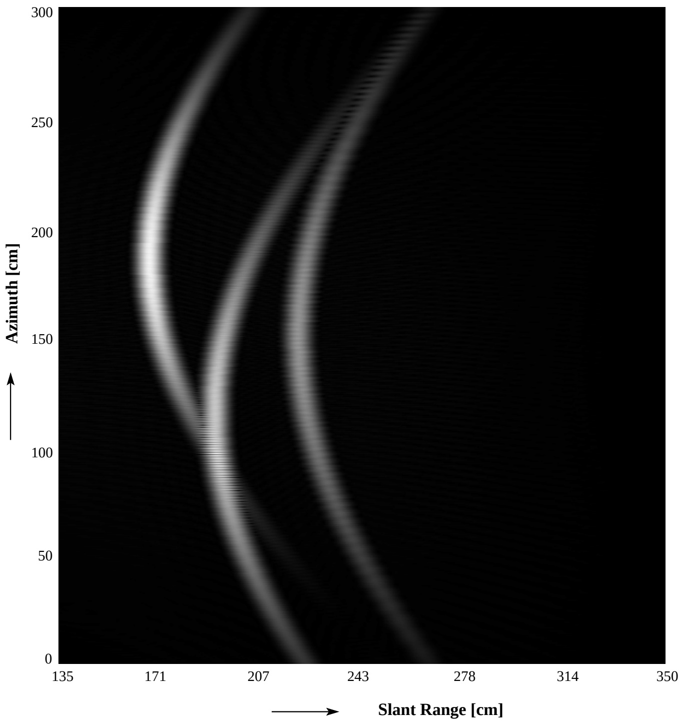

Figure 4.14: *Inverse synthetic aperture radar (ISAR) range compressed data matrix of line 1 prior to azimuth compression.*

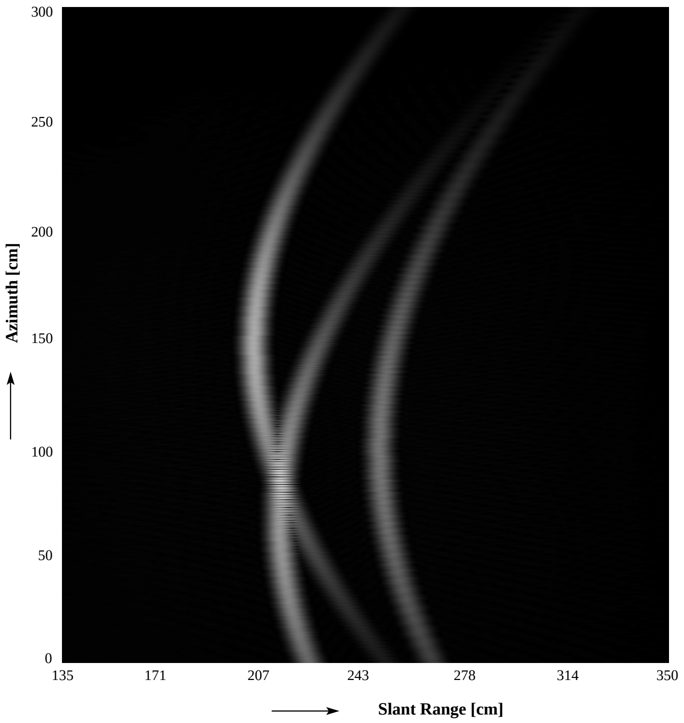

Figure 4.15: *Inverse synthetic aperture radar (ISAR) range compressed data matrix of line 2 prior to azimuth compression.*

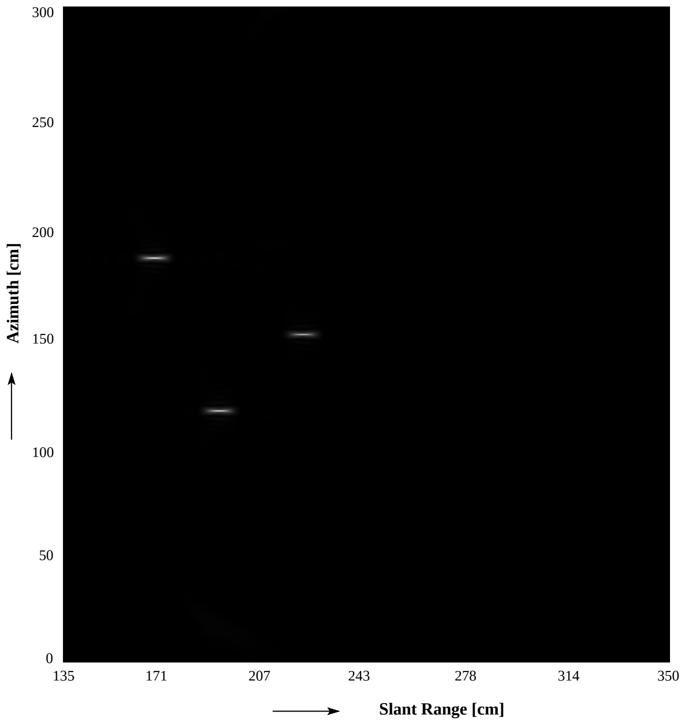

Figure 4.16: *Inverse synthetic aperture radar (ISAR) azimuth compressed data matrix of line 1.*

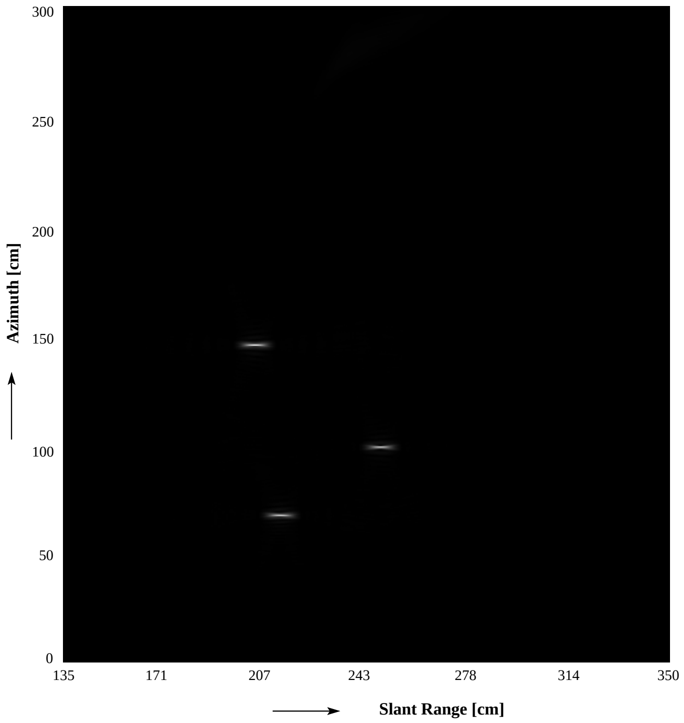

Figure 4.17: *Inverse synthetic aperture radar (ISAR) azimuth compressed data matrix of line 2.*

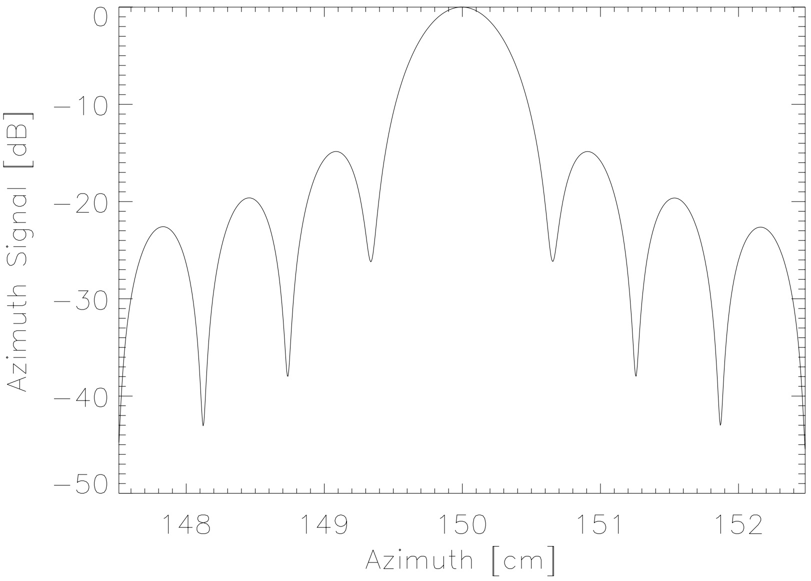

Figure 4.18: *A dB plot across a single point scatterer azimuth compressed profile.*

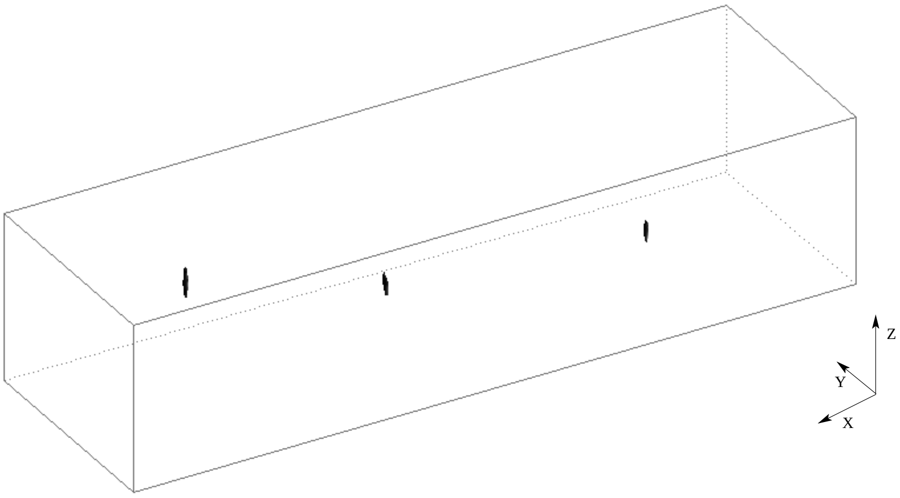

Figure 4.19: *Reconstructed 3-D image from simulated radar images taken from different view angles.*

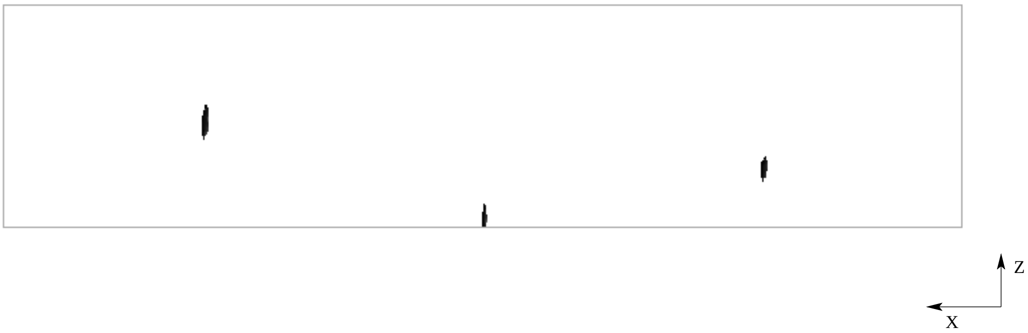

Figure 4.20: *X-Z projection of the 3-D reconstructed image using simulated radar images.*

Figure 4.21: *X-Y projection of the 3-D reconstructed image using simulated radar images.*

4.8 Real Acoustic Measurement in Air

Obtaining multiple borehole radar data in real geophysical applications is a time-consuming and expensive process. The Radar Remote Sensing Group (RRSG) at UCT is planning to build a step-frequency borehole radar, which will be deployed in South African mines for high resolution subsurface imaging. As the research progresses, we will thus obtain multiple borehole radar data that will allow us to reconstruct subsurface orebodies in 3-D with sub-meter resolution. Trials in South African mines have established that wide-band VHF borehole radars, working in the 10–100 MHz band, can be used to probe the rock-mass in 2-D over ranges from less than 5 m to as much as 150 m with sub-meter resolution (Mason et al., 2001) using a single borehole.

For those working in this field, the availability of a smaller scale laboratory measurement system is of potential benefit, as it allows easy experimentation with different imaging geometries. A coherent sonar SAR emulator system operating at 40 kHz in air has been developed at UCT to allow acoustic data to be captured in a laboratory environment (Korda and Trninic, 2002). This system has been used for the first time in this thesis to capture the acoustic data from two different trajectories for 3-D image reconstruction (Wilkinson et al., 2004).

4.8.1 Real Coherent Sonar SAR Emulator Data

System Hardware

The philosophy behind the sonar hardware was to design a system that could be easily operated from within the MATLAB programming environment, and which would also demonstrate hardware techniques, such as frequency heterodyning, employed in radar systems. The initial prototype was developed as an undergraduate student project at the University of Cape Town (Korda and Trninic, 2002). A centre frequency of 40 kHz was chosen for the transmitted pulse, which travels at approximately 340 m/s in air. The corresponding wavelength of 8.5 mm is a practical dimension for the scale of imaging. Piezoelectric transducers were readily available with bandwidths of 4 kHz, corresponding to an achievable range resolution of about 4 cm in air.

Receiver-Transmitter Hardware

A block diagram of the system hardware is shown in Figure 4.22. MATLAB is used to control the PC sound card, which generates a chirp pulse with spectral components in the audio range between 8 kHz and 12 kHz. This pulse is then mixed with a 50 kHz oscillator, generating a lower sideband at 40 kHz and an upper sideband at 60 kHz. The 40 kHz sideband is passed through a bandpass filter, amplified and fed to the transmitter transducer.

The pulse radiates, is reflected from the scene, and the echo is received by a receiving transducer. The two-way 3-dB beamwidth is approximately 40^0. The received signal is amplified and translated down again into the audio range of the sound card, sampled and stored for subsequent digital signal processing. The MATLAB "wavplay" and "wavrecord" commands are used to generate and record the waveforms. The sample rate is set to 44.1 kHz, the maximum rate available on most PC sound cards. In MATLAB, however, it was not possible to ensure accurate syncronization between the start of playing and recording. This problem was circumvented by simultaneously recording both the transmitted and the received echo on the left and right channels of the sound card, as shown in Figure 4.22, and correlating these recordings. The transducers are shown in Figure 4.23.

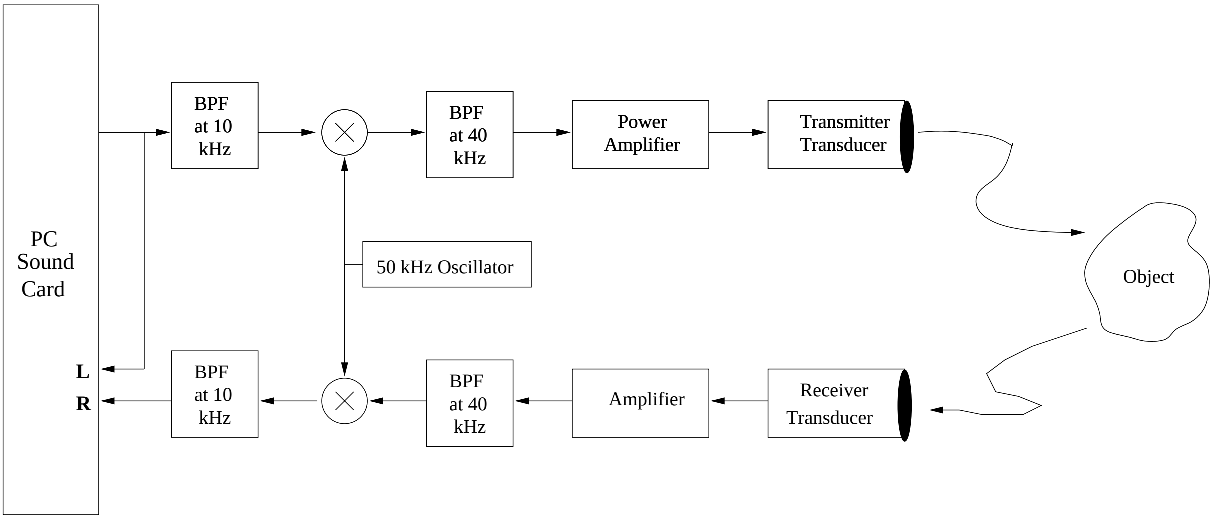

Figure 4.22: *Sonar hardware block diagram.*

Moving Platform

To implement the inverse synthetic aperture imaging technique, the scene must be moved across the beam as illustrated in Figure 4.2. A wooden platform on wheels as shown in Figure 4.24, was constructed with dimensions 2.5 mx1.0 m. This platform could be pulled manually by means of a cord, and its position along its track was recorded by an accurate odometer wheel (Nyareli, 2003), which can be seen on the right hand side of Figure 4.24. The transmitter was synchronized to the odometer, so that pulses could be transmitted and recorded at regular spatial intervals along the track.

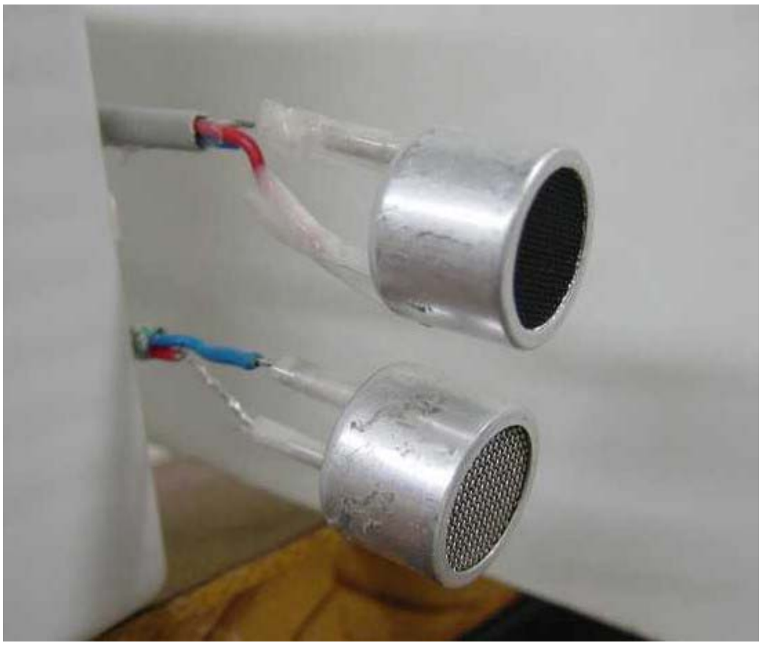

Figure 4.23: *Piezoelectric 40 kHz transmitter and receiver transducers.*

Signal Processing Steps

The focused image is formed by using correlation-type processing, which is carried out in two steps:

1. range compression, using deconvolution processing with frequency domain windowing (for optimal point target response).
2. azimuth focusing, using standard migration processing (also known as time domain synthetic aperture focusing).

As explained in section 4.3.1, the transmitted pulse was chosen to be a chirp pulse, modelled by

$$v_{tx}\left(t\right) = rect\left(\frac{t}{T}\right) \cdot \cos\left(2\pi\left[f_0 t + 0.5Kt^2\right]\right)$$

where f_0 is the centre frequency, T is the pulse length and $K = \frac{B}{T}$ is chirp rate in Hz/sec. A pulse length of $T = 8\,\mathrm{ms}$ was used, corresponding to a physical extent in air of 2.7 m.

The recorded complex baseband signal may be modelled by

$$V_{bb}(f) = H_s(f)\zeta(f + f_0) + N(f + f_0)H_{rec}(f)$$

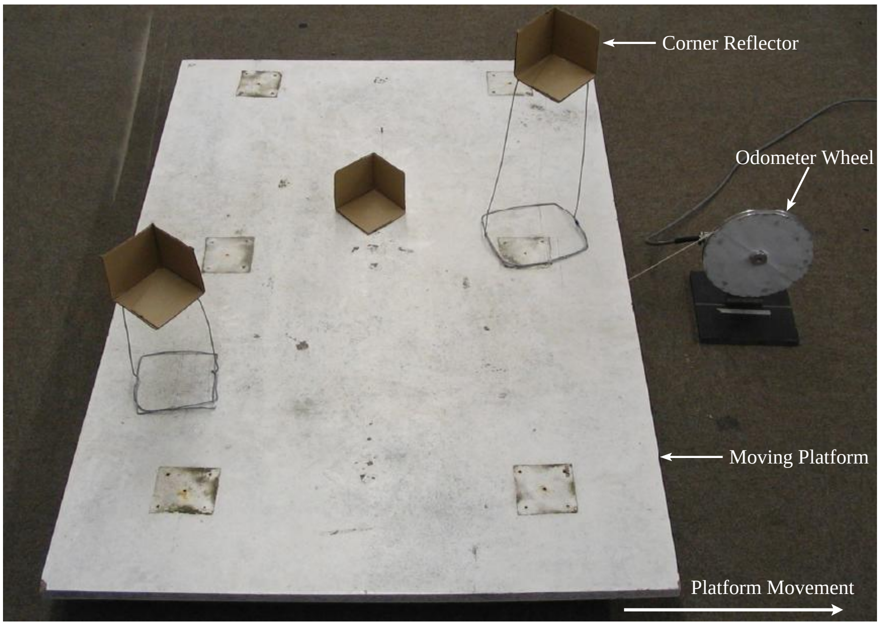

Figure 4.24: *Inverse synthetic aperture imaging setup with ultrasonic SAR emulator in air. The platform moves in two lines, making an angle of 15*^{0} *to each other in the horizontal plane. Three corner reflectors on the platform are located at* $(x, y, z) = (-35, 30, 21)$, $(0, 80, 0)$, $(35, 70, 41)$ *cm respectively. The Y distance between the transducers and Line 1 of the moving platform is* 100 *cm. The odometer wheel can be seen on the right side of the picture.*

where $\zeta(f + f_0)$ is a basebanded version of the analytic representation of the impulse response of the target scene, and $N(f + f_0)$ is the basebanded noise referred to as the input of the first amplifier. All linear system effects affecting the target response are modelled by the equivalent baseband system transfer function

$$H_s(f) = P(f)H_1(f)H_2(f)H_3(f)H_4(f)H_5(f)H_6(f)$$

where

H_1 = models the first BPF at 10 kHz
H_2 = models the BPF and power amplifier at 40 kHz
H_3 = models the transmitting transducer
H_4 = models the receiving transducer
H_5 = models the receiver amplifier and BPF at 40 kHz
H_6 = models the BPF at 10 kHz
$P(f)$ = models the baseband transmitted pulse

The noise is shaped by receiver transfer function $H_{rec}(f) = H_5(f) \cdot H_6(f)$.

Range Profiling

The pulse bandwidth was chosen to be 4 kHz, covering the passband of the transducers. For optimal SNR, under additive noise conditions, the received echo is processed by matched filtering, i.e. the output signal is computed by

$$v_0\,(t) = IFFT[H_{MF}(f) \cdot V_{bb}(f)]$$

for which $H_{MF}(f) = H_s^*(f)/\sqrt{S_n(f)}$ where $S_n(f)$ is the power spectral density of the noise. If passband is fairly flat, with white noise, then $H_{MF}(f) \approx P^*(f)$.

Although optimal for SNR, matched filtering results in an undesirable point target response if the passband of the transducers are not flat in magnitude and linear in phase. This was the case in this sonar system, as the desired 4 kHz bandwidth extended into the roll-off of the transducers.

Instead, a deconvolution processing approach was adopted, in which the baseband signal was passed through the filter $H(f) = [1/H_s(f)]\, rect(f/B)$. A special calibration procedure was developed in which the transmitter transducer was aimed directly at the receiving transducer, separated by a distance d equal to two metres. This allowed direct recording of the total system response, allowing $H_s(f)$ to be obtained.

With this filter, the processed baseband response is given by

$$V(f) = rect(f/B)\zeta(f + f_0)$$

For a point target at range r modelled by $\zeta(t) = \zeta_0\delta(t - \tau)$ where ζ_0 is the reflection coefficient, and $\tau = 2r/c$, the processed frequency response is

$$V(f) = rect(f/B)\zeta_0 e^{-j2\pi(f+f_0)\tau}$$

with a corresponding $Sa()$ shaped time response

$$v(t) = \zeta_0 BSa\left(\pi B(t - \tau)\right) \cdot e^{-j2\pi f_0 \tau}$$

The corresponding 3dB range resolution is $\delta R \approx \frac{0.89c}{2B} = 3.8\,\mathrm{cm}$. Frequency domain windowing may also be applied to reduce the side-lobe levels in the response (Mitra, 1999). Application of a Hamming window reduces the first side-lobe to 41 dB below the peak, at the expense of main lobe broadening by a factor of 1.5.

Range Compression Processing Steps

Because of the lack of precise syncronization between transmitting the chirp and the start of recording, an additional step was required in which the range profiles were time aligned by correlating the recorded echo with the recording of the transmitted waveform. The sequence of steps used to form a range profile are listed below (Figure 4.25):

Step 1	The chirp emitted from the output of the sound card and the received echo are recorded on the left and right input channels respectively and stored in vectors v_{tx} and v_{rx}. These signals lie in the 8-12 kHz intermediate frequency band, centred on frequency $f_{IF} = 10$kHz.
Step 2	The received signal v_{rx} is correlated with v_{tx}, in the frequency domain, i.e. $V = FFT(V_{rx}) \cdot FFT(V_{tx})^*$.
Step 3	The deconvolution filter is applied (its formation is described below).
Step 4	A Hamming window is applied.
Step 5	The signal is converted to a complex analytic signal, by zeroing out the negative frequency components, and inverse transforming to the time domain.
Step 6	The complex baseband signal is formed by multiplying by $e^{-j2\pi f_{IF}t}$. This operation translates the spectral components down to baseband .

The creation of the deconvolution filter involves the following steps:

- The transducers are pointed towards one another with a separation distance of $d = 2$m.
- Steps 1 and 2 above are carried out to obtain a time aligned recording.
- To reduce noise, several echoes are averaged and stored in vector v_{ave}, but this must take place after step 2 has been applied, as averaging requires the data to be time aligned.
- A deconvolution filter is created, i.e. $H_d = [1/H_s]e^{-j2\pi f t_d}$ where $H_s = FFT(v_{ave})$ and $t_d = d/c$. A linear phase correction is included to compensate for the 2m separation of the transducers. This will ensure that application of the deconvolution filter to a received echo does not result in a 2m range shift.

Azimuth Focusing

Azimuth focusing was achieved by using standard *time domain synthetic aperture processing* (Bamler and Schattler, 1993), which is computationally inefficient, but accurate for non-linear trajectories, as discussed above (Section 5.3.2). For a two-way idealized beamwidth of approximately 40^0, the spatial bandwidth is approximately 162 cycles/metre, and the expected azimuth resolution is approximately 6 mm. As with the range response, the side-lobe levels of the resulting azimuth point target response may be tailored by appropriately weighting of the summed echoes.

4.8.2 Ultrasonic Experimental Setup in Air

The scene consisting of three corner reflectors (photograph in Figure 4.24) was dragged in two lines across the beam as illustrated in Figure 4.2. Pulses were transmitted at 4.8 mm intervals as the scene progressed along the track, satisfying the azimuth Nyquist criterion. Additionally, at every 10 cm, the corner reflectors were rotated about their phase centres to point in the direction of the transducers, hence simulating the uniform angular response of a point target.

4.8.3 Experimental Results

A plot of the down-range profile of a single target showed the comparison between a range compressed profile using a matched filer and one using deconvolution (Figure 4.26). It is clear that the deconvolution filter improves the range resolution. Figure 4.27 shows a dB plot of the range compressed (deconvolution filter) down-range profile of a single scatterer. The 3-dB range resolution using the Hamming window was measured to be 5.83 cm, which is very close to the theoretical value. The range compressed profiles were assembled into a matrix, and are shown in Figure 4.28 and Figure 4.29. The point targets result in characteristic hyperbolic shaped signatures.

These data were then compressed in azimuth, and the resulting azimuth compressed images are shown in Figure 4.30 and Figure 4.31. A dB plot across a single azimuth compressed point target was shown in Figure 4.32. The 3-dB azimuth resolution was measured to be 8.2 mm, a factor of 1.5 greater than calculated with the approximate 40° beamwidth. The difference may be attributed to several factors, such as a lack of accurate compensation for the amplitude and phase response across the two-way sensor beam, as well as departure of the corner reflectors from idealized point targets (although considerable care was taken to point the corner reflectors in the direction of the transducers).

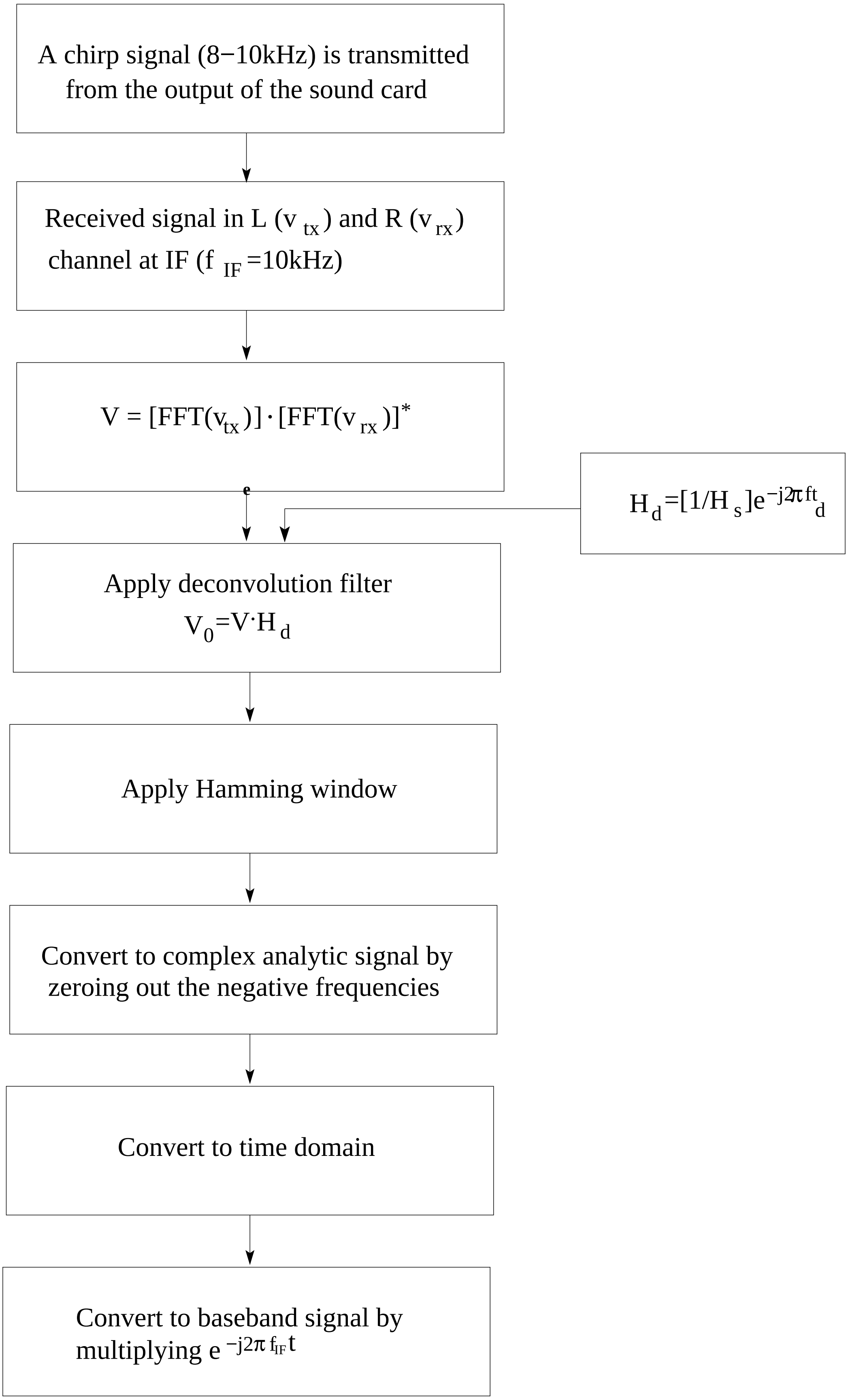

Figure 4.25: *Flowchart of processing real sonar data captured in air.*

The 3-D image was reconstructed by using the afore mentioned algorithm, where we used the focused sonar magnitude images from two lines. The 3-D reconstructed image is shown in Figure 4.33. The 3-D locations of the point scatterer were also reconstructed. The X-Z and X-Y projection of the reconstructed image are shown in Figure 4.34 and 4.35 respectively. The reconstructed grid spacing was taken as $\Delta x = 3.2$mm, $\Delta y =$11mm and $\Delta z = 10.8$mm.

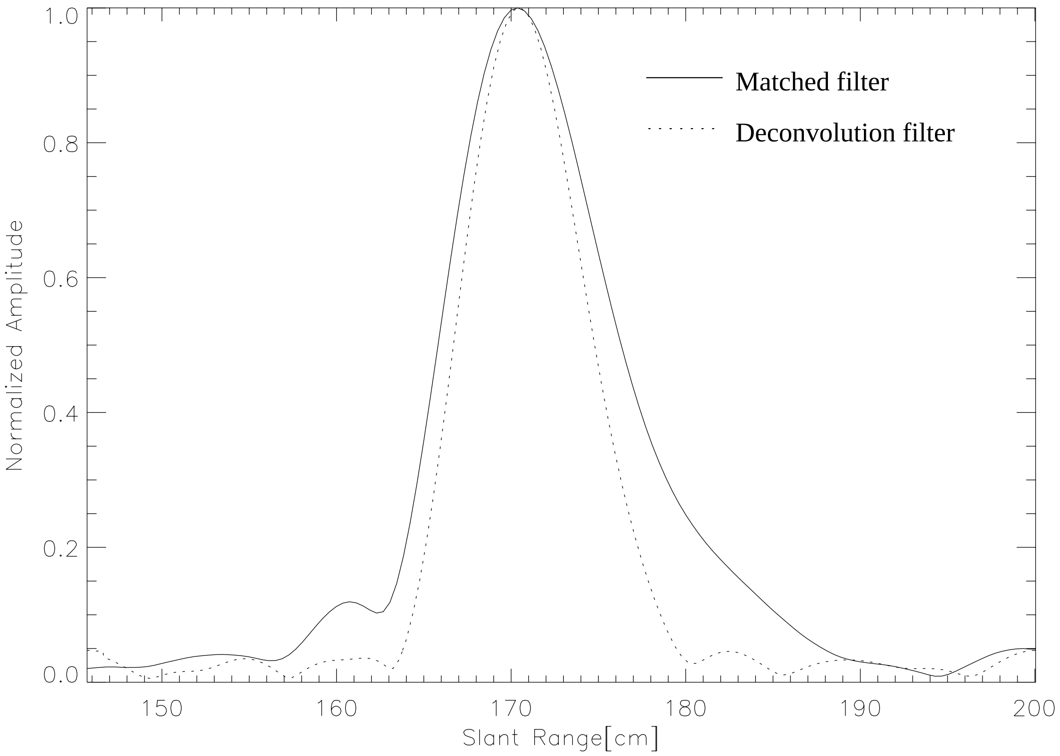

Figure 4.26: *A comparison of range compression using matched filter and deconvolution filter.*

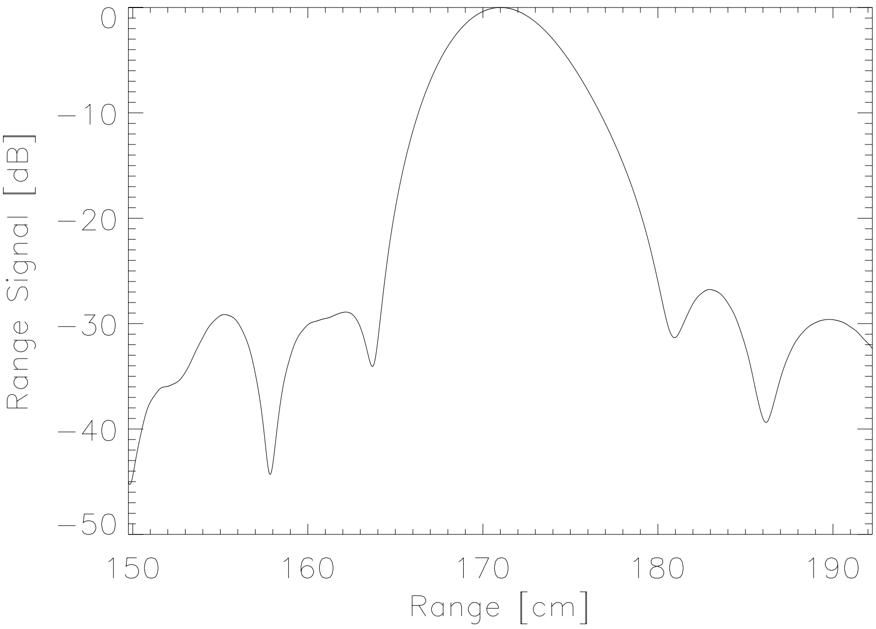

Figure 4.27: *Cross section of a single target in the range direction after applying deconvolution filter (dB plot).*

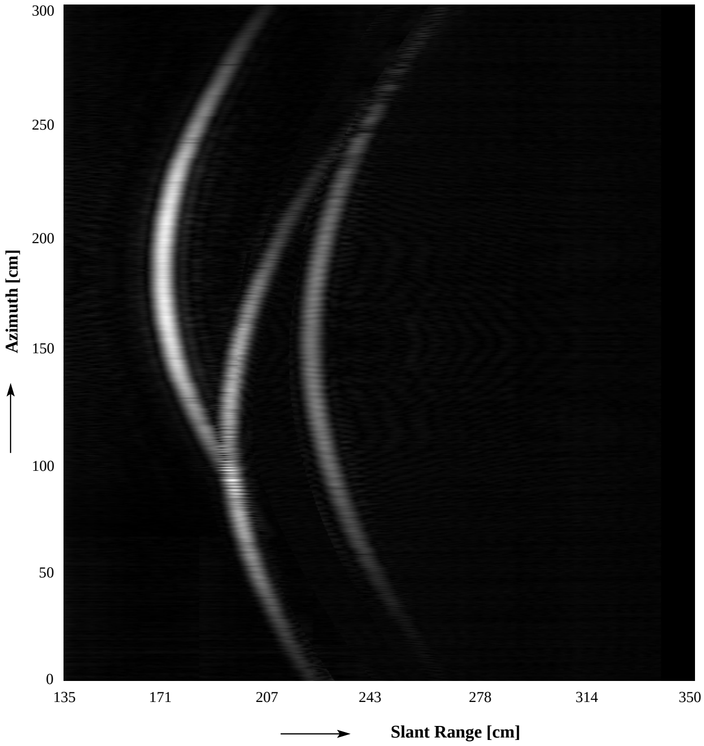

Figure 4.28: *Inverse synthetic aperture sonar range compressed data matrix prior to azimuth compression of line 1.*

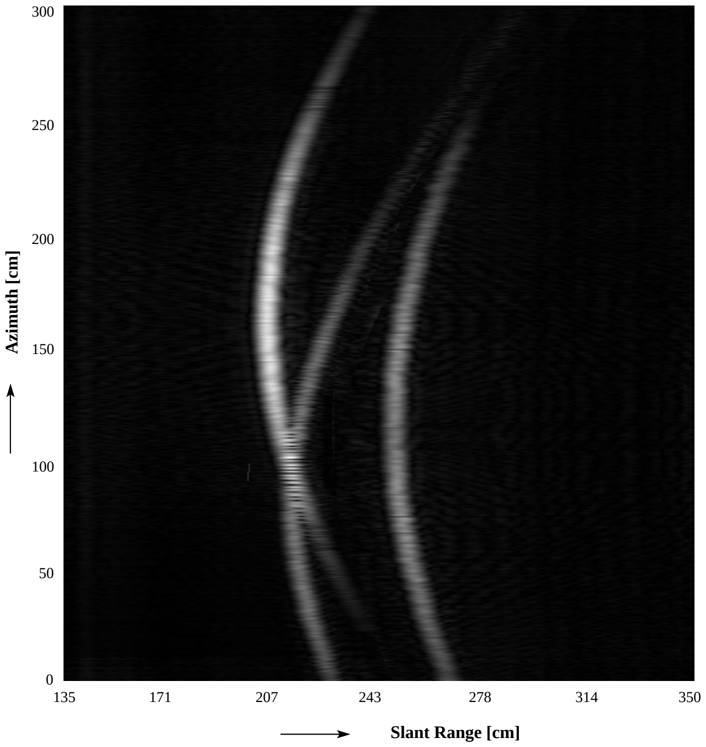

Figure 4.29: *Inverse synthetic aperture sonar range compressed data matrix prior to azimuth compression of line 2.*

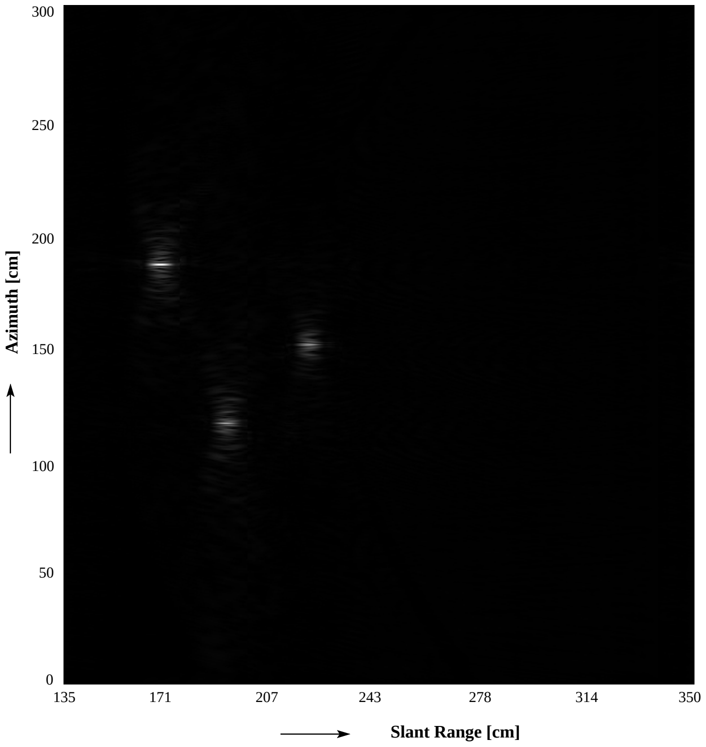

Figure 4.30: *Inverse synthetic aperture sonar azimuth compressed data matrix of line 1.*

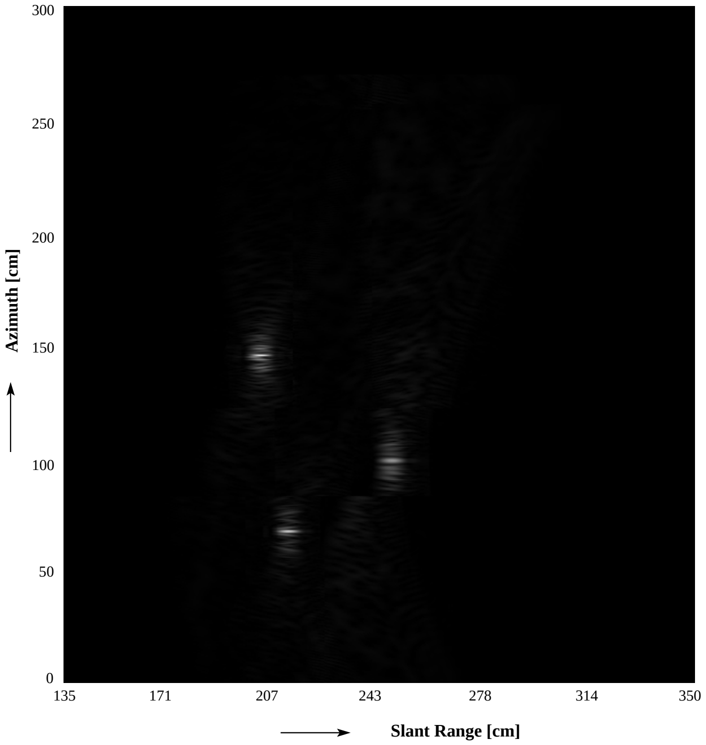

Figure 4.31: *Inverse synthetic aperture sonar azimuth compressed data matrix of line 2.*

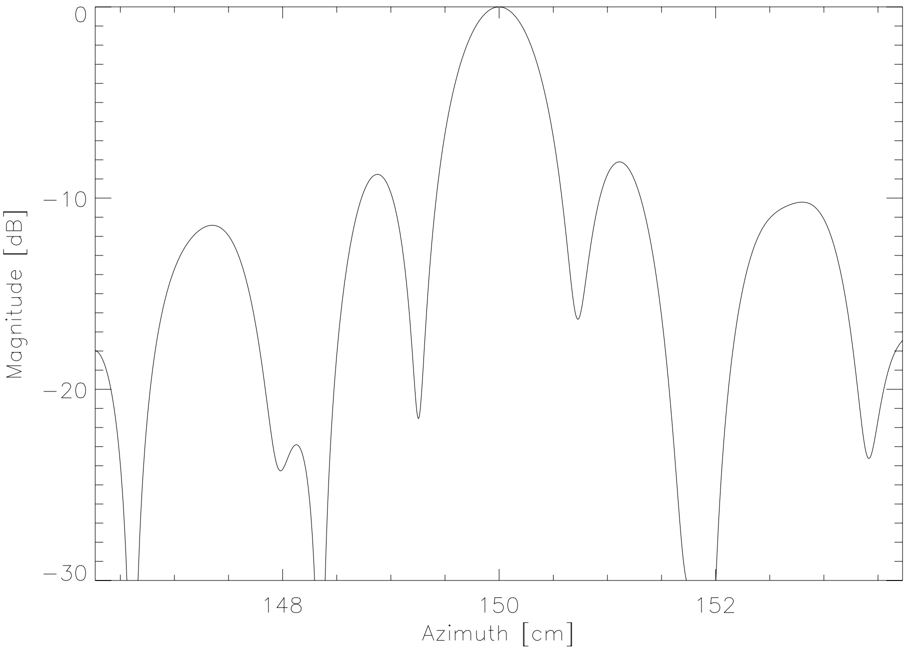

Figure 4.32: *Cross section of a single target in the azimuth direction after azimuth compression (dB plot).*

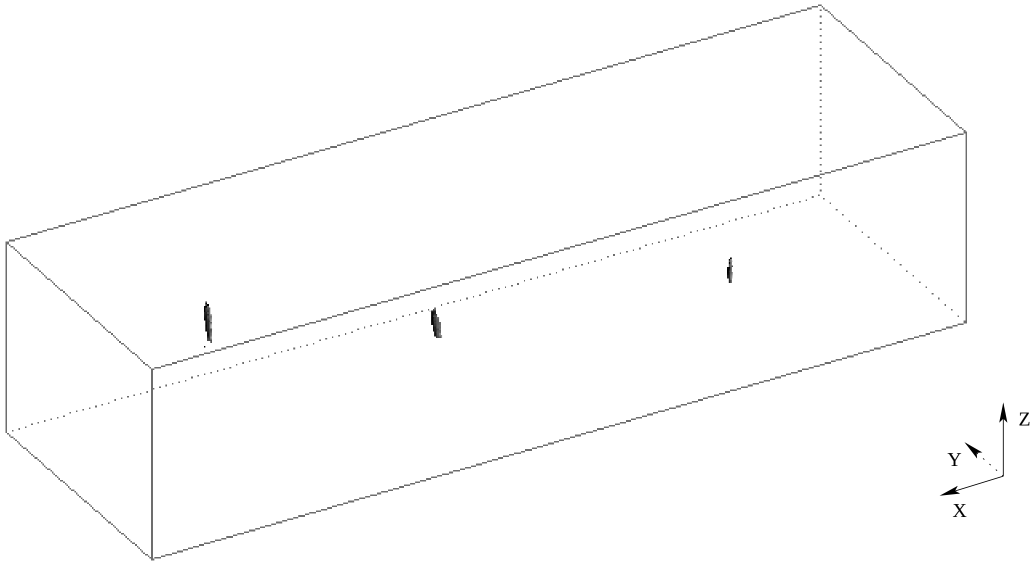

Figure 4.33: *Reconstructed 3-D image from two focused magnitude radar images taken from different view angles*.

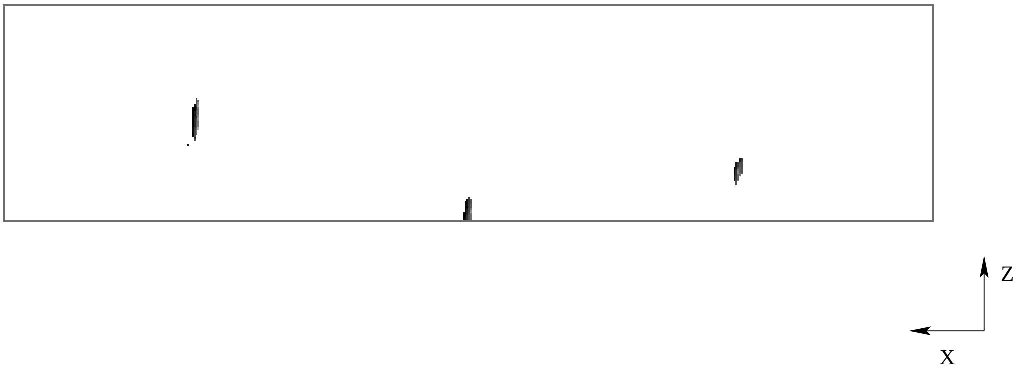

Figure 4.34: *X-Z projection of the reconstructed image.*

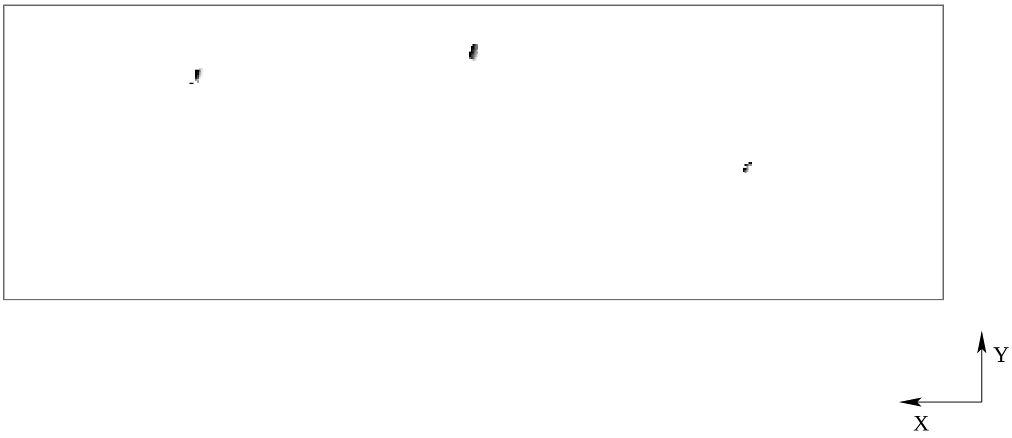

Figure 4.35: *X-Y projection of the reconstructed image.*

4.9 Real Acoustic Data Captured in a Water Tank[1]

4.9.1 Ultrasonic System in Water

The system consisted of a 25 mm diameter, 50 mm focal length broadband 750 kHz to 1.5 MHz ultrasonic transducer. A centre frequency of 1.0 MHz was chosen for the transmitted pulse, which travels at 1483 m/s in water (at water temperature $20°$C) (Zemansky, 1957). The corresponding wavelength is about 1.5 mm. At each station the transducer was rocked about its focal point (to simulate the broad axial beamwidth of the real radar) and the echoes were stacked to allow the angular coverage of the transducers. The data acquisition system is shown in Figure 4.36 and the transducers are mounted on the left side of the figure.

4.9.2 Ultrasonic Experimental Setup in Water

The experimental model is shown in the Figure 4.37. Four point targets made up of 6 mm diameter aluminium spheres were placed on the end of long thin pins. The mount for the spheres was composed of several sheets of perspex and contained a regular grid of holes to allow for the position of the pins to be changed. The mount for the spheres was placed at a $30°$ angle to the horizontal. The model was placed in a water-filled tank. Synthetic apertures were built up by collecting traces at 0.76 mm intervals along each line, satisfying the Nyquist criteria. The echoes were collected by scanning over the spheres in

---

[1] We are grateful to Prof. Iain Mason and Naomi Osman, for supplying this acoustic data from their test facility at Sydney University.

two lines angled at approximately 30^0 to each other. At each point of the transducers, the pulses were sent and received, the transducers were rocked about their focal point, and the received echos were stacked. The real acoustic data in water was captured in the acoustic experimental lab at Sydney University, Australia and sent to us for further processing.

4.9.3 Experimental Results

Close inspection reveals that the spheres give double echoes. The arrivals swing first positive and then negative in this instance (Mason et al., 2001). This may be because we are getting reflection from the front face of the sphere as well as from the inner wall. Figures 4.38 and 4.39 show the received pulses after stacking, captured in two lines, at an angle of 30^0 to each other. The received pulses shown in Figures 4.38 and 4.39 are at a centre frequency of 1.0 MHz. A very short pulse was transmitted and thus, no range compression filter was applied. The received real pulses were converted into analytical form by zeroing out the negative frequencies, and were subsequently basebanded by shifting the spectral component around zero. The basebanded analytical received pulses were then compressed in azimuth, using the time domain focusing algorithm. The two-way azimuth beamwidth was assumed to be 20^0. The azimuth compressed data matrices were shown in Figures 4.40 and 4.41. A dB plot across a single azimuth compressed target was shown in Figure 4.42. The 3-dB azimuth resolution was measured to be 2.09 mm using a 20° two-way azimuth beamwidth.

The reflection from the perspex sheet (shown in Figure 4.37) was removed from both the focused images before applying the 3-D reconstruction algorithm. The 3-D image was reconstructed using the afore mentioned algorithm (Section 4.4), which meant that we used the magnitude image from two lines as shown in Figure 4.43. An X-Y and X-Z projection of the reconstructed images are shown in Figures 4.44 and 4.45 respectively. The reconstructed grid spacing is taken as $\Delta x = 1.6\,$mm, $\Delta y = 1.7\,$mm and $\Delta z = 0.37\,$mm. Table 4.1 shows the comparison between the expected and achieved resolutions in range and azimuth, both for simulated as well as real experimental data for both air and water sonars.

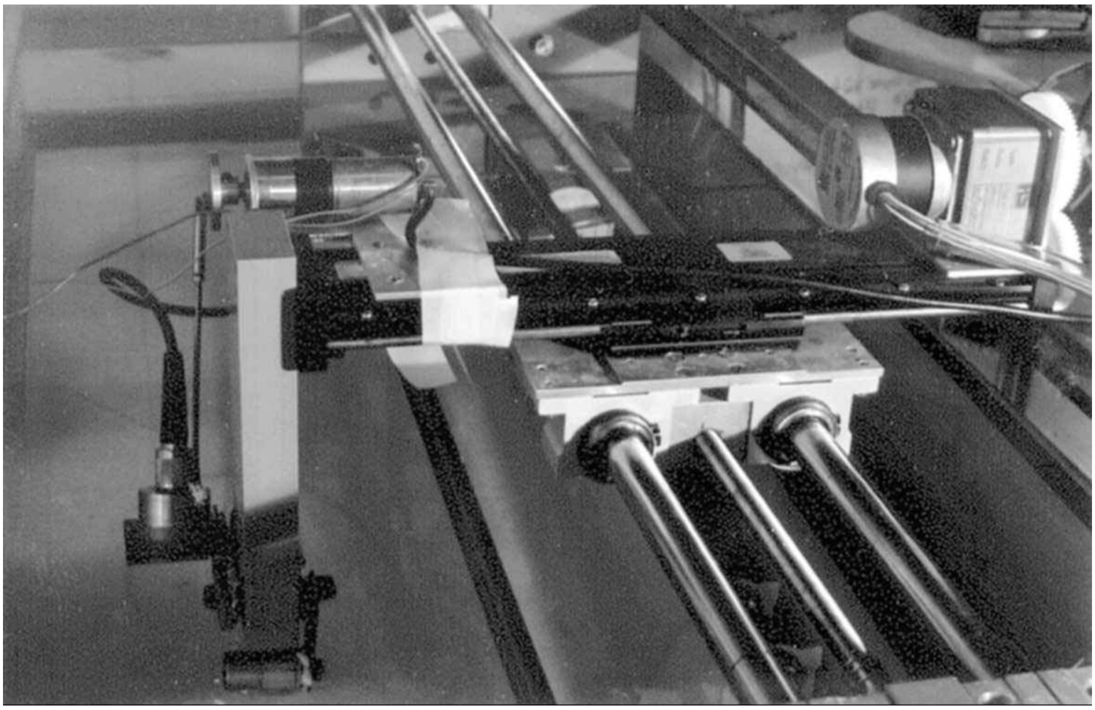

Figure 4.36: *Ultrasonic data acquisition system in water.*

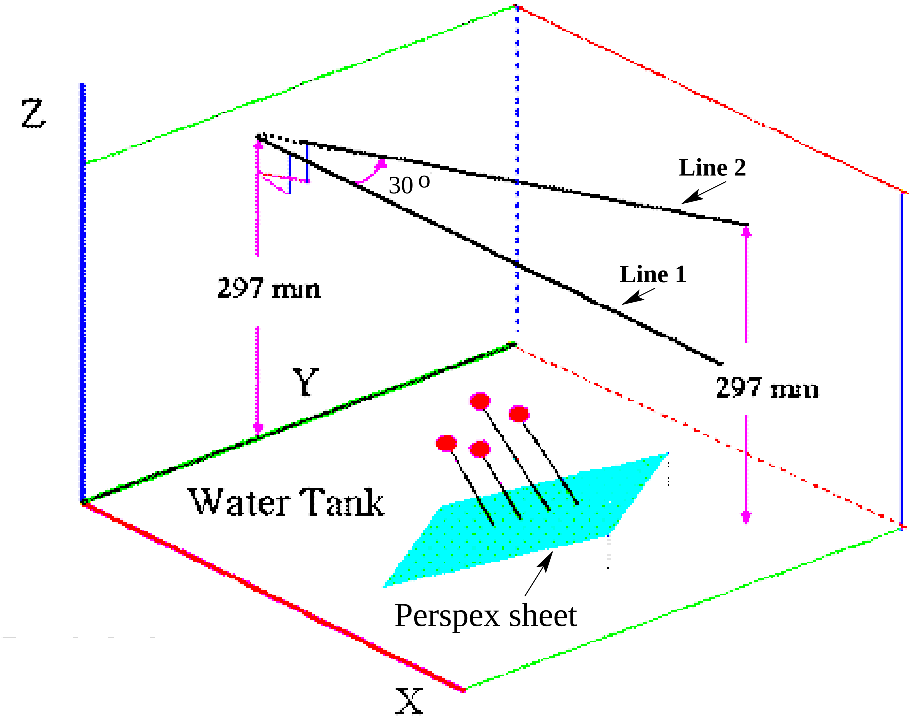

Figure 4.37: *Experimental synthetic aperture data capture model in the water tank.*

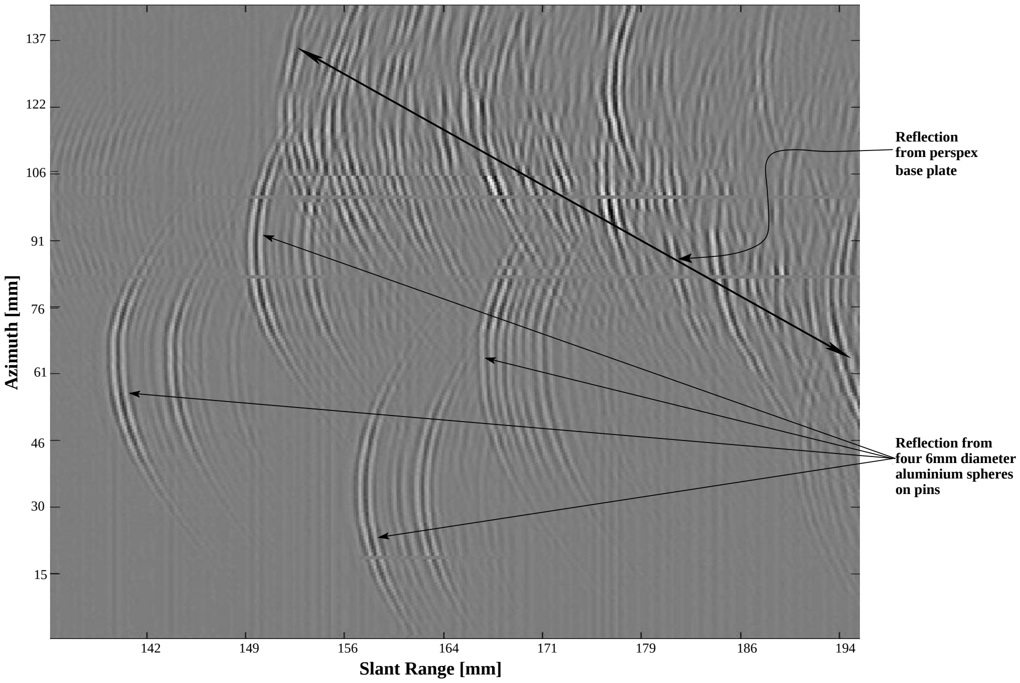

Figure 4.38: *Synthetic aperture sonar received real data matrix from line 1 prior to azimuth compression.*

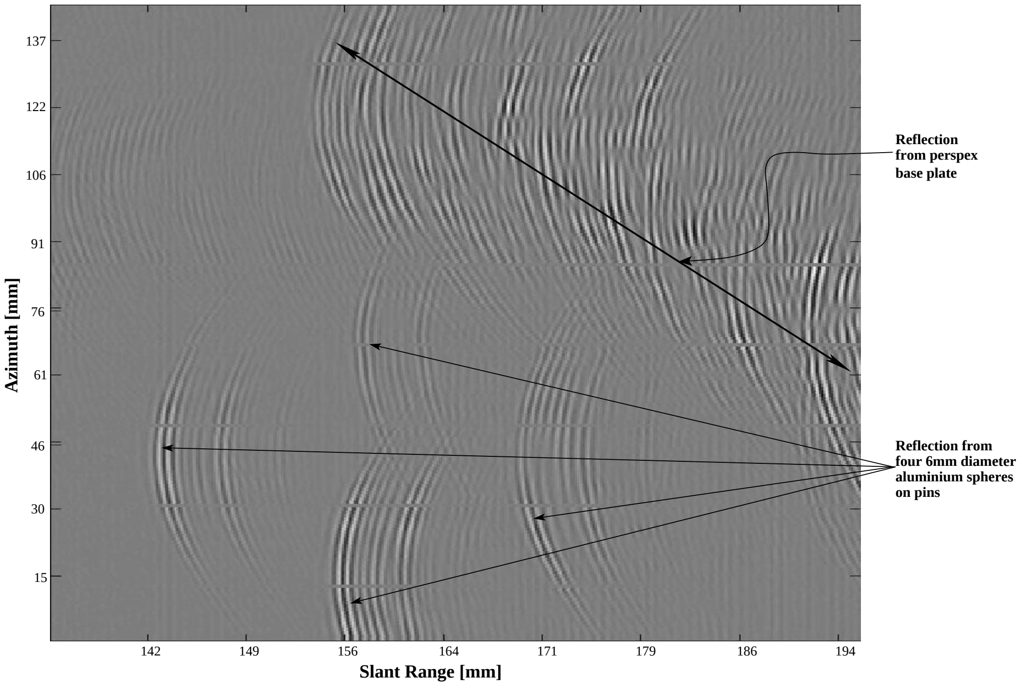

Figure 4.39: *Synthetic aperture sonar received real data matrix from line 2 prior to azimuth compression.*

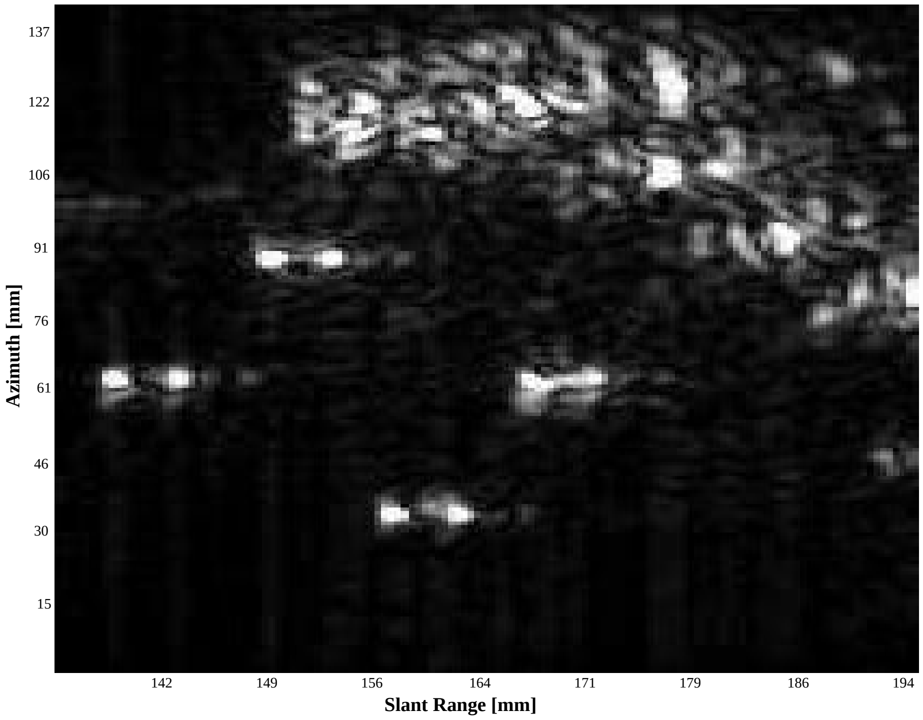

Figure 4.40: *Synthetic aperture sonar azimuth compressed data matrix of line 1.*

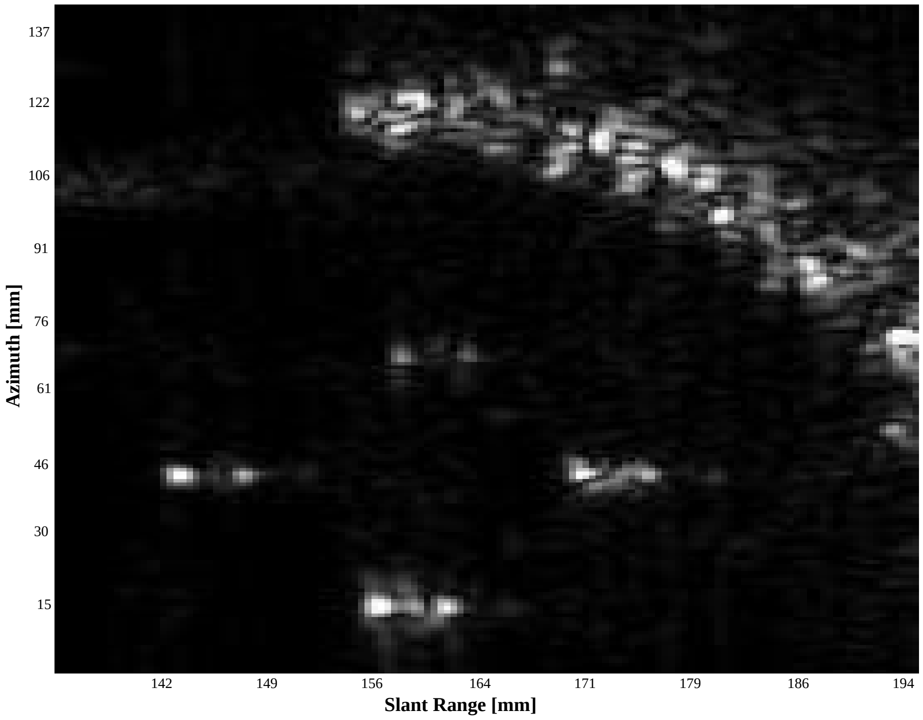

Figure 4.41: *Synthetic aperture sonar azimuth compressed data matrix of line 2.*

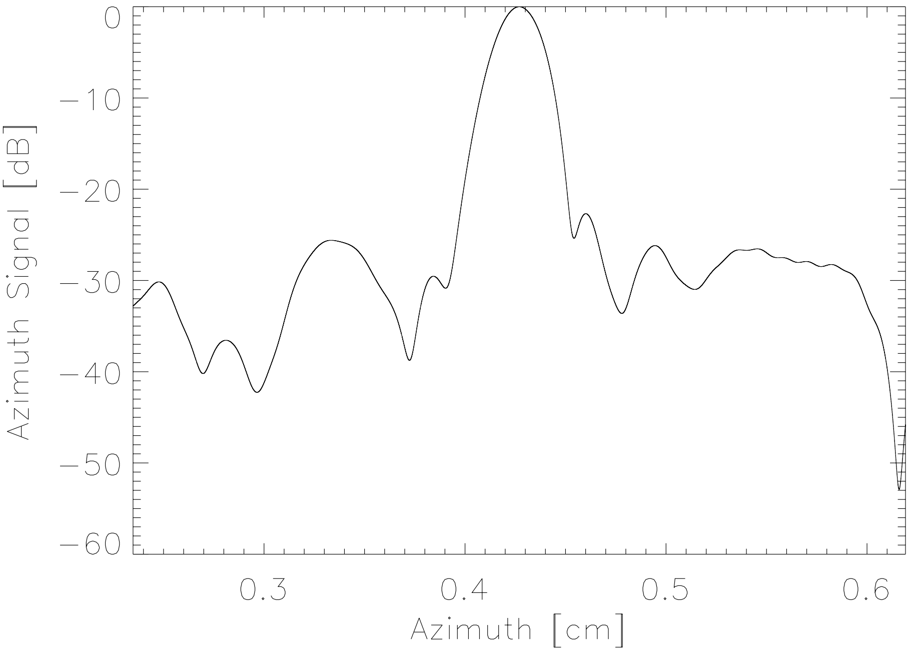

Figure 4.42: *Cross section of a single target in the azimuth direction after azimuth compression (dB plot).*

Figure 4.43: *Reconstructed 3-D image from two focused magnitude sonar images taken from different view angles in a water tank.*

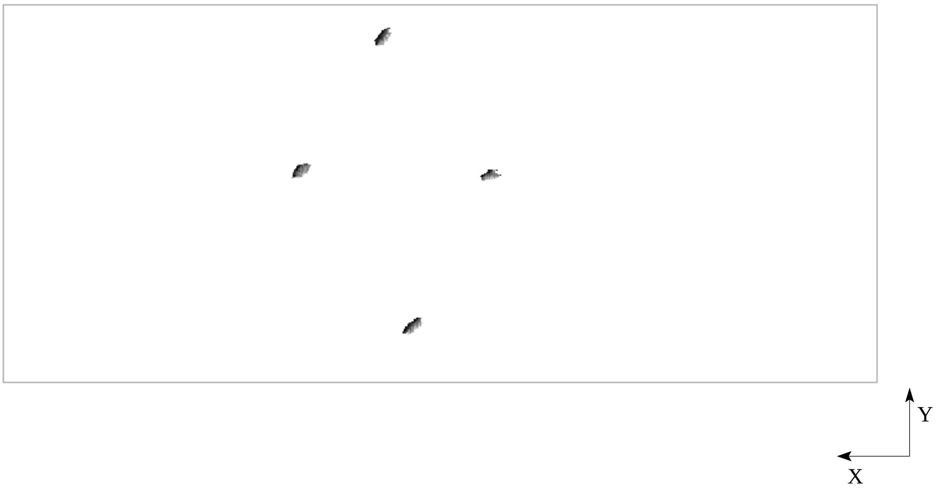

Figure 4.44: *X-Y projection of the reconstructed image.*

Figure 4.45: *X-Z projection of the reconstructed image.*

	Range Resolution		Azimuth Resolution	
	Expected	Measured	Expected	Measured
Simulation in air	5.53 cm	5.58 cm	0.55 cm	0.56 cm
Sonar experiment in air	5.55 cm	5.83 cm	0.55 cm	0.82 cm
Sonar experiment in water	short pulse	short pulse	1.90 mm	2.09 mm

Table 4.1: *3-dB range and azimuth resolution for simulated as well as real experiment.*

4.10 Summary

The process of using the SAR and ISAR (ISAS) image formation technique for achieving high azimuth resolution was discussed in this chapter. It was explained that range compression can be achieved via a standard matched filter process (for optimal SNR) or a deconvolution filter process (for optimal point target response). The use of a time domain focusing algorithm in a homogeneous medium for azimuth focusing was discussed in detail. This algorithm could easily be modified for focusing data acquired in layered media. In such a case, the two-way time delay and the synthetic aperture length would need to be calculated by using the electrical properties of the respective medium. In a real borehole radar experiment, the error between actual borehole geometry and measured borehole geometry should be less than $\frac{\lambda}{8}$ in order to obtain a good azimuth focused image. This focusing technique has accordingly been applied to both simulated borehole radar data and to real acoustic data captured in air and water. This focusing method is well suited for focusing small scale data captured in a deviating trajectory, with the assumption that the scene orientation is known from other survey data.

For the first time, an experiment was carried out, using an air-based 40kHz sonar system to emulate ISAR data in the context of real borehole measurements. In this regard, the method of designing a practical deconvolution filter was discussed. These techniques will be used thereafter to investigate the processing of real borehole radar data.

A 3-D reconstruction algorithm was developed herein by using magnitude images from multiple boreholes, and this algorithm was tested with simulation radar data as well as real acoustic data captured in air and water. In order to apply this reconstruction algorithm in a real borehole configuration, it is essential to calculate the grid spacing correctly. The sampling issue for 3-D reconstruction was consequently discussed in detail for a borehole trajectory fanning outward from the borehole centre. Lastly, it was discussed in detail how to solve the problem of rotational ambiguity that comes from using an omni-directional antenna, by using three non-collinear boreholes.

Chapter 5

Three-dimensional Borehole Radar Modelling Study using the Finite Difference Time Domain Method

5.1 Introduction

A borehole radar is an electromagnetic tool for detecting discontinuities in rock formations. Deployment of borehole radar to image the subsurface orebody poses a particular challenge for the engineering community due to the high attenuation of EM waves in the host rock. The modelling of transient electromagnetic wave propagation is very important for a wide range of applications, such as geophysical prospecting, radar scattering, well logging and environment testing. The finite difference time domain (FDTD) method, introduced by K.S. Yee (1966), is a full-wave, dynamic, and powerful tool for solving Maxwell's equations. The FDTD method is furthermore ideal for modelling transient EM fields in inhomogeneous media. Complex geological and antenna structures fit relatively easily into the finite-difference grid, and absorbing boundary conditions can truncate the grid to simulate an infinite region (Chen and Oristaglio, 2002). Finite-difference modelling data provides estimates of the distributions of velocity and the attenuation of EM waves in the media (Wang and McMechan, 2002). In the process of migration/focusing of the borehole radar data, this propagation velocity information is very useful.

In Chapters 3 and 4 we investigated two different types of 3-D borehole radar imaging techniques. In real borehole radar measurements, the media through which the EM wave propagates are often complex in nature, and the shape of the target orebody also tends to be different from the ideal (e.g., point, plane, cylinder and sphere). Modelling transient electromagnetic (TEM) problems in three dimensions is important for understanding the physics of observed responses, and for providing insight for data interpretation (Wang and Hohmann, 1993). Modelling can also be applied to assist in the design of antenna systems that are not affected by conductive borehole water (Vogt, 2004).This modelling will help us to better understand the implementation of the migration/focusing techniques on real borehole radar data and the multiple borehole 3-D image reconstruction algorithm.

In this chapter, we will first discuss the implementation issue of a 3-D FDTD code of modelling EM wave propagation in a conductive medium by using the Uniaxial Perfectly Matched Layer (UPML) absorbing boundary condition, followed by the application of our code in three subsurface borehole EM propagation examples in different geological settings, namely: borehole EM wave propagation in a sedimentary layer, an EM wave reflection from a geological reverse fault, and reflection from pothole-type structure. The effect of host rock conductivity on th reflected radar traces will be discussed. Thereafter, the effects of borehole mud and the size of the borehole on radar traces will be discussed.

The implementation of a parallel version of the 3-D FDTD C code to improve both the processing speed and memory requirements by using Parallel Virtual Machine (PVM) as middleware running on a Beowulf-type Linux cluster will be discussed. Thereafter, a comprasion between a serial FDTD simulator and a parallel simulator will be presented.

Finally, this Chapter will conclude with a summary of the results achieved via a series of simulation experiments.

5.2 A Uniaxial Perfectly Matched Layer

One of the greatest challenges faced by the FDTD method is the efficient and accurate solution of electromagnetic wave interaction problems in unbounded regions. Absorbing Boundary Conditions (ABCs) are usually designed for mesh truncation on an open structure. An ideal ABC will not result in any reflection of an electromagnetic wave under any frequency and with any incident angle. Although there are many methods used for open region truncation, the most successful among them is the Perfectly Matched Layer (PML), introduced by Berenger (1994). Three main kinds of PML formulation currently exist:

1. Berenger split field formulation;
2. Stretched coordinate formulation;
3. Uniaxial anisotropic formulation.

The first of these, Berenger's PML method, provides an efficient and highly accurate means of truncating the FDTD lattice. The limitations of Berenger's PML, however, are that it is based on a non-Maxwellian formulation, that there is no physical insight for application to general problems, and lastly that, due to field splitting, it uses additional memory and significant CPU power.

The original split-field formulation was thereafter restated in a stretched-coordinate form. This was first independently introduced by Chew and Weedon (1994) and Rappaport (1995). This form allows the use of the PML in cylindrical and spherical coordinate systems (Teixeira and Chew, 1997). The stretched-coordinate formulation was also based on a mathematical model.

Thirdly, an alternate form of Berenger's split-field formulation was first introduced by Sacks et al. (1995), using a uniaxial anisotropic media with magnetic and electric permittivity tensors. This was originally formulated for frequency-domain methods, and then extended to the FDTD method by Gedney (1996a,b). This PML formulation, which is based on a uniaxial anisotropic medium (UPML) also provides perfect absorption and is directly based on Maxwell's equations. The application of this formulation to the FDTD method is computationally more efficient because it is in a form that avoids field splitting. This formulation can also be extended to non-orthogonal and unstructured grid techniques (Gedney, 1996*a*). Ziolkowski (1997) has investigated such a UPML medium to give physical insight into the use of such material. Because of its true physical significance, it is easy to implement in the FDTD lattice space. Consequently, this UPML formulation is implemented in our present 3-D FDTD code.

5.2.1 Performance of the Uniaxial Perfectly Matched layer as an Absorbing Boundary Condition

Theoretically, there should be zero reflection at a UPML interface to the continuously impinging electromagnetic waves for any angle of incidence, polarization or frequency. However, in a discrete FDTD lattice space, two assumptions are made, which prevent the UPML from being a perfect absorber. Firstly, there will be a reflection error due to finite spatial sampling in a discrete FDTD representation. Secondly, the PML must have a finite thickness layer and must be terminated by the outer lattice boundary. If the outer boundary is a perfectly electric conductor (PEC) wall, then the incident field would be reflected back into the primary FDTD region. For a PML with thickness d, the *reflection error,* a nonphysical reflection due to the PEC wall that backs the PML (Gedney and Taflove, 1998), can be computed as

$$R(\theta) = e^{-2\sigma_x \eta d \cos(\theta)} \tag{5.1}$$

where θ is the incident angle relative to the x-directed surface normal, d is the PML thickness, and σ_x and η are the PML's characteristic conductivity and wave impedance respectively.

Berenger postulated that the largest reflection error would occur at the PML interface (Berenger, 1996*b*, 1997). He furthermore proposed that the error could be reduced by scaling the PML parameters along the PML axis. The most successful way of scaling the UPML parameters is by polynomial scaling with depth (Berenger, 1996*b*), as

$$\sigma_x(x) = \left(\frac{x}{d}\right)^m \cdot \sigma_{x,max} \qquad\qquad k_x(x) = 1 + (k_{x,max} - 1) \cdot \left(\frac{x}{d}\right)^m \tag{5.2}$$

where m is the order of the polynomial, $\sigma_{x,max}$ and $k_{x,max}$ are the x-normal plane maximum values of σ_x and k_x at $x = d$ respectively.

Substituting Equation 5.2 into 5.1 yields

$$R(\theta) = e^{-2\sigma_{x,max}\eta d\cos(\theta)/(m+1)} \tag{5.3}$$

Through extensive experimental studies, demonstrated by Gedney (1996*a*), it has been found that for a broad range of applications an optimal choice for a 10-cell thick polynomially scaled PML is $R(0) \approx e^{-16}$, and for a 5-cell thick PML it is $R(0) \approx e^{-8}$. This leads to an optimal choice for σ_{max} as

$$\sigma_{opt} \approx \frac{m+1}{150\pi \triangle \sqrt{\epsilon_r}} \tag{5.4}$$

where $\triangle$ is the spatial discretization (in meters) along the normal axis of the PML layer, m is the order of the polynomial and ϵ_r is the effective relative permittivity for the inhomogeneous medium. This specific expression of σ_{opt} has been used in this thesis with regard to FDTD simulation studies.

5.2.2 Implementation: Update Equations in a Conductive Medium

A brief introduction to the FDTD method is presented in Appendix B. A summary of the key technical points required to implement the UPML boundary absorber in the present 3-D FDTD code is presented here. The detail description will be found in Gedney and Taflove (1998).

Maxwell's curl equations in a conductive medium can be written (Gedney and Taflove, 1998) as

$$\nabla \times \vec{E} = -j\omega\mu \overline{\overline{s}} \vec{H} \tag{5.5}$$

$$\nabla \times \vec{H} = j\omega\epsilon_0 \left(\epsilon_r + \frac{\sigma}{j\omega\epsilon_0}\right) \overset{=}{s}\ \vec{E} \tag{5.6}$$

where

$\vec{E}$ and $\vec{H}$	is the electric and magnetic field
$\omega = 2\pi f$	is the angular frequency
$\mu = \mu_0\mu_r$	is the magnetic permeability of the medium
ϵ_0	is the permittivity in free space
ϵ_r	is the relative permittivity of the medium
σ	is the conductivity of the medium

The conductive material is modelled as $\left(\epsilon_r + \frac{\sigma}{j\omega\epsilon_0}\right)$ and $\overset{=}{s}$ is the diagonal tensor defined by

$$\overset{=}{s} = \begin{bmatrix} \frac{s_y s_z}{s_x} & 0 & 0 \\ 0 & \frac{s_x s_z}{s_y} & 0 \\ 0 & 0 & \frac{s_x s_y}{s_z} \end{bmatrix} \tag{5.7}$$

Using non-unity real part, the multiplicative components of the diagonal elements of $\overset{=}{s}$ are given as

$$s_x = k_x + \frac{\sigma_x}{j\omega\epsilon_0}; \qquad s_y = k_y + \frac{\sigma_y}{j\omega\epsilon_0}; \qquad s_z = k_z + \frac{\sigma_z}{j\omega\epsilon_0} \tag{5.8}$$

where s_x, s_y and s_z are associated with the x, y, and z-normal planes respectively.

Using Equation 5.7, Ampere's Law in a matched UPML is expressed as

$$\begin{bmatrix} \frac{\delta Hz}{\delta y} - \frac{\delta Hy}{\delta z} \\ \frac{\delta Hx}{\delta z} - \frac{\delta Hz}{\delta x} \\ \frac{\delta Hy}{\delta x} - \frac{\delta Hx}{\delta y} \end{bmatrix} = j\omega\epsilon_0 \left(\epsilon_r + \frac{\sigma}{j\omega\epsilon_0}\right) \begin{bmatrix} \frac{s_y s_z}{s_x} & 0 & 0 \\ 0 & \frac{s_x s_z}{s_y} & 0 \\ 0 & 0 & \frac{s_x s_y}{s_z} \end{bmatrix} \begin{bmatrix} E_x \\ E_y \\ E_z \end{bmatrix} \tag{5.9}$$

where

$E_{x,y,z}$	are the x,y and z component of the electrical field
$H_{x,y,z}$	are the x,y and z component of the magnetic field

We can now introduce the fields $\overrightarrow{D}$ and $\overrightarrow{P}$, where

$$\begin{bmatrix} P_x \\ P_y \\ P_z \end{bmatrix} = \epsilon_0 \begin{bmatrix} \frac{s_z}{s_x} \\ \frac{s_x}{s_y} \\ \frac{s_y}{s_z} \end{bmatrix} \begin{bmatrix} E_x \\ E_y \\ E_z \end{bmatrix} \tag{5.10}$$

and

$$\begin{bmatrix} D_x \\ D_y \\ D_z \end{bmatrix} = \left(\epsilon_r + \frac{\sigma}{j\omega\epsilon_0} \right) \begin{bmatrix} P_x \\ P_y \\ P_z \end{bmatrix} \tag{5.11}$$

The partial derivatives in both time and space domains can then be discretized on the standard Yee lattice (Yee, 1966). Time averaging is applied according to the semi-implicit scheme as

$$\frac{\sigma_x}{\epsilon_0} D_x = \frac{\sigma_x}{\epsilon_0} \left(\frac{D_x|^{n+1}_{i+\frac{1}{2},j,k} + D_x|^{n}_{i+\frac{1}{2},j,k}}{2} \right) \tag{5.12}$$

where n is the time index and i, j, k is the $x, y, z-$direction spatial index.

The detailed derivation of the fields $\overrightarrow{D}$, $\overrightarrow{P}$ and $\overrightarrow{E}$ can be found in Gedney and Taflove (1998). Here, we are merely presenting the final expressions of the x-component of the electric fields $\overrightarrow{D}$, $\overrightarrow{P}$ and $\overrightarrow{E}$ and the magnetic fields $\overrightarrow{B}$ and $\overrightarrow{H}$.

By using 5.10 and 5.11 in Equation 5.9, we obtain D_x as

$$\begin{aligned} D_x|^{n+1}_{i+\frac{1}{2},j,k} \quad = \quad & \left[\frac{2k_y(j)\,\epsilon_0 - \sigma_y(j)\,\triangle t}{2k_y(j)\,\epsilon_0 + \sigma_y(j)\,\triangle t} \right] D_x|^{n}_{i+\frac{1}{2},j,k} + \left[\frac{2\epsilon_0 \triangle t}{2k_y(j)\,\epsilon_0 + \sigma_y(j)\,\triangle t} \right] \cdot \\ & \left[\frac{H_z|^{n+\frac{1}{2}}_{i+\frac{1}{2},j+\frac{1}{2},k} - H_z|^{n+\frac{1}{2}}_{i+\frac{1}{2},j-\frac{1}{2},k}}{\triangle y} - \frac{H_y|^{n+\frac{1}{2}}_{i+\frac{1}{2},j,k+\frac{1}{2}} - H_y|^{n+\frac{1}{2}}_{i+\frac{1}{2},j,k-\frac{1}{2}}}{\triangle z} \right] \end{aligned} \tag{5.13}$$

where

$\triangle t$	is the time increment.
$\triangle y$ and $\triangle z$	are the grid sizes in the y and z direction.

The P_x component is obtained from Equation 5.11 as

$$P_x|^{n+1}_{i+\frac{1}{2},j,k} \quad = \quad \left[\frac{2\epsilon_0\epsilon_r - \sigma\triangle t}{2\epsilon_0\epsilon_r + \sigma\triangle t} \right] P_x|^{n}_{i+\frac{1}{2},j,k} + \left[\frac{2\epsilon_0}{2\epsilon_0\epsilon_r + \sigma\triangle t} \right] \cdot$$

$$\left[D_x\big|^{n+1}_{i+\frac{1}{2},j,k} - D_x\big|^{n}_{i+\frac{1}{2},j,k} \right] \tag{5.14}$$

Finally, the E_x component of the electric field is obtained from Equation 5.10 as

$$\begin{aligned} E_x\big|^{n+1}_{i+\frac{1}{2},j,k} = {} & \left[\frac{2k_z\left(k\right)\epsilon_0 - \sigma_z\left(k\right)\triangle t}{2k_z\left(k\right)\epsilon_0 + \sigma_z\left(k\right)\triangle t}\right] E_x\big|^{n}_{i+\frac{1}{2},j,k} + \left[\frac{1}{2k_z\left(k\right)\epsilon_0 + \sigma_z\left(k\right)\triangle t}\right] \cdot \\ & \left[\left(2k_x\left(i+\frac{1}{2}\right)\epsilon_0 + \sigma_x\left(i+\frac{1}{2}\right)\triangle t\right) P_x\big|^{n+1}_{i+\frac{1}{2},j,k} - \right. \\ & \left. \left(2k_x\left(i+\frac{1}{2}\right)\epsilon_0 - \sigma_x\left(i+\frac{1}{2}\right)\triangle t\right) P_x\big|^{n}_{i+\frac{1}{2},j,k} \right] \end{aligned} \tag{5.15}$$

A similar expression can also be derived for the E_y and E_z field components.

In a similar fashion, using the curl Equation 5.5 of the electric field, the B_x and H_x components are obtained as

$$\begin{aligned} B_x\big|^{n+\frac{1}{2}}_{i,j+\frac{1}{2},k+\frac{1}{2}} = {} & \left[\frac{2k_y\left(j+\frac{1}{2}\right)\epsilon_0 - \sigma_y\left(j+\frac{1}{2}\right)\triangle t}{2k_y\left(j+\frac{1}{2}\right)\epsilon_0 + \sigma_y\left(j+\frac{1}{2}\right)\triangle t}\right] B_x\big|^{n-\frac{1}{2}}_{i,j+\frac{1}{2},k+\frac{1}{2}} + \\ & \left[\frac{2\epsilon_0 \triangle t}{2k_y\left(j+\frac{1}{2}\right)\epsilon_0 + \sigma_y\left(j+\frac{1}{2}\right)\triangle t}\right] \cdot \\ & \left[\frac{E_y\big|^{n+1}_{i,j+\frac{1}{2},k+1} - E_y\big|^{n+1}_{i,j+\frac{1}{2},k}}{\triangle z} - \frac{E_z\big|^{n+1}_{i,j+1,k+\frac{1}{2}} - E_z\big|^{n}_{i,j,k-\frac{1}{2}}}{\triangle y}\right] \end{aligned} \tag{5.16}$$

where $B_x = \mu\left(\frac{s_z}{s_x}\right) H_x$

$$\begin{aligned} H_x\big|^{n+\frac{1}{2}}_{i,j+\frac{1}{2},k+\frac{1}{2}} = {} & \left[\frac{2k_z\left(k+\frac{1}{2}\right)\epsilon_0 - \sigma_z\left(k+\frac{1}{2}\right)\triangle t}{2k_z\left(k+\frac{1}{2}\right)\epsilon_0 + \sigma_z\left(k+\frac{1}{2}\right)\triangle t}\right] H_x\big|^{n-\frac{1}{2}}_{i,j+\frac{1}{2},k+\frac{1}{2}} + \\ & \left[\frac{1}{\mu\left(2k_z(k+\frac{1}{2})\epsilon_0 + \sigma_z(k+\frac{1}{2})\triangle t\right)}\right] \cdot \\ & \left[\left(2k_x\left(i\right)\epsilon_0 + \sigma_x\left(i\right)\triangle t\right) B_x\big|^{n+\frac{1}{2}}_{i,j+\frac{1}{2},k+\frac{1}{2}} - \right. \\ & \left. \left(2k_x\left(i\right)\epsilon_0 - \sigma_x\left(i\right)\triangle t\right) B_x\big|^{n-\frac{1}{2}}_{i,j+\frac{1}{2},k+\frac{1}{2}} \right] \end{aligned} \tag{5.17}$$

A similar expression can also be derived for the H_y and H_z field components.

In this way, the update equations can be applied in the entire lattice space. Inside the computational space, the values of $\sigma_{x,y,z}$ will be zero and the $k_{x,y,z}$ values will be one. Careful consideration should thus be paid to the values of $k_{x,y,z}$ and $\sigma_{x,y,z}$ when updating the UPML parameters. For example, in equation 5.15, k_z and σ_z must be calculated at $k \cdot \triangle z$, and k_x and σ_x at $\left(i + \frac{1}{2}\right) \cdot \triangle x$ physical coordinate space.

It is important to properly implement the UPML parameters at the boundaries in order to get the desired result. Using this polynomial scaling of UPML parameters, the final expressions for σ_z, k_z, $\sigma_x$and k_x of Equation 5.15 on the left side of the PML are given as

$$\sigma_z(i) = \left[\frac{N-i}{N}\right]^m \cdot \sigma_{z,max} \tag{5.18}$$

$$\sigma_x(i) = \left[\frac{N-i-\frac{1}{2}}{N}\right]^m \cdot \sigma_{x,max} \tag{5.19}$$

$$k_z(i) = 1 + (k_{z,max} - 1) \cdot \left[\frac{N-i}{N}\right]^m \tag{5.20}$$

$$k_x(i) = 1 + (k_{x,max} - 1) \cdot \left[\frac{N-i-\frac{1}{2}}{N}\right]^m \tag{5.21}$$

where N is the number of the PML-cell and *i* = 0,1,2,3...N-1

From Equation 5.18, we can thus see that the value of σ_z is zero at $x = 0$, the surface of the PML, and maximum $\sigma_{z,max}$ at $x = d$, the PEC outer boundary. The other UPML parameters should be calculated in a similar fashion.

5.3 Finite Difference Time Domain Modelling of Borehole Radar Imaging in a Conductive Medium

To test the accuracy of our implemented code, a 2-D simulation study was conducted (see Appendix C), and the achieved results were compared to the published result (Gedney and Taflove, 1998). To show the application of our FDTD code in different geological settings, we have used our 3-D FDTD code to simulate two types of geological settings. As the 3-D FDTD code uses a rectangular grid, the cylindrical borehole surface was modelled by an averaged staircase approximation. The materials used in the simulation model are homogeneous and isotropic, and the electromagnetic properties are not frequency dependent. The source function in all our present FDTD simulations is the first derivative of the Blackman-Harris window function (Harris, 1978; Chen et al., 1997), which is given by

$$f(t) = \begin{cases} \Sigma_{n=0}^{3} a_n \cos\left(\frac{2n\pi t}{T}\right) & 0 < t < T \\ 0 & \text{otherwise} \end{cases} \tag{5.22}$$

where T is the duration of the source function and is given by

$$T = \frac{1.55}{\mathrm{f}_c} \tag{5.23}$$

where f_c is the centre frequency.

The co-efficients used are

$$\begin{aligned} a_0 &= 0.35322222 \\ a_1 &= -0.488 \\ a_2 &= 0.145 \\ a_3 &= 0.010222222 \end{aligned} \tag{5.24}$$

The co-efficients used here are slightly different from those used in the original Blackman-Harris window function (Harris, 1978) to make the pulse vanish completely after time period T (Chen et al., 1997). The source wavelet and the spectrum with a nominal frequency of 100 MHz and a centre frequency of around 80 MHz are shown in Figure 5.1.

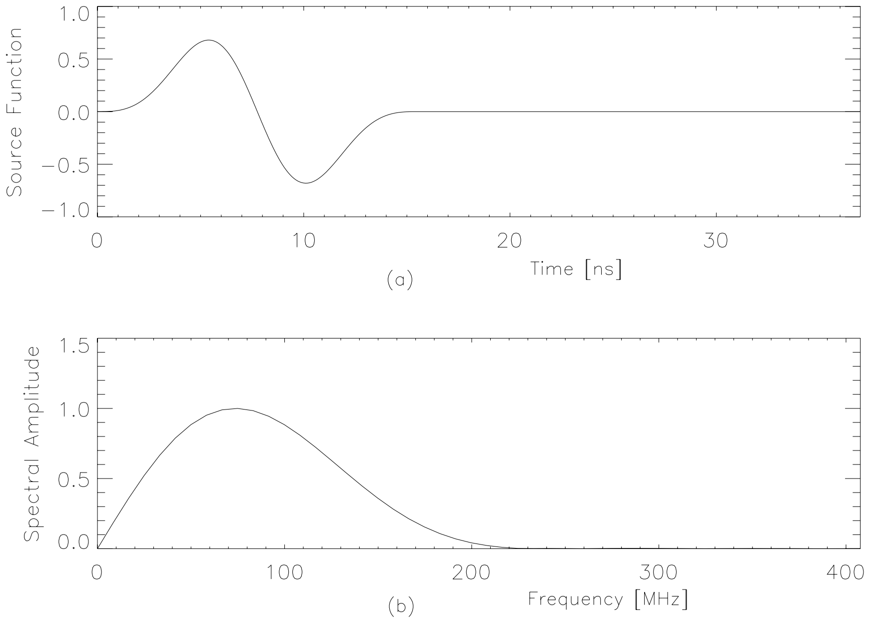

Figure 5.1: *The first derivative of the Blackman-Harris window function with a nominal frequency of 100 MHz: (a) Time-domain pulse; (b) Spectrum.*

5.4 Layered Media Electromagnetic Wave Propagation Study in Cross-well Borehole Radar Experiment

5.4.1 Introduction

During the past decade, there has been a huge increase in the application of ground penetrating radar to study near-surface sediments (Bristow and Jol, 2003; Bristow, 2004). Valuable information, such as water content of soil, depth of water table, buried objects and void detection can be obtained from this investigation. The study of subsurface stratigraphy using radar traces improves our understanding of the geometry of lithofacies and bounding surfaces, offsets across faults and active tectonics (Bristow, 2004). The cross-well radar method is a useful tool for understanding the mechanism of subsurface sediments in detail. Near-surface sediments often form layered structures. In the case of EM wave propagation through layered media, the radar traces are affected by the thickness of the sediment layer (e.g. clays and sands), and thus studying these changes in the traces can be used to quantify the subsurface stratigraphy (Wright et al., 1998). The layering of sediments moreover causes radar traces to propagate as a *guided wave*. A study has been conducted by Ellefsen (1999) to investigate the effects of layered sediments on the guided wave in cross-well radar data using a 3-D model. In his study, however, he did not consider the effects of the borehole and its filling medium on the radar traces. In this section, we have carried out a similar numerical simulation in a 3-D Cartesian coordinate system, using the same electrical parameters as used for sand and clay layers by Ellefsen. Some of the results have been compared with the results obtained by Ellefsen and are discussed below. A borehole has also been included in this simulation, and thus the effect of borehole mud and the size of the borehole have also been discussed.

5.4.2 Simulation Setup

Experiment 1

Figure 5.2 shows a plane view of the 3-D geological model of the sedimentary layer media used in this simulation study, where d is the distance between transmitting and receiving locations, h_s is the sand layer thickness and h_c is the clay layer thickness. The electrical properties of the materials are shown in Table 5.1. The model consisted of a sand layer ($\epsilon_r = 20$ and $\sigma = 0.1$ mS/m) with thickness $h_s = 4.0$ m surrounded by two clay layers ($\epsilon_r = 40$ and $\sigma = 0.5$ S/m), each with a thickness $h_c = 0.2$ m. The transmitting antenna was placed in the middle of the sand layer at $(x, y, z) = (0.5, 1.1, 2.2)$ m and was simulated by a vertical electric dipole (E_z) with infinitesimal length. The source function (a Blackman-Harris window function) with a nominal frequency of 100 MHz was added to the E_z component at the source location at each time step. The receiving locations were also situated in the middle of the sand layer at $(x, y, z) = (2.5, 1.1, 2.2)$ m, $(4.5, 1.1, 2.2)$ m and $(5.75, 1.1, 2.2)$ m. We only recorded the vertical component of the electric field (E_z) at the receiver locations. In some prototype tools, both the electric field and the magnetic field components were measured (Nickel et al., 1983).

The problem space was discretized into a size of 7.0 m, 2.2 m and 4.4 m in the $X-$,$Y-$,Z-directions respectively, with a uniform grid size of 0.016 m. The 10 PML layer was added outside the computational grid, and the resultant grid was 457 × 158 × 295 along the $X-$,$Y-$,Z-directions respectively. The PML was matched perfectly to the material ($\epsilon_r = 40$) in the $Z-$ direction, but the material profile was inhomogeneous along the $X-$ and $Y-$ directions. As explained in Appendix C, the sand layer ($\epsilon_r = 20$) occupied most of the spaces in the $X-$ and $Y-$ directions, and thus a value of $\epsilon_r = 24$ was chosen in these directions to calculate σ_{opt}, which is closer to the relative permittivity of the sand layer.

Experiment 2

Figure 5.3 shows the same plane of the 3-D sedimentary layered media, but this time with a 64 mm diameter borehole placed along the Z-axis at $(x, y) = (0.5, 1.1)$ m. The receiving locations were also situated in the middle of the sand layer at $(x, y, z) = (2.5, 1.1, 2.2)$ m, $(4.5, 1.1, 2.2)$ m and $(5.75, 1.1, 2.2)$ m. As before, the vertical component of the electric field (E_z) was recorded by the receivers. In this experiment, the sand-layer thickness was also $h_s = 4.0$ m and each clay layer thickness was $h_c = 0.2$ m. The borehole mud was also modelled as a wet clay, which has a relative dielectric permittivity $\epsilon_r = 70$ and conductivity $\sigma = 0.15$ S/m. The problem space was discretized with the same uniform grid size of 0.016 m to make it possible to compare the results with the previous experiment. A value of $\epsilon_r = 45$, close to the clay layer value, was chosen for the Z-direction and $\epsilon_r = 24$ was chosen for the X- and Y-directions to calculate the σ_{opt} value.

5.4.3 Results and Discussions of Experiment 1 and 2

Effect of layering on radar traces [without a borehole, experiment 1]

Figure 5.4 (relating to Figure 5.2) shows the received radar traces in the middle of the sand layer at different x positions with the sand layer thickness $h_s = 4.0$ m. The sand-clay layer model traces are compared with the homogeneous model (which has the properties

Electrical Parameter	Sand Layer	Clay Layer	Borehole Mud
Electrical conductivity, σ [mS/m]	0.1	500.0	150.0
Relative dielectric permittivity, ϵ_r	20.0	40.0	70.0
Relative magnetic permeability, μ_r	1.0	1.0	1.0

Table 5.1: *Electrical properties of the materials used in Experiment 1 and 2.*

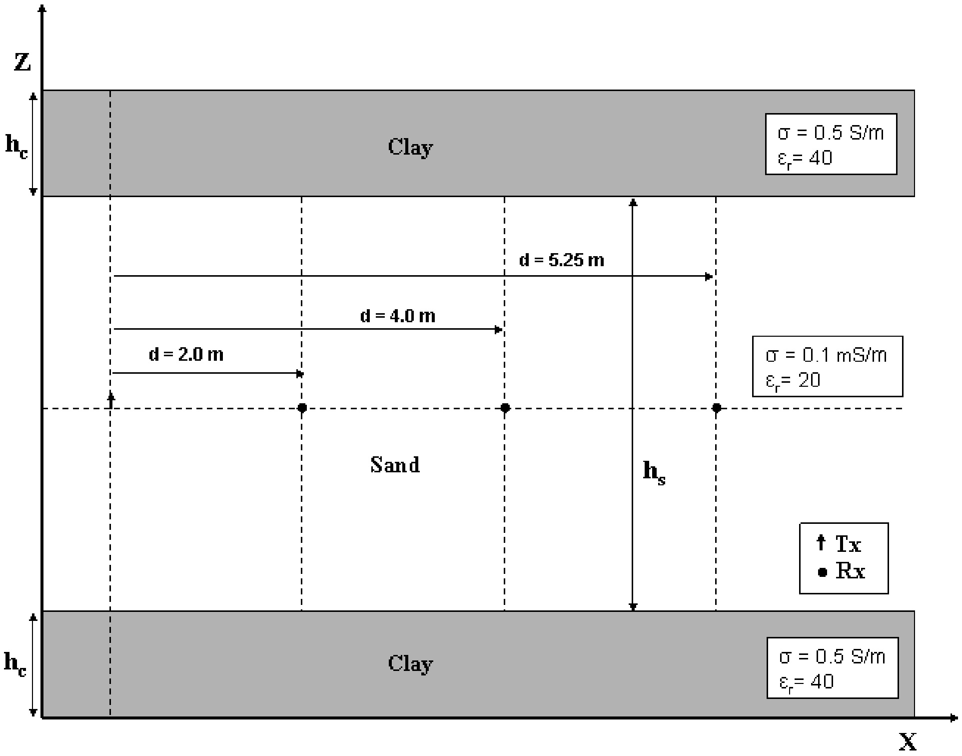

Figure 5.2: *A plane view of the 3-D sand-clay layer model.*

of the sand layer only). All the traces in Figure 5.4 have the same ranges on the axes, allowing relative amplitudes and time locations of the pulses to be compared. There are three different types of waves visible on the radar traces. The first of these, the *direct wave,* travels directly from the transmitter to the receiver location. Thereafter, the *first reflected wave,* which is the superposition of the reflected wave from the top and the bottom of the sand-clay layer. Lastly, there is the *second reflected wave,* which is the superposition of the reflected wave from the top and the bottom of the sand-clay layer and from the bottom and the top of the sand-clay layer. It is noted that the shape of the direct wave is not identical to the injected waveform (first derivative of the Blackman-Harris

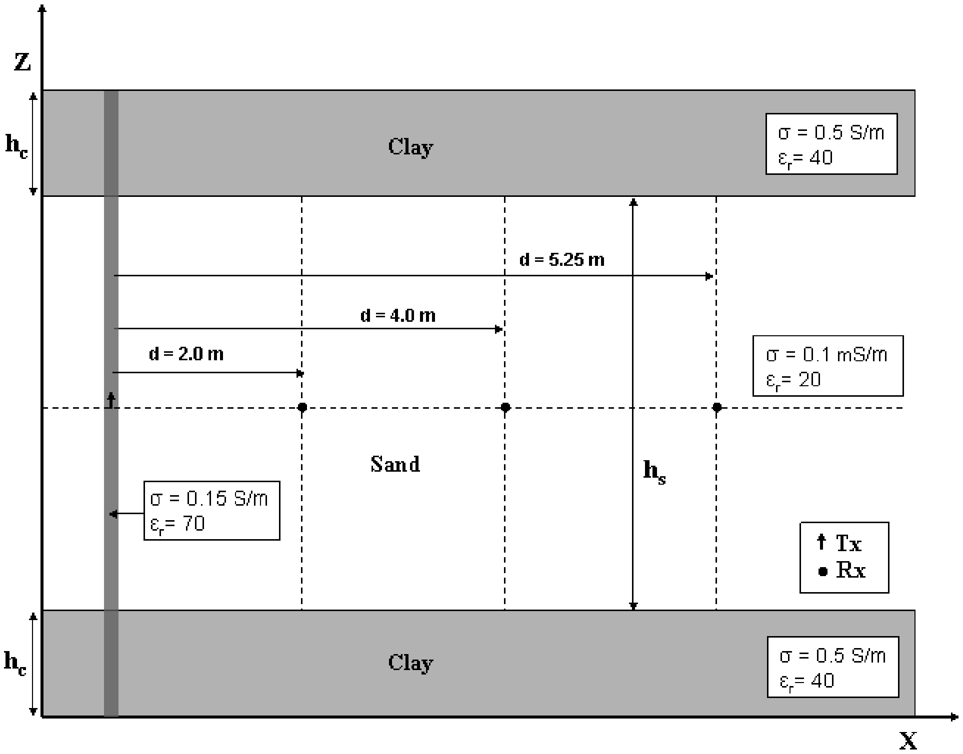

Figure 5.3: *A plane view of the 3-D sand-clay layer model with a borehole at the transmitter location.*

window function), as it changes shape as it propagates through the lossy medium. As the distance between the transmitter and the receiver location increases, the amplitude of the received traces decreases. This is due to radiation losses and also due to attenuation of the wave in the sand layer.

Figure 5.5 shows the radar traces obtained by Ellefsen (1999) in his 3-D numerical experiment. In our 3-D simulation experiment, the electrical property of the materials are the same but the source wavelet is different. A comparision of the radar trace of Figure 5.4(c) with the third trace from the top of Figure 5.5 reveals that the same three kinds of waves are also visible in trace 5.4(c) which verifies the accuracy of our modelling study. In our 3-D simulation model, both the transmitting and receiving point also lie in the same plane. However, in the case where the transmitting and receiving point does not lie in the same plane, which is the case in most of the real borehole experiments, a 3-D simulation is necessary. As the radiation energy of the pulses is a function of distance, in this 3-D simulation, the amplitude decrease with distance will be high (due to spherical spreading).

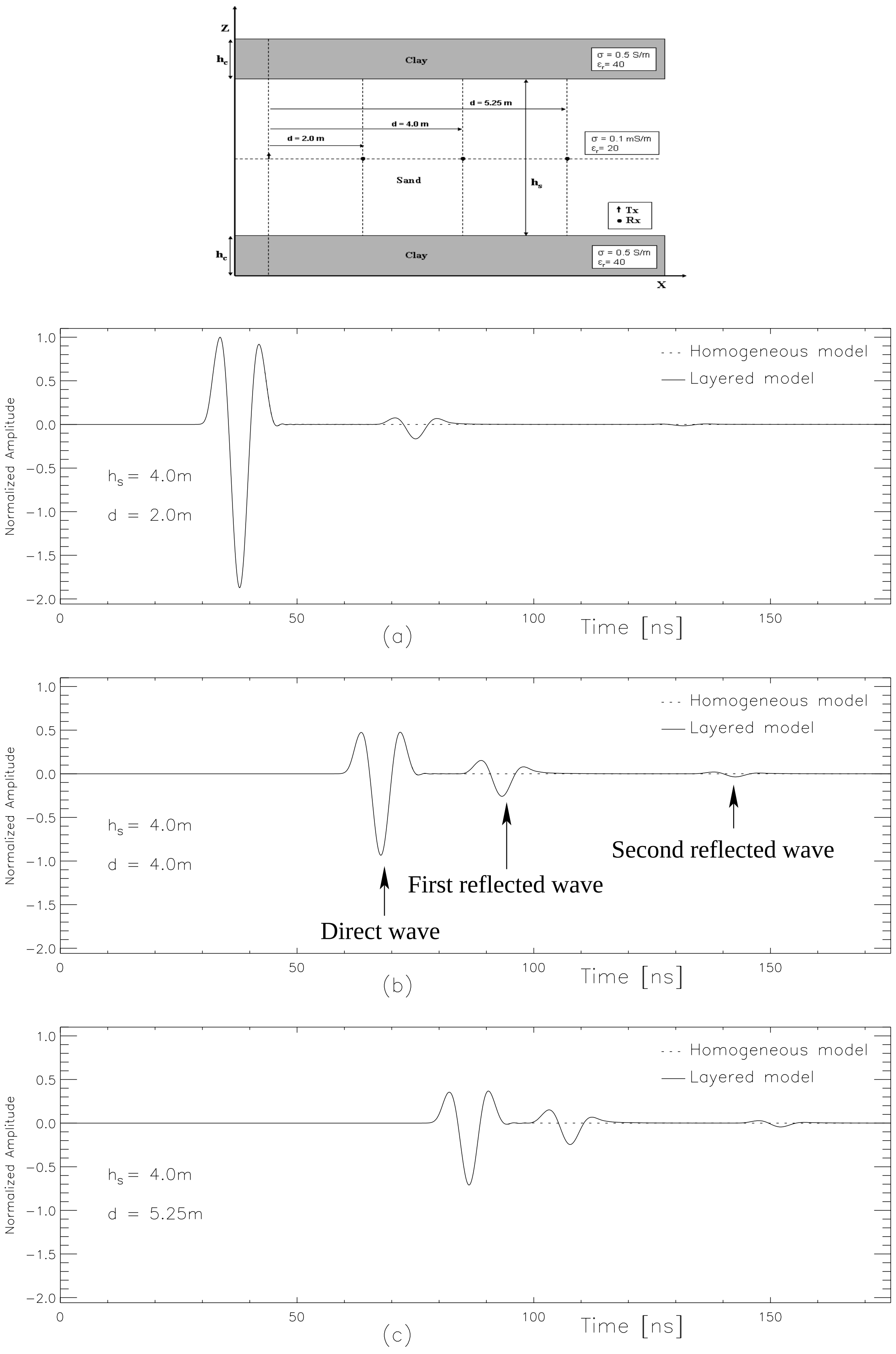

Figure 5.4: *Radar traces in the middle of the sand layer with different transmitter-receiver separations: (a) d = 2.0 m, (b) d = 4.0 m, (c) d = 5.25 m. The dotted line depicts the traces of the homogeneous model (properties of sand layer only). Note that the dotted line is not visible in places where it lies on top of the solid trace.*

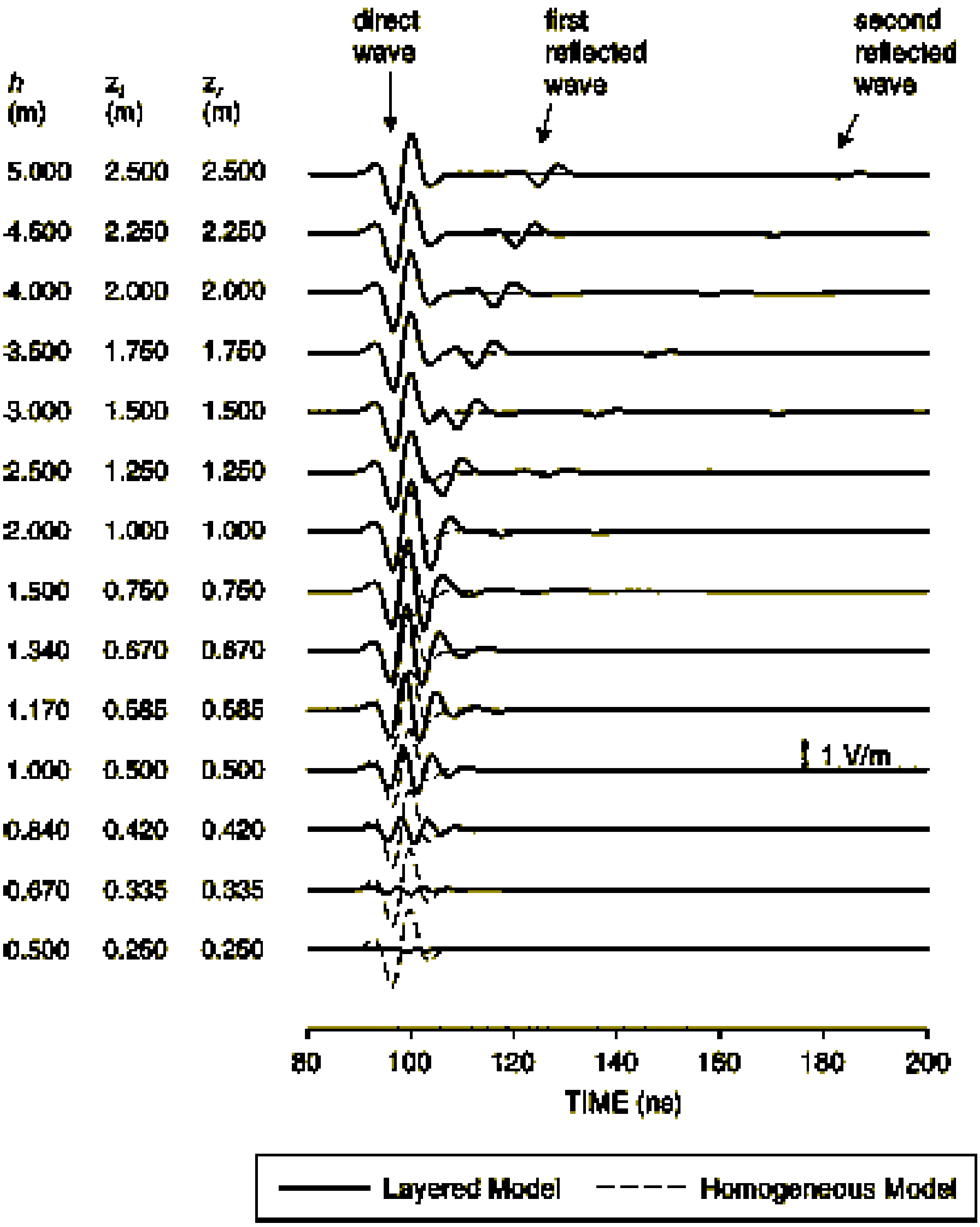

Figure 5.5: *Effect of the thickness of the sand layer on the radar wave. The thickness of the sand layer and the antenna heights are listed on the left. [This figure has been taken from Ellefsen (1999)]*

Effect of layering on radar traces [with a borehole at the transmitter location, experiment 2]

Figure 5.6 shows the received radar traces in the middle of the sand layer at different x positions, with the sand-layer thickness $h_s =$ 4.0 m, but in this case a 64mm diameter borehole was placed at the transmitter location. All the traces in Figure 5.6 have been saturated with the same maximum amplitude for purpose of comparison. In this case, too, three different types of waves are visible on all the radar traces, namely the *direct wave*, the *first reflected wave* and the *second reflected wave*.

Effect of borehole on cross-well radar traces

Figure 5.7 shows the plot of the radar traces both with and without a borehole at a distance of $d = 5.25$ m with a sand-layer thickness $h_s =$ 4.0 m. Clearly, the signatures of the radar traces, with and without the borehole, are different. In the case, without the borehole, the two positive peaks of the *direct wave* are almost similar to each other. However, in the trace with the borehole, the first positive peak of the *direct wave* is much higher than the next one. This may be because the borehole mud has different electrical properties than the host material (sand layer). There will thus be multiple reflections at the boundary between the borehole and the sand layer. These reflections will interfere with the transmitting pulse, and consequently will reshape the travelling wave (which acts as a filter in the frequency domain). Therefore, the amplitude of the *direct wave*, in the presence of the borehole, is not as symmetric as the one without the borehole (dotted curve in Figure 5.7).

Moreover, the amplitude of the trace with the borehole is larger than that of the trace without the borehole. The borehole mud has a lower impedance ($\eta = \sqrt{\frac{\mu}{\epsilon}}$; $\epsilon_r = 70$) than the host material ($\epsilon_r = 20$). The first impression is that more power has been launched into the medium than in the previous case. The increase in amplitude, through, is not simply the result of lower impedance. As we are not modelling the antenna configuration in this work, we can't directly discuss the effect of antenna impedance. Briefly put, when the material has finite conductivity, the intrinsic impedance is a complex number. The dielectric constant will have more effect on the antenna impedance, and the conductivity will affect the absorption of the energy radiated from the antenna. In this simulation, we kept the E-field strength constant, but in a real situation, a more realistic condition would have to be considered. For instance, the open voltage applied to the antenna would need to be kept constant, independently of the surrounding material. The input impedance of the antenna will strongly be influenced by the surronding material, and the impedance matching condition will also change. Therefore, the power radiated into the medium is a function of the input impedance of the antenna, which can be studied once a proper antenna configuration will be included in the simulation work. This was, however, beyond the scope of the present thesis.

As the borehole diameter is very small (64 mm), very little energy is trapped in the borehole. To analyzed the effect of borehole on radar traces, both the traces with and without the borehole are normalized by their corresponding received power. (as shown in Figure 5.8). A very small time delay has been noticed, which is due to the low velocity of borehole mud. The amplitudes of both the traces are almost the same, and the slight change is due to internal reflection and a small fraction of energy being trapped in the borehole.

Thereafter, to analyzed the effect of borehole mud conductivity on radar traces, both the traces with varying the borehole mud conductivity are normalized by their corresponding received power. (as shown in Figure Figure 5.9). In this case, too, the change is not significant. The effect of attenuation on the received radar trace (in case of high conductive mud, dotted trace) is more significantly pronounced in the later stage of the received trace rather in the earlier stage. This may be because of the multiple reflected waves in the borehole are affected by the high attenuation caused due to more conductive borehole mud.

Effect of receiver location on radar traces [experiment 1]

Figure 5.10 shows the effect of changing the height of the receiving antenna, while keeping the transmitting antenna fixed in the middle of the sand layer ($h_s = 4.0$ m). This is the same as a common source gathering. Two important differences are observed. Firstly, as we move from the middle of the layer to the top, the reflections from the top and the bottom became separated. When the source and the receiver location are in the middle of the sand layer, the total distance between the transmitting location, the top layer and the receiving location is same as the total distance between the transmitting location, the bottom layer and the receiving location are same, a first *reflected wave*, which is indicated above, is the superposition of the reflected waves from the upper and lower sand layer is visible in the radar trace. As the receiver is moved towards the upper sand-clay layer, the reflections from the upper and lower sand-clay layers separate from each other, and when the receiver is close to the upper sand-clay layer, the reflected wave from this layer superimposes on the direct wave; as a result of the interference, the amplitude of the wave decreases. Secondly, the amplitude of the received traces decreases sharply as the receiver location is moved into the clay layer. Once the receiver is in the upper clay layer, the amplitude of the received trace is thus very small in relation to the other traces, because only a fraction of the incident energy is transmitted into the clay layer due to the high dielectric contrast at the boundary and also due the intrinsic high attenuation in the clay layer.

Effect of sand layer thickness on radar traces [without a borehole, experiment 1]

Figure 5.11 (relating to Figure 5.2) shows the received radar traces in the middle of the sand layer at different x positions, but in this case the sand layer thickness considered is $h_s = 1.0$ m. All the traces in Figure 5.11 have the same ranges on the axes, allowing relative amplitudes and time locations of the pulses to be compared; they have also been compared to the homogeneous model traces. The amplitude of the received trace decreases as the distance between transmitter and receiver increases, but the times of arrival of the guided wave and of the direct wave of the homogeneous model are identical. In this case, however, the thickness of the sand layer is close to the significant wavelength (3-dB point) of the transmitting pulse (the wavelengths in sand layer are between 0.4 and 1.3 m at corresponding frequencies of 175 and 50 MHz), and thus all reflected waves are superimposed on the *direct wave* and thus form the *guided wave*. The superposition of the reflected waves on the direct wave will cause interference. The amplitude of the *guided wave* will thus either increase or decrease, depending on the relative path lengths between the direct wave and the reflected wave, which is a function of the sand layer thickness. Figure 5.12 shows the results achieved by Ellefsen (1999) in his 3-D numerical simulation study. From Figure 5.11 and Figure 5.12, we can see that all the reflected waves are superimposed on the *direct wave* and form the *guided wave*. It is also evident that the amplitude of the guided wave decreases in both scenarios, as the waves travel further from the transmitter.

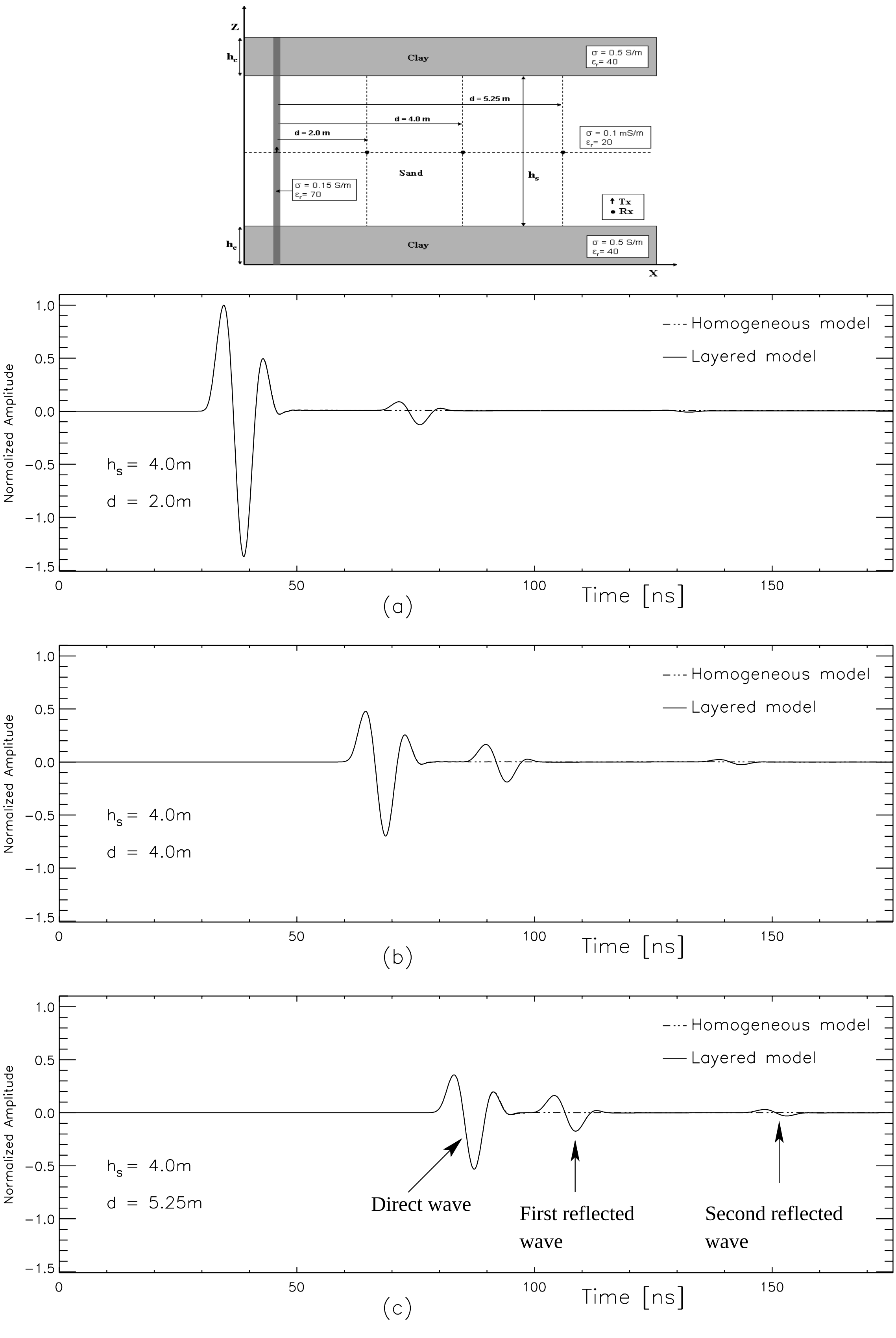

Figure 5.6: *Radar traces in the middle of the sand layer with different transmitter-receiver separations. A borehole of diameter 64 mm is located at the transmitter location: (a) d = 2.0 m, (b) d = 4.0 m, (c) d = 5.25 m. The dotted line illustrates the traces from a homogeneous model.*

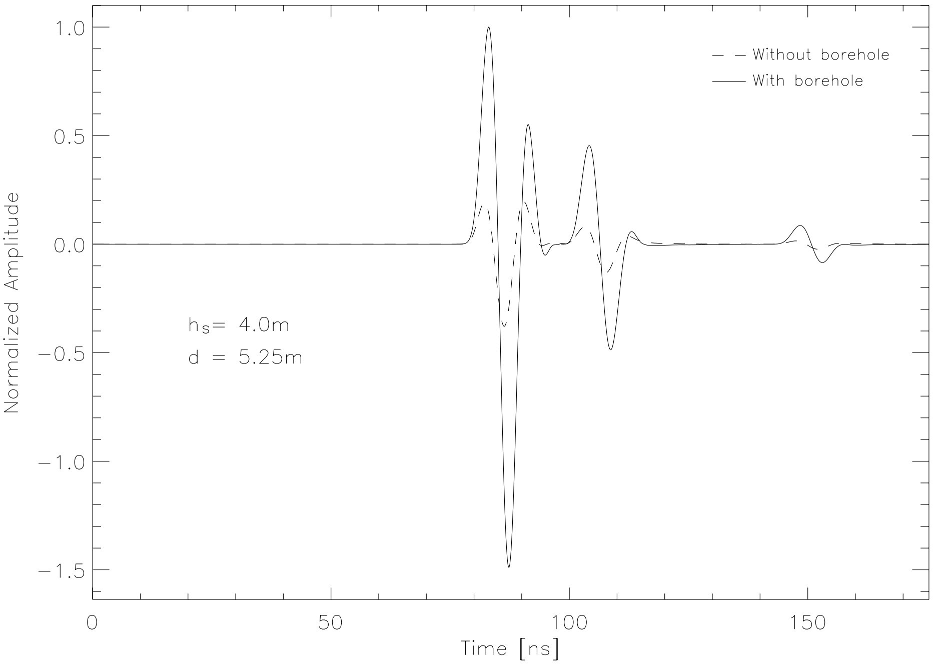

Figure 5.7: *Effect of borehole on radar traces.*

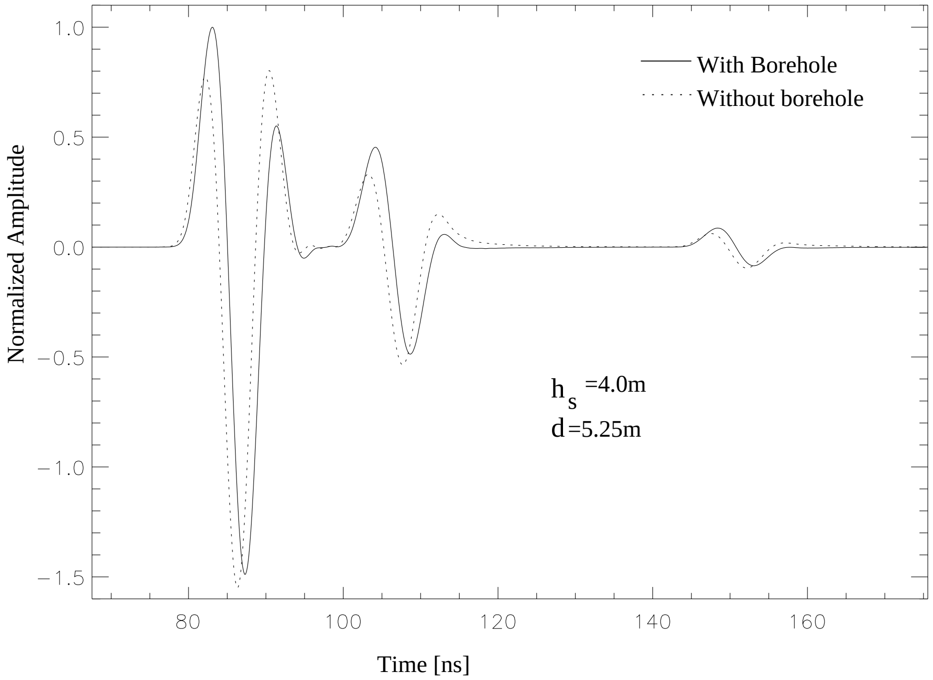

Figure 5.8: *Effect of borehole on radar traces. Both the radar traces have been normalized by the corresponding received energy.*

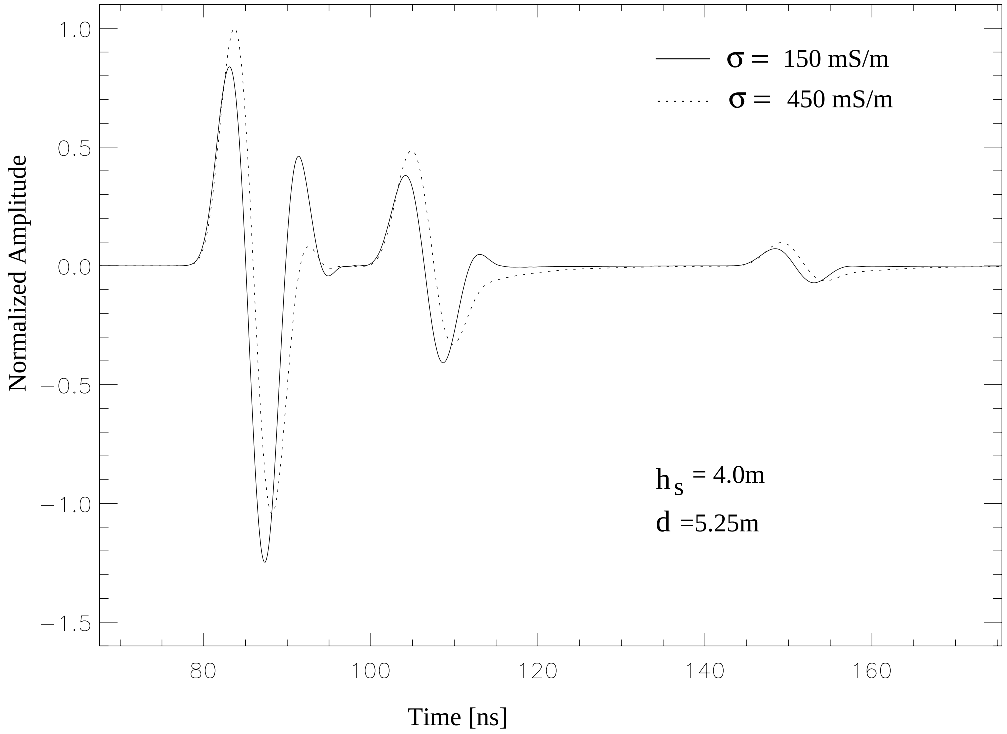

Figure 5.9: *Effect of borehole mud conductivity on radar traces. Both the radar traces have been normalized by the corresponding received energy.*

Effect of sand layer thickness on radar traces [with a borehole at the transmitter location, experiment 2]

Figure 5.13 (relating to Figure 5.3) shows the received radar traces in the middle of the sand layer at different x positions with the sand-layer thickness $h_s = 1.0$ m, and with a 64mm diameter borehole at the transmitter location. All the traces in Figure 5.13 have the same ranges on the axes, allowing relative amplitudes and time locations of the pulses to be compared. As before, all the traces have been compared with those of the homogeneous model. In this case, too, the *guided wave* is visible in all the traces. The signatures of the traces are similar to the ones without the borehole (Figure 5.11), but there are some differences when compared to the homogeneous model traces. Specifically, when there is a borehole, the second positive peak in all three traces is much closer to the homogeneous one than in the traces without the borehole, which suggests that at the later stage the waves are affected by multiple reflections.

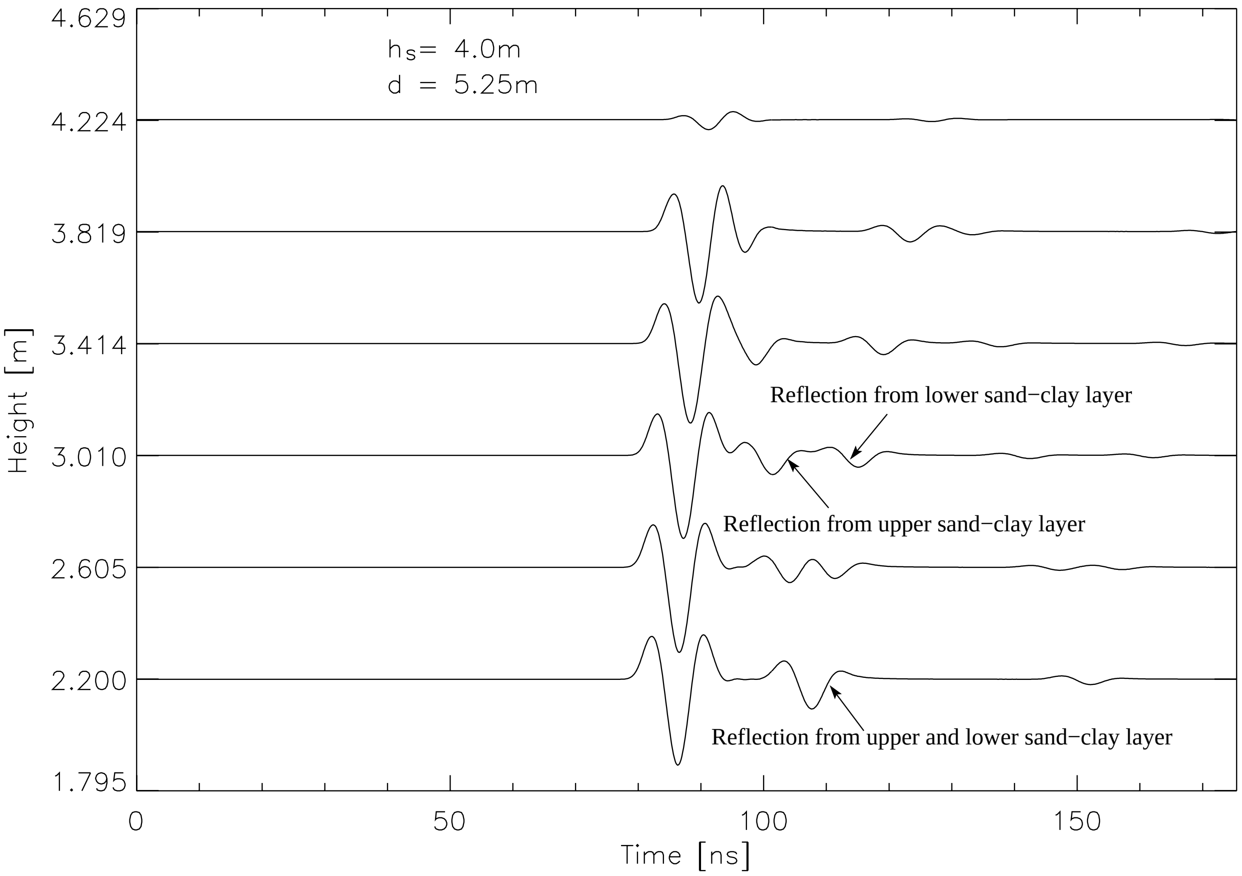

Figure 5.10: *Effects on radar traces when changing the height of the receiver location. The vertical axis is the height ($Z-$axis in Figure) of the receiver location.*

Effect of borehole at transmitting and receiving location on radar traces

Figure 5.14 shows a comparison between the radar traces recorded by using the borehole only at the transmitting location and then at both the transmitting and the receiving location. The signatures of both traces are similar. Nonetheless, there are some time differences with regard to the time of arrival. This is because, in the former case, the pulse travels a smaller distance through the borehole mud, where the velocity of propagation is less. The amplitude of the latter trace is thus slightly higher than that of the former. This may be due to internal reflection from the borehole wall and also due to the different electrical conductivity of the borehole mud and the host medium.

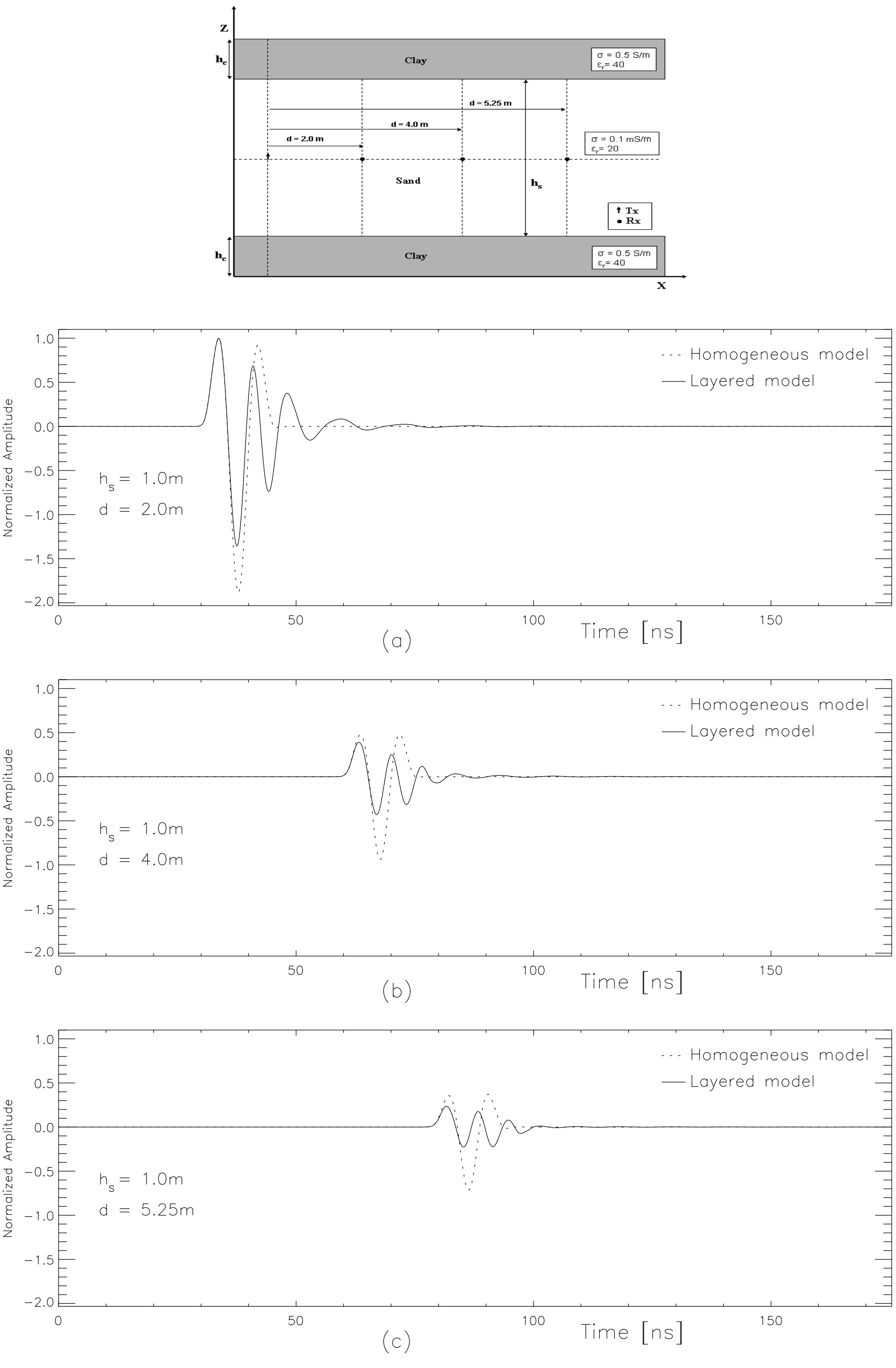

Figure 5.11: *Radar traces in the middle of the sand layer with different transmitter-receiver separations (without a borehole): (a) d = 2.0 m, (b) d = 4.0 m, (c) d = 5.25 m.*

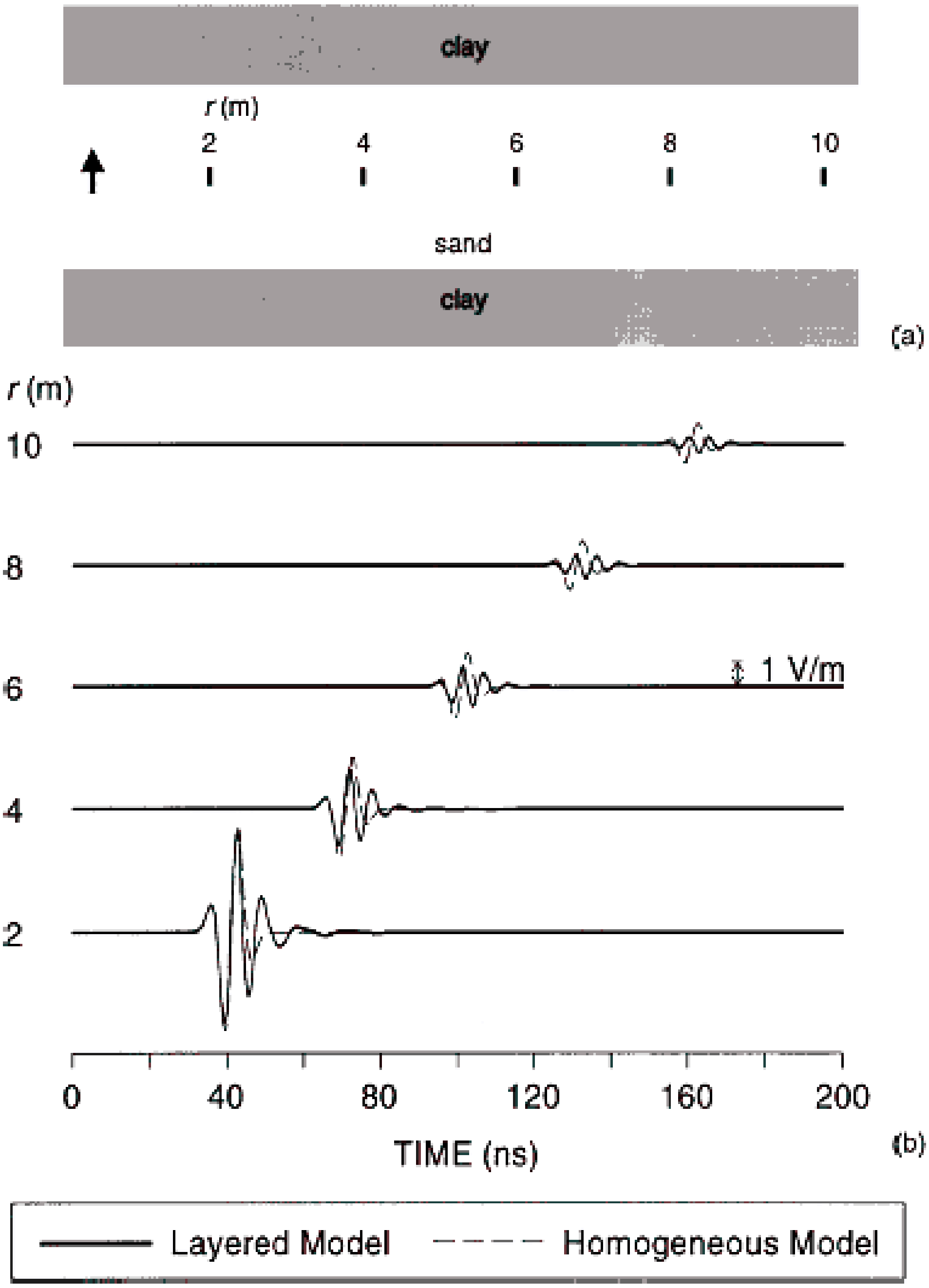

Figure 5.12: *Effect of changes in the radial distance between the antennas. (a) Model showing the locations of the antennas. (b) Radar traces. The radial distances are listed on the left. [This figure has been taken from Ellefsen (1999)]*

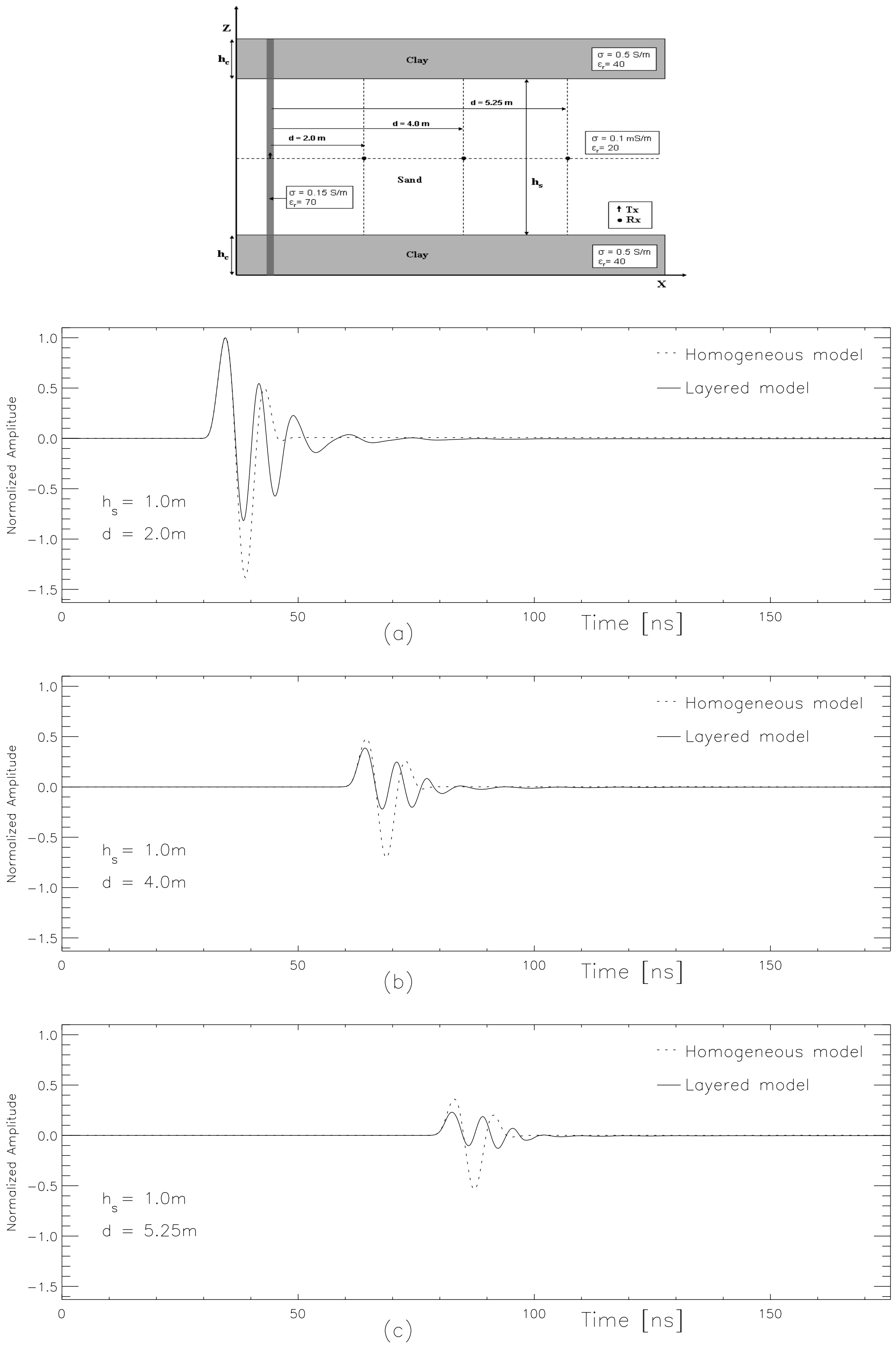

Figure 5.13: *Radar traces in the middle of the sand layer with different transmitter-receiver separations. A borehole of diameter 64 mm is located at the transmitter location: (a) d = 2.0 m, (b) d = 4.0 m, (c) d = 5.25 m. The dotted line illustrates the traces from a homogeneous model. The sand layer thickness is* $h_s = 1.0$*m.*

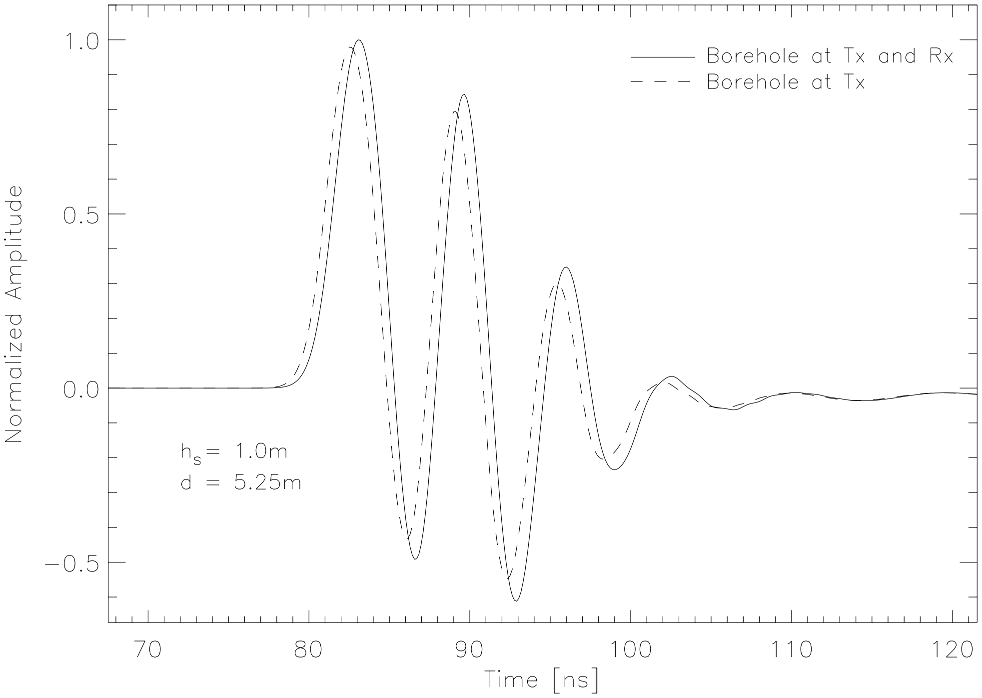

Figure 5.14: *Radar traces at d = 5.25 m with a 64 mm diameter borehole: (a) at only transmitter location ; (b) at both transmitter and receiver location.*

5.5 Electromagnetic Reflection Study of a Geological Reverse Fault in a Conductive Host Rock

5.5.1 Introduction

A *fault* is a fracture in the Earth's crust resulting from the displacement of one section in relation to an adjacent section. *A reverse fault* is a dip-slip fault. Movement within a dip-slip fault is parallel to the dip of the fault surface. In a *reverse fault,* the rock above the fault plane (the hanging wall) has moved upward relative to the rock below the fault plane (the footwall). This is because the compressional pressure is pushing the crust layer closer together, which shortens the distance between the components of the crust. Bodies of rock which are compressed horizontally thus often contain reverse faults. From a practical point of view, one cause of fatal injury in underground mines is being hit by falling objects as a result of geological roof faults (Molinda, 2003; Driscoll and Healey, 1999). It is therefore very important to study the potential of BHR for detecting such faults.

5.5.2 Simulation Setup

Experiment 3

Figure 5.15 shows the plane view of a reverse fault in a conductive host rock. The host rock was modelled with $\epsilon_r = 12$ and $\sigma = 0.001$ S/m, and the target orebody was modelled with $\epsilon_r = 7$ and $\sigma = 0.005$ S/m. The electromagnetic properties of the materials are given in Table 5.2. The materials were considered to be homogeneous and isotropic, and the electromagnetic properties were not frequency dependent. The transmitting antenna was aligned along the Y-axis at a distance of 5.3 m $(x, y, z) = (0.4, 5.3, 1.7)$ m and was simulated by a vertical electric dipole with infinitesimal length. The same source function (the Blackman-Harris window function), with a nominal frequency of 70 MHz, was added to the E_y component at the transmitter location on the Y-axis at each time step (soft source). The receiving locations were also aligned axially along the Y-axis, and in this case the transverse magnetic field component H_x at a constant interval of 0.5 m along the Y-axis was recorded. The data acquision mode used in this experiment is called *common source gather or WARR* survey, as discussed in chapter 2 (section 2.6.2).

Figure 5.19 shows the plane view of a 3-D flat surface in a conductive host rock. The reflecting surface starts at a height of 2.4 m, equal to the distance of the hanging wall in Figure 5.15. Figure 5.21 shows the plane view of a 3-D flat surface in a conductive host rock. The reflecting surface starts at a height of 3.5 m, equal to the distance of the foot wall in Figure 5.15.

The problem space was discretized into a size of 4.4 m, 11.0 m and 3.4 m in the $X-$,$Y-$,Z-directions respectively, with a uniform grid size of 0.025 m. The 10 PML layer was added outside the computational grid, and the resultant grid size was 196x460x156 along the $X-$,$Y-$,Z-directions respectively. In this simulation model the PML was matched perfectly to the material ($\epsilon_r = 12$ and $\epsilon_r = 7$) in the X direction (homogeneous). But this was not true in the Y and Z directions (inhomogeneous). The host rock material ($\epsilon_r = 12$) was mainly occupied in the Y and Z -directions. A value $\epsilon_r = 10$ is thus chosen in these directions to calculate σ_{opt} by using equation 5.4, which is closer to the relative permittivity of the host rock material.

Experiment 4

Figure 5.16 shows the same fault plane with a 100 mm diameter borehole placed along the Y-axis. The transmitter location was the same as before (Figure 5.15), at $(x, y, z) = (0.4, 5.3, 1.7)$ m. The receiving locations were also aligned axially on the Y-axis, and recorded the transverse magnetic field component H_x at a constant interval of 0.5 m along the borehole axis. The borehole mud was modelled as wet clay, which has a relative

Electrical Parameter	Host rock	Orebody	Borehole Mud
Electrical conductivity, σ [mS/m]	1.0	5.0	150.0
Relative dielectric permittivity, ϵ_r	12.0	7.0	70.0
Relative magnetic permeability, μ_r	1.0	1.0	1.0

Table 5.2: *Electrical properties of the materials used in Experiment 3 and 4.*

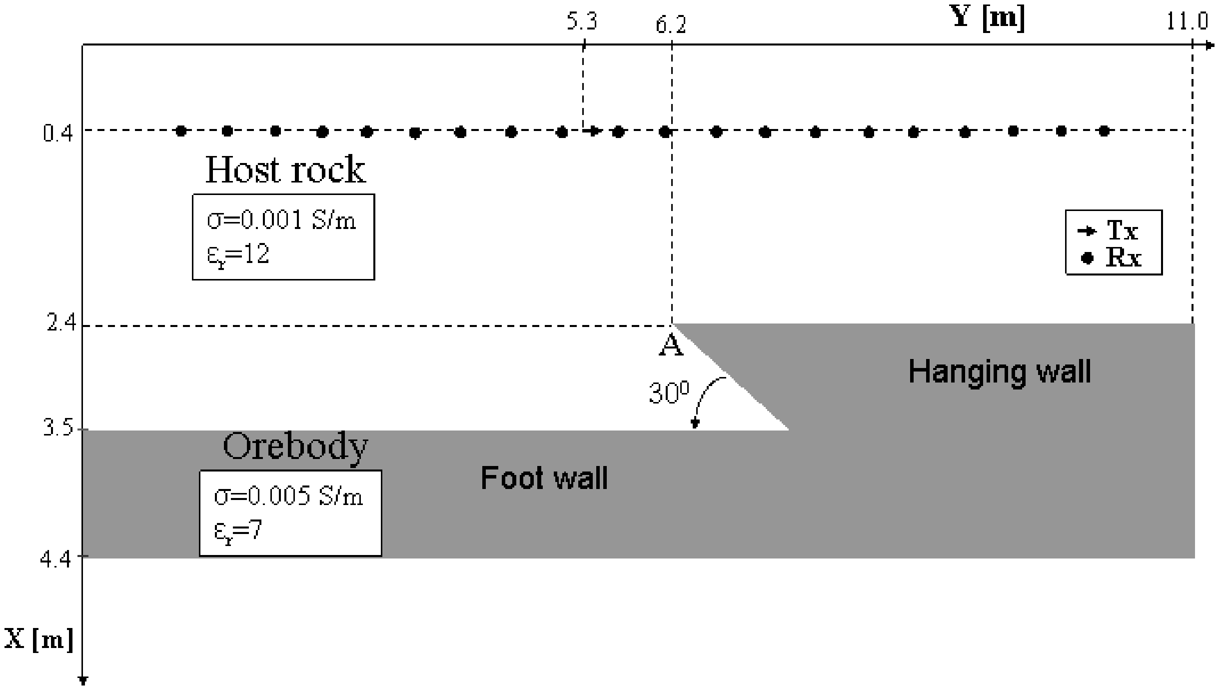

Figure 5.15: *A plane view of the geological reverse fault in a conductive host rock.*

dielectric permittivity $\epsilon_r = 70$ and conductivity $\sigma = 0.15$ S/m. The problem space was discretized with a uniform grid size of 0.025 m. In this simulation model, the PML was matched perfectly to the material ($\epsilon_r = 12$ and $\epsilon_r = 7$) on the top ($x = 0$) and bottom ($y = 4.4\,\text{m}$) sides. A value $\epsilon_r = 17$ was chosen in the Y direction, close to the host rock permittivity, and $\epsilon_r = 10$ was chosen in the Z direction to calculate σ_{opt}.

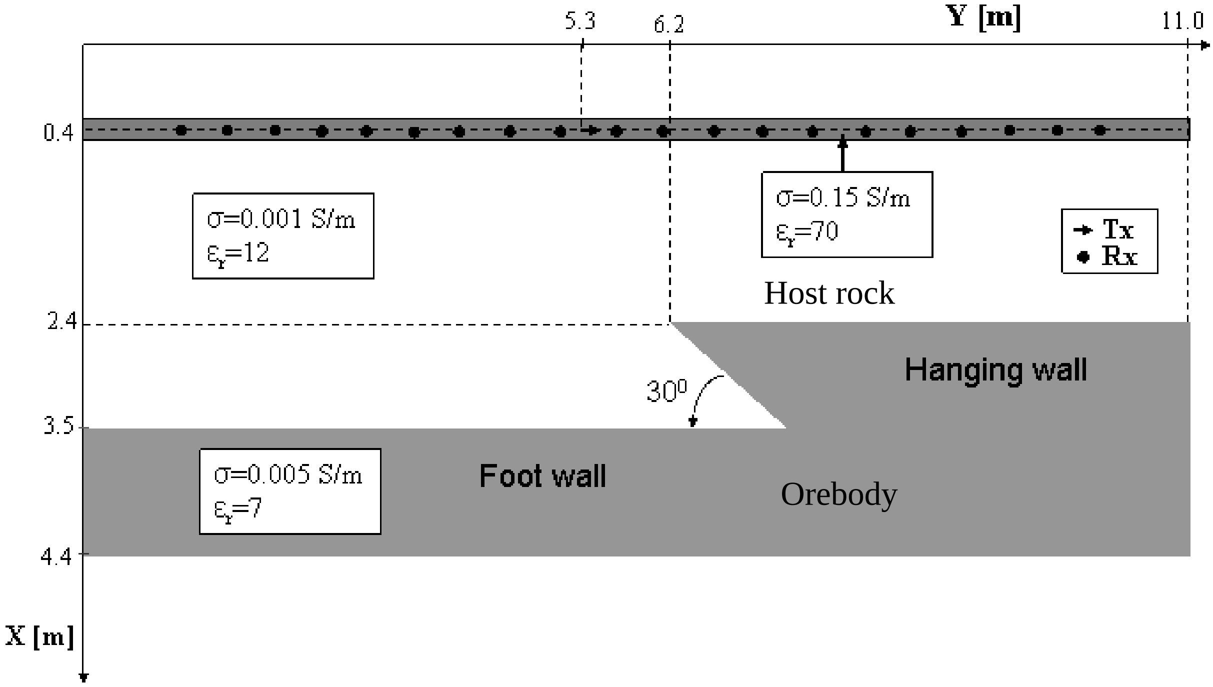

Figure 5.16: A *plane view of the reverse fault with a borehole at the transmitting and receiving end. The transmitter is located at* $Y = 5.3$*m.*

5.5.3 Results and Discussions

Experiment 3

Figure 5.17 shows the received waveforms at the receiver locations specified by their positions in metres. The receiver location is in the $Y-$direction as shown in Figure 5.15. As we can see, the received waveforms are dominated by the first arrivals, which are the direct waves that have travelled through the host rock to the receiver location. The reflections from the fault surface are not strongly visible, because the dielectric contrast between the host rock and the fault surface material is low. These direct waves should be removed from the recorded waveform to view the reflection from the fault surface. This can be done by recording the received waveform in the absence of the reverse fault and then by subtracting it from the total field.

Figure 5.18 shows the reflected waveform resulting from the hanging wall and foot wall of the fault surface. The existence of a reverse fault in the conductive host, as indicated by the hanging wall and the foot wall surface, is clearly visible in the reflected waveform. The amplitude of the waveform reflected from the hanging wall is greater than the waveform reflected from the foot wall. This is due to the loss of energy of the waveform in the conductive host and also energy lost due to spherical spreading. Figure 5.20 (relating to Figure 5.19) clearly shows the reflected waveform from the flat reflecting orebody surface; the orebody surface starts at a distance equal to the hanging wall surface of Figure 5.15. Figure 5.22 (relating to Figure 5.21) shows the reflected waveform from the flat reflecting orebody surface, which starts at a distance equal to the foot wall surface of Figure 5.15. These results (Figures 5.20 and 5.22) are presented here to see the nature of the waveform if there was no faulting. All the reflected waveforms are normalized with the same amplitude for the purpose of comparison.

Effect of scattering on radar traces [experiment 3]

The scattering from the sharp edge of the reverse fault (marked A in Figure 5.15), however, does interfere noticeably with the reflected wave from the hanging wall at the start of the traces (near point A), although, as one moves further along the receiver path, the effect becomes minimal, as we can see from the fact that the amplitude increases away from the sharp edge discontinuity. This effect on the reflection from the foot wall is minimal, because the lateral distance between them is long, and also because of the intrinsic attenuation in the host media. To validate this statement, we carried out a simulation study with only the hanging wall (before faulting), as well as with only the foot wall surface. Figure 5.23 shows the effect of scattering from the fault plane to the reflected traces. The amplitude of the trace, close to the sharp edge, is most affected by the interference, as shown in Figure 5.23(b).

Experiment 4

Figure 5.24 shows the waveform received at the receiver locations. In this case, too, the recorded waveform was dominated by the direct arrival. Figure 5.25 shows the reflected waveform resulting from the hanging wall and foot wall of the fault in the presence of a borehole at both the transmitter and the receiver end. In this case, too, the presence of a hanging wall and a foot wall is clearly visible from the reflected traces. In addition, the effect of the borehole on the received waveform is quite significant. The amplitude of the received traces without the borehole is much lower than that of those with the borehole. This is because the transmitter and the receiver are both inside the borehole (low impedance zone), and because both the transmitted and the reflected waves undergo internal multiple reflections at the borehole wall and host rock discontinuity.

Effect of borehole on reflected traces [experiment 4]

Figure 5.26(a) shows the effect of the borehole on radar traces; clearly, the signatures of the two traces are different, and the width of the trace with the borehole is also longer than that of the one without the borehole. The amplitude of the radar trace with the borehole was saturated drastically to allow us to compare it with the signature of the trace without the borehole. The diameter of the borehole and the relative permittivity of the borehole mud also affect the radar traces (see Figure 5.26(b) and (c)). It has been seen that the diameter of the borehole does not have much of an effect on the radar traces; the time delay is largely due to the longer distance that the pulse propagates through the borehole mud. The relative permittivity of the mud, however, does have a significant effect on both the shape and the amplitude of the traces.

Effect of scattering on radar traces [experiment 4]

Figure 5.27 shows the effect of scattering on the radar traces at the near and far end from the fault plane. The amplitude of the traces closer to the fault plane is more affected than at the far end. The path difference between the scattered wave and the reflected wave from the hanging wall is smaller close to the fault plane than at the far end. The interference, too, is stronger near to the fault plane than at the far end. To validate this statement, the traces were compared with the traces in absence faulting.

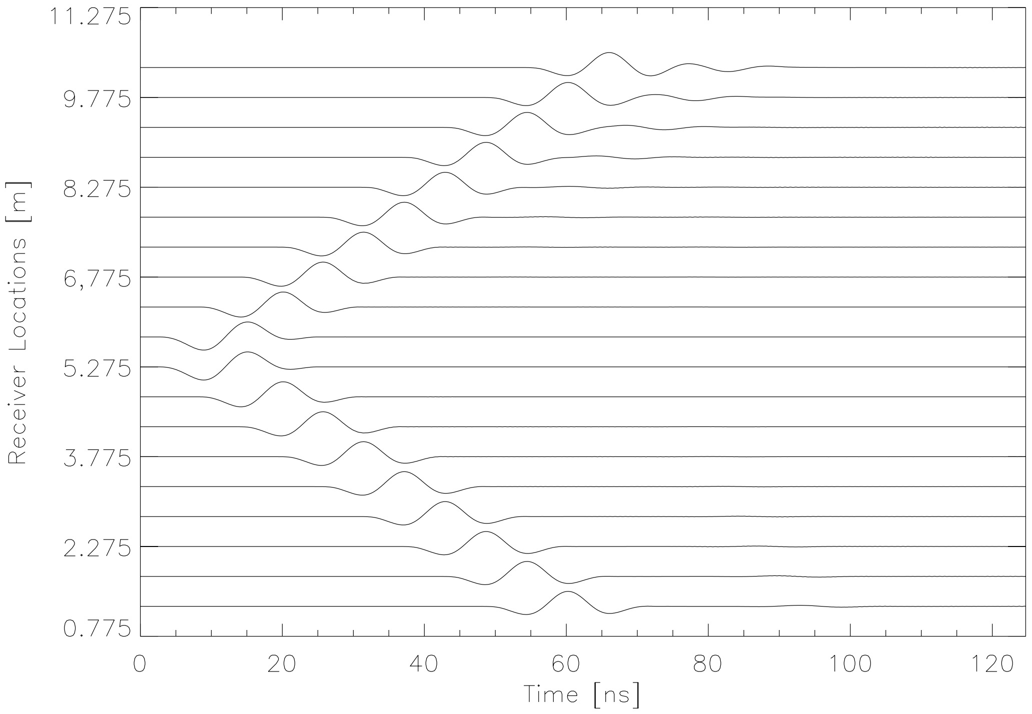

Figure 5.17: *Recorded radar traces at the receiver locations.*

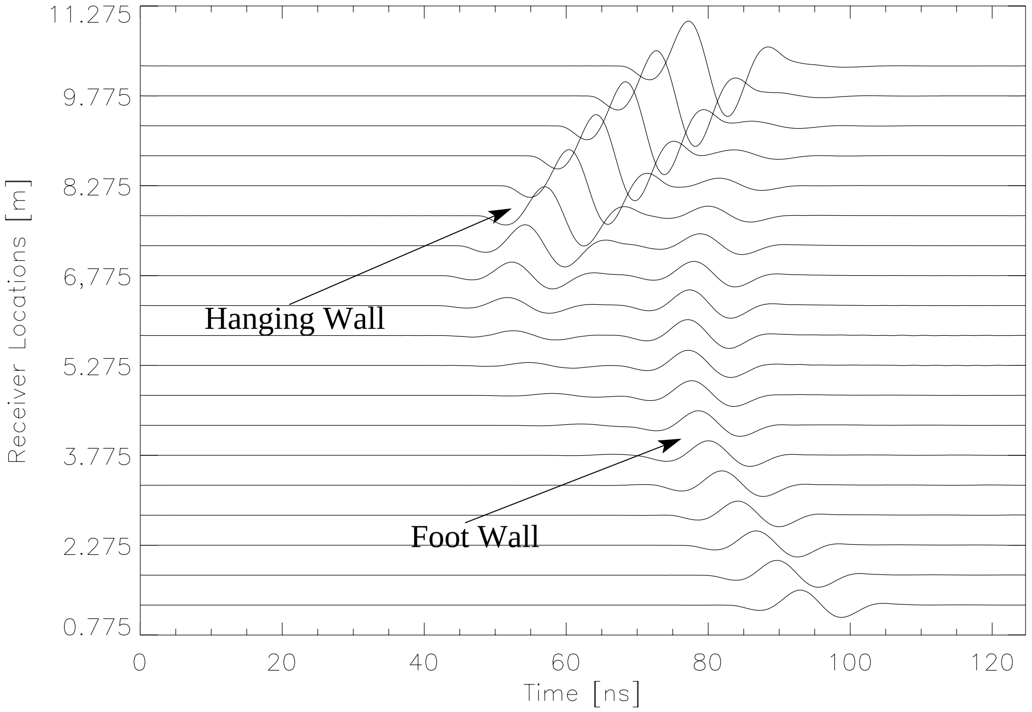

Figure 5.18: *Reflected waveform from the hanging wall and foot wall of the reverse fault. The direct waves have been removed from the recorded waveform.*

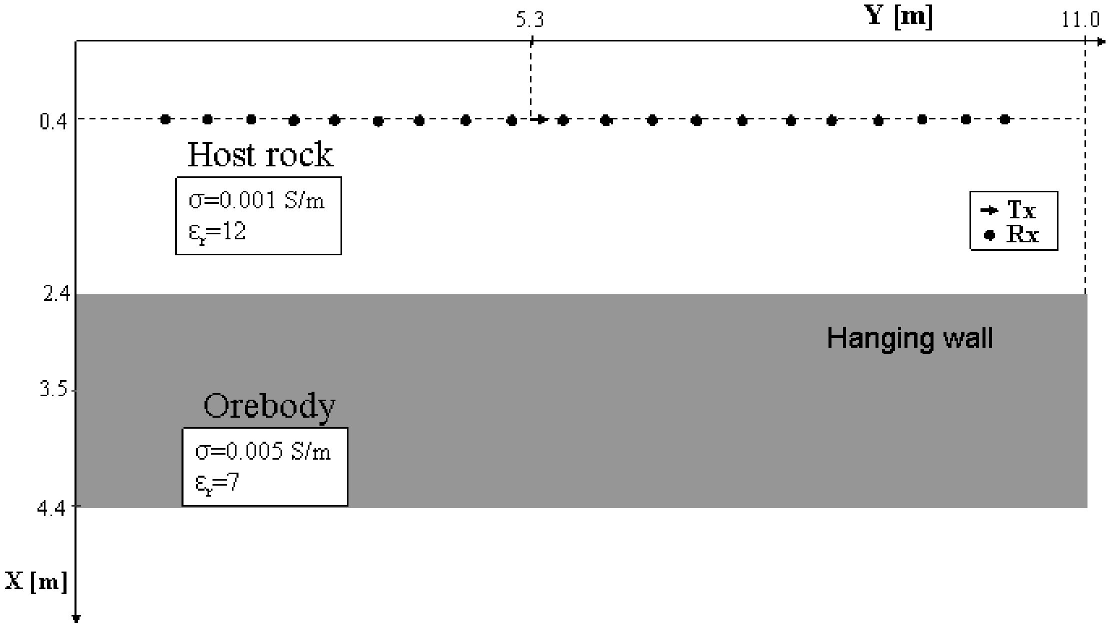

Figure 5.19: *A plane view of the flat orebody surface in a conductive host rock. The flat orebody starts at the height of the hanging wall surface (Figure 5.15).*

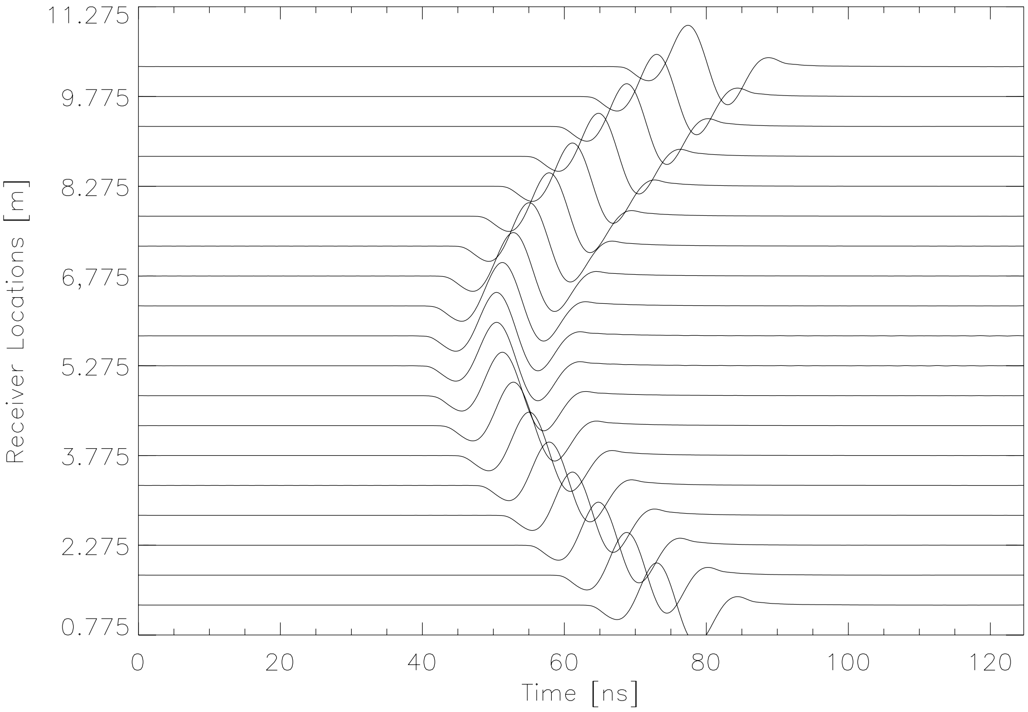

Figure 5.20: *Reflected waveform from the orebody surface (Figure 5.19). The flat orebody surface starts at a distance of 2.4m in the X-direction, equal to the distance of the hanging wall surface of Figure 5.15. The direct waves have been removed from the recorded waveform.*

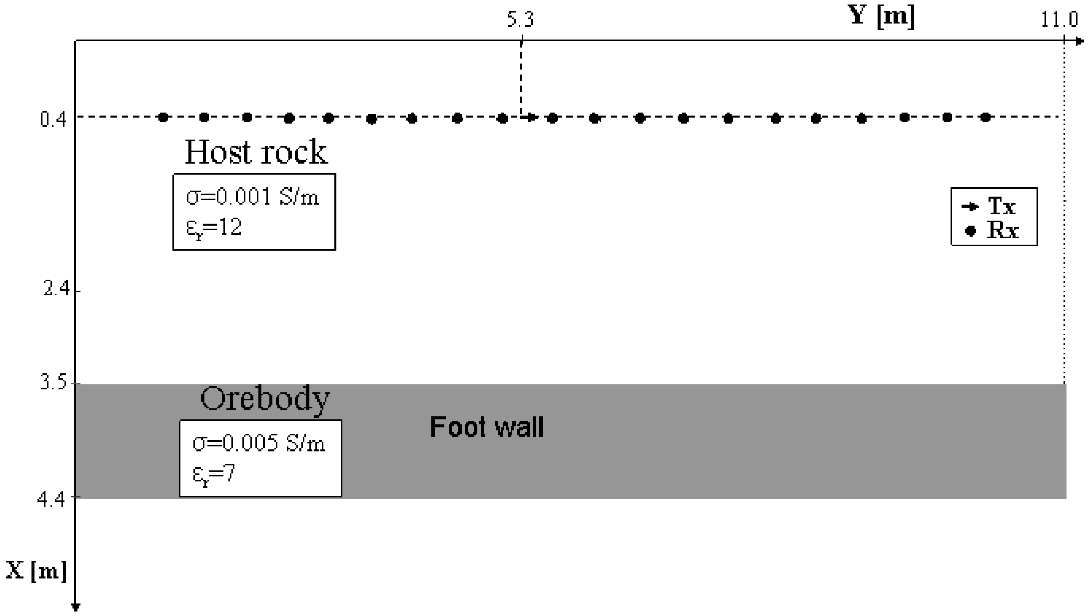

Figure 5.21: *A plane view of the flat orebody surface in a conductive host rock. The flat orebody starts at the height of the foot wall surface (Figure 5.15).*

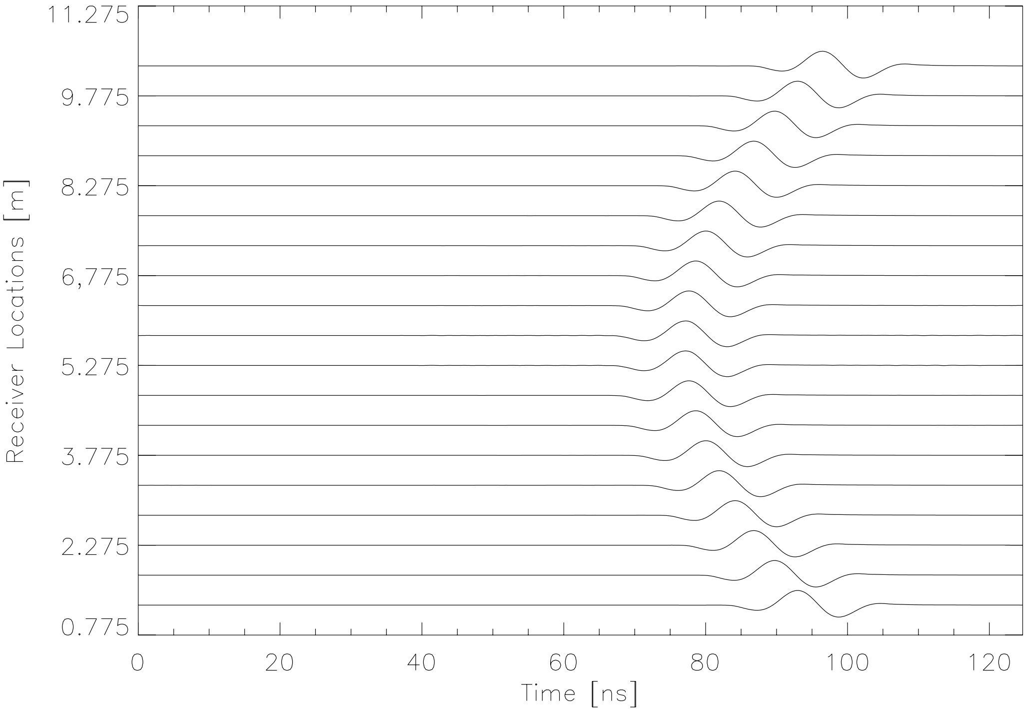

Figure 5.22: *Reflected waveform from the orebody surface (Figure 5.21). The flat orebody surface starts at a distance of 3.5m in the X-direction, equal to the distance of the foot wall surface of Figure 5.15. The direct waves have been removed from the recorded waveform.*

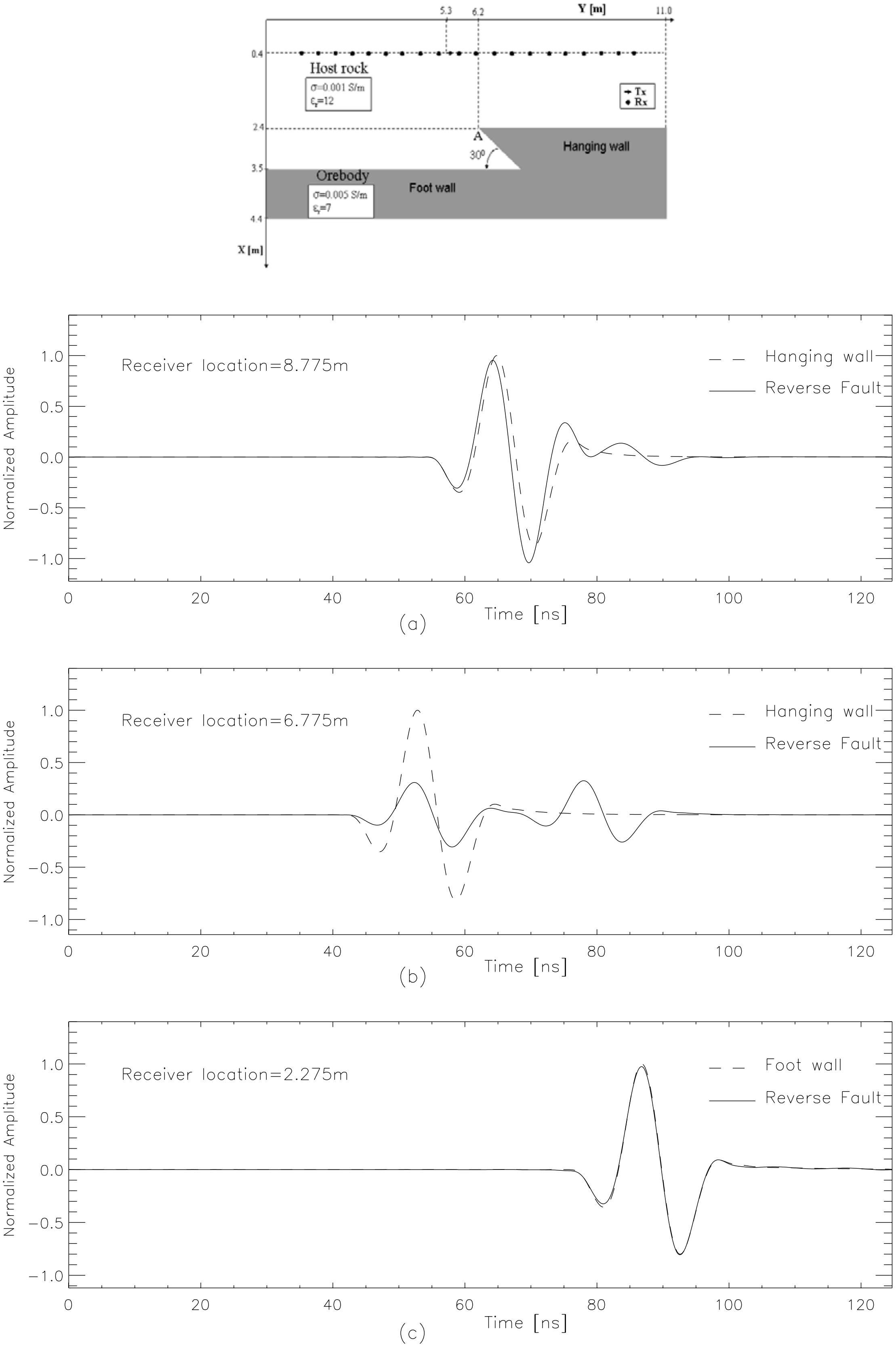

Figure 5.23: *Effect of scattering on the reflected traces from the fault plane (marked A in Figure 5.15). (a) on the hanging wall side; (b) close to A; (c) on the foot wall side.*

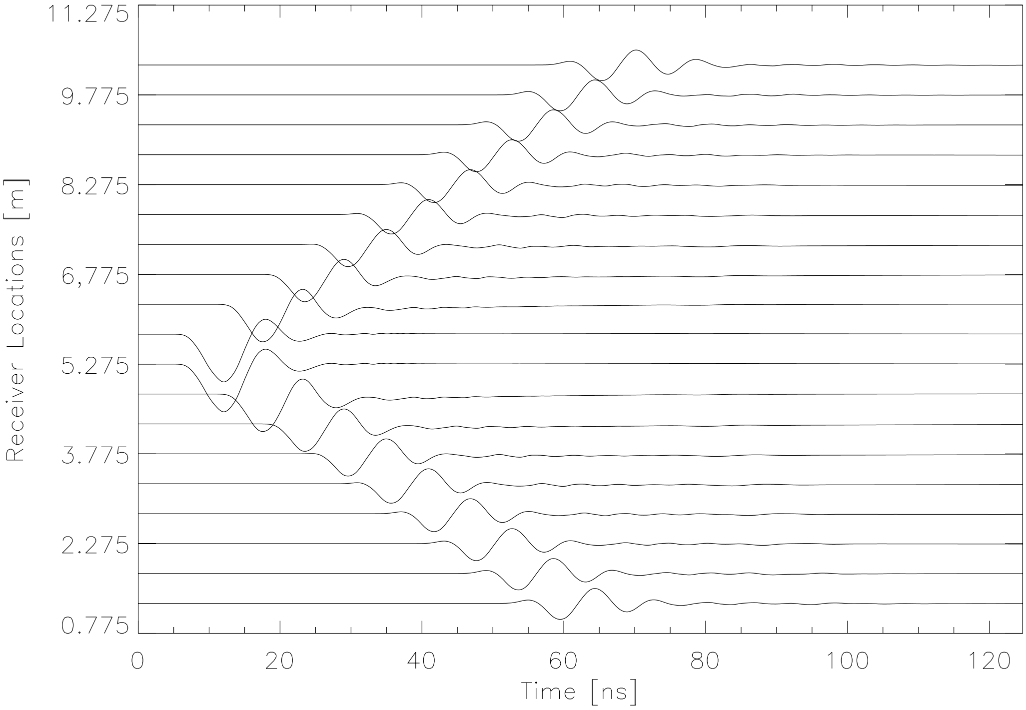

Figure 5.24: *Recorded radar traces reflected from the reverse fault. In this case, a borehole of 100 mm diameter was added at the transmitting and receiving locations.*

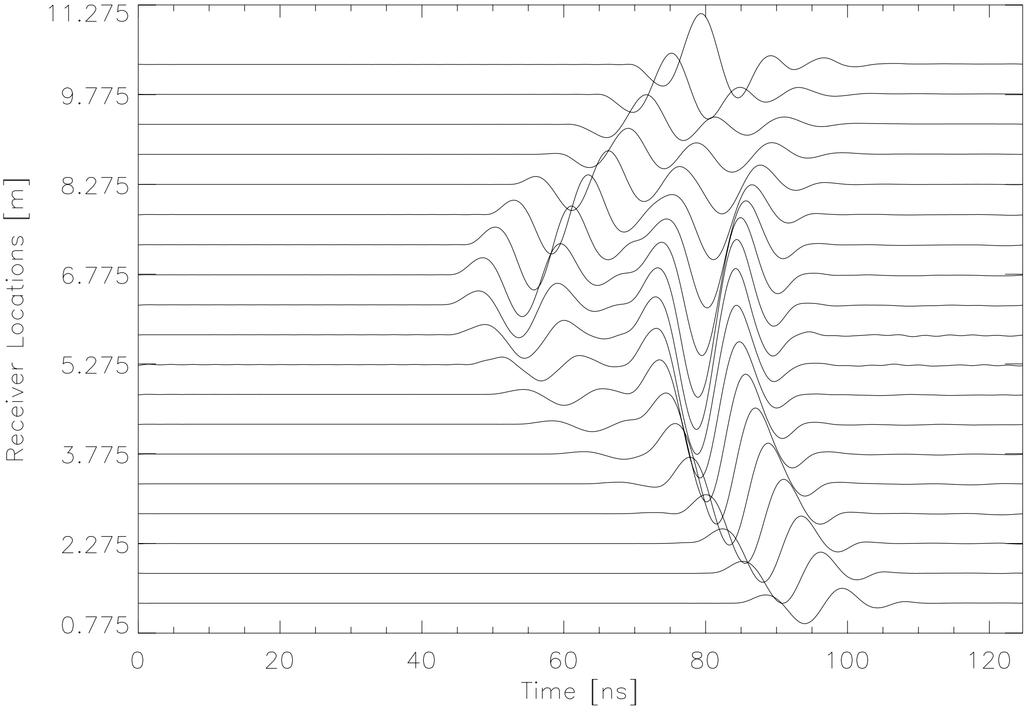

Figure 5.25: *Reflected waveform from the hanging wall and foot wall of the reverse fault with a borehole of 100 mm diameter.*

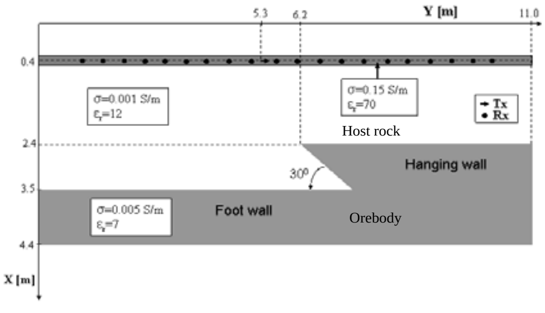

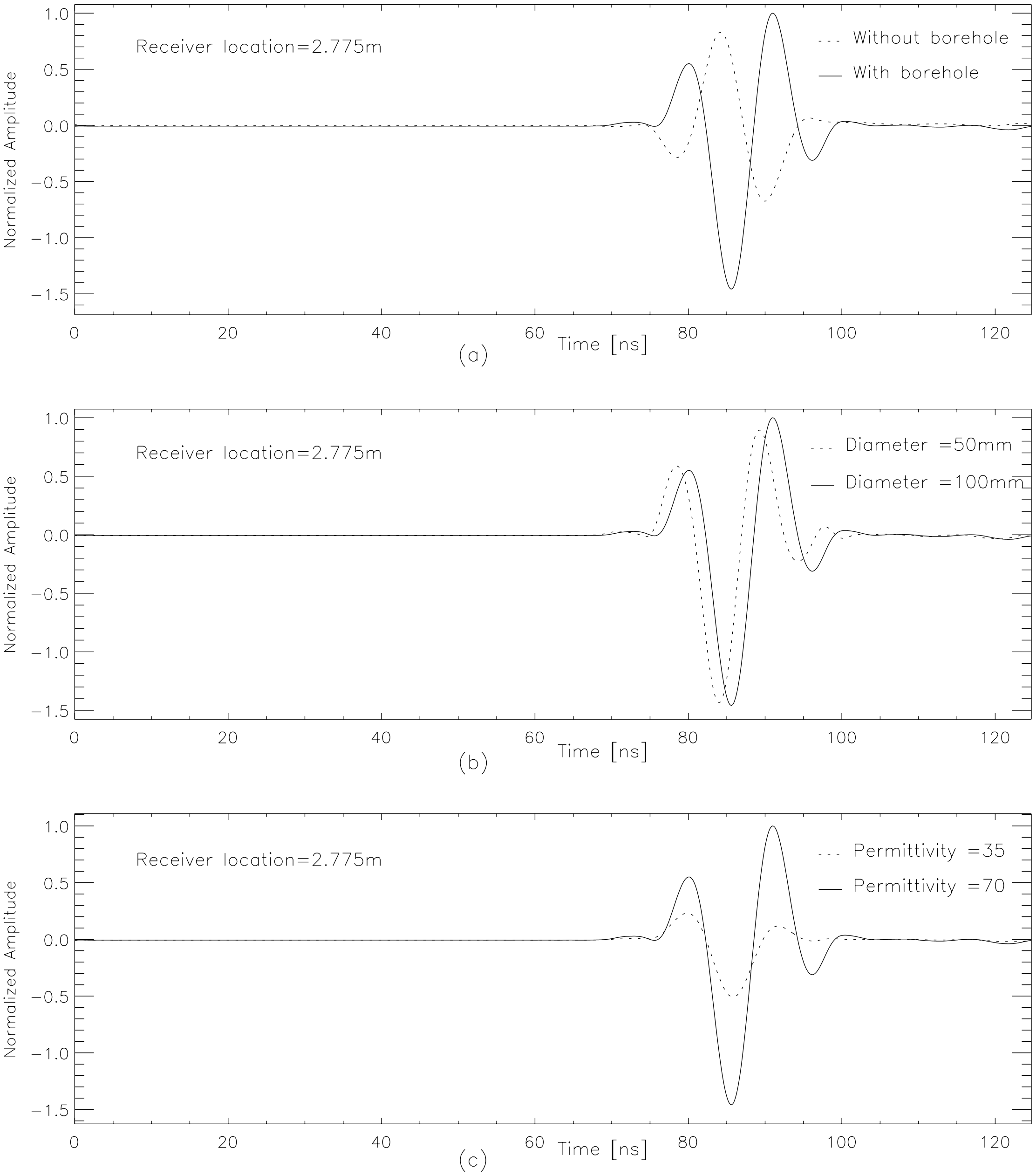

Figure 5.26: *Effect of borehole on reflected traces: (a) Traces with and without borehole; borehole trace has been saturated drastically to allow comparison between them; (b) traces with borehole diameter of 100 mm and 50 mm; (c) traces with borehole mud that has a relative permittivity of 70 and 35 respectively.*

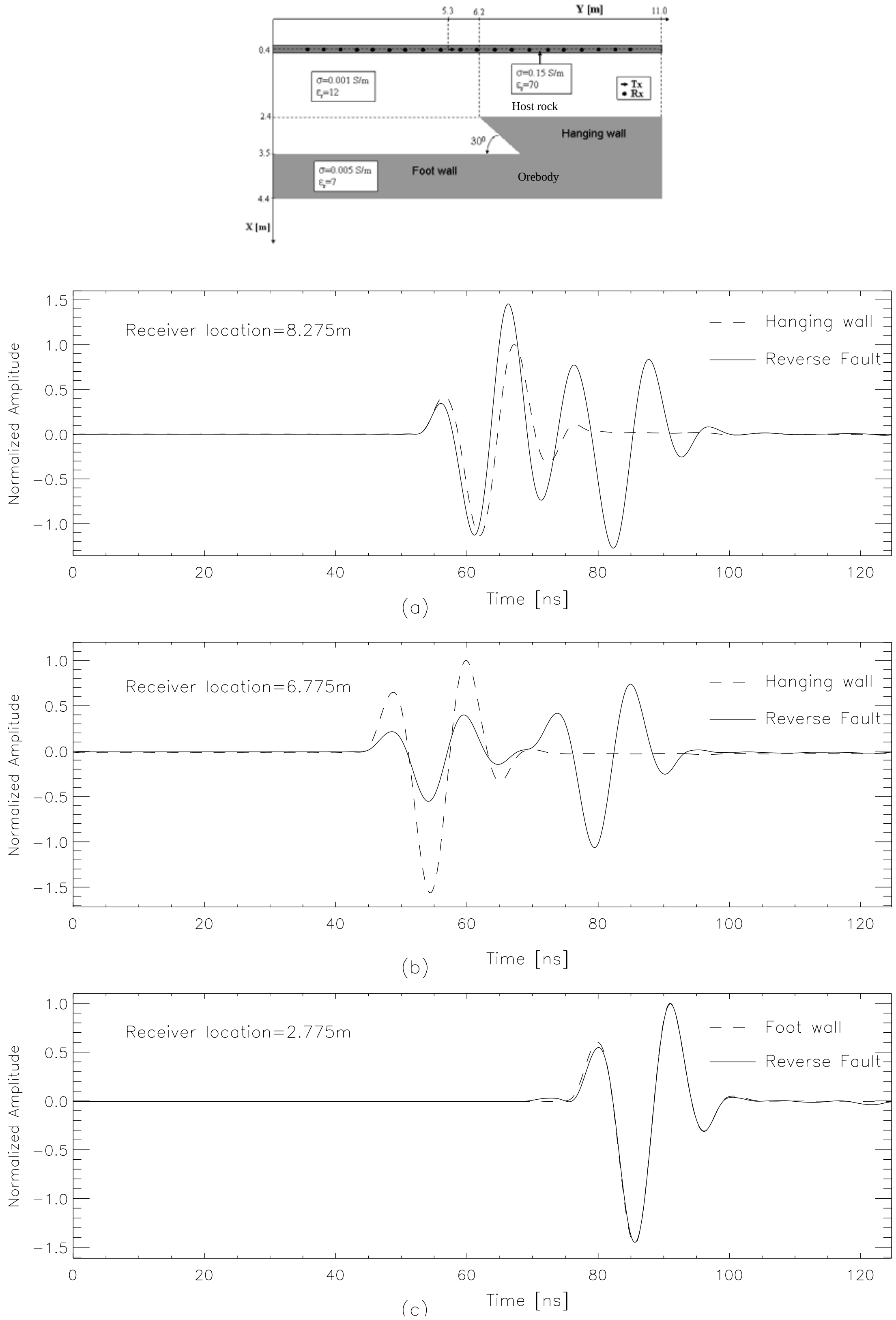

Figure 5.27: *Effect of scattering from the fault plane (sharp edge) on the reflected traces: (a) Traces from the reverse fault and only from the hanging wall (before faulting); (b) close to the fault plane; reverse fault and hanging wall; (c) reverse fault and only from the foot wall surface. All the traces have been simulated with a borehole of diameter 100 mm.*

5.6 Imaging pothole-type orebody using common offset data acquisition mode

Experiment 5

A pothole-type structure is defined as a semispherical hole in the bedrock of a stream bed, formed by abrasion of small pebbles and cobbles in a strong current. Figure 5.28 shows a 3-D view of the geological model used in this experiment, where a pothole-type orebody structure was embedded in a conductive host rock. The electrical properties of the materials are shown in Table 5.3.

The common offset data acquisition mode, discussed in section 2.5.1, is the most common data acquisition mode in usual borehole radar surveys. Figure 5.29 shows the 2-D section of the 3-D pothole structure and the data acquision antenna configuration. The separation between transmitting and receiving locations was kept fixed (0.25m), and they were moved along the X-axis, inside the borehole of diameter 150mm (Synthetic Aperture Radar image formation mode). The borehole mud was modelled as conductive clay (see Table 5.3). The cylindrical borehole surface was modelled by an averaged staircase approximation. The curved pothole structure was also modelled in this way.

The distance between the borehole axis and the nearest orebody surface was kept at $dd = 4.5\,m$. The pothole structure has a diameter of $h = 2.0\,m$ and depth of $d = 1.5\,m$. In this case, too, the transmitting antenna was simulated by a vertical electric dipole (E_x) with infinitesimal length. The source function (a Blackman-Harris window function) with a nominal frequency of 70 MHz (see Figure 5.1) was added to the E_x component at the source location at each time step (soft source). We recorded the vertical component of the electric field (E_x) at the receiver locations.

The problem space was discretized into a size of 9.0 m, 4.0 m and 6.0 m in the $X-$,$Y-$,Z-directions respectively, with a uniform grid size of 0.025 m. The 10 PML layer was added outside the computational grid, and the resultant size was 9.525 × 4.525 × 6.525 along the $X-$,$Y-$,Z-directions respectively. A borehole filled with conductive mud was placed at the top of the pothole structure along the X-axis with the Y- and Z- location at $(y, z) = (2.26, 5.0)$.

The PML was matched perfectly to the material ($\epsilon_r = 40$ and $\epsilon_r = 10$) in the $Z-$ direction, but the material profile was inhomogeneous along the $X-$ and $Y-$ directions. The gravel type (bedrock) layer ($\epsilon_r = 10$) occupied most of the spaces in the $X-$ and $Y-$ directions, and thus a value of $\epsilon_r = 24$ was chosen in these directions to calculate UPML parameters, which is closer to the relative permittivity of the host rock.

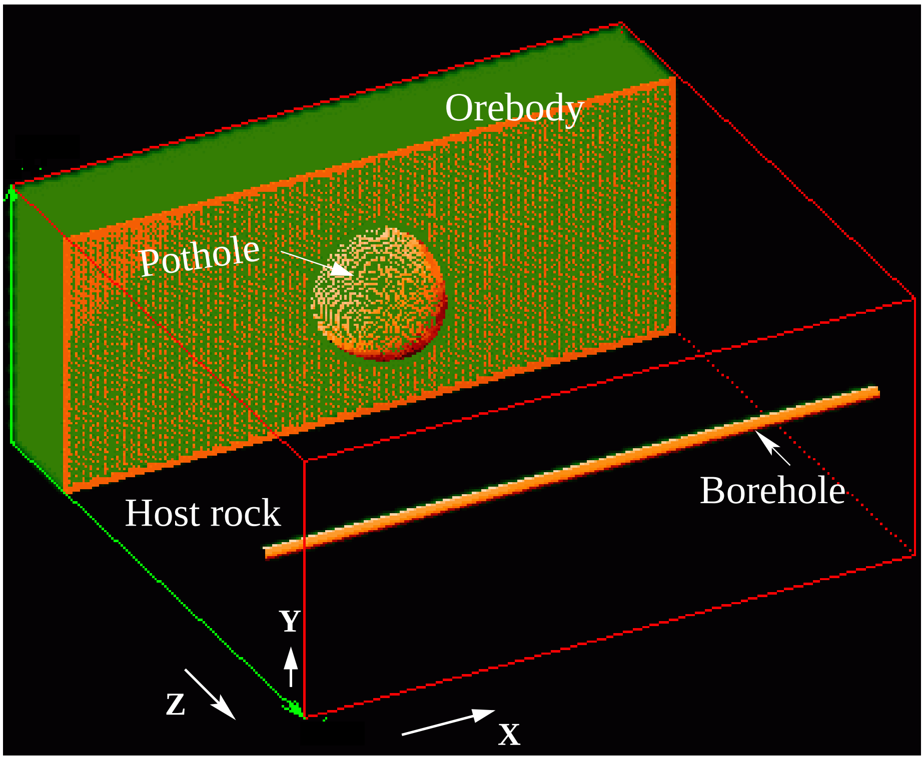

Figure 5.28: *A 3-D view of the pothole geometry used in experiment 5.*

Electrical Parameter	Host rock	Orebody	Borehole Mud
Electrical conductivity, σ [mS/m]	0.05	100.0	150.0
Relative dielectric permittivity, ϵ_r	10.0	40.0	70.0
Relative magnetic permeability, μ_r	1.0	1.0	1.0

Table 5.3: *Electrical properties of the materials used in Experiment 5.*

Results and Discussions of Experiment 5

Figure 5.30 shows the reflected waveforms received at the receiving locations, which are called *wiggle displays*. The direct wave has been removed from the received waveform. Figure 5.31 shows the same waveform in colour. In both figures, the reflections from the pothole structure (syncline structure) and from the basement (flat surface) in a conductive host rock are clearly visible (as labeled in Figure 5.31). The exact location of the subsurface orebodies can be found by means of wave field migration (focusing).

Due to limited number of traces in the azimuth (borehole) direction, in all 2-D grey scale

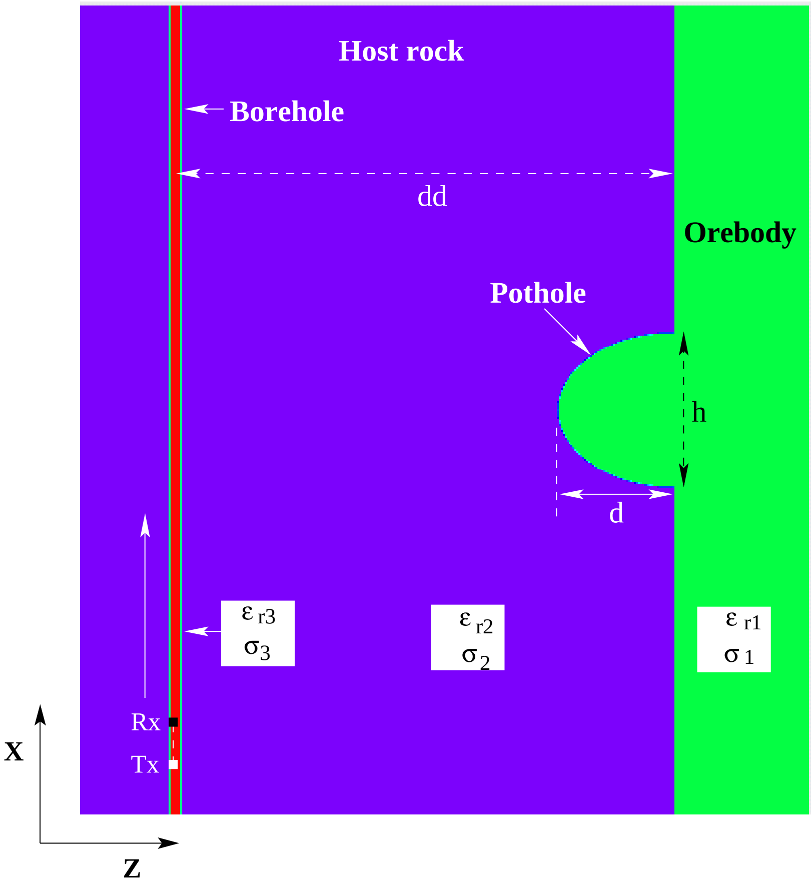

Figure 5.29: *A plane view (X-Z) of the common offset (SAR) imaging experiment 5.*

and colour display, the data has been interpolated linearly by using the CONGRID function of the IDL programming language.

Some well known authors, most importantly Chen et al., (1997), have already used the approach of removing the strong direct waves from the total received waves in a simulation environment. The purpose of this is to show clearly the presence of weak reflections. Although this is possible in a simulation environment, it is not possible to do so in real field measurements. Nonetheless, as my study was primarily a simulation study, I did used this approach in the previous sections. In real world measurement, the most often used method is called the *automatic gain control* process, which reduces high amplitudes and boosts small amplitudes. Figure 5.32 shows the grey scale display of the same waveform, but in this case the *automatic gain control* process has been applied. We can see the reflections from the target orebody in the presence of high ampliture direct waves in Figure 5.32.

To study the effect of electrical conductivity of the host rock medium on the radar traces, two experiments were conducted. In the first experiment, the electrical properties of the material of the model remains same as above (see Table 5.3), except that the electrical conductivity of the host rock has changed to 0.5 mS/m. In the second experiment, the conductivity of the host rock has changed to 5 mS/m. Such changes might be caused, for example, by changes in the salinity of the pore fluids. The effects of changes in the electrical conductivity of the host rock are shown in Figures 5.33 and 5.34. These two figures are the grey scale display of the received waveform, and the *automatic gain control* process has been applied to reduce the strong amplitudes and boosts the weak amplitudes. The reflection from the orebody structures are visible in Figure 5.33, but not visible in Figure 5.34. As the conductivity of the host rock increases and, hence, intrinsic attenuation increases, the amplitude of the reflected wave decreases.

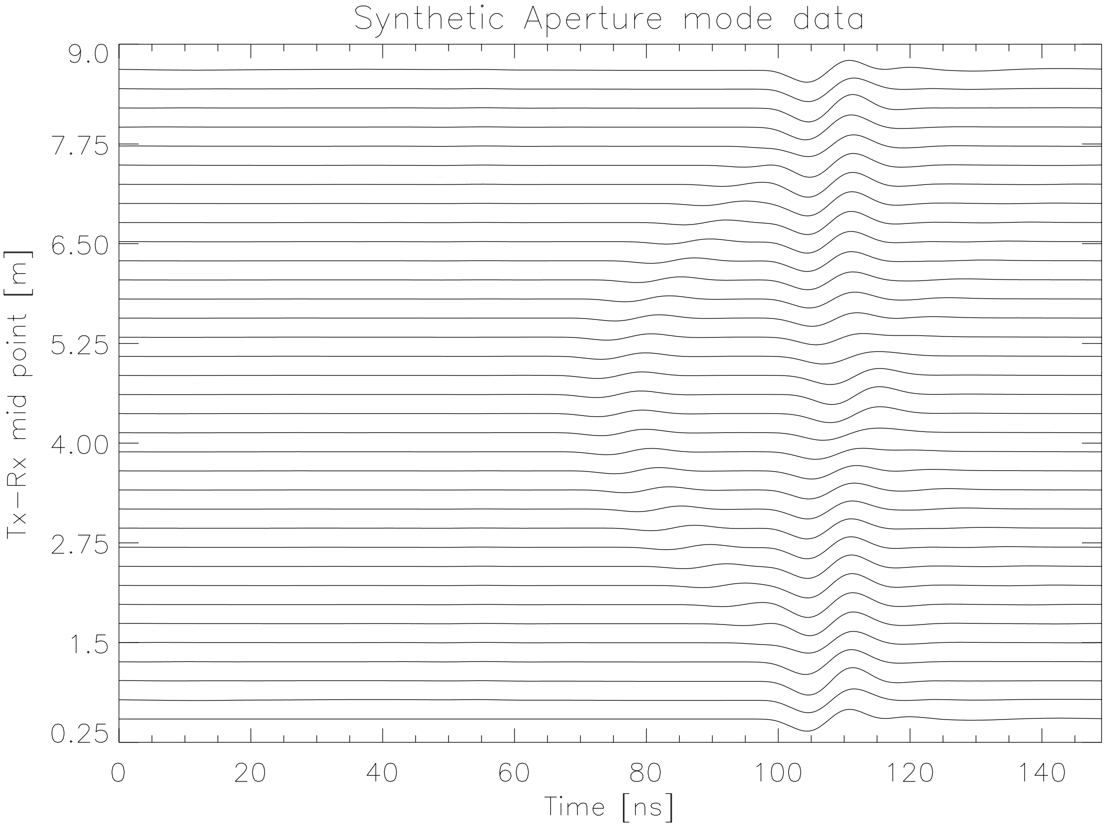

Figure 5.30: *Wiggle plots of the received radar traces at the receiver locations. The direct waves have been removed from the waveform.*

Experiment 6

It often happens that the imaging structure does not always present exactly above the borehole plane. The target orebody may thus present at an off-nadir location. A 3-D FDTD simulator is essential in this kind of modelling configuration. Figure 5.35 shows a

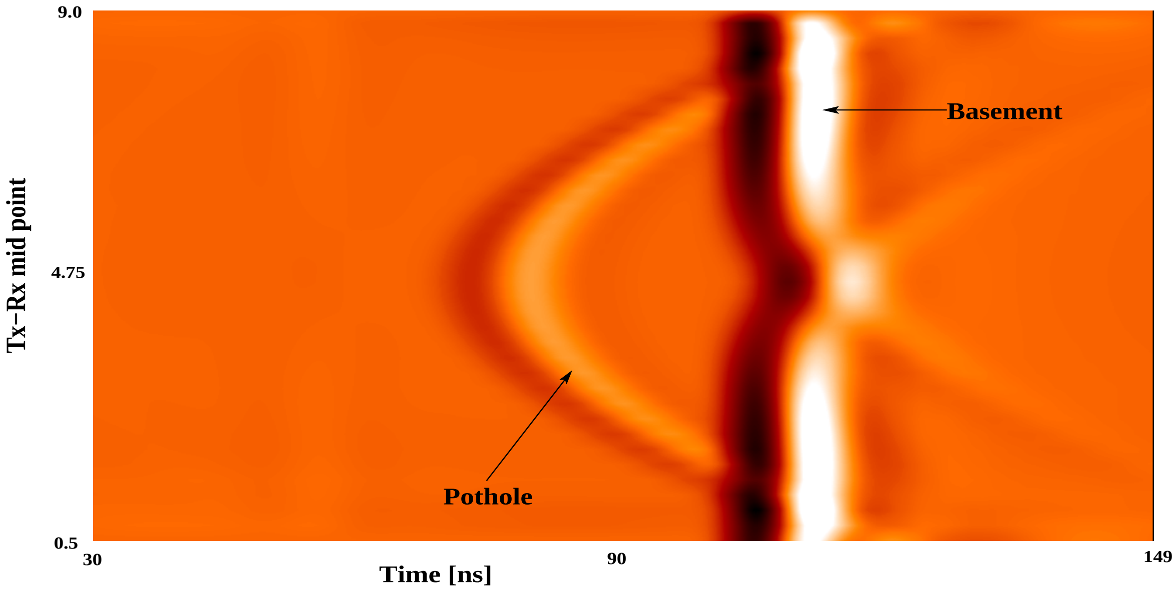

Figure 5.31: *Colour display of the received radar traces. The direct waves have been removed from the waveform. The conductivity of the host rock was 0.05 mS/m.*

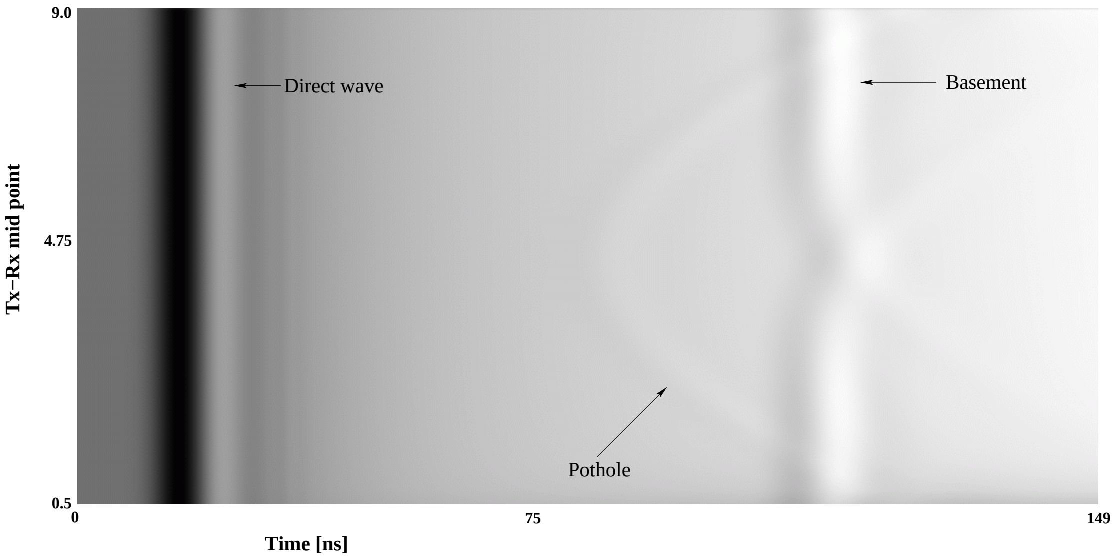

Figure 5.32: *A grey scale display of the received radar traces. Automatic gain control scaling has been applied to reduce high amplitudes and boost small amplitudes. The conductivity of the host rock was 0.05 mS/m.*

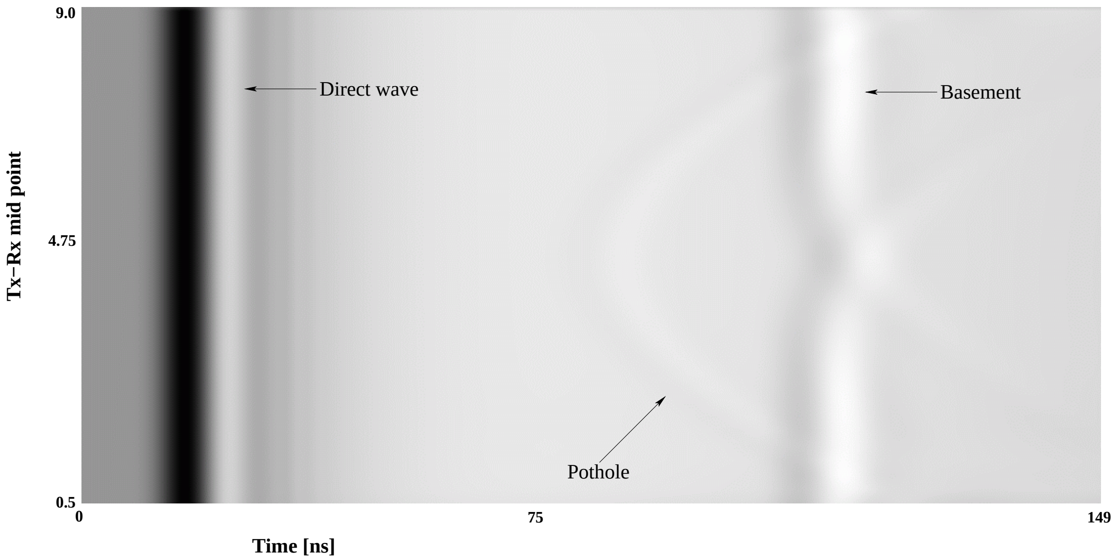

Figure 5.33: *Effect of host rock conductivity on radar traces. A grey scale display of the received radar traces. Automatic gain control scaling has been applied to reduce high amplitudes and boost small amplitudes. The conductivity of the host rock was 0.5 mS/m.*

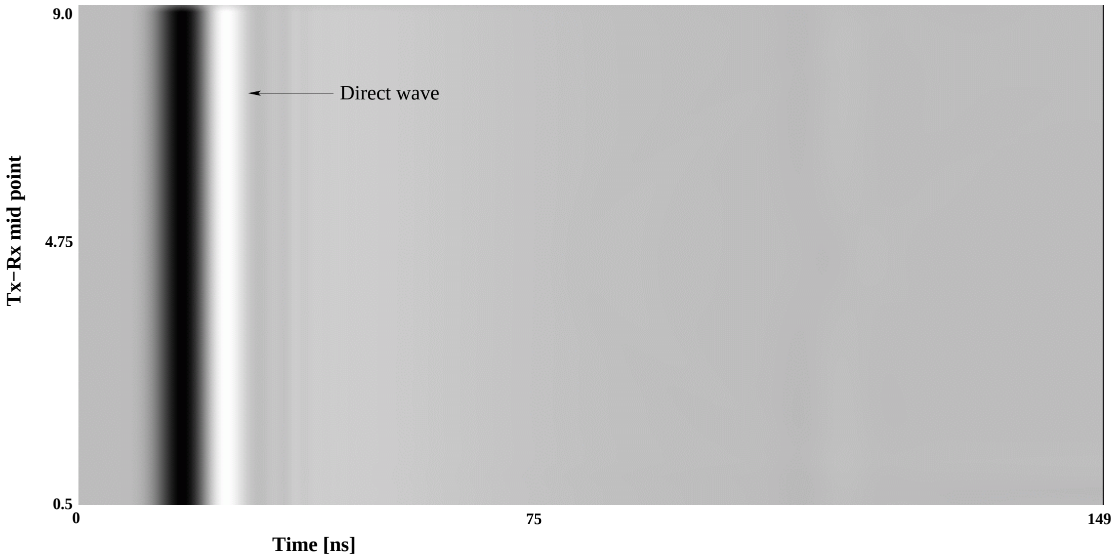

Figure 5.34: *Effect of host rock conductivity on radar traces. A grey scale display of the received radar traces. Automatic gain control scaling has been applied to reduce high amplitudes and boost small amplitudes. The conductivity of the host rock was 5.0 mS/m.*

3-D view of such a structure. A 2-D view of the pothole structure is shown in Figure 5.36. The electrical properties of the materials are shown in Table 5.3.

The distance between the borehole axis and the nearest orebody surface was kept at $dd = 4.0\,m$. The pothole structure has a diameter of $h = 2.5\,m$ and depth $d = 2.5\,m$. The centre of the pothole structure was not at the centre of the model, and was at $(x, y, z) = (4.76, 4.0, 0.0)m$.

The problem space was discretized into a size of 9.0 m, 6.0 m and 6.0 m in the $X-$,$Y-$,Z-directions respectively, with a uniform grid size of 0.025 m. The 10 PML layer was added outside the computational grid, and the resultant size was 9.525 × 6.525 × 6.525 along the $X-$,$Y-$,Z-directions respectively. A borehole filled with conductive mud was placed at the off-nadir position with respect to the pothole structure along the X-axis with the Y- and Z- location at $(y, z) = (2.0, 4.75)$. The data has been collected by common offsets data acquisition mode. All the other model parameters were the same as those of experiment 5.

Figure 5.37 shows the grey scale display of the received waveform. The image has been displayed by applying the *automatic gain control* process. The direct wave as well as the reflections from the pothole structure and basement are clearly visible in the received waveform.

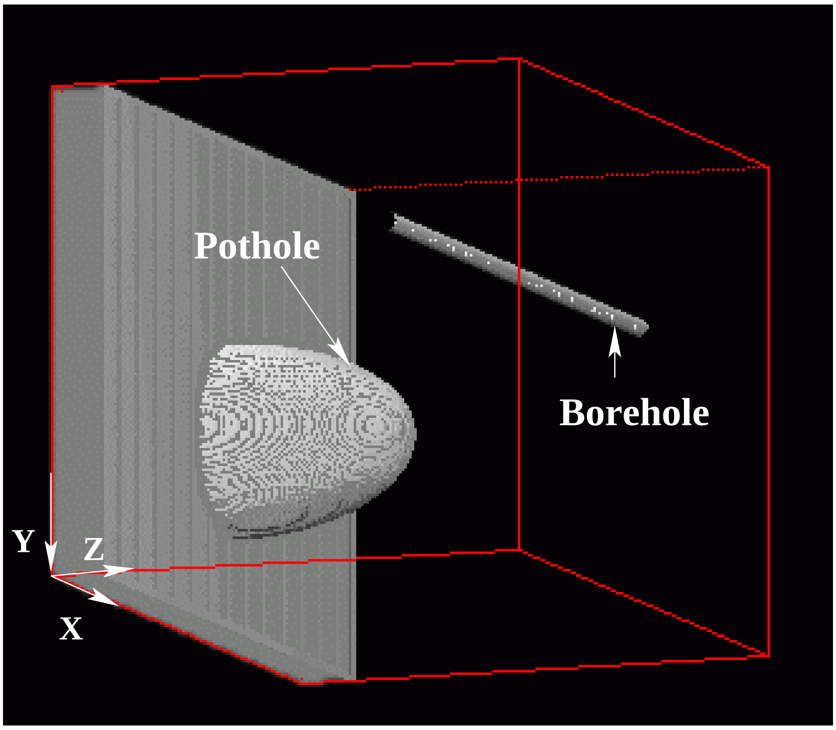

Figure 5.35: *A 3-D view of the pothole geometry used in experiment 6.*

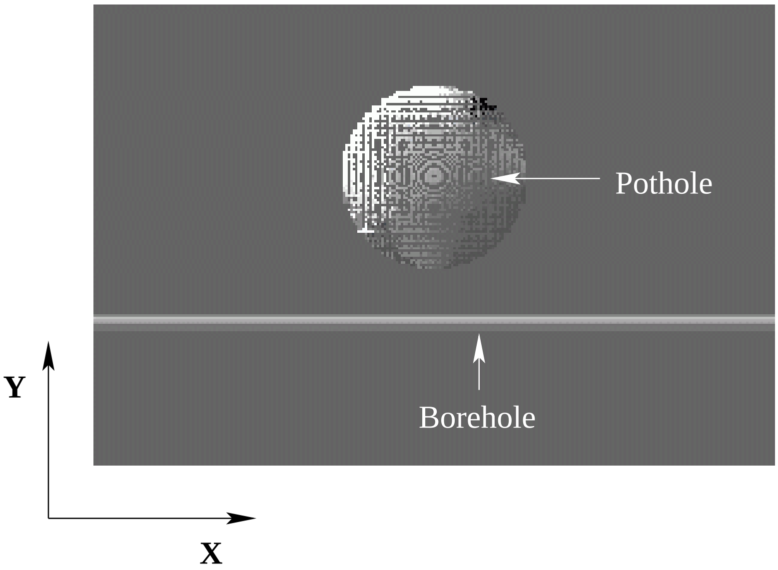

Figure 5.36: *A plane view (X-Z) imaging experiment 6.*

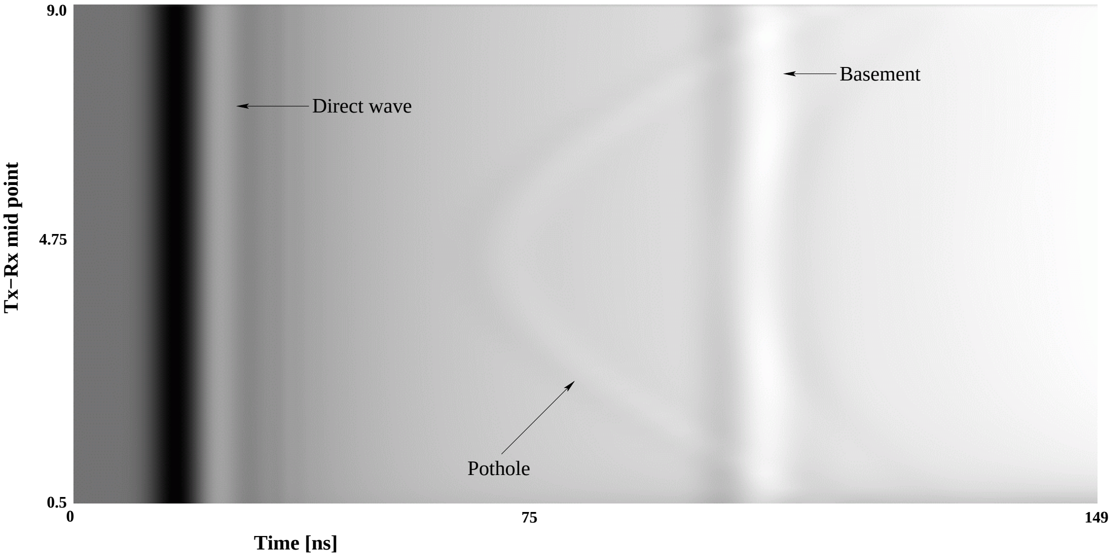

Figure 5.37: *A grey scale display of the received radar traces. Automatic gain control scaling has been applied to reduce high amplitudes and boosts small amplitudes. The conductivity of the host rock was 0.05mS/m. The pothole structure was placed at off-nadir location.*

5.7 A Parallel Implementation of the 3-D FDTD Algorithm

5.7.1 Introduction

Initially, the 3-D FDTD simulator has been implemented in the IDL programming language and thereafter the simulator has been implemented in the C programming code. It was noticed that the C code simulator is six times faster than the IDL code simulator. To ensure the accuracy and stability of the FDTD method, the discrete step size of the simulation needs to be set to less than 1/10 of the minimum significant wavelength. Therefore, for realistic 3-D simulations, there is a requirement for large matrices to be allocated and processed, which easily exceed the limit of a standard desktop PC in terms of memory and speed. In order to overcome these limitations, it is highly beneficial to make a parallel version of the FDTD algorithm. The FDTD algorithm can be described as a ’single program multiple data’ (SPMD) parallel architecture, which means that each process executes the same program. In this section, we will discuss the design and implementation of a parallel FDTD algorithm, implemented in C using Parallel Virtual Machine (PVM) as *middleware* running on a *Beowulf-type* Linux cluster.

5.7.2 Parallel Processor Implementation and Comparison of Serial to Parallel Version

The Radar Remote Sensing Group (RRSG) has a Beowulf Cluster called Gollach, which was the hardware benchmark for this work. The cluster hardware specifications are: one dual-CPU Intel Pentium II, 350 MHz, with 256 MB RAM and two single-CPU Intel Pentium II, 350 MHz, with 256 MB RAM per machine. The machines were connected to each other via a Fast Ether-Net 100 Mb switch.

The FDTD algorithm best fits into Flynn's taxonomy (Bannett, 2001) of parallel computers, as a single program multiple data (SPMD) type architecture. The slave processes behave according to set parameters, depending upon the sources, boundary conditions and material properties. Figure 5.38 shows the program flow of the parallel FDTD software implementation. The FDTD computational grid is divided equally between the slave processes, so that each slave process has an identical processing load, which ensures the efficiency of the parallel FDTD algorithm. The slave processes need to communicate with each other when it is at its data boundary. This 2-D interface data has been packed and communicated between the slave processes by using routines from the PVM library. The data is sent and received using the pvm_send() and pvm_recv() routines. The master process has been used only for initialisation of the slave processes.

Results and Discussions

The model geometry was the same as in experiment 2, except that a smaller computational size has been used (3.0 m, 2.2 m and 1.4 m in the $X-$,$Y-$,Z-directions respectively). Both the FDTD serial and parallel algorithms have been implemented successfully. Figure 5.39 shows the XPVM printout of the inter-communication between the processes, and Figure 5.40 shows the XPVM printout of the CPU utilisation, where green indicates computing and red indicates waiting on communication. The interpretation of this is that most of the processing time on the cluster is taken up with processing the data, and thus the parallel algorithm utilises the available computing resources efficiently.

A comparision of precessing time between the serial code simulation and the parallel code simulation is shown in Figure 5.41. A speed up of 2.7 was achieved, which corresponds to a 90% efficiency, where a speed of 3 for three slave processors is considered to be 100% efficient (Figure 5.42).

Due to CPU memory and speed limitations and the fact that there were only three nodes in the Gollach cluster, the speed-up tests were limited to a small data set. However, it is noted that, if the size of the data set size increases, the network load will scale up proportionately, and will consequently degrade the efficiency.

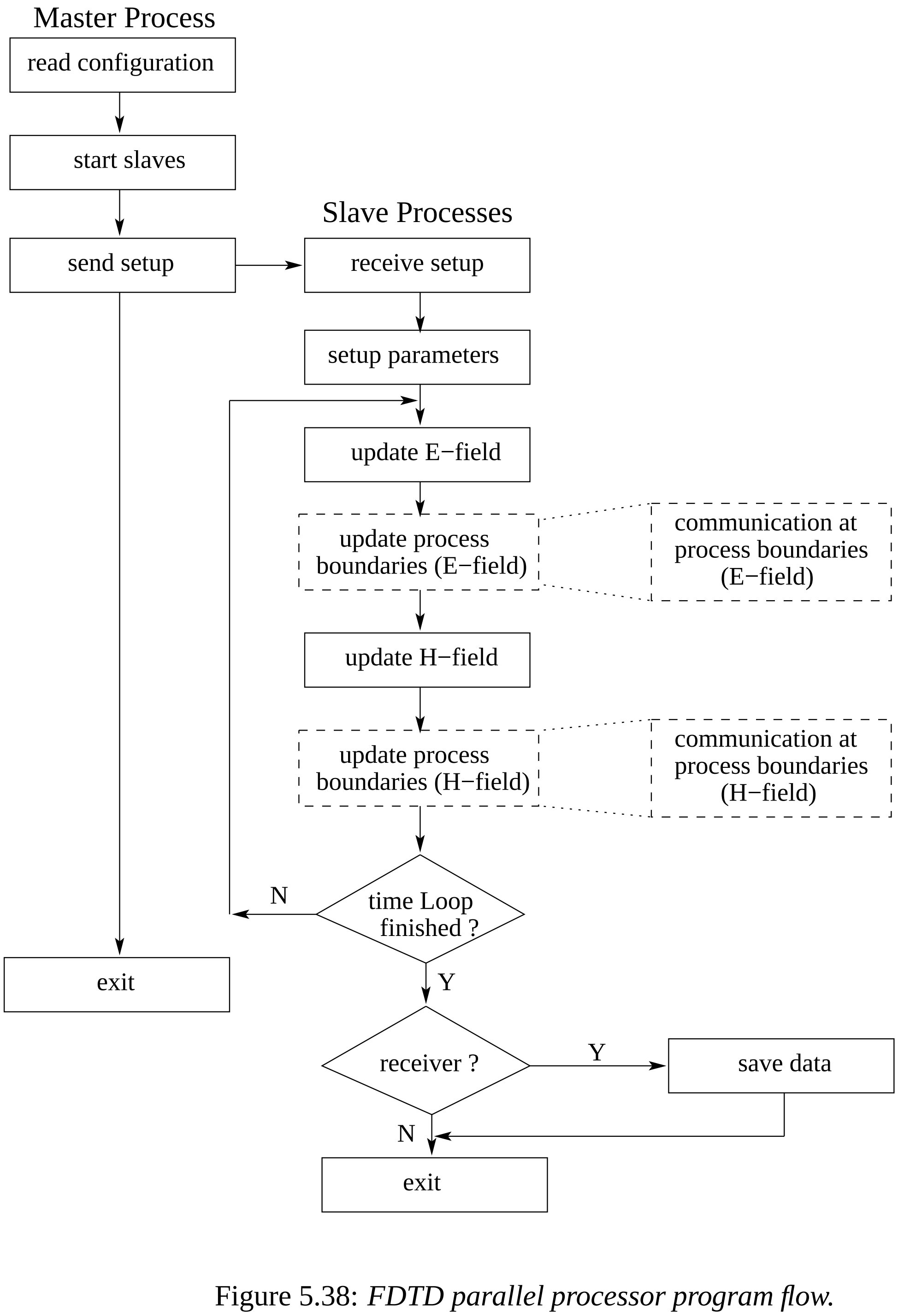

Figure 5.38: *FDTD parallel processor program flow.*

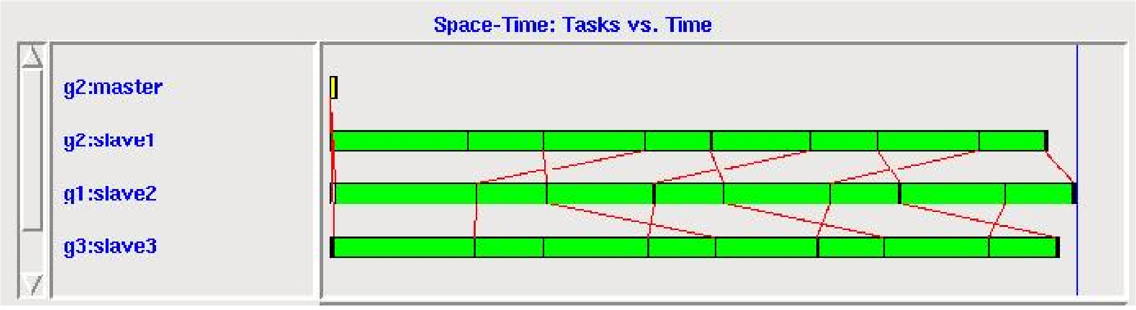

Figure 5.39: *Inter-communication between different nodes.*

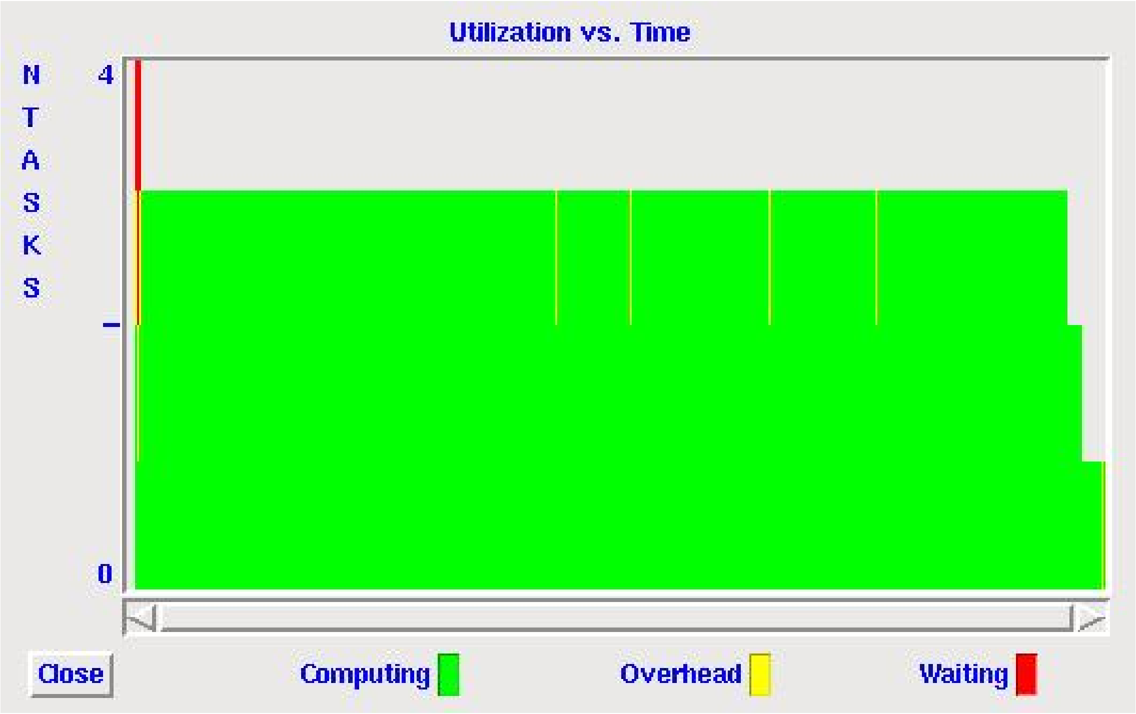

Figure 5.40: *CPU utilization in parallel process.*

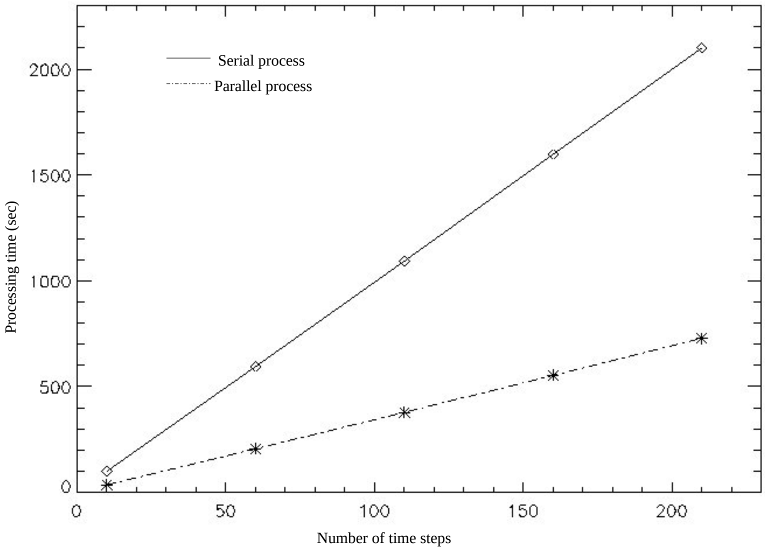

Figure 5.41: *Serial vs parallel processing time.*

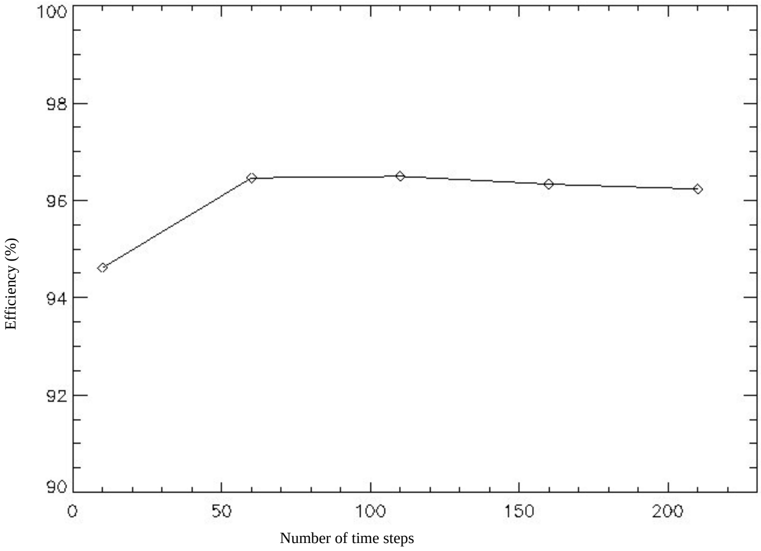

Figure 5.42: *Efficiency in parallel process.*

5.8 Summary

To summarize the discussion above, the 3-D FDTD code based on a UPML formation was implemented in Cartesian coordinates to study borehole EM wave propagation in a conductive medium. The performance of the UPML with regard to layered media propagation was tested and compared to published results (Gedney and Taflove, 1998), as shown in Appendix C. In this case, the reflection error achieved was below -75dB, which suggests that the UPML is a good absorber for layered media EM propagation studies. To illustrate some of the possible applications of the technique analysed herein, the code was used to simulate and analyse three particular subsurface geological conditions in 3-D, i.e. the propagation of EM waves in a sedimentary layer, the reflection from a geological reverse fault and the reflection from a pothole-type structure in a conductive host.

A first set of simulation experiment was carried out to study the propagation of EM waves in a sedimentary layer (sand-clay). A transillumination (cross-hole) data acquisition mode was employed. Furthermore, a borehole, which is modelled by an averaged staircase approximation, was added and the effect of such a borehole (e.g. borehole size and electrical properties of borehole mud) on the radar traces was discussed. When the thickness of the sand layer is close to the maximum wavelength of the transmitting pulse (3-dB point), a *guided wave* is propagated between two clay layers. It was also seen that the amplitude and signature of the radar traces vary with respect to the receiver location, with the transmitter fixed in the middle of the sand layer.

A second set of simulation study was carried out in a conductive medium, where a geological reverse fault was present. A common source data acquisition mode was employed. The hanging wall and the foot wall of the reverse fault were clearly visible. The scattering from the sharp discontinuity of the reverse fault interfered with the reflected wave from the fault surface. This effect was more dominant closer to the sharp discontinuity than further away. The scattering effect on the waveform received from the foot wall side was less, though, primarily due to the longer distance and the intrinsic attenuation in the host rock. The electrical property of the borehole mud and the size of the borehole, however, also had a significant effect on the received radar traces.

Finally, a simulation study that has been conducted to image a pothole-type structure in a conductive host. In this simulation experiment, the most usual borehole data acquisition mode, the common offsets mode, has been considered. The pothole structure has been placed in both nadir and off-nadir locations with respect to the borehole plane. When the target orebody structure is present at the off-nadir location with respect to the borehole plane, a 3-D FDTD is essential. The received traces have been displayed as wiggle plots, grey scale plots and colour scale plots. The effect of host rock conductivity on radar traces has also been investigated.

Realistic 3-D simulations, require large matrices to be allocated and processed, which easily exceed the limits of a standard desktop PC in terms of memory and speed. In order to overcome these limitations, it is highly beneficial to make a parallel version of the FDTD algorithm. The code was first written by using the IDL programming language and later was implemented by using the C programming language. As a result, the processing speed became six times faster. A parallel version of the code was then implemented by using the Message Passing Interface (PVM: Parallel Virtual Machine), which reduced both the computational time needed for the method analysed herein and also reduced the memory requirement. In this way, a speed up of 2.7 was achieved, which corresponds to a 90% efficiency, where a speed of 3 for three slave processors is considered to be 100% efficient.

In conclusion, then, it was found that this 3-D EM simulation tool is very useful for studying EM wave propagation in a complex geological medium. In future, the 3-D FDTD code needs to be modified to include borehole antenna structures and to study EM wave dispersion.

Chapter 6

Conclusions and Scope for Future Research

6.1 Conclusions

Borehole radar is an emerging electromagnetic tool in the mining industry, which is used to image subsurface orebodies at a high resolution. The primary concerns of using this tool are the attenuation of the EM wave in the host rock (the tragets has to be seen by the radar eye's), and the practical constraints encountered when using an antenna in a narrow borehole. The accurate, three-dimensional imaging of the subsurface orebody geometry by using two-dimensional aperture synthesis, however, requires many boreholes and is thus not economically feasible.

The detailed study of propagation of EM waves in the subsurface host rock and the subsequent effects, such as attenuation, dispersion and inhomogeneity, in detail is beyond the scope of this present thesis.

The main objectives of this thesis, therefore, have been to investigate of the following three aspects of borehole radar imaging:

1. Borehole synthetic aperture radar interferometry (InSAR) for high resolution 3-D subsurface imaging. An interferometric simulation study was conducted, using a sidelooking borehole radar antenna configuration to reconstruct the height of the subsurface orebody.

2. 3-D reconstruction of orebody structures by means a correlation type processing, using the magnitude images from multiple non-parallel boreholes. Range focusing was achieved by using both a matched filter and a deconvolution filter. This technique made use of a time- domain focusing algorithm to implement the azimuth

focusing. Azimuth focusing/migration to achieve high azimuth resolution is a very important issue in both radar as well as seismic imaging. Some unique features of the time-domain SAR focusing technique in the context of the borehole radar imaging have been discussed in detail.

3. 3-D finite difference time domain (FDTD) modelling of borehole radar EM wave propagation in a conductive medium. A 3-D FDTD code was thus written and implemented, using a UPML boundary absorber. The code was applied to geological settings, such as EM wave propagation in a layered sediment, reflection from a geological reverse fault, and reflection from a pothole-type structure. The 3-D simulations were carried out in different data acquisition modes, such as common offsets, common source, and transillumination mode. A borehole was added in the simulation, and the effect of the borehole size and the borehole mud on the received radar traces was studied as well. In order to overcome the limitations of large memory requirements and processing speed, a parallel version of the 3-D FDTD C code using Parallel Virtual Machine (PVM) has been implemented, and thereafter the results achieved have been discussed.

Interferometric Synthetic Aperture Radar (InSAR) is a well-established space-borne/air-borne technique for creating high-resolution images of the Earth's surface. An interferometric SAR simulation study was carried out by using a sidelooking antenna configuration in the borehole environment. The interferometric phase noise is a function of receiver noise, registration errors, temporal decorrelation, baseline decorrelation etc. A design analysis was performed in this context, and this can be very useful for any kind of interferometric experiment (space-borne/air-borne as well as in boreholes). In the case of an electro-magnetically transparent host rock and an isolated orebody geometry, where the layover problem is not pronounced, using a multiple borehole sidelooking antenna configuration, the subsurface orebody can be imaged with high resolution.

In general, though, the borehole radar antenna radiation pattern is omni-directional. In some real borehole radar imaging situations, the host rock may not be perfectly homogeneous (most importantly in lateral inhomogeneity), transparent, and the reflecting orebody surface may not be isolated. In those situations where the layover problem is seveir, there will be a superposition of signals from equal slant ranges from different directions, which will eventually degrade the quality of the interferometric phase and, hence, the reconstructed height. This technique will work properly, but these limitations need to be kept in mind before conducting a borehole InSAR experiment.

Moreover, the medium through which the EM wave propagates will also exhibit dispersion. The pioneer workers in the GPR field, such as Prof. Ian Mason (e.g. Simmat et al, GPR, 2002) and Prof. Gary Olhoeft (Olhoeft, G.R., Geophysics, 2000), have demonstrated that coherent addition (migration) does work with real GPR data (although there must have been some dispersion). The fact that such migration works in real GPR data sets shows that the dispersion effect does not completely prevent coherent processing. Furthermore, the fact that SAR (coherent addition) processing is possible, shows that the interferometric processing technique will work. As the radar signals (in the case of two borehole radars) travel through the same medium (assuming that the lateral inhomogeneity is not too severe), the dispersion will be common to both signals, and ought not to corrupt the interferometric phase. The spectral shift between the two signals gives rise to the interferometric phase, which will still be present. Therefore, it is still feasible to perform interferometric experiments (i.e. to produce an interferogram) to map bedrock surfaces, even though there might be dispersion.

In general, bandwidths of 75% of the centre frequency are typical for borehole radar, while Interferometric SAR (InSAR) systems have bandwidths that are typically less than 5% of the centre frequency. The subsurface orebody geometry can be reconstructed in 3-D by means of correlation-type processing, using magnitude images of multiple boreholes coming from different view angles, which is more suitable for wide-band/ultra wide-band borehole radar signals. A 3-D reconstruction method was thus developed and tested in this thesis by using a simulation of magnitude images from multiple borehole radars, as well as real acoustic images that had been captured in air and water media. In order to apply this reconstruction algorithm in a real borehole configuration, it is essential to calculate the grid spacing correctly. The sampling issue for 3-D reconstruction was consequently discussed in detail for a borehole trajectory fanning outward from the borehole centre. It was also discussed in detail how to solve the problem of rotational ambiguity that comes from using an omni-directional antenna, by using three non-collinear boreholes. A high signal-to-noise ratio is needed to apply this 3-D reconstruction algorithm, otherwise the reconstructed image quality would be degraded. In an over-populated region, especially of bodies with a steep slope, there will be false images. This problem can be tackled by using prior target body information (Barclay et al., 2003). In the context of the formation of focused images, a deconvolution filter would give a better range compressed image if the passband of the transducers was not flat in magnitude and linear in phase. A time domain azimuth focusing technique would be well suited for processing data acquired from deviating boreholes.

In this thesis, we used for the first time a 40kHz air-based sonar system in the laboratory environment to emulate ISAR data in the context of the real borehole experiment.

In the case of a homogeneous, isotropic and non-dispersive medium, we looked at straight-line wave propagation to calculate the azimuth and slant range positions. In a real situation, however, we would need an accurate EM propagation model. Firstly, this is necessary to focus the images captured in different boreholes. Secondly, it allows us to calculate the azimuth and range position correctly in the corresponding images. For this purpose, modelling the EM wave propagation in a complex geological environment and utilizing a similarly complex antenna structure are very important.

Modelling electromagnetic problems in three-dimensions is important, firstly, for understanding the physics of observed responses in complex media. Secondly, modelling of the EM wave is very useful for proper interpretation of the processed data. Thirdly, forward modelling can be used as a front-end tool to study the EM wave in the host rock before taking a real borehole measurement. For the purpose of modelling borehole EM propagation in a conductive medium, a 3-D FDTD code was written and implemented in a Cartesian coordinate system by using a UPML boundary wave absorber. The accuracy of the implemented code was first tested against published results. Thereafter, the code was used to simulate the EM responses from various geological settings. It was seen that, in the case of cross-well borehole EM wave propagation, the wave starts propagating as a guided wave when the thickness of the host layer is close to the significant wavelength (3-dB point) of the transmitting pulse. The radar traces, both transmitted as well as reflected, are affected by the size of the borehole and the electrical properties of the borehole mud. However, modelling of the borehole radar antenna was not a part of this present thesis. A practical borehole radar antenna modelling would be very useful for studying the borehole effects quantatively (e.g. frequency domain analysis).

A parallel version of the 3-D FDTD C code was implemented by using the Message Passing Interface (PVM: Parallel Virtual Machine), which reduces the computational time needed for the method analysed herein and requires less memory. A speed up to of 2.7 was achieved, which corresponds to a 90% efficiency, where a speed of 3 for three slave processors is considered to be 100% efficient. However, it is noted that, if the size of the data set were to increase, the network load would scale up proportionately, and would consequently lower the efficiency.

In conclusion, then, this thesis has investigated two quite different imaging approaches for 3-D subsurface imaging (Chapter 3 and 4) using a limited number of boreholes. To verify the borehole interferometric height reconstruction technique and issues, such as the effect of inhomogeneity, layover, and dispersion, we need real data. In the absence of real borehole data, the 3-D FDTD EM simulator can, however, be used to produce a subset of real data.

Signal processing techniques were explored in this thesis by using real sonar data, which can be applied to real borehole/EM simulation data. A useful simulation study was thus carried out in the context of real borehole radar measurements. A prior knowledge about the target orebody needs to apply the 3-D height reconstruction technique (Chapter 4) to image a surface structure successfully. In this case, too, in absence of other survey data being available, in the University environment, 3-D FDTD EM simulator can be utilized.

A version of our present 3-D FDTD simulator would make it easier to deal with large dimension 3-D simulations. Finally, the 3-D FDTD simulation is the only way of validating the proposed algorithm in realistic geological conditions.

6.2 Future Work

Scope for future work includes:

- The effect of the layover problem in the interferometric phase needs to be investigated in a real subsurface borehole environment. More work needs to be carried out to develop an algorithm to solve or at least reduce the layover problem in the interferometric phase.
- The reflection properties of the subsurface target orebody in a host rock need to be investigated. Future work is required to study the kind of reflection a subsurface orebody creates by taking into account the electrical properties of the subsurface host rock and the target orebody. A quantative analysis needs to be carried out to study the effect of dispersion on the interferometric height reconstruction technique under realistic geological conditions.
- The effect of over-populated/continuous regions on the 3-D reconstructed image, using multiple borehole radar magnitude images is worth investigating. This problem can be overcome by using prior orebody geometry information. Further work is, however, required to develop an algorithm based on the prior knowledge of the orebody structure (using, for example, the approach of Bayesian Inference) for resolving this problem (Barclay et al., 2003). In this regard, 3-D simulation data will be very useful in the absence of other geophysical survey data being available.
- Future work is required to calibrate accurately the 40kHz sonar system, compensating for the transducer's angular and spectral response to achieve better results.
- In both our 3-D image reconstruction techniques, we were considering a straight-line EM wave propagation in a homogeneous, isotropic and non-dispersive medium to calculate the azimuth and slant range positions. Future work would be required to calculate the range and azimuth position of the target by using an accurate EM wave propagation model (FDTD) in a realistic environment (i.e an inhomogeneous,

non-isotropic and dispersive medium). The azimuth focusing algorithm would also need to be modified to account for realistic EM propagation effects.

- 3-D FDTD modelling of EM wave propagation in a complex geological and antenna structure is very important. A realistic borehole radar antenna modelling will help us to study the borehole effects quantatively (e.g. frequency domain analysis). A realistic, non-homogeneous and dispersive medium could be included in investigating the effect of the host medium on three-dimensional imaging to establish limits before expensive trials are carried out.
- In order to model the cylindrical nature of the borehole more accurately, future work is required to implement the FDTD update equations in cylindrical coordinates. The code should be modified to take into account more realistic antenna configurations.
- It would be instructive and useful to investigate and explore the time domain SAR focusing algorithm to the data acquired in the SAR image formation mode therein by applying the 3-D reconstruction algorithm to the orebody geometry.
- The present 3-D FDTD code needs to be extended to take into account a near to far field transformation to calculate far field antenna pattern.

Appendix A

Computing Target Location in Three-dimension

The vector diagram shown in Figure A.1, represents a general dual pass interferometric imaging geometry in three dimension. Table A.1 contains a list of parameters which define the vector geometry of Figure A.1. As shown in the Figure A.1, $\overrightarrow{r_1}$ is obtained by solving the following three simultaneous equations:

$$\overrightarrow{b} \cdot \overrightarrow{r_1} = \left|\overrightarrow{b}\right| \cdot \left|\overrightarrow{r_1}\right| \cos\delta_1 = r_1 b \sin\theta \tag{A.1}$$

$$\left|\overrightarrow{r_1}\right| = r_1 \tag{A.2}$$

$$\overrightarrow{v_1} \cdot \overrightarrow{r_1} = \frac{c_1 r_1 f_{D1}}{2 f_1} \tag{A.3}$$

We simplify the notation by making the following variable substitutions:

$$\overrightarrow{r_1} \equiv \overrightarrow{r} = r_x \hat{x} + r_y \hat{y} + r_z \hat{z} \tag{A.4}$$

$$\overrightarrow{b} = b_x \hat{x} + b_y \hat{y} + b_z \hat{z} \tag{A.5}$$

$$\overrightarrow{v_1} \equiv \overrightarrow{v} = v_x \hat{x} + v_y \hat{y} + v_z \hat{z} \tag{A.6}$$

$$f_{D1} = f_D \tag{A.7}$$

$$c_1 = c \tag{A.8}$$

The solution of range from antenna to point target is given as

$$r_x = -\frac{b_y v_z \rho - b_y \left(\frac{c r f_D}{2f}\right) - b_z v_y \rho + (r b \sin\theta) v_y}{-b_x v_y + b_y v_x} \tag{A.9}$$

$$r_y = \frac{-v_x b_z \rho + v_x(rb\sin\theta) + v_z b_x \rho - b_x\left(\frac{crf_D}{2f}\right)}{-b_x v_y + b_y v_x} \tag{A.10}$$

$$r_z = \rho \tag{A.11}$$

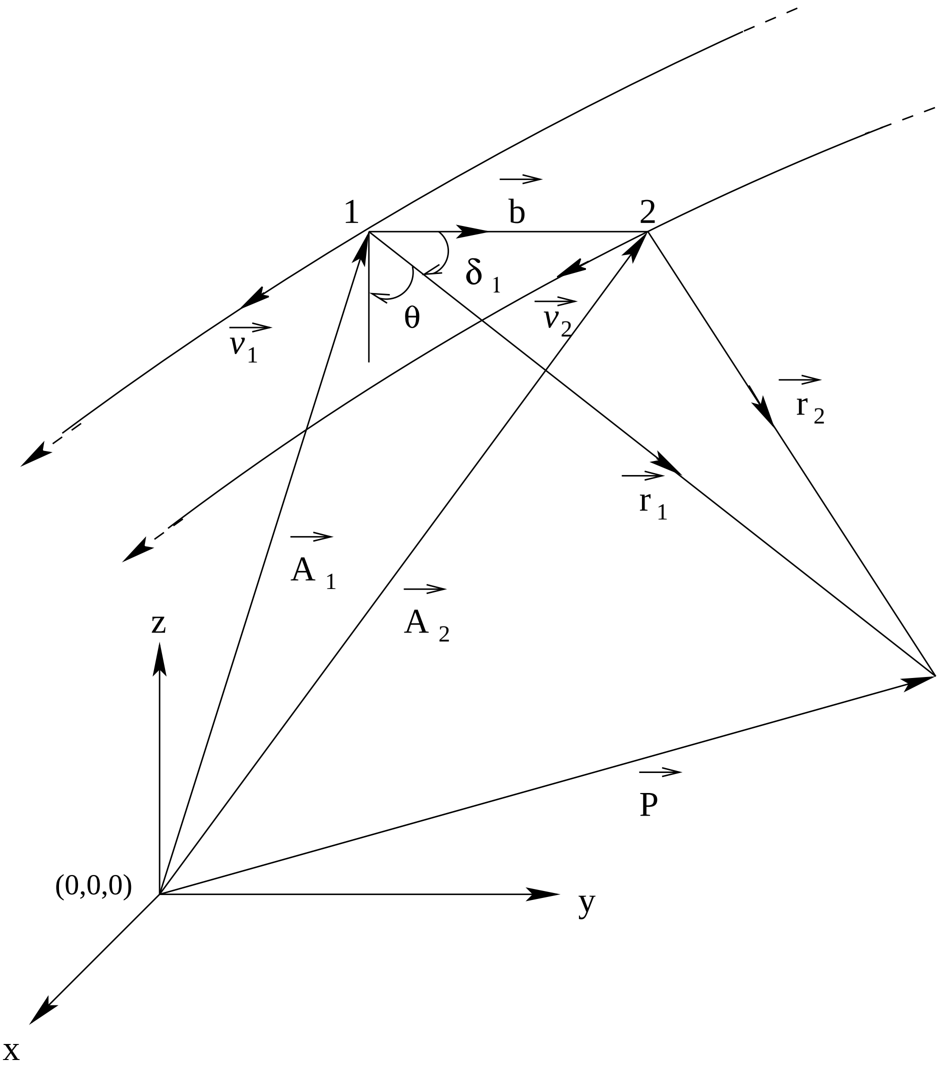

Figure A.1: *Three-dimensional vector model of a dual-pass InSAR system.*

where ρ is the root of the quadratic equation

$$\alpha\rho^2 + \beta\rho + \gamma = 0$$

$$\begin{aligned} \alpha &= v_x^2 b_z^2 + v_y^2 b_z^2 + v_z^2 b_x^2 + b_x^2 v_y^2 + b_y^2 v_x^2 + b_y^2 v_z^2 \\ &\quad -2v_y b_y v_z b_z - 2v_x v_z b_x b_z - 2b_x v_y b_y v_x \qquad \text{(A.12)} \\ \beta &= (rb\sin\theta)\left(2v_x v_z b_x + 2v_y b_y v_z - 2b_z v_x^2 - 2b_z v_y^2\right) + \end{aligned}$$

Parameter	**Symbol**
Propagation speed	c_1
Location of antenna 1	$\overrightarrow{A_1} \equiv (A_{1x}, A_{1y}, A_{1z})$
Location of antenna 2	$\overrightarrow{A_2} \equiv (A_{2x}, A_{2y}, A_{2z})$
Velocity of antenna 1	$\overrightarrow{v_1} \equiv (v_{1x}, v_{1y}, v_{1z})$
Velocity of antenna 2	$\overrightarrow{v_2} \equiv (v_{2x}, v_{2y}, v_{2z})$
Point target location	$\overrightarrow{P} \equiv (P_x P_y, P_z)$
Range from 1 to point P	$\overrightarrow{r_1} \equiv (r_{1x}, r_{1y}, r_{1z})$
Range from 2 to point P	$\overrightarrow{r_2} \equiv (r_{2x}, r_{2y}, r_{2z})$
Doppler shift between 1 and P	f_{D1}
Doppler shift between 1 and P	f_{D2}

Table A.1: *Parameter definitations used in 3-D analysis.*

$$\left(\frac{crf_D}{2f}\right)(2v_xb_xb_z - 2b_x^2v_z + 2v_yb_yb_z - 2v_zb_y^2) \tag{A.13}$$

$$\begin{aligned} \gamma &= \left(\frac{crf_D}{2f}\right)^2 (b_y^2 + b_x^2) + (rb\sin\theta)^2(v_x^2 + v_y^2) \\ &\quad + \left(\frac{crf_D}{2f}\right)(rb\sin\theta)(-2v_yb_y - 2v_xb_x) \\ &\quad - r^2b_y^2v_x^2 - r^2v_y^2b_x^2 + 2r^2v_yb_xb_yv_x \end{aligned} \tag{A.14}$$

There are two solutions corresponding to the two roots of the quadratic. The ambiguity can be resolved by selecting the solution closest to the expected target location.

Appendix B

Finite Difference Time Domain Method for Solving Maxwell's Equations

B.1 Introduction

The Finite Difference Time Domain (FDTD), introduced by K.S.Yee in 1966, is a full-wave, dynamic, and powerful tool for solving the Maxwell's equations. The FDTD method is frequently used to analyse the EM properties of complex structures. The fundamental ingredient of the algorithm involves direct discretizations of the time dependent Maxwell's equations by writing the spatial and time derivatives in a central finite difference form. This approximation is second-order accurate in both space and time, and it requires the electric and magnetic fields to be offset from one another in space.

The FDTD update algorithm requires the electric and magnetic fields to be updated at staggered half-time steps. This algorithm is explicit, so new values of EM field components depend only on these values at previous time and half-time steps.

B.2 Implementation of Finite Difference Time Domain Algorithm

In a general form, the curl of Maxwell's equations can be written as

$$\bigtriangledown \times \vec{E} = -\mu_0\mu_r \cdot \frac{\delta \vec{H}}{\delta t} \tag{B.1}$$

$$\bigtriangledown \times \vec{H} = \epsilon_0\epsilon_r \cdot \frac{\delta \vec{E}}{\delta t} + \sigma\vec{E} \tag{B.2}$$

where ϵ_r, μ_r and σ are known as the relative permittivity, the relative permeability, and the electric conductivity of the material respectively.

Figure B.1 shows a standard Yee's lattice. Notice that all electric field components lie tangentially on the lattice boundaries, and are half-cell apart from the reference point (i, j, k). On the other hand, all magnetic field components lie normally on the surfaces of the Yee's cell, and are located half-cell apart from the electric fields defined in the cell.

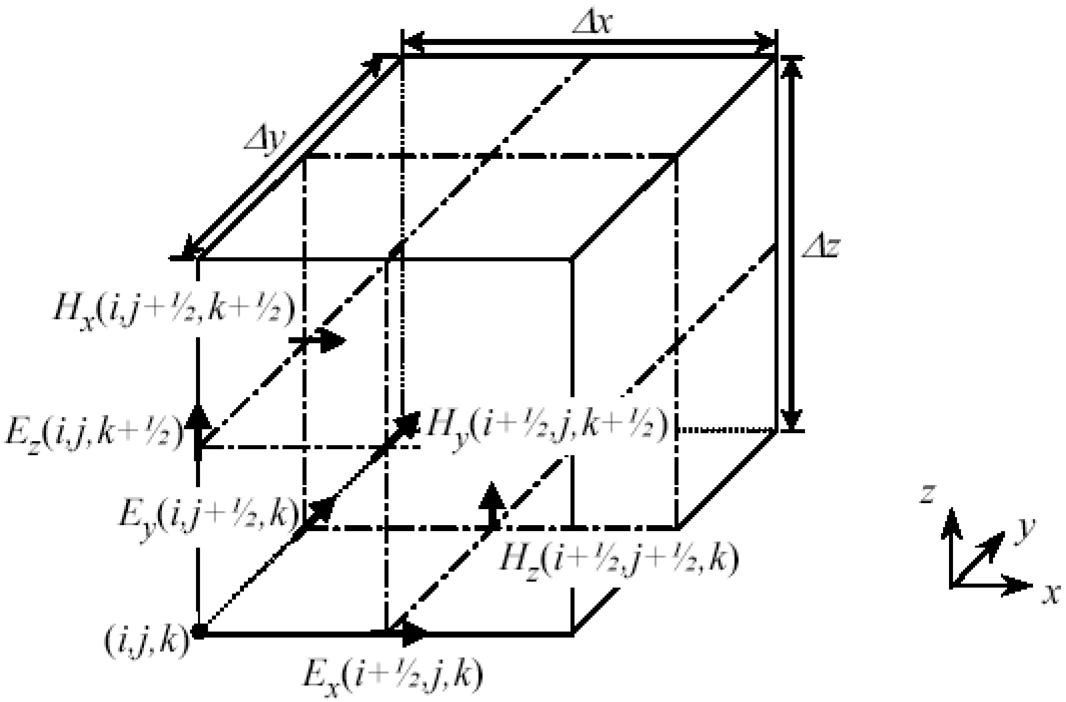

Figure B.1: *A standard Yee's lattice.*

In the FDTD notation, we use following notations to discretize the spatial and time coordinates $(x, y, z; t)$ and field quantities as

$$(x, y, z; t) \Rightarrow (i \bigtriangleup x, j \bigtriangleup y, k \bigtriangleup z; n \bigtriangleup t) \Rightarrow (i, j, k; n) \tag{B.3}$$

where i, j, k are positive integer and represent the spatial index and n is a positive integer and represent time index.

The field quantities are represented as

$$E_\beta(x, y, z; t) \quad \Rightarrow \quad E_\beta(i \bigtriangleup x, j \bigtriangleup y, k \bigtriangleup z; n \bigtriangleup t) = E^n_\beta(i, j, k) \quad (\beta \Rightarrow x, y, z) \tag{B.4}$$

$$H_\beta(x, y, z; t) \quad \Rightarrow \quad H_\beta(i \bigtriangleup x, j \bigtriangleup y, k \bigtriangleup z; (n + \frac{1}{2}) \bigtriangleup t) = H^{n+\frac{1}{2}}_\beta(i, j, k) \tag{B.5}$$

The Maxwell's equations (Equation B.1 and B.2) can be written in the matrix form as

$$\begin{bmatrix} \frac{\delta E_z}{\delta y} - \frac{\delta E_y}{\delta z} \\ \frac{\delta E_x}{\delta z} - \frac{\delta E_z}{\delta x} \\ \frac{\delta E_y}{\delta x} - \frac{\delta E_x}{\delta y} \end{bmatrix} = -\mu_0\mu_r \begin{bmatrix} \frac{\delta H_x}{\delta t} \\ \frac{\delta H_y}{\delta t} \\ \frac{\delta H_z}{\delta t} \end{bmatrix} \tag{B.6}$$

$$\begin{bmatrix} \frac{\delta H_z}{\delta y} - \frac{\delta H_y}{\delta z} \\ \frac{\delta H_x}{\delta z} - \frac{\delta H_z}{\delta x} \\ \frac{\delta H_y}{\delta x} - \frac{\delta H_x}{\delta y} \end{bmatrix} = \epsilon_0\epsilon_r \begin{bmatrix} \frac{\delta E_x}{\delta t} \\ \frac{\delta E_y}{\delta t} \\ \frac{\delta E_z}{\delta t} \end{bmatrix} + \begin{bmatrix} E_x \\ E_y \\ E_z \end{bmatrix} \tag{B.7}$$

Since the procedure for driving all six equations is quit similar, herein we are deriving simply one component of electric (E_x) and magnetic field (H_x).

Expanding the first equation of B.6, one gets

$$\mu_0\mu_r\frac{\delta H_x}{\delta t} = \frac{\delta E_y}{\delta z} - \frac{\delta E_z}{\delta y} \tag{B.8}$$

By referring the field spatial position in Yee's cell, we can write

$$\frac{H_x^{n+\frac{1}{2}}(i,j+\frac{1}{2},k+\frac{1}{2}) - H_x^{n-\frac{1}{2}}(i,j+\frac{1}{2},k+\frac{1}{2})}{\triangle t} = \left\{\frac{1}{\mu_0\mu_r(i,j+\frac{1}{2},k+\frac{1}{2})}\right\}\cdot$$
$$\left\{\frac{E_y^n(i,j+\frac{1}{2},k+1) - E_y^n(i,j+\frac{1}{2},k)}{\triangle z} - \frac{E_z^n(i,j+1,k+\frac{1}{2}) - E_z^n(i,j,k+\frac{1}{2})}{\triangle y}\right\}$$

The final update expression of $H_x^{n+\frac{1}{2}}(i,j+\frac{1}{2},k+\frac{1}{2})$ is given by

$$H_x^{n+\frac{1}{2}}(i,j+\frac{1}{2},k+\frac{1}{2}) = H_x^{n-\frac{1}{2}}(i,j+\frac{1}{2},k+\frac{1}{2}) + \left\{\frac{\triangle t}{\mu_0\mu_r(i,j+\frac{1}{2},k+\frac{1}{2})}\right\}$$
$$\left\{\frac{E_y^n(i,j+\frac{1}{2},k+1) - E_y^n(i,j+\frac{1}{2},k)}{\triangle z} - \frac{E_z^n(i,j+1,k+\frac{1}{2}) - E_z^n(i,j,k+\frac{1}{2})}{\triangle y}\right\}$$

The update equation of $H_y^{n+\frac{1}{2}}(i+\frac{1}{2},j,k+\frac{1}{2})$ and $H_z^{n+\frac{1}{2}}(i+\frac{1}{2},j+\frac{1}{2},k)$ can be derived in the similar fashion.

Expanding the first equation of B.7, one gets

$$\epsilon_0\epsilon_r\frac{\delta E_x}{\delta t} + \sigma E_x = \frac{\delta H_z}{\delta y} - \frac{\delta H_y}{\delta z} \tag{B.9}$$

Similarly, by referring the field spatial position in Yee's cell, we can write

$$\epsilon_0\epsilon_r(i+\frac{1}{2},j,k+\frac{1}{2})\frac{E_x^{n+1}(i+\frac{1}{2},j,k)-E_x^n(i+\frac{1}{2},j,k)}{\triangle t} \quad + \quad \sigma(i+\frac{1}{2},j,k)E_x^{n+\frac{1}{2}}(i+\frac{1}{2},j,k) = \left\{\frac{H_z^{n+\frac{1}{2}}(i+\frac{1}{2},j+\frac{1}{2},k)-H_z^{n+\frac{1}{2}}(i+\frac{1}{2},j-\frac{1}{2},k)}{\triangle y} \quad - \right. \left. \frac{H_y^{n+\frac{1}{2}}(i+\frac{1}{2},j,k+\frac{1}{2})-H_y^{n+\frac{1}{2}}(i+\frac{1}{2},j,k-\frac{1}{2})}{\triangle z}\right\}$$

Since $E_x^{n+\frac{1}{2}}(i+\frac{1}{2},j,k)$ does not exist in this discretization system, it can be further approximated by an average of $E_x^n(i+\frac{1}{2},j,k)$ and $E_x^{n+1}(i+\frac{1}{2},j,k)$. The final expression of $E_x^n(i+\frac{1}{2},j,k)$ is given by

$$\begin{aligned} E_x^{n+1}(i+\frac{1}{2},j,k) \quad = \quad & \left(\frac{2\epsilon_0\epsilon_r(i+\frac{1}{2},j,k+\frac{1}{2})-\triangle t\sigma(i+\frac{1}{2},j,k)}{2\epsilon_0\epsilon_r(i+\frac{1}{2},j,k+\frac{1}{2})+\triangle t\sigma(i+\frac{1}{2},j,k)}\right)E_x^n(i+\frac{1}{2},j,k)+ \\ & \left\{\frac{2\triangle t}{2\epsilon_0\epsilon_r(i+\frac{1}{2},j,k+\frac{1}{2})+\triangle t\sigma(i+\frac{1}{2},j,k)}\right\}\cdot \\ & \left\{\frac{H_z^{n+\frac{1}{2}}(i+\frac{1}{2},j+\frac{1}{2},k)-H_z^{n+\frac{1}{2}}(i+\frac{1}{2},j-\frac{1}{2},k)}{\triangle y} - \right. \\ & \left. \frac{H_y^{n+\frac{1}{2}}(i+\frac{1}{2},j,k+\frac{1}{2})-H_y^{n+\frac{1}{2}}(i+\frac{1}{2},j,k-\frac{1}{2})}{\triangle z}\right\} \end{aligned}$$

The update equation of $E_y^{n+1}(i,j+\frac{1}{2},k)$ and $E_z^{n+1}(i,j,k+\frac{1}{2})$ can be derived in the similar fashion.

B.3 Accuracy and Stability Criteria

It is very critical to properly select the spatial steps, $\triangle x$, $\triangle y$ and $\triangle z$, and the time step $\triangle t$ in order to secure the accuracy and the stability of the computations. A good choice for selection of the spatial steps is to set them to be at most one-fifteenth or one-twentieth of the minimum wavelength within the frequency range of interest (Taflove, 1995), i.e.,

$$\triangle x_{max}, \triangle y_{max} \text{ and } \triangle z_{max} \leqslant \frac{1}{15}\lambda_{min} \text{ or } \frac{1}{15}\lambda_{max} \tag{B.10}$$

where

$$\lambda_{min} = \frac{c}{f_{max}\sqrt{\mu_{r,max}\epsilon_{r,max}}} \tag{B.11}$$

and c is the speed of light in the free-space, μ_{max} and ϵ_{max} are the maximum value relative permeability and relative permittivity of the material in the computational domain, and f_{max} indicates the upper limit of the frequency range of interest.

The stability of FDTD algorithm is ensured by choosing the time step, $\triangle t$, to satisfy the inequality:

$$\triangle t \leqslant \frac{1}{v_{max}\sqrt{\left(\frac{1}{\triangle x}\right)^2 + \left(\frac{1}{\triangle y}\right)^2 + \left(\frac{1}{\triangle z}\right)^2}} \tag{B.12}$$

or

$$\triangle t \leqslant \frac{dtfactor}{v_{max}\sqrt{\left(\frac{1}{\triangle x}\right)^2 + \left(\frac{1}{\triangle y}\right)^2 + \left(\frac{1}{\triangle z}\right)^2}} \tag{B.13}$$

where v_{max} is the maximum velocity in the lattice. Equation B.12 or B.13 is known as the Courant stability condition. The factor, $dtfactor$, is bounded between zero and one, and usually chosen as either 0.95 or 0.995. This factor influence the time of computation but not affect the accuracy of computations.

Appendix C

Validation of the FDTD code implemented by using UPML

To match the PML to a material, the material should extend normally through the PML. From Equation 5.4 (see section 5.2.1), we have seen that the relative permittivity of the material is involved in calculating the UPML parameter σ_{opt}, the optimum value of σ in UPML wall. In the case of layer medium propagation, there will be inhomogeneity along the axial direction. If we thus choose different values of σ_{opt} at different positions along the inhomogeneous axis, then we are violating Gauss's Law, which will lead to instability. To avoid such instability, there must be only one value of σ_{opt} within each of the inhomogeneous axes. Figure C.1 shows a 40x40-cell TE$_z$ FDTD grid, where a 10-cell polynomial-graded UPML has been used. There are two half-space regions, one free space and one conductive. The conductive medium is modelled with relative dielectric permittivity $\epsilon_r = 10$ and conductivity $\sigma = 0.3$ S/m, and extends with these parameters completely through the UPML to its PEC outer boundary. The square grid size was chosen as $\triangle$x=0.4mm and $\triangle$y=0.4mm. We chose a time-step equal to 2.924 ps, which is 0.98 times the Courant limit. The grid was excited by applying a vertical electric current source at the centre of the grid, two cells above the conductive half-space. The source used here is the first derivative of the Blackman-Harris window function Harris (1978); Chen et al. (1997) with a nominal frequency of 11 GHz.

The E-field is probed at point A, two cells above the conductive half-space and two cells from the left PML surface, and at point B, two cells from the bottom and left PML surface, in the conductive half-space, as shown in Figure C.1. Time-stepping runs over 1000 iterations, well past the steady-state response. In this case, the reference solution E$_{ref}\ |_{i,j}^{n}$ at the grid of the same (i, j) locations of A and B was obtained by extending the grid from

40x40 cell to 1240x1240. The reflection error at time step n was calculated by

$$\mathrm{R}_{error} \,|_{i,j}^{n} = \frac{\mathrm{E}_y \,|_{i,j}^{n} - \mathrm{E}_{y,ref} \,|_{i,j}^{n}}{\mathrm{E}_{y,ref,max}} \tag{C.1}$$

The reflection errors at point A and B are shown in Figure C.2 using the UPML parameters $\sigma_{max} = 1.2\sigma_{opt}$, $k_{max} = 1$, and $m = 3.5$, where σ_{opt} is given by Equation 5.4. An average value of $\epsilon_r = 5.5$ was chosen for the left and right side of the UPML to calculate the value of σ_{opt}. For the bottom, $\epsilon_r = 10$ and for the top $\epsilon_r = 1$ has been chosen for the σ_{opt} calculation. The reflection error at both points is shown in Figure C.2. The error at both the points is below -75 dB, in agreement with Gedney and Taflove (1998).

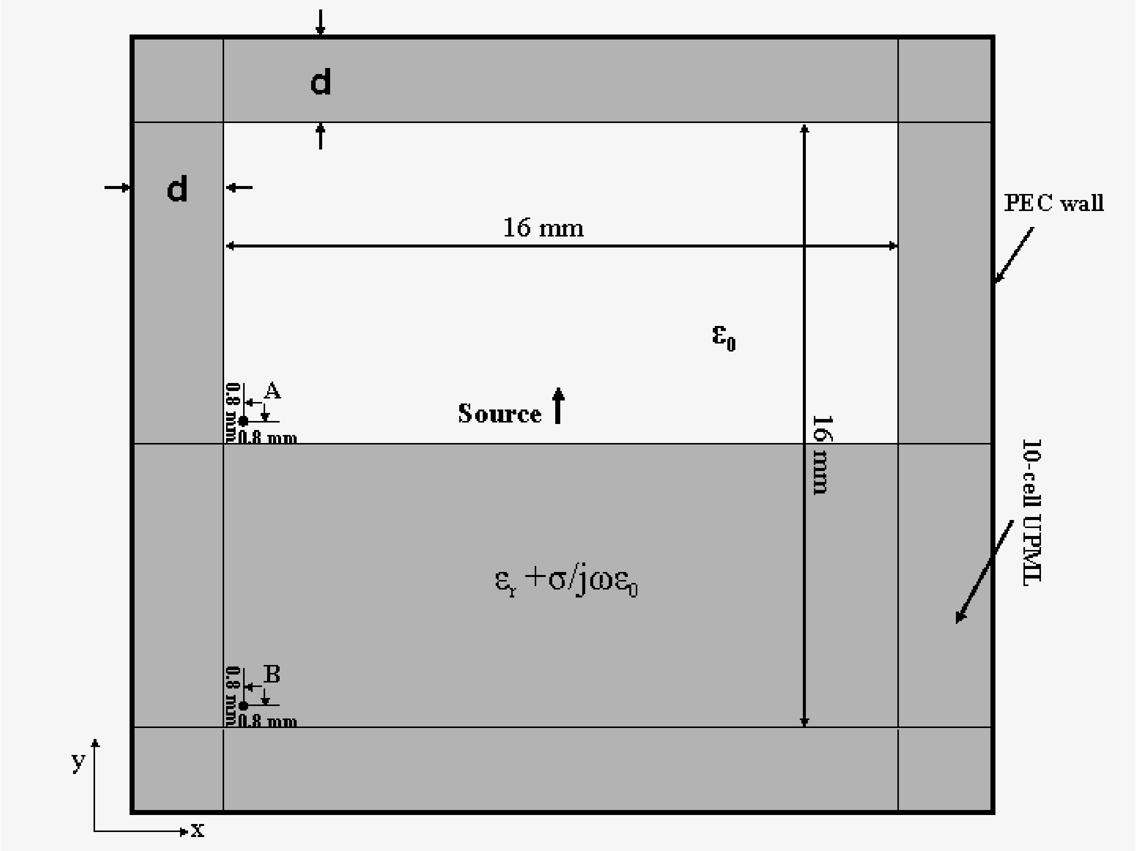

Figure C.1: *Geometry of the FDTD simulation model of a TE$_Z$ polarized wave excited by a vertical electrical current source above a lossy half space.*

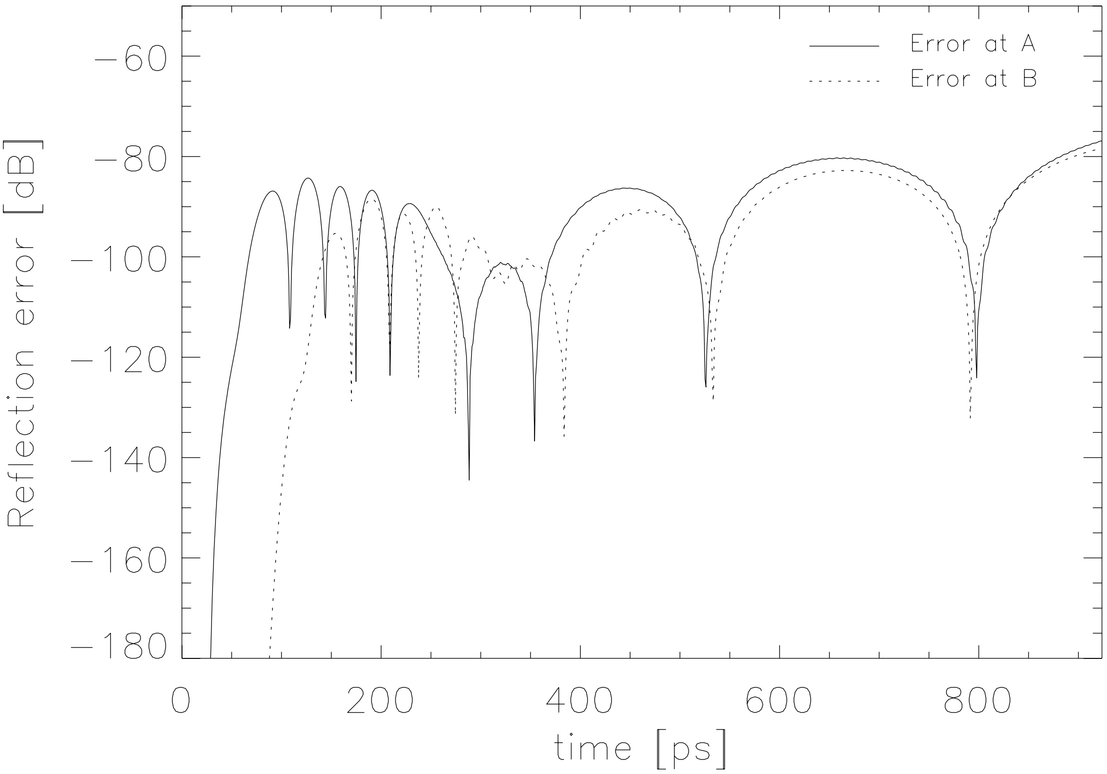

Figure C.2: *Relative error at points A and B with a 10-cell UPML.*

Bibliography

Alumbaugh, D.L. and G.A. Newman (1996), Electromagnetic modeling of perfect conductors in a arbitrary host, *in* 'SEG 1996 International Exposition and 66nd Annual Meeting', Society of Exploration Geophysicists.

Annan, A.P. (1996), 'Transmission dispersion and GPR', *Journal of Environmental Engineering and Geophysics* **0**, 125–136.

Annan, A.P. and J.L. Davis (1976), 'Impulse radar sounding in permafrost', *Radio Science* **11**, 383–394.

Annan, A.P. and J.L. Davis (1977), 'Radar Range Analysis for Geological Materials', *Report of Activities: Part B. Geological Survey of Canada* **77**(1B), 117–124.

Ashok, A. (2001), Implementation and Analysis of A Bayesian Approach to Topographic Reconstruction with Multiple Antenna Synthetic Aperture Radar Interferometry, Master's thesis, University of Cape Town.

Ashok, A. and A.J. Wilkinson (2001), Topographic Mapping with Multiple Antenna SAR Interferometry: A Bayesian Model-Based Approach, *in* 'Proceedings of IGARSS'.

Balanis, C.A. (1989), *Advanced engineering electromagnetics*, John Wiley and Sons, New York.

Balanis, C.A. (1996), *Antenna Theory: Analysis and Design*, John Wiley and Sons, New York.

Bamler, E. and B. Schattler (1993), *SAR Data Acquision and Image Formation*, Chapter 3, in book Geocoding: ERS-1 SAR Data and Systems.

Bamler, R. and P. Hartl (1998), 'Synthetic Aperture Radar Interferometry', *Inverse Problems* **14**(4), 1–54.

Bannett, T. (2001), Development of a parallel SAR processor on a Beowulf cluster, Master's thesis, University of Cape Town.

Barclay, P.J., M.P. Hayes and P.T. Gough (2003), ‘Reconstructing seafloor bathymetry with a multi-frequency, multi-channel broadband InSAS using belief propagation’, *Oceans, IEEE/MTS* pp. 2149–2155.

Bellefleur, G. and M. Chouteau (2001), ‘Massive sulphide delineation using borehole radar: Tests at the McConnell nickel deposit, Sudbury, Ontario’, *Journal of Applied Geophysics* **47**, 45–61.

Berenger, J.-P. (1994), ‘A Perfectly Matched Layer for the Absorption of Electromagnetic Waves’, *Journal of Computational Physics* **114**(1), 185–200.

Berenger, J.-P. (1996*a*), ‘An Anisotropic Perfectly Matched Layer-Absorbing Medium for the Truncation of FDTD Lattices’, *IEEE Transactions on Antennas and Propagation* **44**, 1630–1639.

Berenger, J.-P. (1996*b*), ‘Perfectly matched layer for the FDTD solution of wave-structure interaction problems’, *IEEE Transactions on Antennas and Propagation* **51**, 110–117.

Berenger, J.-P. (1997), ‘Improved PML for the FDTD solution of wave-structure interaction problems’, *IEEE Transactions on Antennas and Propagation* **45**, 466–473.

Berkhout, A.J. (1981), ‘Wave field extrapolation techniques in seismic migration, a tutorial’, *Geophysics* **46**(12), 1638–1656.

Berlin, G.L., M.A. Tarabzouni, A.H. Al-Naser, K.M. Sheikho and R.W. Larson (1986), ‘SIR-B Subsurface Imaging of a Sand-Buried Landscape: Al Labbah Plateau, Saudi Arabia’, *IEEE Transactions on Geoscience and Remote Sensing* **24**(4), 595–602.

Bradley, J.A. and D.L. Wright (1987), ‘Microprocessor-based data-aquisition system for a borehole radar’, *IEEE Transactions on Geoscience and Remote Sensing* **GE-25**, 441–447.

Bristow, C.S. (2004), GPR in Sediments: Recent advances in stratigraphic applications, *in* ‘Proceedings of 10th International Conference on GPR’, pp. 569–572.

Bristow, C.S. and H.M. Jol (2003), Ground Penetrating Radar in Sediments, *in* ‘Geological Society London Special Publication 211’.

Cai, J. and G.A. McMechan (1999), ‘2-D ray-based tomography for velocity, layer shape, and attenuation from GPR’, *Geophysics* **64**, 1579–1593.

Cardarelli, E., C. Marrone and L. Orlando (2003), ‘Evaluation of tunnel stability using integrated geophysical methods’, *Journal of Applied Geophysics* **52**, 93–102.

Chen, Y.-H. and M.L. Oristaglio (2002), ‘A modeling study of borehole radar for oil-field applications’, *Geophysics* **67**(5), 1486–1494.

Chen, Y.-H., W.C. Chew and M.L. Oristaglio (1997), ‘Application of perfectly matched layers to the transient modeling of subsurface problems’, *Geophysics* **62**(6), 1730–1736.

Chew, W.C. and W.H. Weedon (1994), ‘A 3D perfectly matched medium from modified Maxwell’s equations with stretched coordinates’, *IEEE Microwave and Guided Wave Letters* **4**, 599–604.

Church, R.H., W.E. Webb and J.B. Salsman (1988), Dielectric Properties of Low-loss Minerals, Technical report, Report of Investigations 9194, US Bureau of Mines.

Claassen, D.M. (1995), Electromagnetic Characterisation of a Wideband Borehole Radar Imaging System, PhD thesis, University of Oxford.

Clarke, R.H. (1979), *Acoustic and Electromagnetic Waves Propagating in a Tenuous Random Medium*, Imperial College, London.

Clarke, R.H. and J. Brown (1980), *Diffraction Theory and Antennas*, Ellis Horwood Limited,Chichester.

Clement, W.P. and M.D. Knoll (1998), Tomographic Inversion Of Crosshole Radar Data: Confidence In Results, *in* ‘Proceedings of the Symposium on the Application of Geophysics to Environmental and Engineering Problems’, pp. 553–562.

Commer, M. and G. Newman (2004), ‘A parallel finite-difference approach for 3D transient electromagnetic modeling with galvanic sources’, *Geophysics* **69**(5), 1192–1202.

Cook, C.E. and M. Bernfeld (1993), *Radar Signals - An Introduction to Theory and Application*, Artech House, Norwood, MA.

Coon, J.B., J.C. Fowler and C.J. Schafers (1981), ‘Experimental uses of short pulse radar in coal seams’, *Geophysics* **46**, 1163–1168.

Curlander, J.C. and R.N. McDonough (1991), *Synthetic Aperture Radar: Systems and Signal Processing*, John Wiley and Sons, New York.

Daily, W. (1984), ‘Underground oil-shale retort monitoring using geotomography’, *Geophysics* **49**, 1701–1707.

Daniels, D.J. (1996), *Surface Penetrating Radar*, Institute of Electrical Engineers (United Kingdom).

Daniels, D.J., D.J. Gunton and H.F. Scott (1988), 'Introduction to subsurface radar', *IEE Proceedings* **135**(4), 277–320.

Davis, J.L. and A.P. Annan (1989), 'Ground-penetrating radar for high-resolution mapping of soil and rock', *Geophysical Prospecting* **37**, 531–551.

Debye, P. (1929), 'Polar molecules', *Chemical Catalog Co., NY* .

Dines, K.A. and R.J. Lytle (1979), 'Computerized geophysical tomography', *Proceedings of the IEEE* **67**, 1065–1073.

Domik, G. and F. Leberl (1987), 'Image based SAR product simulation', *Proc. American Society of Photogrammetry and Remote Sensing, 53rd Annual Convention, Baltimore, MD* pp. 355–364.

Doyle, G.S. and M.R. Inggs (2002), Prospects for Borehole Radar In Kimberlite Pipe Dimensioning: Venetia Geological Setting, Technical report, RRSG, University of Cape Town.

Drinkwater, M.R., R. Kwok and E. Rignot (1990), Synthetic Aperture Radar Polarimetry of Sea Ice, *in* 'Proceedings of IGARSS '.

Driscoll, T. and S. Healey (1999), Work-related fatalities in the opal mining industry in Australia, 1989 to 1992, Technical report, National Occupational Health and Safety Commission, Australia.

Ebihara, S., M. Sato and H. Niitsuma (1996), Estimation of Reflector Position by a Directional Borehole Radar Using a Cylindrical Conformal Array, *in* 'Proceedings of 6th International Conference on GPR'.

Ebihara, S., M. Sato and H. Niitsuma (2000), 'Super-Resolution of Coherent Targets by Directional Borehole Radar', *IEEE Transactions on Geoscience and Remote Sensing* **38**(4), 1725–1732.

Elachi, C., L.E. Roth and G.G. Schaber (1984), 'Spaceborne Radar Subsurface Imaging in Hyperarid Regions', *IEEE Transactions on Geoscience and Remote Sensing* **22**(4), 383–387.

Ellefsen, K.J. (1999), 'Effects of layered sediments on the guided wave in crosswell radar data', *Geophysics* **64**(6), 1698–1707.

Evans, D.L., T.G. Farr, J.J. van Zyl and H.A. Zebker (1988), 'Radar Polarimetry: Analysis Tools and Applications', *IEEE Transactions on Geoscience and Remote Sensing* **26**(6), 774–789.

Evans, S. (1963), ‘Radio techniques for the measurement of ice thickness’, *Polar Record* **11**, 406–410.

Farhat, N.H., C.L. Werner and T.H. Chu (1984), ‘Prospects for three-dimensional projective and tomographic imaging radar networks’, *Radio Science* **19**, 1347–55.

Fechner, T., U. Pippig, T. Richter, L. Corin, L. Halleux and R. Westermann (1998), Borehole radar surveys for limestone investigation, *in* ‘Proceedings of 7th International Conference on GPR’, pp. 743–746.

Francheschetti, G., M. Migliaccio and D. Riccio (1999), ‘On ocean SAR raw signal simulation’, *IEEE Transactions on Geoscience and Remote Sensing* **36**(1), 84–100.

Francheschetti, G., M. Migliaccio, D. Riccio and G. Schirinzi (1992), ‘SARAS: A Synthetic Aperture Radar (SAR) Raw Signal Simulator’, *IEEE Transactions on Geoscience and Remote Sensing* **30**(1), 110–123.

Fullagar, P.K. and D. Livelybrooks (1994), Trial of tunnel radar for cavity and ore detection in the Sudbury mining camp, Ontario, *in* ‘Proceedings of 5th International Conference on GPR’.

Fullagar, P.K., P. Zhang, Y. Wu and M.-J.Bertrand (1996), Application of radio frequency tomography to delineation of nickel sulphide deposits in the Sudbury basin, *in* ‘66th Annual Meeting, SEG’, pp. 2065–2068.

Galagedara, L.W., G.W. Parkin, J.D. Redman and A.L. Endres (2002), Temporal and spatial variation of soil water content measured by borehole GPR under irrigation and drainage, *in* ‘Proceedings of 9th International Conference on GPR’, pp. 180–185.

Gedney, S.D. (1996*a*), ‘An Anisotropic Perfectly Matched Layer-Absorbing Medium for the Truncation of FDTD Lattices’, *IEEE Transactions on Antennas and Propagation* **44**, 1630–1639.

Gedney, S.D. (1996*b*), ‘An Anisotropic PML Absorbing Media for the FDTD simulation of fields in lossy and dispersive media’, *Electromagnetics* **16**, 399–415.

Gedney, S.D. and A. Taflove (1998), *Perfectly Matched Layer Absorbing Boundary Conditions*, Chapter 7, in book Computational Electrodynamics: The Finite-Difference Time Domain Method, Boston, MA: Artech House.

Gelautz, M., H. Frick, J. Raggam, J. Burgstaller and F. Leberl (1998), ‘SAR image simulation and analysis of alpine terrain’, *ISPRS Journal of Photogrammetry and Remote Sensing* **53**, 17–38.

Geology of South Africa, Online (2003), ‘Impala Platinum Holdings’, *http://www.implats.co.za/operations/geology.asp* .

Gilson, E.W., J.D. Redman, J. Pilon and A.P. Annan (1996), Near Surface Applications of Borehole Radar, *in* ‘Proceedings of the Symposium on the Application of Geophysics to Environmental and Engineering Problems’, pp. 647–656.

Giroux, B., E. Gloaguen and M. Chouteau (2004), Geotechnical Application of Borehole GPR, *in* ‘Proceedings of 10th International Conference on GPR’, pp. 249–252.

Goldstein, R.M., H.A. Zebker and C.L. Werner (1988), ‘Satellite radar interferometry: two-dimensional phase unwrapping’, *Radio Science* **23**(4), 713–720.

Guindon, B. (1993), ‘Development of a SAR data acquisition planning tool (SARPLAN) based on image simulation’, *Int. J. Remote Sensing* **14**(2), 333–344.

Halleux, L., P. Feller, A. Monjoie and R. Pissart (1992), Ground penetrating and borehole radar surveys in the Borth salt mine (FRG), *in* ‘Proceedings of 4th International Conference on GPR’.

Hammon-III, W.S., X. Zeng and R.M. Corbeanu (2002), ‘Estimation of the spatial distribution of fluid permeability from surface and tomographic GPR data and core, with a 2-D example from the Ferron Sandstone, Utah’, *Geophysics* **67**(5), 1505–1515.

Harris, F.J. (1978), ‘On the use of windows for harmonic analysis with the discrete Fourier transform’, *Proceedings of IEEE* **66**, 51–83.

Herselman, P., W.J.A. van Brakel, W.J. Croukamp, G.S. Doyle and M. Rutschlin (2001), KLEINZEE: Arnot se Kop Trial Borehole Radar Survey on the Dikgat Farm, Technical report, University of Stellenbosch.

Holliger, K. and T. Bergmann (1999), Finite difference modeling of borehole georadar data, *in* ‘69th Annual Meeting, SEG’, pp. 457–460.

Holliger, K. and T. Bergmann (2002), ‘Numerical modeling of borehole georadar data’, *Geophysics* **67**(4), 1249–1258.

Holtzman, J., V. Frost, J. Abbott and V. Kaupp (1978), ‘Radar Image Simulation’, *IEEE Transactions on Geoscience and Remote Sensing* **16**(4), 296–303.

Hovanessian, S.A. (1984), *Radar System Design and Analysis*, Artech House, Norwood, MA.

Hovland, H.A., J.A. Johannessen and G. Digranes (1994), Slick Detection in SAR Images, *in* ‘Proceedings of IGARSS’.

Hulsmeyer, C. (1904), *German Patent*, No. 165546.

Inggs, M.R. (2002*a*), 3-D Imaging Utilising Non-Parallel Boreholes: Problem Definition, Technical report, RRSG, University of Cape Town.

Inggs, M.R. (2002*b*), Prospects for Borehole Radar In Kimberlite Pipe Dimensioning: Problem Definition Report, Technical report, RRSG, University of Cape Town.

Inggs, M.R., P.K. Mukhopadhyay and A.J. Wilkinson (2001), Borehole Interferometric SAR: A preliminary study, *in* ‘Proceedings of IGARSS’.

Inggs, M.R., P.K. Mukhopadhyay and A.J. Wilkinson (2002), 3-D Imaging Utilising Non-Parallel Boreholes: Interim Report, Technical report, RRSG, University of Cape Town.

Inggs, M.R. and R.H. Clarke (1979), A Computer Simulation of Propagation Through a Tenuous Random Medium, *in* ‘1979 IEEE Antennas and Propogation Society Symposium, AP/S 1997’, Institute of Electrical and Electronic Engineers.

Isaacson, A.R. (2002), A 500kHz to 5MHz Stepped Frequency Borehole Tomographic Imaging System, Master’s thesis, University of Cape Town.

Jha, P.C., V.R. Balasubramaniam, N. Sandeep, Y.V. Sivaram and R.N. Gupta (2004), GPR applications in mapping barrier thickness in coal mines: Some case studies, *in* ‘Proceedings of 10th International Conference on GPR’, pp. 605–608.

Johnson, D., C. Furse and A.C. Tripp (1998), FDTD Modelling of the Borehole EM Response of a Conductive Ore Deposit in a Lossy Dielectric, *in* ‘68th Annual Meeting, SEG’.

Jung, Y. and J.-H. Kim (1999), ‘Application of anisotropic georadar tomography to monitor rock physical property changes’, *Journal of Environmental and Engineering Geophysics* **4**, 87–92.

Just, D. and R. Bamler (1994), ‘Phase Statistics of Interferograms with Applications to Synthetic Aperture Radar’, *Applied Optics* **33**, 4361–4368.

Kim, J.-H., S.-J. Cho, M.-J. Yi and M. Sato (2004), Application of anisotropy borehole radar tomography in Korea, *in* ‘Proceedings of 10th International Conference on GPR’, pp. 241–244.

Korda, S. and M. Trninic (2002), *Design and Construction of a Ultrasonic Radar Emulator*, BSc Thesis, Department of Electrical Engineering, University of Cape Town.

Lane, J.W., F.P. Haeni and F.D. Day-Lewis (1998), Use of time-lapse attenuation-difference radar tomography methods to monitor saline tracer transport in fractured crystalline bedrock, *in* ‘Proceedings of 7th International Conference on GPR’, pp. 533–538.

Langman, A. (2002), The Design of Hardware and Signal Processing for a Stepped Frequency Ground Penetrating Radar, PhD thesis, University of Cape Town.

Langman, A. and M.R. Inggs (2001), Pulse versus Stepped Frequency Continuous Wave Modulation for Ground Penetrating Radar, *in* ‘Proceedings of IGARSS ’.

Leberl, F. (1990), *Radargrammetric image processing*, Artech House, Norwood, MA.

Leimbach, G. and H. Lowy (1910), *German Patent*, No. 237944.

Lengenfelder, R. (1998), The Design and Implementation of a Radar Simulator, Master’s thesis, University of Cape Town.

Leuschen, C. and R. Plumb (2000*a*), ‘A matched-filter approach to wave migration’, *Journal of Applied Geophysics* **43**(1-3), 271–280.

Leuschen, C. and R. Plumb (2000*b*), ‘A matched-filter approach to wave migration’, *Journal of Applied Geophysics* **43**, 271–280.

Li, F.K. and M.R. Goldstein (1990), ‘Studies of Multibaseline Spaceborne Interferometric Synthetic Aperture Radars’, *IEEE Transactions on Geoscience and Remote Sensing* **28**(1), 88–97.

Liu, L., J.W. Lane and Y. Quan (1998*a*), ‘Radar attenuation tomography using the centroid frequency downshift method’, *Journal of Applied Geophysics* **40**, 105–116.

Liu, L., J.W. Lane and Y. Quan (1998*b*), ‘Radar attenuation tomography using the centroid frequency downshift method’, *Journal of Applied Geophysics* **40**, 105–116.

Liu, Q., N. Osman, P. Manning, J. Hargreaves and G. Turner (1998), Borehole radar reflection characteristics of nickel sulphide ore shoots, *in* ‘Proceedings of the 1998 Australian Mining Technololgy Conference’, pp. 336–346.

Lomberg, K.G., E.S. Martin, M.A. Patterson and J.E. Venter (2000), ‘The Morphology of Potholes in the UG2 Chromitite Layer and Merensky Reef (Pothole Reef Facies)’, *at Union Section Rustenburg Platinum Mines* **ibid**, 209–220.

Lopez-Sanchez, J.M. and J. Fortuny-Guasch (2000), '3-D Radar Imaging Using Range Migration Techniques', *IEEE Transactions on Antennas and Propagation* **48**(5).

Lynne, G.J. and G.R. Taylor (1986), 'Geological Assessment of SIR-B Imagery of the Amadeus Basin, N.T., Australia', *IEEE Transactions on Geoscience and Remote Sensing* **24**(4), 575–581.

Lytle, R.J., E.F. Laine, D.L. Lager and D.T. Davis (1979), 'Cross-borehole electromagnetic probing to locate high-contrast anomalies', *Geophysics* **44**, 1667–1676.

Mala GeoScience, Online (2004), 'RAMAC/GPR Product', *http://ramac.malags.com/* .

Mason, I., N. Osman, Q. Liu, C. Simmat and M. Li (2001), 'Broadband Synthetic Aperture Borehole Radar Interferometry', *Journal of Applied Geophysics* **47**, 299–308.

Massonnet, D., M. Rossi, C. Carmona, F. Adragna, G. Peltzer and T. Rabaute (1993), 'The displacement field of the Landers earthquake mapped by radar interferometry', *Nature* **364**, 138–142.

McCann, D.M., P.D. Jackson and P.J. Fenning (1988), 'Comparison of seismic and ground probing radar methods in geological surveying', *IEE Proceedings* **135**(4), 380–391.

McCauley, J.F., C.S. Breed, G.G. Schaber, W.P. McHugh, B. Issawi, C.V. Haynes, M.J. Grolier and A.E. Kilani (1986), 'Paleodrainages of Eastern Sahara - The Radar Rivers Revisited', *IEEE Transactions on Geoscience and Remote Sensing* **24**(4), 624–648.

Mitra, S.K. (1999), *Digital Signal Processing: A Computer-Based Approach*, Tata McGraw-Hill Publishing Company Limited, New Delhi.

Miwa, T., M. Sato and H. Niitsuma (1999), 'Subsurface Fracture Measurement with Polarimetric Borehole Radar', *IEEE Transactions on Geoscience and Remote Sensing* **37**, 828–837.

Molinda, G.M. (2003), Geological Hazards and Roof Stability in Coal Mines, Technical report, U.S Department of health and human services, Publication No. 2003-152.

Moran, M.L., R.J. Greenfield, S.A. Arcone and A.J. Delaney (2000), 'Multidimensional GPR array processing using Kirchhoff migration', *Journal of Applied Geophysics* **43**(1-3), 281–295.

Morey, R.M. (1974), Continuous sub-surface profiling by impulse radar, *in* 'Proceedings Conference on Subsurface Exploration for Underground Excavation and Heavy Construction', pp. 213–232.

Morey, R.M. (1998), Crosshole radar and resistivity tomography, *in* ‘Proceedings of 7th International Conference on GPR’, pp. 527–532.

Moulton, C.W., D.L. Wright, S.R. Hutton, D.V. Smith and J.D. Abraham (2002), Basalt-flow imaging using a high-resolution directional borehole radar, *in* ‘Proceedings of 9th International Conference on GPR’, pp. 542–547.

Mukhopadhyay, P.K., A.J. Wilkinson and M.R. Inggs (2005), Synthetic Aperture Sonar 3-D Imaging of Targets using Multiple, non-Parallel Shot Lines, *in* ‘Proceedings of IGARSS’.

Mukhopadhyay, P.K., M.R. Inggs and A.J. Wilkinson (2001), Borehole Radar Interferometry, *in* ‘South African Geophysical Association’.

Mukhopadhyay, P.K., M.R. Inggs and A.J. Wilkinson (2004), Three-dimensional finite difference time domain modelling of borehole radar in mining applications, *in* ‘Proceedings of the 15th Annual Symposium of the PRASA, Cape Town, SA’.

Mukhopadhyay, P.K., M.R. Inggs and A.J. Wilkinson (2005), FDTD modelling of a borehole radar wave propagation: a 3-D simulation,study in conductive media, *in* ‘Proceedings of IGARSS’.

Mukhopadhyay, P.K., M.R. Inggs, R.T. Lord and A.J. Wilkinson (2002), 3-D Borehole Radar Imaging using Synthetic Aperture Time Domain Focusing., *in* ‘SEG 2002 International Exposition and 72nd Annual Meeting’, Society of Exploration Geophysicists.

Mukhopadhyay, P.K., R.T. Lord, M.R. Inggs, A.B. Wessel and J.H. Cloete (2002), Noise test experiment at Stellenbosch University, Technical report, University of Stellenbosch.

Mukhopadhyay, P.K., T. Bennett, M.R. Inggs and A.J. Wilkinson (2005), Borehole radar EM wave simulation for mining applications using a parallel implementation of the 3-D FDTD algorithm, *in* ‘South African Geophysical Association’.

Newitton, N. (2003), *Inverse Synthetic Aperture Imaging*, BSc Thesis, Department of Electrical Engineering, University of Cape Town.

Nickel, H., F. Sender, R. Thierbach and H. Weichart (1983), ‘Exploring the interior of salt domes from boreholes’, *Geophysical Prospecting* **31**, 131–148.

Nickel, H. and I. Cerny (1989), ‘More effective underground exploration for ores using radio waves’, *Expl. Geophysics* **20**, 371–377.

Noon, D.A. (1996), Stepped-frequency radar design and signal processing enhances ground penetrating radar performance, PhD thesis, University of Queensland.

Nyareli, T. (2003), Development of a Cable Odometer with a Network Interface, Master's thesis, University of Cape Town.

Olhoeft, G. R. (1998), Electrical, magnetic, and geometric properties that determine ground penetrating radar performance, *in* 'Proceedings of 7th International Conference on GPR', pp. 177–182.

Olhoeft, G.R. (1976), *Electrical properties of rocks, in the Physics and Chemistry of Rocks and Minerals*, Wiley,London.

Olhoeft, G.R. (1988*a*), Interpretation of hole-to-hole radar measurements, *in* 'Proceedings of 3rd Symposium on Tunnel Detection', pp. 616–629.

Olhoeft, G.R. (1988*b*), Selected bibliography on ground penetrating radar, *in* 'Proceedings of the Symposium on the Applications of Geophysics to Engineering and Environmental Problems, March 28-31, 1988, Golden, CO'. p. 462-520.

Olhoeft, G.R. (2000), 'Maximizing the information return from ground penetrating radar', *Journal of Applied Geophysics* **43**(1-3), 175–188.

Olsson, O., E. Falk, O. Forslund, L. Lundmark and E. Sandberg (1992), 'Borehole radar applied to the characterization of hydraulically conductive fracture zones in crystalline rock', *Geophysical Prospecting* **40**, 109–142.

Pitts, B. and A. Kramers (1996), The application of high resolution crosswell radio wave tomography in the exploration of base metal ore deposits, *in* '66th Annual Meeting, SEG', pp. 622–625.

Power, M., G. Belcourt and E. Rockel (2004), 'Geophysical methods for kimberlite exploration in northern Canada', *The Leading Edge* **23**(11), 1124–1134.

Pratt, R.G., W.J. McGaughey and C.H. Chapman (1993), 'Anisotropic velocity tomography: A case study in a near-surface rock mass', *Geophysics* **58**, 1748–1763.

Pretorius, C.C., W.F. Trewick and C. Irons (1997), 'Application of 3-D seismics to mine planning at Vaal Reefs Gold Mine, number 10 shaft, RSA', *Proceedings of Exploration 97: Fourth Decennial International Conference on Mineral Exploration* .

Ralston, C.J. (2000), Use of Ground Penetrating Radar in underground coal mining, *in* 'Proceedings of 8th International Conference on GPR', pp. 731–736.

Ramirez, A.L. and W.D. Daily (1987), ‘Evaluation of alterant geophysical tomography in welded tuff’, *Journal of Geophysical Research* **92**, 7843–7853.

Rao, V.M. and I.B.R. Rao (1983), ‘The radio wave absorption technique in Mailaram copper mines, India’, *Geophysics* **48**, 391–395.

Rappaport, C.M. (1995), ‘Perfectly matched absorbing boundary conditions based on anisotropic lossy mapping of space’, *IEEE Microwave and Guided Wave Letters* **5**, 90–92.

Reigber, A. and A. Moreira (2000), ‘First demonstration of airborne SAR tomography using multibaseline L-band data’, *IEEE Transactions on Geoscience and Remote Sensing* **38**, 2142–2152.

Reynolds, J.M. (2000), *An Introduction to Applied and Environment Geophysics*, John Wiley and Sons.

Rubin, L.A., J.C. Fowler and G.G. Marino (1978), Borehole radar, Technical report, Ensco Project 1114. Enso, Springfield, Virginia, U.S.A.

Rucareanu, M., M. Chouteau and G. Bellefleur (2000), Application of self-correcting tomographic inversion to a borehole radar test survey, *in* ‘Proceedings of 8th International Conference on GPR’, pp. 647–652.

Rutschlin, M. and J.H. Cloete (2000), Survey of Directional Antennas for Borehole Radar, Technical report, University of Stellenbosch.

Sacks, Z.S., D.M. Kingsland, R. Lee and J.F. Lee (1995), ‘A perfectly matched anisotropic absorber for use as an absorbing boundary condition’, *IEEE Transactions on Antennas and Propagation* **43**, 1460–1463.

Sato, M. and R. Thierbach (1991), ‘Analysis of borehole radar in crosshole mode’, *IEEE Transactions on Geoscience and Remote Sensing* **29**, 899–904.

Sato, M., T. Ohkubo and H. Niitsuma (1995), ‘Cross-Polarization Borehole Radar Measurements with a Solt Antenna’, *Journal of Applied Geophysics* **33**, 53–61.

Sato, M. and T. Tanimoto (1992), A Shielded Loop Array Antenna for a Directional Borehole Radar, *in* ‘Proceedings of 4th International Conference on GPR’.

Schaber, G.G., J.F. McCauley, C.S. Breed and G.R. Olhoeft (1986), ‘Shuttle Imaging Radar: Physical Controls on Signal Penetration and Subsurface Scattering in the Eastern Sahara’, *IEEE Transactions on Geoscience and Remote Sensing* **24**(4), 603–623.

Senechal, P., F. Hollender and G. Bellefleur (2000), GPR velocity and attenuation tomography corrected or artifacts due to media anisotrophy, borehole trajectory error and instrumental drift, *in* ‘Proceedings of 8th International Conference on GPR’, pp. 402–407.

Sheriff, R.E. and L.P. Geldart (1982), *Exploration Seismology*, Cambridge University Press (New York).

Siever, K. (2000), Three-Dimensional Borehole Radar Measurements - A Standard Logging Method, *in* ‘Proceedings of 8th International Conference on GPR’.

Simmat, C.M., N. Osman, J.E Hargreaves and I.M. Mason (2002), Borehole Radar Imaging from Deviating Boreholes, *in* ‘Proceedings of 9th International Conference on GPR’, pp. 404–409.

Skolnik, M.I. (1988), *Introduction to Radar Systems*, 2nd Edition, McGraw-Hill International Editions.

Stremler, F.G. (1990), *Introduction to Communication Systems*, Addision-Wesley Publishing Company, New York.

Taflove, A. (1995), *Computational electrodynamics : the finite-difference time-domain method*, Boston, Mass.:Artech House.

Taylor, J.D. (1995), *Introduction to Ultra-Wideband Radar Systems*, CRC Press.

Teixeira, F.L. and W.C. Chew (1997), ‘PML-FDTD in cylindrical and spherical coordinates’, *IEEE Microwave and Guided Wave Letters* **7**, 285–287.

Thierbach, R. (1974), ‘Electromagnetic reflections in salt deposits’, *Journal of Geophysics* **40**, 633–637.

Thierbach, R. (1994), Twenty years of ground probing radar in salt and potash mines, *in* ‘Proceedings of 5th International Conference on GPR’.

Thomson, S., J. Young and N. Sheard (1992), ‘Base metal applications of the radio imaging method: Current status and case studies’, *Exploration Geophysics* **23**, 367–372.

Topp, G.C., J.L. Davis and A.P. Annan (1980), ‘Electromagnetic determination of soil water content: Measurements in coaxial transmission lines’, *Water Resources Research* **16**, 574–528.

Trickett, J.C., F. Stevenson, D. Vogt, I.M. Mason, J. Hargreaves, H. Eybers, R. Fyn and M. Meyering (2000), The application of Borehole Radar to South African's ultra-deep gold mining environment, *in* 'Proceedings of 8th International Conference on GPR', pp. 676–681.

Tronicke, J., H. Paasche, K. Holliger and A.G. Green (2002), Combining cross-hole georadar velocity and attenuation tomography for site characterization: A case study in an unconsolidated aquifer, *in* 'Proceedings of 9th International Conference on GPR', pp. 170–175.

Tronicke, J. and K. Holliger (2004), 'Effects of gas- and water-filled boreholes on the amplitudes of crosshole georadar data as inferred from experimental evidence', *Geophysics* **69**(5), 1255–1260.

Turner, G. and A.F. Siggins (1994), 'Constant Q attenuation of subsurface radar pulses', *Geophysics* **59**(8), 1192–1200.

Ulaby, F.T., R.K. Moore and A.K Fung (1981), *Microwave Remote Sensors - Active and Passive*, Vol. 1, Addison-Wesley, Reading, Mass., USA.

Ulaby, T.F., R.K. Moore and A.K. Fung (1982), *Microwave Remote Sensing: Active and Passive. Volume II: Radar remote sensing and surface scattering and emission theory*, Addison-Wesley Publising House.

Ulander, M.H.Lars. and P.O.Frolind (1998), 'Ultra-Wideband SAR Interferometry', *IEEE Transactions on Geoscience and Remote Sensing* **36**(5), 1540–1550.

Ulriksen, C.P.F. (1982), Application of impulse radar to civil engineering, PhD thesis, Lund University of Technology, Sweden.

Unterberger, R.R. (1978), 'Radar Propagation in rock salt', *Geophysical Prospecting* **26**, 312–328.

Valle, S., L. Zanzi and F. Rocca (1999), 'Radar tomography for NDT: Comparison of techniques', *Journal of Applied Geophysics* **41**, 259–269.

van Brakel, W.J.A., M.D. van Wyk, M. Rutschlin and J.H. Cloete (2002), Effect of wet drilling in kaolinitic strata on borehole radar performance, *in* 'Proceedings of 9th International Conference on GPR', pp. 392–396.

van Dyk, C., A.J. Wilkinson and M.R. Inggs (2000), An Implementation and Characterisation of the Minimum Cost Flow Phase Unwrapping Algorithm, *in* 'Proceedings of EUSAR'.

van Leijen, Freek. (2001), Simulator for Radar Interferometry, Technical report, RRSG, University of Cape Town.

Vasco, D.W., J.E. Peterson and K.H. Lee (1997), ‘Ground penetrating radar velocity tomography in heterogeneous and anisotropic media’, *Geophysics* **62**, 1758–1773.

Vogt, D. (2001), A Borehole Radar System Design, *in* ‘South African Geophysical Association’.

Vogt, D. (2002), Borehole radar for mapping geological structure near the borehole, *in* ‘Workshop on Drilling Active Faults in South Africa Mines’.

Vogt, D. (2004), The Effect of Conductive Borehole Water on Borehole Radar, *in* ‘Proceedings of 10th International Conference on GPR’, pp. 217–220.

Wahl, T. and A. Skoelv (1994), ERS-1 SAR Imaging of Ocean Features in the Vestfjorden Area, *in* ‘Proceedings of IGARSS’.

Walford, M. (1985), ‘Exploration of temperate glaciers’, *Physics Bulletin* **36**, 108–109.

Wang, D. and G.A. McMechan (2002), ‘Finite-difference modeling of borehole ground penetrating radar data’, *Journal of Applied Geophysics* **49**, 111–127.

Wang, T. and G.W. Hohmann (1993), ‘A finite-difference time-domain solution for three-dimensional electromagnetic modeling’, *Geophysics* **58**(6), 797–809.

Wanstedt, S., S. Carlsten and S. Tiren (2000), ‘Borehole radar measurements aid structure geological interpretation’, *Journal of Applied Geophysics* **43**, 227–237.

Wehner, D.R. (1987), *High Resolution Radar*, Artech House, Norwood, MA.

Wilkinson, A.J. (1997), Techniques for 3-D Surface Reconstruction using Synthetic Aperture Radar Interferometry, PhD thesis, University College of London.

Wilkinson, A.J. (2001), Lecture notes on the Radar Signal Processing Fundamentals, Technical report, University of Cape Town.

Wilkinson, A.J., P.K. Mukhopadhyay, N. Lewitton and M.R. Inggs (2004), Inverse Synthetic Aperture Imaging using a 40 kHz Ultrasonic Laboratory Sonar, *in* ‘Proceedings of the 15th Annual Symposium of the PRASA, Cape Town, SA’.

Wilkinson, A.J., R.T. Lord and M.R. Inggs (1998), Stepped-Frequency Processing by Reconstruction of Target Reflectivity Spectrum, *in* ‘Proceedings of the 1998 IEEE South African Symposium on Communications and Signal Processing’, pp. 101–104.

Wilkinson, A.J., R.T. Lord and M.R. Inggs (2001), Repeat Pass SAR Interferometry at VHF Band, *in* ‘Proceedings of IGARSS’.

Wray, L.S. (2001), Synthetic Aperture Radar Image Simulator for Interferometry, Master’s thesis, University of Cape Town.

Wright, D.L., J.D. Abraham, K.J. Ellefsen and J. Rossabi (1998), Borehole radar tomography and dielectric logging at the Savannah River site, *in* ‘Proceedings of 7th International Conference on GPR’, pp. 539–544.

Wright, D.L. and R.D. Watts (1982), A single-hole, short-pulse radar system, Technical report, Geophysical investigations in connection with geological disposal of radioactive waste. OECD/NEA, Ottawa, Canada.

Xu, W. and B. Cumming (1997), Simulator for repeat-pass satellite InSAR studies, *in* ‘Proceedings of IGARSS’.

Yee, K.S. (1966), ‘Numerical solution of initial boundary value problems involving Maxwell’s equations in isotropic media’, *IEEE Transactions on Antennas and Propagation* **AP-14**(3), 302–307.

Zebker, A.H. and P. Rosen (1994), On the derivation of Coseismic Displacement Fields using Differential Radar Interferometry, *in* ‘Proceedings of IGARSS ’.

Zemansky, W.M. (1957), *Heat and Thermodynamics*, McGraw-Hill.

Zhou, B. and P.K. Fullagar (2000), Borehole radar conductivity and permittivity tomography, *in* ‘Proceedings of 8th International Conference on GPR’, pp. 542–547.

Zhou, C., L. Liu and J.W. Lane (2001), ‘Nonlinear inversion of borehole-radr tomography data to reconstruct velocity and attenuation distribution in earth materials’, *Journal of Applied Geophysics* **47**, 271–284.

Ziolkowski, R.W. (1997), ‘Time-derivative Lorentz materials and their utilization as electromagnetic absorbers’, *Physical Review E* **55**, 7696–7703.